frontiers | Research Topics

Noise and vibrations in offshore wind farms and their impact on aquatic species

Edited by
Rui He, Lijun Dong, Xiaomei Xu
and Apostolos Tsouvalas

Published in
Frontiers in Marine Science

ISSN 1664-8714
ISBN 978-2-8325-3698-8
DOI 10.3389/978-2-8325-3698-8

About Frontiers

Frontiers is more than just an open access publisher of scholarly articles: it is a pioneering approach to the world of academia, radically improving the way scholarly research is managed. The grand vision of Frontiers is a world where all people have an equal opportunity to seek, share and generate knowledge. Frontiers provides immediate and permanent online open access to all its publications, but this alone is not enough to realize our grand goals.

Frontiers journal series

The Frontiers journal series is a multi-tier and interdisciplinary set of open-access, online journals, promising a paradigm shift from the current review, selection and dissemination processes in academic publishing. All Frontiers journals are driven by researchers for researchers; therefore, they constitute a service to the scholarly community. At the same time, the *Frontiers journal series* operates on a revolutionary invention, the tiered publishing system, initially addressing specific communities of scholars, and gradually climbing up to broader public understanding, thus serving the interests of the lay society, too.

Dedication to quality

Each Frontiers article is a landmark of the highest quality, thanks to genuinely collaborative interactions between authors and review editors, who include some of the world's best academicians. Research must be certified by peers before entering a stream of knowledge that may eventually reach the public - and shape society; therefore, Frontiers only applies the most rigorous and unbiased reviews. Frontiers revolutionizes research publishing by freely delivering the most outstanding research, evaluated with no bias from both the academic and social point of view. By applying the most advanced information technologies, Frontiers is catapulting scholarly publishing into a new generation.

What are Frontiers Research Topics?

Frontiers Research Topics are very popular trademarks of the *Frontiers journals series*: they are collections of at least ten articles, all centered on a particular subject. With their unique mix of varied contributions from Original Research to Review Articles, Frontiers Research Topics unify the most influential researchers, the latest key findings and historical advances in a hot research area.

Find out more on how to host your own Frontiers Research Topic or contribute to one as an author by contacting the Frontiers editorial office: frontiersin.org/about/contact

Noise and vibrations in offshore wind farms and their impact on aquatic species

Topic editors
Rui He — Hohai University, China
Lijun Dong — Institute of Deep-Sea Science and Engineering, Chinese Academy of Sciences (CAS), China
Xiaomei Xu — Xiamen University, China
Apostolos Tsouvalas — Delft University of Technology, Netherlands

Citation
He, R., Dong, L., Xu, X., Tsouvalas, A., eds. (2023). *Noise and vibrations in offshore wind farms and their impact on aquatic species*. Lausanne: Frontiers Media SA.
doi: 10.3389/978-2-8325-3698-8

Table of contents

04 Editorial: Noise and vibrations in offshore wind farms and their impact on aquatic species
Rui He, Apostolos Tsouvalas, Xiaomei Xu and Lijun Dong

06 Second-order Stokes wave-induced dynamic response and instantaneous liquefaction in a transversely isotropic and multilayered poroelastic seabed
Zhiqing Zhang, Bohao Zhou, Xibin Li and Zhe Wang

25 Underwater noise characteristics of offshore exploratory drilling and its impact on marine mammals
Long-Fei Huang, Xiao-Mei Xu, Liang-Liang Yang, Shen-Qin Huang, Xin-Hai Zhang and Yang-Liang Zhou

36 Assessing differences in acoustic characteristics from impact and vibratory pile installation and their potential effects on the large yellow croaker (*Pseudosciaena crocea*)
Fuqiang Niu, Jiarui Xie, Xuexin Zhang, Ruichao Xue, Benqing Chen, Zhenwen Liu and Yanming Yang

46 Managing human activity and marine mammals: A biologically based, relativistic risk assessment framework
Brandon L. Southall, Dominic Tollit, Jennifer Amaral, Christopher W. Clark and William T. Ellison

61 The influence of contact relaxation on underwater noise emission and seabed vibrations due to offshore vibratory pile installation
Timo Molenkamp, Apostolos Tsouvalas and Andrei Metrikine

75 Vector acoustic properties of underwater noise from impact pile driving measured within the water column
Peter H. Dahl, Alexander MacGillivray and Roberto Racca

85 Indo-Pacific finless porpoises presence in response to pile driving on the Jinwan Offshore Wind Farm, China
Liang Fang, Min Li, Xinxing Wang, Yujian Chen and Tao Chen

93 Measurements of underwater operational noise caused by offshore wind turbine off the southwest coast of Korea
Young Geul Yoon, Dong-Gyun Han and Jee Woong Choi

102 A multi-physics approach for modelling noise mitigation using an air-bubble curtain in impact pile driving
Yaxi Peng, Antonio Jarquin Laguna and Apostolos Tsouvalas

Frontiers in Marine Science

TYPE Editorial
PUBLISHED 28 September 2023
DOI 10.3389/fmars.2023.1293733

Check for updates

OPEN ACCESS

EDITED AND REVIEWED BY
Hervé Claustre,
Centre National de la Recherche Scientifique (CNRS), France

*CORRESPONDENCE
Rui He
herui@hhu.edu.cn

RECEIVED 13 September 2023
ACCEPTED 22 September 2023
PUBLISHED 28 September 2023

CITATION
He R, Tsouvalas A, Xu X and Dong L (2023) Editorial: Noise and vibrations in offshore wind farms and their impact on aquatic species.
Front. Mar. Sci. 10:1293733.
doi: 10.3389/fmars.2023.1293733

Editorial: Noise and vibrations in offshore wind farms and their impact on aquatic species

Rui He[1]*, Apostolos Tsouvalas[2], Xiaomei Xu[3] and Lijun Dong[4]

[1]College of Harbor, Coastal and Offshore Engineering, Hohai University, Nanjing, China, [2]Department of Civil Engineering and Geosciences, Delft University of Technology, Delft, Netherlands, [3]College of Ocean and Earth Sciences, Xiamen University, Xiamen, China, [4]Institute of Deep-sea Science and Engineering, Chinese Academy of Sciences (CAS), Sanya, China

KEYWORDS

underwater noise, vibration, offshore wind turbine, offshore pasture, dynamic safety, noise reduction, vibration control, aquatic species

Editorial on the Research Topic
Noise and vibrations in offshore wind farms and their impact on aquatic species

1 Introduction

Offshore wind energy is environmentally friendly for humans, but it may not be so for aquatic life. Underwater noise and seabed vibrations are generated during the construction, maintenance, operation and decommissioning of offshore wind farms. The potential impact of the generated noise and the seabed vibrations on aquatic species may hinder further deployment of offshore wind farms and marine ranching. Thus, it is of great importance to understand the physics of the generation and propagation of the underwater noise (Reinhall and Dahl, 2011; Lippert et al., 2016; Tsouvalas, 2020; He et al., 2023), the seabed vibrations and their impact on aquatic species during the whole lifetime of a wind farm. Moreover, it becomes urgent to propose marine biological acoustic protection technology (Madsen et al., 2006; Helen et al., 2010; U.S. Offshore Wind Synthesis of Environmental Effects Research, 2022).

The aim of this Research Topic is to discuss the underwater noise and seabed vibrations generated during the construction and operation of offshore wind farms and their potential impact on aquatic species, as well as relevant underwater noise and vibration mitigation strategies. It is hoped that the papers published in this Research Topic will help one to better understand the interactions between offshore wind farms and aquatic species, and to summarise the latest achievements in relevant acoustic mitigation technologies.

2 Vibrations and underwater noise and their impact on aquatic species

In total, nine papers have been published in this Research Topic. The papers are of high quality and cover a wide range of topics related to seafloor vibrations and underwater noise. Southall et al. presented a biologically based framework for assessing the overall risk to marine mammals from human disturbance in defined scenarios. The aim is to provide a simple tool to objectively assess potential biological risk and to identify actionable risk reduction measures. Zhang et al. proposed a semi-analytical solution for the dynamic response of a multilayered seafloor under nonlinear ocean waves. Dahl et al. investigated the vector acoustic properties of underwater noise from pile driving. The well-known Mach wave characteristics are observed in both pressure and particle motion measurements. It provides an experimental reference for the choice of instrumentation for acoustic monitoring of offshore pile driving. The impact of underwater survey noise was studied in detail by Huang et al. From the field data, hammering noise is an impulsive sound with the dominant frequency below 10 kHz, which can cause a high risk of hearing damage to marine mammals. Vibrating and drilling sounds, on the other hand, are periodic sounds that can only cause hearing damage to marine mammals at a distance of about 40 meters. Fang et al. recorded the responses of Indo-Pacific finless porpoises to pile-driving activity at the Jinwan offshore wind farm, China. They found that there was a significant negative correlation between porpoise acoustic activities and pile driving, and that the interval between porpoise acoustic activities during pile driving increased compared to the period without pile driving. Yoon et al. measured underwater noise near a 3 MW wind turbine off the southwest coast of Korea. The underwater noise was found to be highly related to the acceleration of the tower vibration, the wind speed and the rotor speed. The peak level of the underwater noise at a frequency of 198 Hz increased by at least 20 dB at the rated rotor speed. Based on collected field data, Niu et al. analysed the differences between underwater noise from impact pile driving and vibratory pile driving, and the effects of the two types of noise on the large yellow croaker. The range of behavioral disturbance for adult large yellow croaker is predicted to be 4798 m and 1779 m for impact pile driving and vibratory pile driving, respectively. Molenkamp et al. investigated underwater noise and seabed vibrations from vibratory pile driving using pile-soil contact spring elements to account for the influence of pile-soil contact relaxation. It is found that the pile-soil interaction becomes crucial in the case of vibratory pile driving while in the case of impact pile driving this is of secondary importance. Finally, Peng et al. proposed a multi-physics model for modelling underwater pile driving noise mitigation including multiple air-bubble curtains. This multi-physics model can help investigating the water- and ground-borne wave transmission paths in a systematic way. The difference between single air-bubble curtain and double air- bubble curtain is also evaluated. The adopted modelling framework can help the offshore industry to optimize the deployment of the air-bubble curtain systems to achieve maximum noise reduction.

Author contributions

RH: Writing – original draft. AT: Writing – review & editing. XX: Writing – review & editing. LD: Writing – review & editing.

Funding

The first author would like to acknowledge the Grant No. BK20190074 from the Natural Science Foundation of Jiangsu Province.

Acknowledgments

The authors are grateful for the supports from all authors and reviewers.

Conflict of interest

The authors declare that the research was conducted in the absence of any commercial or financial relationships that could be construed as a potential conflict of interest.

Publisher's note

All claims expressed in this article are solely those of the authors and do not necessarily represent those of their affiliated organizations, or those of the publisher, the editors and the reviewers. Any product that may be evaluated in this article, or claim that may be made by its manufacturer, is not guaranteed or endorsed by the publisher.

References

Helen, B., Bridget, S., Dave, S., Jan, R., Gordon, P., and Paul, M. T. (2010). Assessing underwater noise levels during pile-driving at an offshore wind farm and its potential effects on marine mammals. *Mar. pollut. Bull.* 60, 888–897. doi: 10.1016/j.marpolbul.2010.01.003

He, R., Xiang, Y.H., and Guo, Z. (2023). A Poroelastic Model for Near-Field Underwater Noise Caused by Offshore Monopile Driving. *J. Sound. Vib.* 564, 117878.

Lippert, S., Nijhof, M., Lippert, T., Wilkes, D., Gavrilov, A., Heitmann, K., et al. (2016). COMPILE–a generic benchmark case for predictions of marine pile-driving noise. *IEEE J. Oceanic. Eng.* 41, 1061–1071. doi: 10.1109/JOE.2016.2524738

Madsen, P., Wahlberg, M., Tougaard, J., Lucke, K., and Tyack, P. (2006). Wind turbine underwater noise and marine mammals: Implications of current knowledge and data needs. *Mar. Ecol. Prog. Ser.* 309, 279–295. doi: 10.3354/meps309279

Reinhall, P. G., and Dahl, P. H. (2011). Underwater Mach wave radiation from impact pile driving: Theory and observation. *J. Acoust. Soc. Am.* 130, 1209–1216. doi: 10.1121/1.3614540

Tsouvalas, A. (2020). Underwater noise emission due to offshore pile installation: A review. *Energies* 13, 3037. doi: 10.3390/en13123037

U.S. Offshore Wind Synthesis of Environmental Effects Research (2022). *Underwater noise effects on marine life associated with offshore wind farms. Report by national renewable energy laboratory and pacific northwest national laboratory for the U.S* (Department of Energy, Wind Energy Technologies Office). Available at: https://tethys.pnnl.gov/seer.

frontiers | Frontiers in Marine Science

TYPE Original Research
PUBLISHED 20 December 2022
DOI 10.3389/fmars.2022.1082337

Check for updates

OPEN ACCESS

EDITED BY
Rui He,
Hohai University, China

REVIEWED BY
Junliang Gao,
Jiangsu University of Science and Technology, China
Wenbing Wu,
China University of Geosciences, China

*CORRESPONDENCE
Xibin Li
ytulxb@zafu.edu.cn
Zhe Wang
wangzsd@zjut.edu.cn

SPECIALTY SECTION
This article was submitted to Ocean Observation, a section of the journal Frontiers in Marine Science

RECEIVED 28 October 2022
ACCEPTED 28 November 2022
PUBLISHED 20 December 2022

CITATION
Zhang Z, Zhou B, Li X and Wang Z (2022) Second-order Stokes wave-induced dynamic response and instantaneous liquefaction in a transversely isotropic and multilayered poroelastic seabed. *Front. Mar. Sci.* 9:1082337. doi: 10.3389/fmars.2022.1082337

Second-order Stokes wave-induced dynamic response and instantaneous liquefaction in a transversely isotropic and multilayered poroelastic seabed

Zhiqing Zhang[1], Bohao Zhou[2], Xibin Li[1]* and Zhe Wang[2]*

[1]School of Landscape Architecture, Zhejiang A & F University, Hangzhou, Zhejiang, China,
[2]Institute of Geotechnical Engineering, Zhejiang University of Technology, Hangzhou, Zhejiang, China

The ocean waves exhibit obvious non-linearity with asymmetric distribution of wave crests and troughs, which could induce significantly different effect on the seabed compared to the commonly used linear wave theory. In this paper, a semi-analytical solution for a transversely isotropic and multilayered poroelastic seabed under non-linear ocean wave is proposed by virtue of the dual variable and position (DVP) method. The ocean wave and seabed are, respectively, modelled using second-order Stokes theory and Biot's complete poroelastodynamic theory. Then the established governing equations are decoupled and solved *via* the powerful scalar potential functions. Making use of the DVP scheme, the layered solutions are finally gained by combining the boundary conditions of the seabed. The developed solutions are verified by comparing with existing solutions. The selected numerical examples are presented to investigate the effect of main parameters on the dynamic response of the seabed and evaluate the corresponding liquefaction potential. The results show that the anisotropic stiffness and permeability, degree of saturation and stratification have remarkable influence on the dynamic response and liquefaction behavior of the seabed. The present solution is a useful tool to estimate the stability of transversely isotropic and layered seabed sediment in the range of non-linear ocean wave.

KEYWORDS
transverse isotropy, multilayered poroelastic seabed, non-linear wave, dynamic response, liquefaction

1 Introduction

With the increasing utilization of land-based resources, people have begun to turn their attention to the oceans and promote the development of offshore drilling rigs, offshore wind turbines, even the wind power generation in deep water environments (Jouffray et al., 2020; He et al., 2022a; He et al., 2022b). As the main deep foundation elements for marine structures, the vibration characteristics of monopiles under mechanical and seismic loads have received detailed investigations in recent years (Chen et al., 2022a; Chen et al., 2022b; Zhang et al., 2022). It should be pointed out that harbor oscillations induced by infragravity waves or transient wave groups (Gao et al., 2017; Gao et al., 2020; Gao et al., 2021) can interrupt the normal operation of docks, cause the extreme movements of moored ships, and even give rise to the break of mooring lines. Moreover, liquefaction of the seabed induced by sea wave (Jeng, 2015) can cause the destruction of offshore structures, which further affects the safety of human operations in ocean and even leads to accidents (e.g., oil spills) with a negative impact on the marine ecosystem (Soto et al., 2014; Joydas et al., 2017). The United Nations aimed to achieve considerable progress in science and technology areas to generate safe and clean oceans from 2021 to 2030 (Ryabinin et al., 2019). The seabed would liquefy when it is subjected to wave loadings or seismic loadings, and it was found that the liquefaction mechanism for the seabed under wave and earthquake actions is similar (Ye et al., 2018). Considering that the waves are the most frequent load over the seabed in the ocean environment, the dynamic response and liquefaction behavior of the seabed under wave loadings are the key factors in the design of marine structures.

Since the middle of the last century, scholars began to investigate the dynamic response of the seabed under wave load. Due to complexity of the problem, researchers attempted to present the explicit closed-form solution for the wave-induced seabed response based on the quasi-static (QS) governing equation, such as general consolidation equation of Biot (1941) or storage equation of Verruijt (1969). Yamamoto et al. (1978) and Madsen (1978) derived their analytical solutions for the dynamic response of poroelastic seabed under linear wave. Following the work by Yamamoto et al. (1978), Okusa (1985) further considered the effect of seabed saturation and obtained the analytical solution for unsaturated seabed. In addition, various waved-induced seabed response problems have been investigated in terms of the QS governing equation (Mei and Foda, 1981; Hsu et al., 1993; Tsai and Lee, 1995; Jeng and Seymour, 1997; Kitano and Mase, 2001). In view of QS governing equation disregarding the accelerations of the pore fluid and soil skeleton, the subsequent studies mainly based on the fully or partly poroelastodynamic theory by Biot (1956), Biot (1962) and Zienkiewicz et al. (1980). Sakai et al. (1988) considered the effects of the acceleration of pore fluid and solid and the gravity, and derived the analytical solution of the seabed response under small amplitude wave. Jeng et al. (1999); Jeng and Rahman (2000); Jeng and Zhang (2005) used a partly dynamic (PD) formulation in their study and found that the dynamic response of the seabed under certain combinations of different wave and seabed conditions differs significantly from that without considering inertial items. The similar conclusions about the contribution of inertial items can also be found in Yuhi and Ishida (1998) and Quiuqui et al. (2022), who employed the fully dynamic (FD) formulation to solve the related problem. To enhance the practicability of the simplified solutions in engineering, Ulker et al. (2009) presented the scope of application of FD, PD and QS formulations in the frame of linear wave theory. Besides, Le Méhauté (1976) provided the scope of application of different wave models corresponding to different types of ocean waves and seabed conditions. The dynamic response of the seabed under different types of wave loadings has been studied in detail, such as cnoidal wave (Hsu et al., 2019), second-order Stokes wave (Jeng and Cha, 2003) and the combination of wave and currents (Qi et al., 2020).

Seabed tends to exhibit anisotropy and stratification due to the long-time natural sediment process. The researchers gradually paid their effort to seek the influence mechanism of material anisotropy and stratification on the dynamic response of the seabed. Jeng and Seymour (1997) studied the influence of hydraulic anisotropy on the waved-induce seabed response, however the soil is limited to isotropic medium. Gatmiri (1992) carried out the numerical analysis of the dynamic response of sandy seabed considering material anisotropy, and found that the effect of anisotropic parameters on the dynamic response of seabed is significant. Hsu and Jeng (1994) developed an analytical solution for the wave-induced response of the seabed by modelling the seabed material as transversely isotropic (TI) medium. Subsequent study on TI seabed also showed the significant effect of anisotropy on the dynamic response of the seabed (Yuhi and Ishida, 2002). For the layered seabed, Yamamoto (1981) analytically studied the response of multilayered poroelastic seabed to wave and found that the instabilities can be prevented by covering the bed by a layer of concrete blocks or rubble. Ulker's studies on two-layer seabed (Ulker, 2012a; Ulker, 2012b) indicated that material layering has great influence on the dynamic response of the seabed. However, the propagating matrix of the field quantities in his study is too cumbersome, hence the theoretical solution only models the seabed as a two-layer structure. Li et al. (2020) employed the DVP method to establish the propagating matrix among different layers, which greatly improved the computational efficiency. It is noted that DVP method is very powerful and stable, and has been applied in different study areas, such as geophysics (Zhou et al., 2021), time-harmonic load buried in layered poroelastic medium (Zhang and Pan, 2020), moving load over layered poroelastic medium

(Liu et al., 2022), and rigid disc resting on layered subgrade (Zhang and Pan, 2023), etc. Besides, Chen et al. (2022) employed the global dynamic stiffness matrix method to handle the layered structure. The comparison among different propagating matrix methods was reviewed by Pan (2019), which could give better understanding for the researchers to attack the layered problem.

Researchers have found from observations of waves on the sea surface that climatic factors generally cause the wave to show the non-linearity (Lauton et al., 2021). Jeng and Cha (2003) derived the analytical solutions for the dynamic response of a homogeneous seabed to second-order Stokes wave. Zhou et al. (2011) obtained the solution for a two-layer isotropic seabed under the action of second-order Stokes wave. By modelling the seabed as an elasto-plastic material, Chen et al. (2019) numerically analyzed the dynamic characteristics of a homogeneous TI poroelastic seabed under second-order Stokes wave. From previous works, the dynamic response of TI multilayered poroelastic seabed under non-linear wave has not been reported yet. Hence, the objective of the present study is to develop a semi-analytical solution to systematically investigate the dynamic response and liquefaction potential of TI multilayered poroelastic seabed under second-order Stokes wave. To achieve this end, we decouple Biot's complete dynamic equations for TI poroelastic medium using powerful scalar potential functions expressed in the ($\boldsymbol{u}$, p) form and gain the general solution for any homogeneous layer. Then we utilize the DVP method to derive the semi-analytical solutions for the layered seabed. Finally, the influence of the main soil parameters on the dynamic response and liquefaction behavior of seabed under both non-linear and linear waves is analyzed in detail.

2 The boundary-value problem

As shown in Figure 1, the second-order Stokes waves propagating over a TI layered poroelastic seabed with a rigid impermeable bottom is considered in the present study. The layered seabed is arranged from the top surface to the bottom of the seabed in the order of layer 1 to layer n. Following Li et al. (2020), the coordinate z is vertically upwards with the negative value below the mudline, hence the thickness of layer j ($1\le j\le n$) can be denoted by $h_j=z_{j-1}-z_j$. Each layer is assumed to be composed of homogeneous TI poroelastic material and the interfaces between adjacent layers are perfectly connected. Moreover, the wave-height, wavelength and depth of sea water are denoted by H, L and d, respectively.

2.1 Governing equations

Following Biot (1962) and Zienkiewicz et al. (1980), the equations of motion for the poroelastic medium can be expressed in terms of Cartesian coordinate system as

$$\sigma_{ij,j} = \rho\ddot{u}_i + \rho_f\ddot{w}_i \tag{1}$$

$$-p_{,i} = \rho_f\ddot{u}_i + \frac{\rho_f}{\phi}\ddot{w}_i + \frac{\rho_f g}{k_i}\dot{w}_i \tag{2}$$

where the subscript index following a comma and dot above a symbol indicate the derivative with respect to a spatial coordinate and time, respectively; σ_{ij} is the total stress tensor; p is the fluid pressure; ϕ is the porosity; $w_i=\phi(U_i-u_i)$ is the average displacement component of the fluid relative to the solid in which u_i and U_i are the displacement components of the solid skeleton and pore fluid, respectively; $\rho=(1-\phi)\rho_s+\phi\rho_f$ is the density of the solid-fluid mixture with ρ_f and ρ_s being the densities of fluid and solid, respectively; k_i is the permeability coefficient (or called hydraulic conductivity coefficient) in the ith direction; g indicates the acceleration of gravity.

Following generalized Hooke's law, the stress-strain relationship under plane strain condition can be written as

$$\begin{Bmatrix} \sigma_{xx} \\ \sigma_{zz} \\ \sigma_{xz} \\ p \end{Bmatrix} = \begin{bmatrix} A_{11} & A_{12} & 0 & M_{11} \\ A_{12} & A_{22} & 0 & M_{33} \\ 0 & 0 & A_{33} & 0 \\ M_{11} & M_{33} & 0 & M \end{bmatrix} \begin{Bmatrix} u_{x,x} \\ u_{z,z} \\ u_{x,z} \\ \zeta \end{Bmatrix} \tag{3}$$

in which

$$A_{11} = C_{11} + \alpha_1^2 M; A_{12} = C_{13} + \alpha_1\alpha_3 M; A_{22} = C_{33} + \alpha_3^2 M; A_{33} = C_{44};$$
$$M_{11} = -\alpha_1 M; M_{33} = -\alpha_3 M; \zeta = -(\partial w_x/\partial x + \partial w_z/\partial z) \tag{4}$$

$$\alpha_1 = 1 - \frac{C_{11}+C_{12}+C_{13}}{3K_s}; \alpha_3 = 1 - \frac{2C_{13}+C_{33}}{3K_s}$$
$$M = \left(\frac{1-\phi}{K_s} + \frac{\phi}{K_f} - \frac{2C_{11}+C_{33}+2C_{12}+4C_{13}}{9K_s^2}\right)^{-1} \tag{5}$$

where α_i (i=1, 3) and M are the Biot's effective stress coefficients and Biot's modulus, respectively; C_{11}, C_{12}, C_{13}, C_{33}, C_{44} are the elastic constants, and the relation between the elastic constants and engineering parameters is listed in **Appendix A**; K_s and K_f are bulk moduli of solid skeleton and the pore fluid, respectively.

When seabed is in the unsaturated state with very small amount of gas, the following relation holds

$$\frac{1}{K_f} = \frac{1}{K_w} + \frac{1-S_r}{P_{w0}} \tag{6}$$

where S_r is the degree of saturation; K_w is the true bulk modulus of elasticity of water which is generally selected as 2×10^9Pa; $P_{w0}=\rho_f gd$ is the absolute pore-fluid pressure with d being the depth of the sea water.

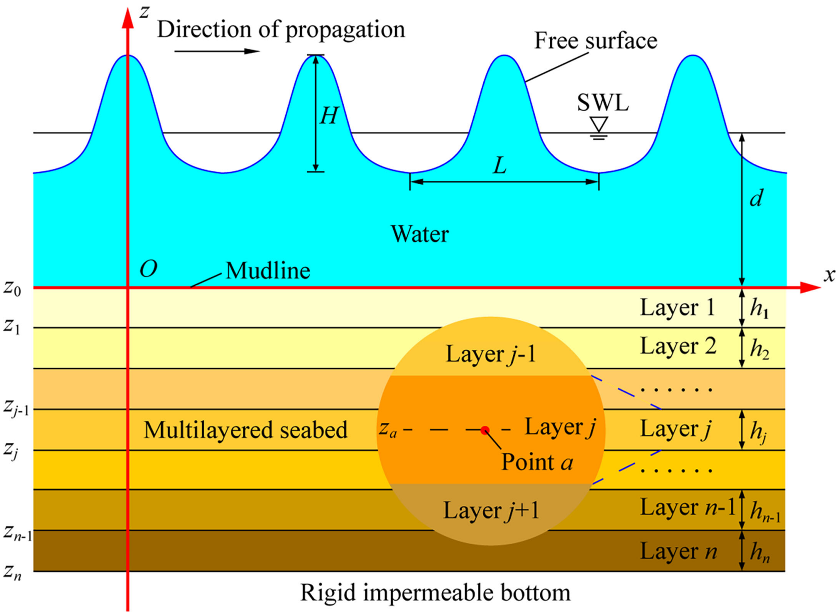

FIGURE 1
Interaction between the ocean wave and TI layered poroelastic seabed.

2.2 Continuity conditions

As already mentioned, we have assumed that any layer interface of the multilayered seabed is perfectly connected. Hence, the continuity conditions on $z=z_f$ can be written as ($i=x$, z; $j=x$, z)

$$\begin{aligned} u_i(z_{f+}) &= u_i(z_{f-}); \sigma_{ij}(z_{f+}) = \sigma_{ij}(z_{f-}); \\ w_z(z_{f+}) &= w_z(z_{f-}); p(z_{f+}) = p(z_{f-}) \end{aligned} \tag{7}$$

2.3 Boundary conditions

1) Boundary conditions at the seabed surface (z=0)

Based on the linear wave theory proposed by Wang (2017), it is known that the pressure on the seabed surface is maximum when the wave is at the crest and vice versa. According to the study by Jeng and Cha (2003), the dynamic wave pressure at the seabed surface (z=0) under the action of second-order Stokes wave can be expressed as

$$p_b(x,t) = \mathrm{Re}\sum_{m=1}^{2} P_m e^{im(kx-\omega t)} \tag{8}$$

in which

$$P_1 = \frac{\rho_f g H}{2\cosh(kd)} \tag{9}$$

$$P_2 = \frac{3}{4}\gamma_w H\left(\frac{\pi H}{L}\right)\frac{1}{\sinh(2kd)}\left[\frac{1}{\sinh^2(kd)} - \frac{1}{3}\right] \tag{10}$$

where $\mathrm{i}=(-1)^{0.5}$ is an imaginary number; $k=2\pi/L$ is the wavenumber (L=wavelength); $\omega=2\pi/T$ is the angular frequency of wave with period T. It is stated that we solve the problem in the complex variable domain to facilitate the derivation, hence we only take the real part of the complete solutions. Earlier study (Wang et al., 2005) has shown that the dispersion relation of second-order Stokes wave is consistent with linear wave, and ω can be calculated iteratively from the following equation

$$\omega^2 = gk\tanh(kd) \tag{11}$$

At the top surface of the seabed, the vertical effective stress and the shear stress are commonly assumed to be zero. Therefore, the boundary conditions on the top surface of the seabed can be written as

$$\sigma'_{zz} = \tau_{xz} = 0; p = p_b(x,t) \text{ at } z = z_0 = 0 \tag{12}$$

2) Boundary conditions at the seabed bottom

For the seabed of finite thickness with a rigid and impermeable bottom, the boundary condition can be expressed as

$$u_x = u_z = w_z = 0 \text{ at } z = z_n = -h \tag{13}$$

3 Semi-analytical solution for the multilayered poroelastic seabed

3.1 General solution to the governing equations

Since the wave-induced response of the seabed is periodic, we express the field quantities in the form of complex variables as

$$\begin{Bmatrix} u_x(x,z,t) \\ u_z(x,z,t) \\ w_x(x,z,t) \\ w_z(x,z,t) \\ p(x,z,t) \end{Bmatrix} = \sum_{m=1}^{2} \begin{Bmatrix} u_x^{(m)}(x,z,t) \\ u_z^{(m)}(x,z,t) \\ w_x^{(m)}(x,z,t) \\ w_z^{(m)}(x,z,t) \\ p^{(m)}(x,z,t) \end{Bmatrix} = \sum_{m=1}^{2} \mathrm{Re} \begin{Bmatrix} \bar{U}_x^{(m)}(z) \\ \bar{U}_z^{(m)}(z) \\ \bar{W}_x^{(m)}(z) \\ \bar{W}_x^{(m)}(z) \\ \bar{P}^{(m)}(z) \end{Bmatrix} \mathrm{e}^{\mathrm{i}m(kx-\omega t)} \tag{14}$$

where m=1, 2 represents the response caused by the first-order and the second-order waves, respectively. $\bar{U}_x^{(m)}$, $\bar{U}_z^{(m)}$, $\bar{W}_x^{(m)}$, $\bar{W}_z^{(m)}$and $\bar{P}^{(m)}$are the magnitudes of the dynamic response induced by the wave loading. To facilitate the derivation for the solution of the layered system in the following section, the stress components (e.g., $\sigma_{zz}(x, z, t)$, $\tau_{xz}(x, z, t)$) should also be expressed as the similar complex variable form. It is noted that the solution in the complex variables domain can be solved first, then taking the summation of the real part of each order results in the final solution.

Substituting Eq. (14) into Eq. (2), the following relations can be derived

$$\bar{W}_x^{(m)} = \left(\mathrm{i}km\bar{P}^{(m)} - \rho_f m^2\omega^2\bar{U}_x^{(m)}\right)\delta_1^{(m)} \tag{15}$$

$$\bar{W}_z^{(m)} = \left(\frac{\partial \bar{P}^{(m)}}{\partial z} - \rho_f m^2\omega^2\bar{U}_z^{(m)}\right)\delta_3^{(m)} \tag{16}$$

where

$$\delta_1^{(m)} = \left(\rho_f m^2\omega^2/\phi + \mathrm{i}m\omega\rho_f g/k_x\right)^{-1};$$
$$\delta_3^{(m)} = \left(\rho_f m^2\omega^2/\phi + \mathrm{i}m\omega\rho_f g/k_z\right)^{-1} \tag{17}$$

Combining Eqs. (1), (3), (14)-(16) and eliminating w_x and w_z, we have

$$\begin{bmatrix} a_1^{(m)} + C_{44}\mathrm{D}^2 & \mathrm{i}ka_2^{(m)}\mathrm{D} & \mathrm{i}ka_3^{(m)} \\ \mathrm{i}ka_2^{(m)}\mathrm{D} & a_4^{(m)} + C_{33}\mathrm{D}^2 & a_5^{(m)}\mathrm{D} \\ \mathrm{i}ka_3^{(m)} & a_5^{(m)}\mathrm{D} & -a_6^{(m)} - \delta_3^{(m)}\mathrm{D}^2 \end{bmatrix} \begin{bmatrix} \bar{U}_x^{(m)}(z) \\ \bar{U}_z^{(m)}(z) \\ \bar{P}^{(m)}(z) \end{bmatrix} = \begin{bmatrix} 0 \\ 0 \\ 0 \end{bmatrix} \tag{18}$$

where D is the differential operator (i.e., D=∂/∂z); $a_i^{(m)}$ (i=1-6) are the coefficients with being defined as

$$a_1^{(m)} = \rho m^2\omega^2 - m^2k^2C_{11} - \delta_1^{(m)}\rho_f^2 m^4\omega^4;\ a_2^{(m)} = m(C_{13} + C_{44});$$
$$a_3^{(m)} = \delta_1^{(m)}\rho_f m^3\omega^2 - m\alpha_1;$$
$$a_4^{(m)} = \rho m^2\omega^2 - m^2k^2C_{44} - \delta_3^{(m)}\rho_f^2 m^4\omega^4;$$
$$a_5^{(m)} = \delta_3^{(m)}\rho_f m^2\omega^2 - \alpha_3;\ a_6^{(m)} = \tfrac{1}{M} - \delta_1^{(m)}m^2k^2 \tag{19}$$

The potential function $\bar{\Phi}^{(m)}(z)$ is introduced, which has been successfully applied to the dynamic response of the seabed under linear wave (Li et al., 2020). The aforementioned field quantities can be expressed in terms of potential function as

$$\bar{U}_x^{(m)}(z) = -\mathrm{i}k\left[a_2^{(m)}\left(a_6^{(m)} + \delta_3^{(m)}\mathrm{D}^2\right) + a_3^{(m)}a_5^{(m)}\right]\mathrm{D}\bar{\Phi}^{(m)}(z)$$
$$\bar{U}_z^{(m)}(z) = \left[\left(a_6^{(m)} + \delta_3^{(m)}\mathrm{D}^2\right)\left(a_1^{(m)} + C_{44}\mathrm{D}^2\right) - \left(a_3^{(m)}\right)^2k^2\right]\bar{\Phi}^{(m)}(z)$$
$$\bar{P}^{(m)}(z) = \left[a_5^{(m)}\left(a_1^{(m)} + C_{44}\mathrm{D}^2\right) + a_2^{(m)}a_3^{(m)}k^2\right]\mathrm{D}\bar{\Phi}^{(m)}(z) \tag{20}$$

It is noted that the introduced potential function automatically satisfies the first and third equations in Eq. (18). Substituting Eq. (20) into Eq. (18), the final form of the governing equation can be written as

$$r_1^{(m)}\mathrm{D}^6\bar{\Phi}^{(m)}(z) + r_2^{(m)}\mathrm{D}^4\bar{\Phi}^{(m)}(z) + r_3^{(m)}\mathrm{D}^2\bar{\Phi}^{(m)}(z) + r_4^{(m)}\bar{\Phi}^{(m)}(z) = 0 \tag{21}$$

where $r_i^{(m)}$ (i=1-4) are coefficients, whose detailed expressions are given in **Appendix B**.

Through some algebraic calculations, the solution of Eq. (21) can be given as

$$\bar{\Phi}^{(m)}(z) = \sum_{i=1}^{3} A_i^{(m)}\mathrm{e}^{\lambda_i^{(m)}z} + B_i^{(m)}\mathrm{e}^{-\lambda_i^{(m)}z} \tag{22}$$

where $\pm\lambda_i^{(m)}$(i=1-3) are given in **Appendix C**. The values of $A_i^{(m)}$and $B_i^{(m)}$(i=1-3) are to be determined by the boundary conditions.

Substituting Eq. (22) into Eq. (20) and performing some algebraic calculations, the general solutions of displacements, pore pressure and stresses in any homogeneous layer under the action of second-order Stokes wave can be expressed as

$$\begin{aligned} u_x^{(m)}(x,z,t) &= \sum_{i=1}^{3}\chi_i^{(m)}\left(A_i^{(m)}e^{\lambda_i^{(m)}z}-B_i^{(m)}e^{-\lambda_i^{(m)}z}\right)e^{im(kx-\omega t)} \\ u_z^{(m)}(x,z,t) &= \sum_{i=1}^{3}\varphi_i^{(m)}\left(A_i^{(m)}e^{\lambda_i^{(m)}z}+B_i^{(m)}e^{-\lambda_i^{(m)}z}\right)e^{im(kx-\omega t)} \\ p^{(m)}(x,z,t) &= \sum_{i=1}^{3}\xi_i^{(m)}\left(A_i^{(m)}e^{\lambda_i^{(m)}z}-B_i^{(m)}e^{-\lambda_i^{(m)}z}\right)e^{im(kx-\omega t)} \\ w_z^{(m)}(x,z,t) &= \sum_{i=1}^{3}\eta_i^{(m)}\left(A_i^{(m)}e^{\lambda_i^{(m)}z}+B_i^{(m)}e^{-\lambda_i^{(m)}z}\right)e^{im(kx-\omega t)} \end{aligned} \tag{23}$$

$$\begin{aligned} \sigma_{xx}^{(m)}(x,z,t) &= \sum_{i=1}^{3}\left(ikmC_{11}\chi_i^{(m)}+C_{13}\lambda_i^{(m)}\varphi_i^{(m)}-\alpha_1\xi_i^{(m)}\right) \\ &\qquad \left(A_i^{(m)}e^{\lambda_i^{(m)}z}-B_i^{(m)}e^{-\lambda_i^{(m)}z}\right)e^{im(kx-\omega t)} \\ \sigma_{zz}^{(m)}(x,z,t) &= \sum_{i=1}^{3}\left(ikmC_{13}\chi_i^{(m)}+C_{33}\lambda_i^{(m)}\varphi_i^{(m)}-\alpha_3\xi_i^{(m)}\right) \\ &\qquad \left(A_i^{(m)}e^{\lambda_i^{(m)}z}-B_i^{(m)}e^{-\lambda_i^{(m)}z}\right)e^{im(kx-\omega t)} \\ \tau_{xz}^{(m)}(x,z,t) &= \sum_{i=1}^{3}C_{44}\left(ikm\varphi_i^{(m)}+\lambda_i^{(m)}\chi_i^{(m)}\right) \\ &\qquad \left(A_i^{(m)}e^{\lambda_i^{(m)}z}+B_i^{(m)}e^{-\lambda_i^{(m)}z}\right)e^{im(kx-\omega t)} \end{aligned} \tag{24a}$$

$$\begin{aligned} \sigma'_{xx}(m)(x,z,t) &= \sum_{i=1}^{3}\left(ikmC_{11}\chi_i^{(m)}+C_{13}\lambda_i^{(m)}\varphi_i^{(m)}\right) \\ &\qquad \left(A_i^{(m)}e^{\lambda_i^{(m)}z}-B_i^{(m)}e^{-\lambda_i^{(m)}z}\right)e^{im(kx-\omega t)} \\ \sigma'_{zz}(m)(x,z,t) &= \sum_{i=1}^{3}\left(ikmC_{13}\chi_i^{(m)}+C_{33}\lambda_i^{(m)}\varphi_i^{(m)}\right) \\ &\qquad \left(A_i^{(m)}e^{\lambda_i^{(m)}z}-B_i^{(m)}e^{-\lambda_i^{(m)}z}\right)e^{im(kx-\omega t)} \end{aligned} \tag{24b}$$

where $\chi_i^{(m)}$, $\varphi_i^{(m)}$, $\xi_i^{(m)}$and $\eta_i^{(m)}$(i=1-3) are the coefficients given in **Appendix D**. It is noted that the effective stresses in Eq. (24b) are derived *via* the relations between total stress and pore pressure.

3.2. Solution of multilayered seabed

We adopt the dual variable and position (DVP) method (Pan, 2019; Liu et al., 2022) to expand the single-layer solution to the multilayered solution. It is stated again that the layered solution corresponding to different m will be solved separately and then be superposed together to gain the complete solution. To facilitate the derivation, $e^{im(kx\text{-}\omega t)}$ is suppressed, and the vectors and diagonal matrices are defined as

$$\begin{aligned} \mathbf{U}^{(m)}(z) &= [\bar{U}_x^{(m)}(z),\bar{U}_z^{(m)}(z),\bar{W}_z^{(m)}(z)]^{\mathrm{T}}; \\ \mathbf{T}^{(m)}(z) &= \left[\bar{\tau}_{xz}^{(m)}(z),\bar{\sigma}_{zz}^{(m)}(z),\bar{P}^{(m)}(z)\right]^{\mathrm{T}} \end{aligned} \tag{25}$$

$$\begin{aligned} \mathbf{E}_1^{(m)}(z) &= diag[e^{\lambda_1^{(m)}z},e^{\lambda_2^{(m)}z},e^{\lambda_3^{(m)}z}]; \\ \mathbf{E}_2^{(m)}(z) &= diag\left[e^{-\lambda_1^{(m)}z},e^{-\lambda_2^{(m)}z},e^{-\lambda_3^{(m)}z}\right] \end{aligned} \tag{26}$$

where $\bar{\tau}_{xz}^{(m)}(z)$and $\bar{\sigma}_{zz}^{(m)}(z)$are the stress magnitudes.

Then the single-layer solution for jth layer can be rewritten in terms of matrix form as

$$\begin{bmatrix}\mathbf{U}^{(m)}(z)\\ \mathbf{T}^{(m)}(z)\end{bmatrix}=\begin{bmatrix}\mathbf{M}_{11}^{(m)} & \mathbf{M}_{12}^{(m)}\\ \mathbf{M}_{21}^{(m)} & \mathbf{M}_{22}^{(m)}\end{bmatrix}\begin{bmatrix}\mathbf{E}_1^{(m)}(z-z_{j-1}) & 0\\ 0 & \mathbf{E}_2^{(m)}(z-z_j)\end{bmatrix}\begin{bmatrix}\mathbf{K}_+^{(m)}\\ \mathbf{K}_-^{(m)}\end{bmatrix} \tag{27}$$

where $[\mathbf{M}_{ij}^{(m)}]$ is the 3×3 submatrix of 6×6 matrix $M^{(m)}$, the elements of which are given in **Appendix E**.

Substituting z=z_{j-1} and z=z_j into Eq. (27), the solutions for the top and bottom interfaces of jth layer can be written as

$$\begin{bmatrix}\mathbf{U}^{(m)}(z_{j-1})\\ \mathbf{T}^{(m)}(z_{j-1})\end{bmatrix}=\begin{bmatrix}\mathbf{M}_{11}^{(m)} & \mathbf{M}_{12}^{(m)}\mathbf{E}_2^{(m)}(h_j)\\ \mathbf{M}_{21}^{(m)} & \mathbf{M}_{22}^{(m)}\mathbf{E}_2^{(m)}(h_j)\end{bmatrix}\begin{bmatrix}\mathbf{K}_+^{(m)}\\ \mathbf{K}_-^{(m)}\end{bmatrix} \tag{28}$$

$$\begin{bmatrix}\mathbf{U}^{(m)}(z_j)\\ \mathbf{T}^{(m)}(z_j)\end{bmatrix}=\begin{bmatrix}\mathbf{M}_{11}^{(m)}\mathbf{E}_1^{(m)}(-h_j) & \mathbf{M}_{12}^{(m)}\\ \mathbf{M}_{21}^{(m)}\mathbf{E}_1^{(m)}(-h_j) & \mathbf{M}_{22}^{(m)}\end{bmatrix}\begin{bmatrix}\mathbf{K}_+^{(m)}\\ \mathbf{K}_-^{(m)}\end{bmatrix} \tag{29}$$

By eliminating the unknown vectors $\mathbf{K}_+^{(m)}$, $\mathbf{K}_-^{(m)}$ and making use of DVP method, the relation for the layer j can be expressed as

$$\begin{bmatrix}\mathbf{U}^{(m)}(z_{j-1})\\ \mathbf{T}^{(m)}(z_j)\end{bmatrix}=\begin{bmatrix}\mathbf{N}_{11(j)}^{(m)} & \mathbf{N}_{12(j)}^{(m)}\\ \mathbf{N}_{21(j)}^{(m)} & \mathbf{N}_{22(j)}^{(m)}\end{bmatrix}\begin{bmatrix}\mathbf{U}^{(m)}(z_j)\\ \mathbf{T}^{(m)}(z_{j-1})\end{bmatrix} \tag{30}$$

where

$$\begin{aligned} \begin{bmatrix}\mathbf{N}_{11(j)}^{(m)} & \mathbf{N}_{12(j)}^{(m)}\\ \mathbf{N}_{21(j)}^{(m)} & \mathbf{N}_{22(j)}^{(m)}\end{bmatrix} &= \begin{bmatrix}\mathbf{M}_{11}^{(m)} & \mathbf{M}_{12}^{(m)}\mathbf{E}_2^{(m)}(h_j)\\ \mathbf{M}_{21}^{(m)}\mathbf{E}_1^{(m)}(-h_j) & \mathbf{M}_{22}^{(m)}\end{bmatrix} \\ &\qquad \begin{bmatrix}\mathbf{M}_{11}^{(m)}\mathbf{E}_1^{(m)}(-h_j) & \mathbf{M}_{12}^{(m)}\\ \mathbf{M}_{21}^{(m)} & \mathbf{M}_{22}^{(m)}\mathbf{E}_2^{(m)}(h_j)\end{bmatrix}^{-1} \end{aligned} \tag{31}$$

After gaining the layer-matrix relation for layer j+1, utilizing the continuity conditions Eq. (7) and making some algebraic operations leads to the recursive relationship from jth layer to (j+1)th layer

$$\begin{bmatrix}\mathbf{U}^{(m)}(z_{j-1})\\ \mathbf{T}^{(m)}(z_{j+1})\end{bmatrix}=\begin{bmatrix}\mathbf{N}_{11(j:j+1)}^{(m)} & \mathbf{N}_{12(j:j+1)}^{(m)}\\ \mathbf{N}_{21(j:j+1)}^{(m)} & \mathbf{N}_{22(j:j+1)}^{(m)}\end{bmatrix}\begin{bmatrix}\mathbf{U}^{(m)}(z_{j+1})\\ \mathbf{T}^{(m)}(z_{j-1})\end{bmatrix} \tag{32}$$

10.3389/fmars.2022.1082337

in which

$$\begin{aligned}
\left[\mathbf{N}^{(m)}_{11(j:j+1)}\right] &= \left[\mathbf{N}^{(m)}_{11(j)}\mathbf{N}^{(m)}_{11(j+1)}\right] + \left[\mathbf{N}^{(m)}_{11(j)}\mathbf{N}^{(m)}_{12(j+1)}\right] \\
&\qquad \left[\mathbf{I}-\mathbf{N}^{(m)}_{21(j)}\mathbf{N}^{(m)}_{12(j+1)}\right]^{-1}\left[\mathbf{N}^{(m)}_{21(j)}\mathbf{N}^{(m)}_{11(j+1)}\right] \\
\left[\mathbf{N}^{(m)}_{12(j:j+1)}\right] &= \left[\mathbf{N}^{(m)}_{12(j)}\right] + \left[\mathbf{N}^{(m)}_{11(j)}\mathbf{N}^{(m)}_{12(j+1)}\right] \\
&\qquad \left[\mathbf{I}-\mathbf{N}^{(m)}_{21(j)}\mathbf{N}^{(m)}_{12(j+1)}\right]^{-1}\left[\mathbf{N}^{(m)}_{22(j)}\right] \\
\left[\mathbf{N}^{(m)}_{21(j:j+1)}\right] &= \left[\mathbf{N}^{(m)}_{21(j+1)}\right] + \left[\mathbf{N}^{(m)}_{22(j+1)}\right] \\
&\qquad \left[\mathbf{I}-\mathbf{N}^{(m)}_{21(j)}\mathbf{N}^{(m)}_{12(j+1)}\right]^{-1}\left[\mathbf{N}^{(m)}_{21(j)}\mathbf{N}^{(m)}_{11(j+1)}\right] \\
\left[\mathbf{N}^{(m)}_{22(j:j+1)}\right] &= \left[\mathbf{N}^{(m)}_{22(j+1)}\right]\left[\mathbf{I}-\mathbf{N}^{(m)}_{21(j)}\mathbf{N}^{(m)}_{12(j+1)}\right]^{-1}\left[\mathbf{N}^{(m)}_{22(j)}\right]
\end{aligned} \tag{33}$$

where $\mathbf{I}$ denotes the identity matrix.

After obtaining the recurrence relation Eq. (32), the dynamic response of the layered seabed can be solved according to the boundary conditions. For the seabed of finite thickness, the boundary conditions in Eqs. (12) and (13) can be rewritten as

$$T^{(m)}(z_0) = [0, -\alpha_{31}P^{(m)}, P^{(m)}]^T \text{ at } z = z_0 = 0 \tag{34}$$

$$U^{(m)}(z_n) = 0 \text{ at } z = z_n = -h \tag{35}$$

where the subscript 1 in α_{31} denotes the layer number; $P^{(1)}=P_1$ and $P^{(2)}=P_2$.

In order to solve the dynamic response at arbitrary depth $z=z_a$ (say in layer j, see Figure 1), we further divide the homogeneous layer j into two sublayers, i.e., sublayers $a1$ and $a2$ on the top and bottom parts, respectively. We propagate the recursive relation Eq. (32) from layer 1 to sublayer $a1$ and from sublayer $a2$ to layer n, which yields the global matrix as

$$\begin{bmatrix} \mathbf{U}^{(m)}(z_0) \\ \mathbf{U}^{(m)}(z_a) \\ \mathbf{T}^{(m)}(z_a) \\ \mathbf{T}^{(m)}(z_n) \end{bmatrix} = \begin{bmatrix} -\mathbf{I} & \mathbf{N}^{(m)}_{11(1:a1)} & 0 & 0 \\ 0 & \mathbf{N}^{(m)}_{21(1:a1)} & -\mathbf{I} & 0 \\ 0 & -\mathbf{I} & \mathbf{N}^{(m)}_{12(a2:n)} & 0 \\ 0 & 0 & \mathbf{N}^{(m)}_{22(a2:n)} & -\mathbf{I} \end{bmatrix}^{-1} \begin{bmatrix} -\left[\mathbf{N}^{(m)}_{12(1:a1)}\right]\mathbf{T}^{(m)}(z_0) \\ -\left[\mathbf{N}^{(m)}_{22(1:a1)}\right]\mathbf{T}^{(m)}(z_0) \\ 0 \\ 0 \end{bmatrix} \tag{36}$$

Till here, the solutions for the filed quantities corresponding to different m are gained. Then taking the summation of solutions corresponding to m=1 and 2 yields the final solutions. It should be pointed out that for the homogeneous TI poroelastic seabed, the analytical solution can be easily derived by combining the boundary conditions in Eqs. (12) and (13), and general solution in Eqs. (23) and (24). In addition, if the seabed is actually a layered half-space, we only need set the nth layer with a very large thickness to gain the half-space results.

4 Numerical results and discussions

4.1 Verification of the present solution

In order to validate the reliability of the present solution, two cases corresponding to single-layer and multilayered seabed under linear wave are considered first. In the comparison, we take the amplitude of the pore pressure $|p|$ and vertical effective stress $|\sigma'_{zz}|$ as the analyzed physical quantities. That is to say, $|p|$ and $|\sigma'_{zz}|$ are the maximum value of p and σ'_{zz}, respectively. The variable used for normalization is defined as $p_0=\rho_f gH/(2\cosh(kd))$. For the single-layer seabed (e.g., graveled seabed), the solution of Jeng and Lee (2001) and the reduced one of the present study are compared with using the following parameters: T=15 s, d=20 m, H=2 m, h=20 m, ν=1/3, ϕ=0.35, S_r=0.95-1.0, ρ_s=2650 kg/m^3, ρ_f=1000 kg/m^3, $k_x=k_z=1\times10^{-1}$ m/s, $G_h=G_v=5\times10^7$ N/m^2. Moreover, the following poroelastic properties $\alpha_1=\alpha_3$ = 1 and $M=K_f/\phi$ are used in the present solution. Figure 2 shows the comparison of the present reduced solution with that by Jeng and Lee (2001) for a homogeneous isotropic and poroelastic seabed subjected to linear wave. In order to gain the reduced solution for linear wave, we need to fix P_2 = 0 and thus m=1. Notice that the complete Biot's poroelastodynamic theory are considered in both studies. It is observed from Figure 2 that the solution of the present study is in good agreement with that of Jeng and Lee (2001).

We further consider a two-layer seabed under linear wave and compare the reduced results from present study with those by Hsu et al. (1995) as shown in Figure 3. The parameters used for verification are: T=10 s, d=20 m, H=6 m, L=121.12 m, k_{z2} = 10^{-3} m/s, h_1 = 10 m and h_2 = 40 m. The remaining seabed parameters, except for permeability coefficient, are the same for both two layers and taken as ν=1/3, ϕ=0.3, S_r=0.975, ρ_f=1000 kg/m^3, ρ_s=2000 kg/m^3, $G_v=G_h=1\times10^7$ N/m^2, $\alpha_1=\alpha_3$ = 1 and $M=K_f/\phi$. It can be seen from Figure 3 that the results from the reduced solution of present study agree well with those of Hsu et al. (1995). It can be concluded from above two cases that the present solutions are applicable for both the single-layer and multilayered cases.

The present solution is further compared with the existing one for a homogeneous, isotropic and poroelastic seabed under nonlinear wave. In the comparison, the parameters are: T=10 s, d=10 m, L=240 m, H=0.08tanh(kd) m, h=50 m, ν=0.333, ϕ=0.3, ρ_s=2650 kg/m^3, ρ_f=1000 kg/m^3, $k_x=k_z=1\times10^{-3}$ m/s, $G_h=G_v=1\times10^7$ N/m^2, $\alpha_1=\alpha_3$ = 1 and $M=K_f/\phi$. Figure 4 shows

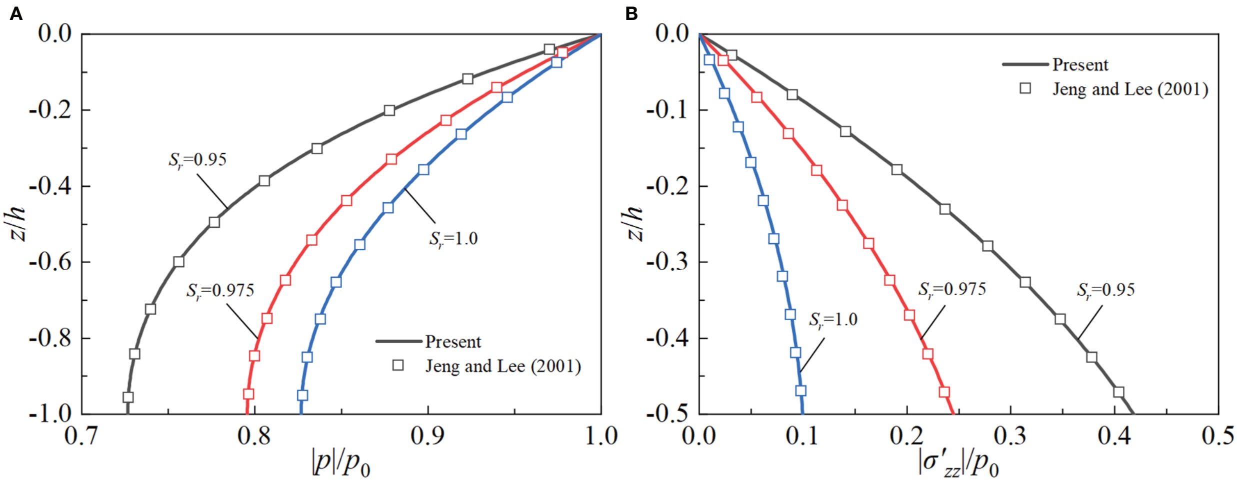

FIGURE 2
Comparison of the present solution with existing one for a homogeneous isotropic and poroelastic seabed under linear wave: **(A)** pore pressure; **(B)** vertical effective stress.

the comparison of the present reduced solution with that by Zhou et al. (2011) for a homogeneous, isotropic and poroelastic seabed subjected to second-order Stokes wave. $|u_z|$ in Figure 4 denotes the amplitude of u_z. It can be observed from Figure 4 that the results from the present study have good agreement with those from Zhou et al. (2011).

4.2 Numerical analysis

It has been mentioned in Li et al. (2020) that the linear wave-induced dynamic response of a finite-thickness seabed is dependent on the properties of the soil, and anisotropic stiffness and permeability have significant effect on the

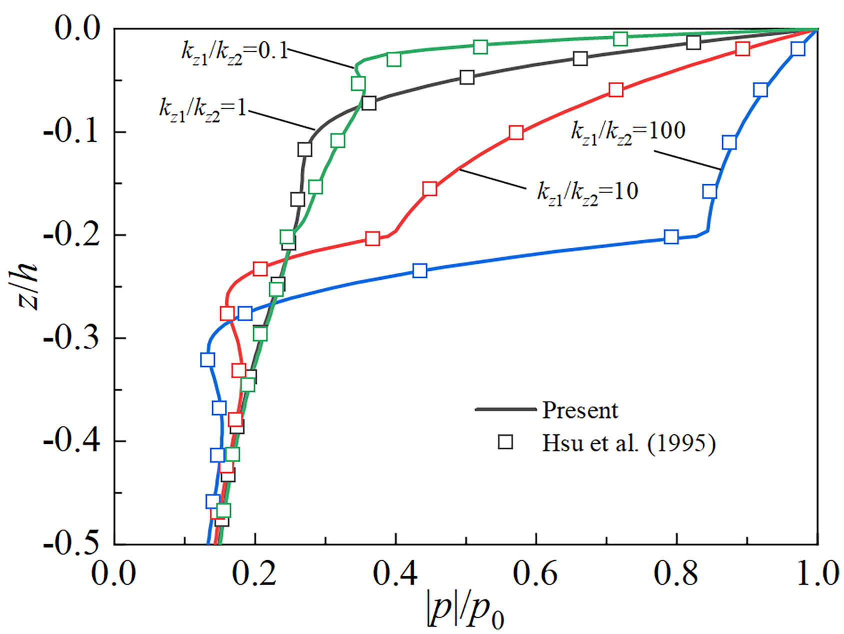

FIGURE 3
Comparison of pore pressure of a layered isotropic poroelastic seabed under linear wave.

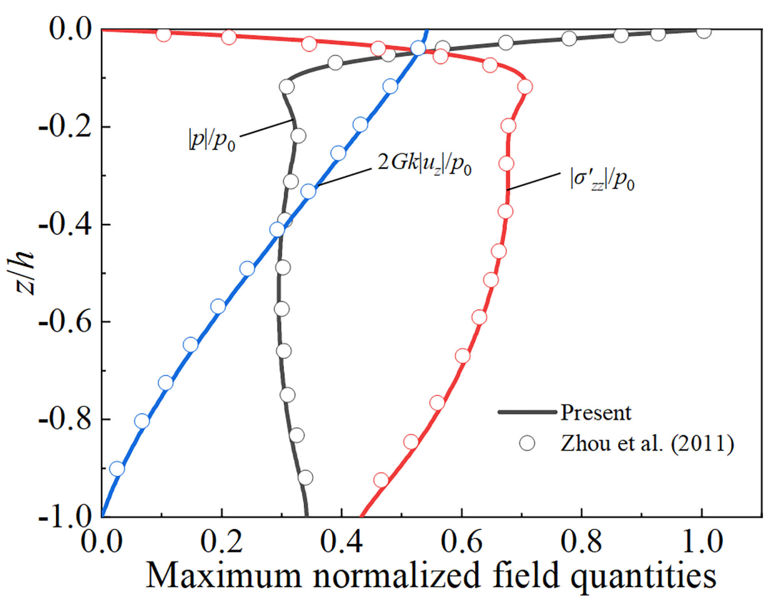

FIGURE 4
Comparison of the present solution with existing one for a homogeneous, isotropic and poroelastic seabed under second-order Stokes wave.

seabed response. However, the dynamic response of the anisotropic seabed under non-linear wave is still unknown. Therefore, in the subsequent study, we will analyze the dynamic response and liquefaction behavior of single-layer and multilayered anisotropic seabed with different anisotropic parameters and degree of saturation and subjected to non-linear wave. The basic poroelastic properties and wave conditions used in the following analysis are listed in Table 1, and it should be pointed out that all parameters are taken from this table if there is no further statement.

Figure 5 shows the comparison of the induced pressures induced by non-linear wave (i.e., second-order Stokes wave) and linear wave at the seabed surface. It can be observed that the wave loading by non-linear wave is different with that by linear wave. Compared to linear wave, the wave loading by non-linear wave shows higher/sharper wave crest and lower/flatter wave trough, and takes on more evident characteristics of asymmetric distribution. As a result, fully understanding the difference in the induced filed quantities (e.g., pore pressure, vertical effective stress) by linear and non-linear waves for different soil properties is of great importance. In the following parts, based on the input data given in Table 1, the influence of anisotropic stiffness, anisotropic permeability, degree of saturation and stratification on the vertical distribution of maximum pore pressure $|p|$, vertical effective stress $|\sigma'_{zz}|$ and shear stress $|\tau_{xz}|$ are analyzed for both linear and non-linear waves. Unless otherwise stated, the solid and dash line denote, respectively, the response of non-linear and line waves in Figures 6–14.

4.2.1 Influence of soil properties

Figure 6 illustrates the influence of anisotropic stiffness on the dynamic response of the seabed under non-linear and linear waves. The anisotropic stiffness is commonly portrayed by two anisotropic moduli ratios, i.e., E_h/E_v and G_v/E_v with reference modulus E_v. For non-linear wave, the maximum pore pressure $|p|$ decreases (increases) with the increase of E_h/E_v (G_v/E_v), while the maximum vertical effective stress $|\sigma'_{zz}|$ shows the opposite changing trend. Moreover, the effect of G_v/E_v is more pronounced than that of E_h/E_v,

TABLE 1 The basic poroelastic properties and wave conditions.

Wave characteristics	*Value*
Wave period T	12 s
Wave height H	8 m
Water depth d	0.125L m
Soil characteristics	*Value*
Seabed thickness h	24 m
Density of soil skeleton ρ_s	2650 kg/m^3
Density of pore fluid ρ_f	1000 kg/m^3
Degree of saturation S_r	0.975
Porosity ϕ	0.35
Poisson's ratio $v_h=v_v$	0.4
True bulk modulus of elasticity of water K_w	2×10^9 Pa
Bulk modulus of soil skeleton K_s	3.6×10^{10} Pa
Permeability coefficient k_x	10^{-4} m/s
Shear modulus G_v	5×10^6 Pa
Young's modulus E_v	1.4×10^7 Pa

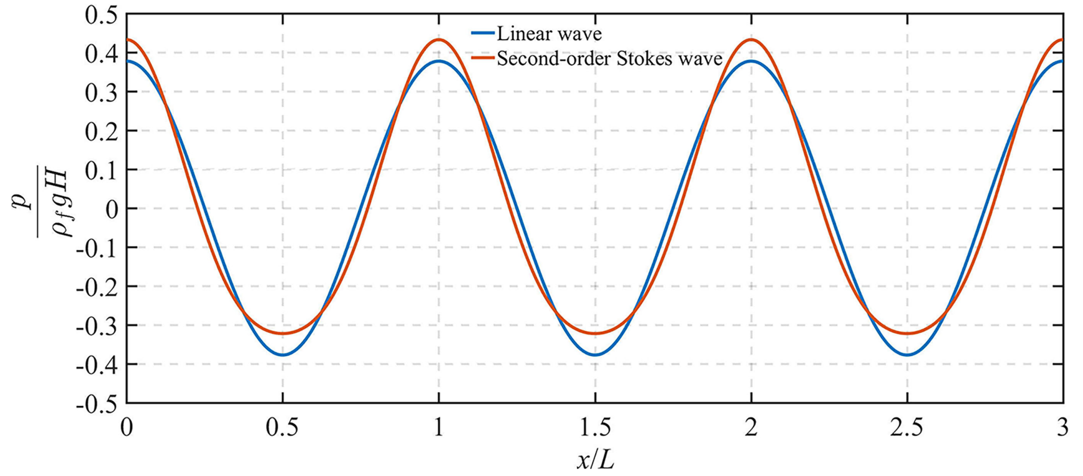

FIGURE 5
Comparison between the induced pressures by second-order Stokes wave and linear wave at the seabed surface.

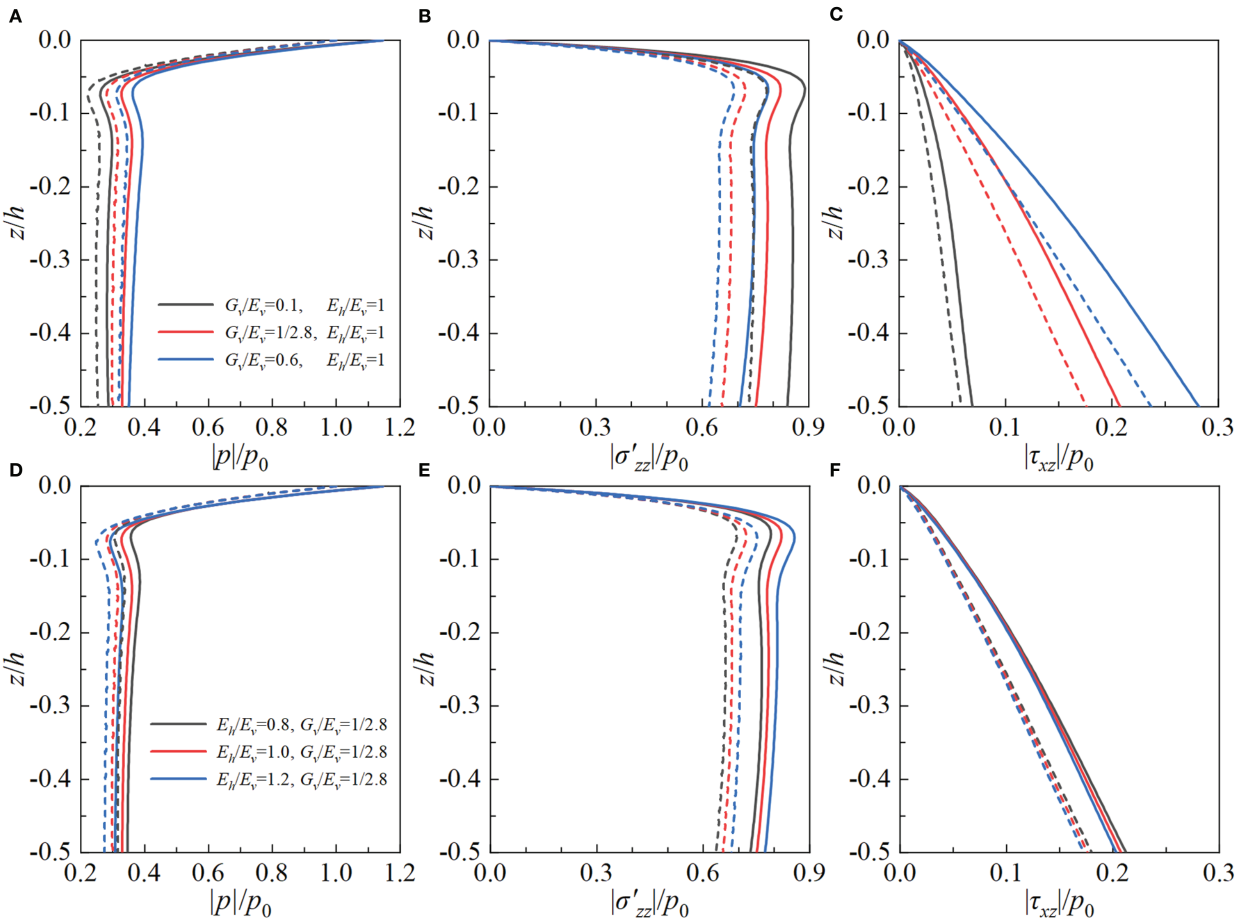

FIGURE 6
Influence of anisotropic stiffness on the dynamic response of the seabed under non-linear and linear waves: anisotropic moduli ratios G_v/E_v in **(A–C)** and E_h/E_v in **(D–F)**.

especially for the influence on the maximum shear stress $|\tau_{xz}|$. It can be also observed that, for both the non-linear and linear waves, the changing trend of field quantities is similar except for the different amplitude. That is to say, for fixed anisotropic moduli ratio, $|p|$, $|\sigma'_{zz}|$ and $|\tau_{xz}|$ by non-linear wave are greater than those by linear wave within the observed depth range.

As known to us, the marine sediments exhibit obvious anisotropic permeability in nature and a small amount of gas is common to be observed in those bulk materials. The anisotropic permeability ratio k_z/k_x is commonly introduced to characterize the anisotropic permeability, while the degree of saturation S_r is defined as the ratio of the volume of water to the total volume of void space to intuitively reflect the content of gas. To clearly reflect the influence of k_z/k_x and S_r, the seabed is assumed to be composed of isotropic poroelastic material. Figures 7, 8 depict the influence of anisotropic permeability and degree of saturation on the dynamic response of homogeneous isotropic poroelastic seabed, respectively. It can be seen from Figures 7, 8 that k_z/k_x and S_r have marked influence on the distribution of the pore pressure and vertical effective stress. Under the action of linear or non-linear wave, $|p|$ ($|\sigma'_{zz}|$) increase (decreases) with increasing k_z/k_x or S_r. However, the effect of k_z/k_x and S_r on $|\tau_{xz}|$ is relatively small, particularly $|\tau_{xz}|$ is not very sensitive to S_r. Similar to the influence of anisotropic

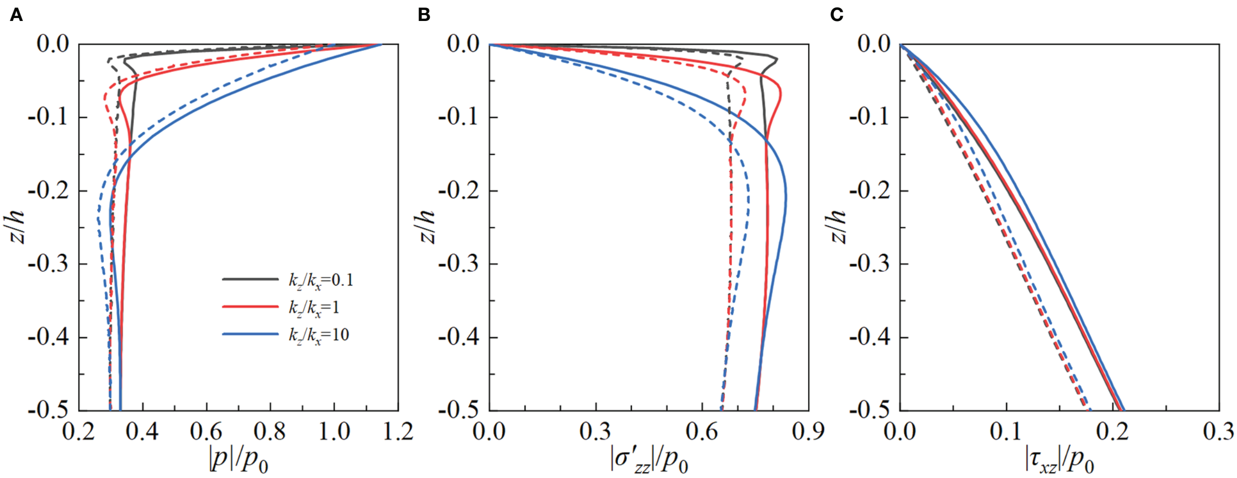

FIGURE 7
Influence of anisotropic permeability on the dynamic response of homogeneous isotropic seabed under non-linear and linear waves. **(A)** pore pressure; **(B)** vertical effective stress; **(C)** shear stress.

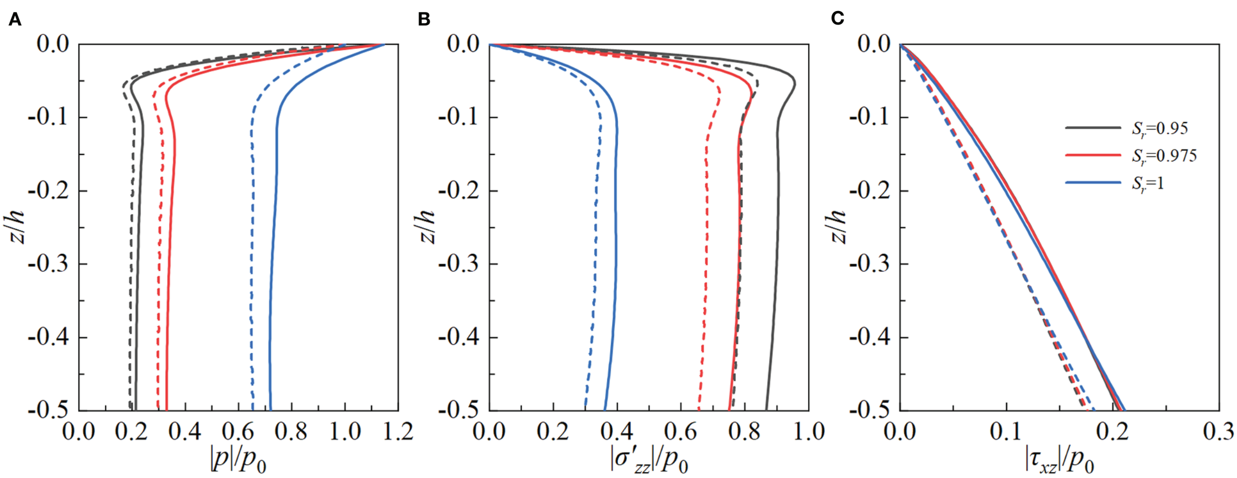

FIGURE 8
Influence of degree of saturation S_r on the dynamic response of homogeneous isotropic seabed under non-linear and linear waves. **(A)** pore pressure; **(B)** vertical effective stress; **(C)** shear stress.

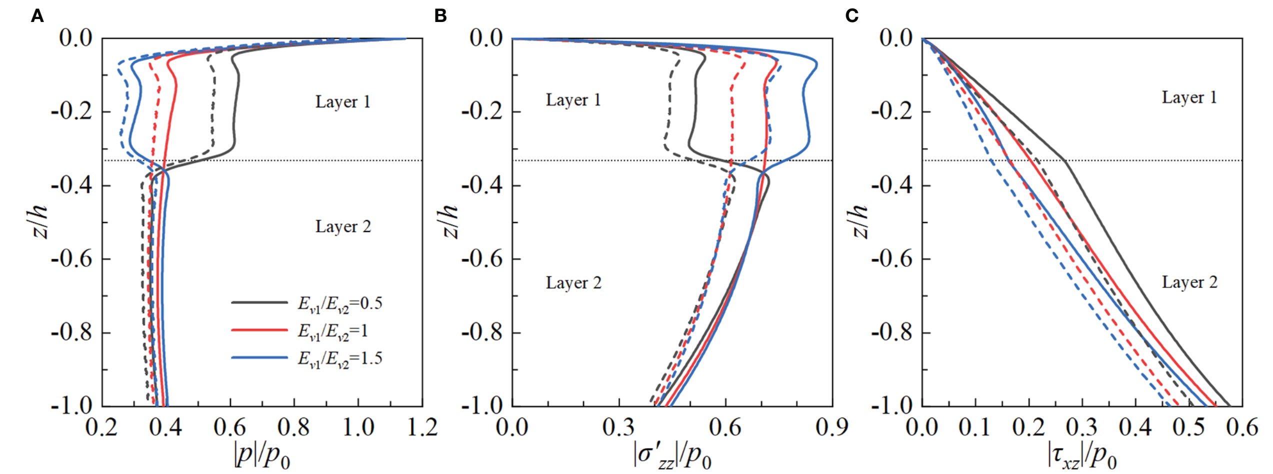

FIGURE 9
Influence of modulus ratio E_{v1}/E_{v2} on the dynamic response of the TI poroelastic seabed under non-linear and linear waves. **(A)** pore pressure; **(B)** vertical effective stress; **(C)** shear stress.

stiffness, $|p|$, $|\sigma'_{zz}|$ and $|\tau_{xz}|$ by the non-linear wave are greater than those by linear wave in the observed depth range.

In practical engineering, the stratification is the intrinsic behavior of the seabed due to the long-time sedimentation process of the soil. To study the effect of stratification, a typical two-layer TI poroelastic seabed with different stiffness is constructed. The thicknesses of two layers are fixed at h_1 = 8 m and h_2 = 16 m, respectively. The specific parameters used in calculation for plotting Figure 9 are E_{hi}/E_{vi}=0.8, G_{vi}/E_{vi}=0.6, k_{zi}/k_{xi}=1 and S_{ri}=0.975 (i=1, 2), and the left parameters are selected from Table 1. As shown in Figure 9, under the action of the non-linear wave, $|p|$ ($|\sigma'_{zz}|$) decreases (increases) roughly with increasing E_{v1}/E_{v2} above the layer interface, while they show the completely opposite changing trend below the layer interface. $|\tau_{xz}|$ decreases with increasing E_{v1}/E_{v2}, and there exists a difference in the changing rate above and below the layer interface. Moreover, the amplitude of induced field quantities by non-linear wave are still larger than that by the linear wave. Therefore, it could be concluded from Figures 6–9 that the maximum pore pressure, vertical effective stress and shear stress by non-linear wave are higher than those by linear wave due to the larger wave crest of non-linear wave.

4.2.2 Analysis of liquefaction

Hsu et al. (1995) reported that that the liquefaction criterion based on effective normal stress may not be valid when effective stress is low. Hence, the 3-D liquefaction criterion proposed by Hsu et al. (1995) is employed in the present study with being defined as

$$-\frac{(1+2K_0)}{3}(\gamma_s-\gamma_w)z \le -(p_b-p) \tag{37}$$

where $K_0=\nu/(1-\nu)$ denotes the lateral earth pressure coefficient at rest. γ_s and γ_w denote the unit weights of the seabed soil and water, respectively. p_b and p denote the wave pressure at the surface of the seabed and the wave-induced pore pressure at depth z in the seabed, respectively. This calculation method considers the left and right sides of Eq. (37) as the initial vertical effective stress and the excess pore pressure, respectively. Eq. (37) indicates that when the excess pore pressure is greater than the initial vertical effective stress, liquefaction of the seabed will potentially occur. In the following part, the liquefaction zone for different parameters under both non-linear and linear waves are analyzed in detail.

The liquefied zone in a homogeneous TI poroelastic seabed for different anisotropic moduli ratios under both linear and non-linear waves is shown in Figure 10. The anisotropic ratios E_h/E_v and G_v/E_v have significant influence on the maximum potential liquefaction depth for two kind of waves. The maximum liquefaction depth increases with increasing E_h/E_v or decreasing G_v/E_v, which indicates that it is necessary to consider the anisotropy of the seabed to accurately judge the liquefaction potential. Moreover, for the same material parameters of the seabed, the maximum liquefaction depth induced by the non-linear wave is markedly lower than that by the linear wave. However, the liquefaction width by the non-linear wave is wider than that by the linear wave. This phenomenon could be due to the fact that the wave trough of the non-linear ocean wave is much lower and flatter than the linear wave.

The liquefaction zone in a homogeneous isotropic poroelastic seabed for various anisotropic permeability ratio is shown in Figure 11. It can be seen from Figure 11 that the anisotropic permeability makes great contribution to the

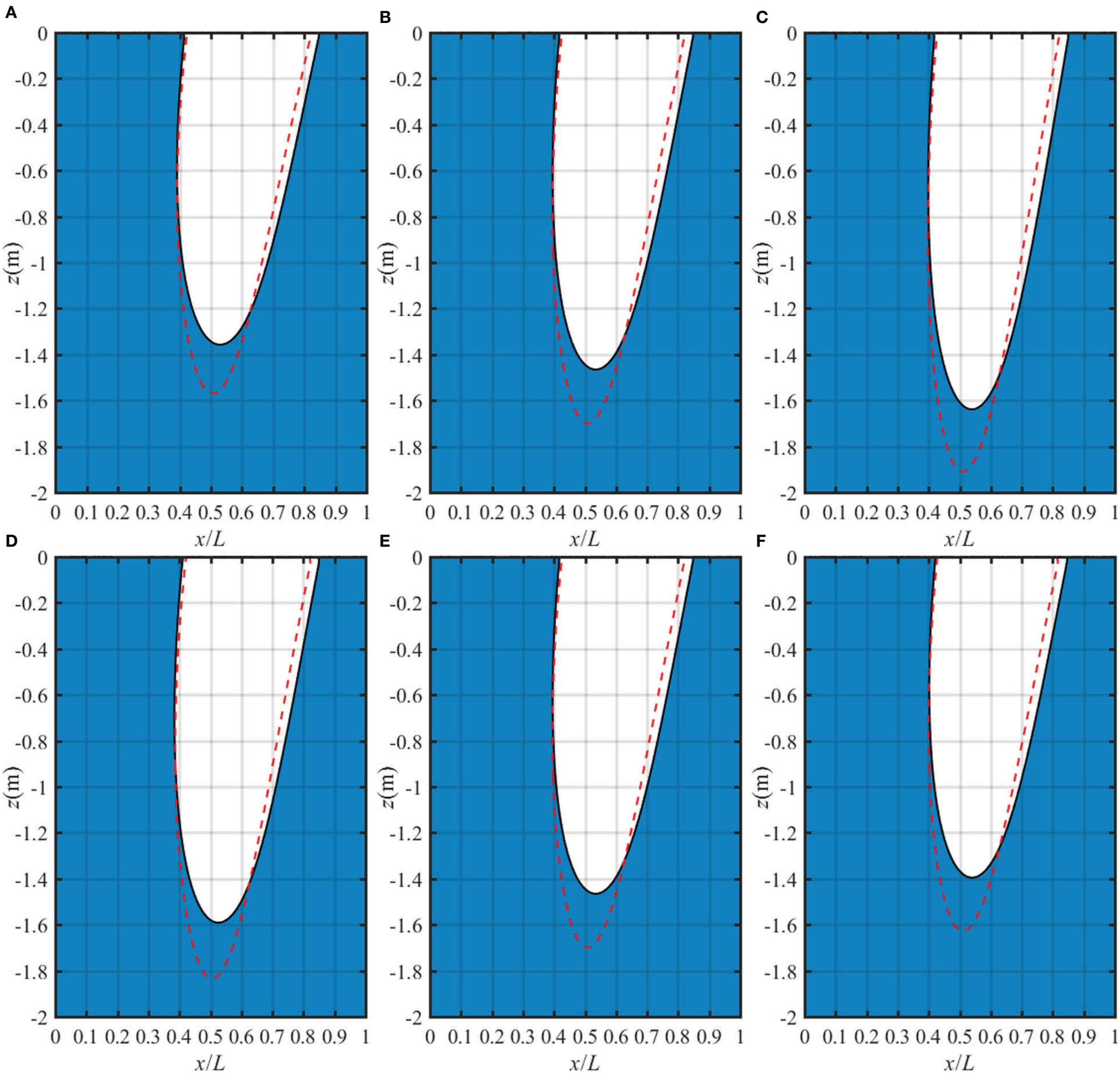

FIGURE 10
Liquefaction zone in a homogeneous TI poroelastic seabed for various anisotropic moduli ratio: **(A)** E_h/E_v=0.5, **(B)** E_h/E_v=1 and **(C)** E_h/E_v=1.5 with fixed G_v/E_v=1/2.8; **(D)** G_v/E_v=0.1, **(E)** G_v/E_v=1/2.8 and **(F)** G_v/E_v=0.6 with fixed E_h/E_v=1.

liquefaction potential. When k_z/k_x=1, the liquefaction depth in the seabed is the biggest. As k_z/k_x decreases (e.g., k_z/k_x<1), the liquefaction depth shows little decrease and liquefaction width shows obvious increase. Through detailed calculation, when k_z/k_x further decreases to 0.0001, the liquefaction depth shows negligible variation indicating there exists a critical value for k_z/k_x. However, when k_z/k_x increases (e.g., k_z/k_x>1), both liquefaction depth and liquefaction width markedly decrease. Through further calculation, when k_z/k_x=10 (the result is not given in the figure), the non-linear wave no longer produces liquefaction and the liquefaction zone produced by the linear wave tends to zero. This phenomenon may be due to the fact that the pore pressure is hard to develop in the soil with better permeability, thus the vertical effective stress makes the controlling contribution. It could be concluded that increasing the vertical permeability of the seabed will greatly reduce the probability of the occurrence of liquefaction.

Figure 12 shows the liquefaction zone in a homogeneous isotropic poroelastic seabed for various degree of saturation. As reported in past studies, when S_r=1 the subgrade would not

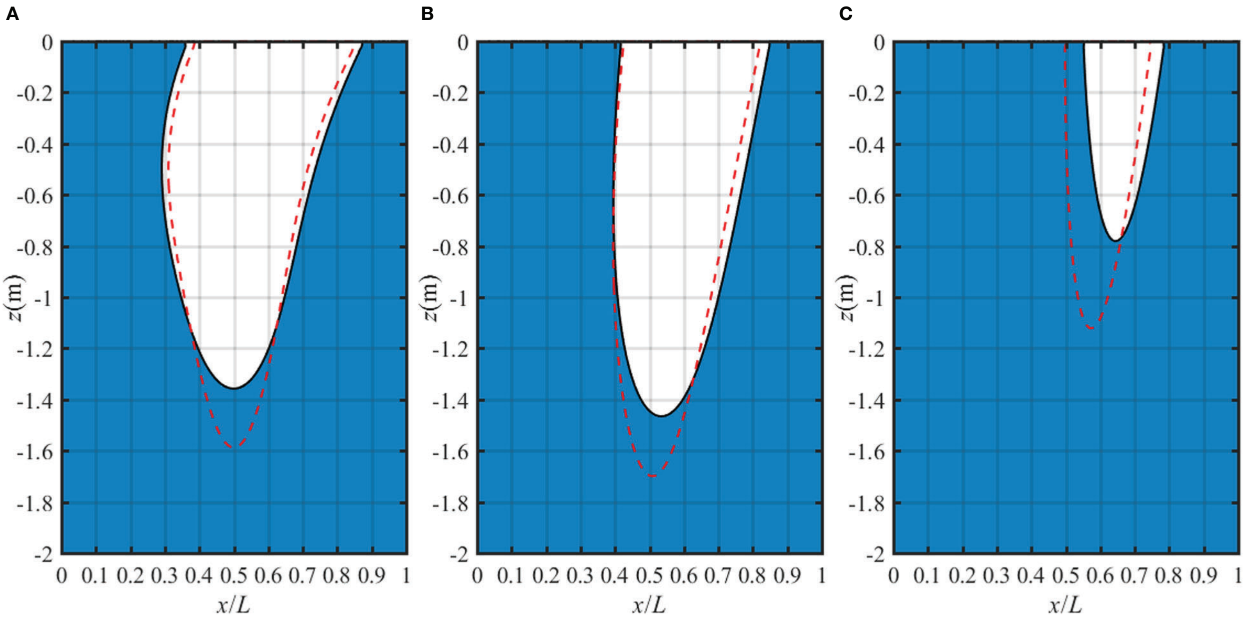

FIGURE 11
Liquefaction zone in a homogeneous isotropic poroelastic seabed for various anisotropic permeability ratio: **(A)** k_z/k_x=0.1, **(B)** k_z/k_x=1 and **(C)** k_z/k_x=5.

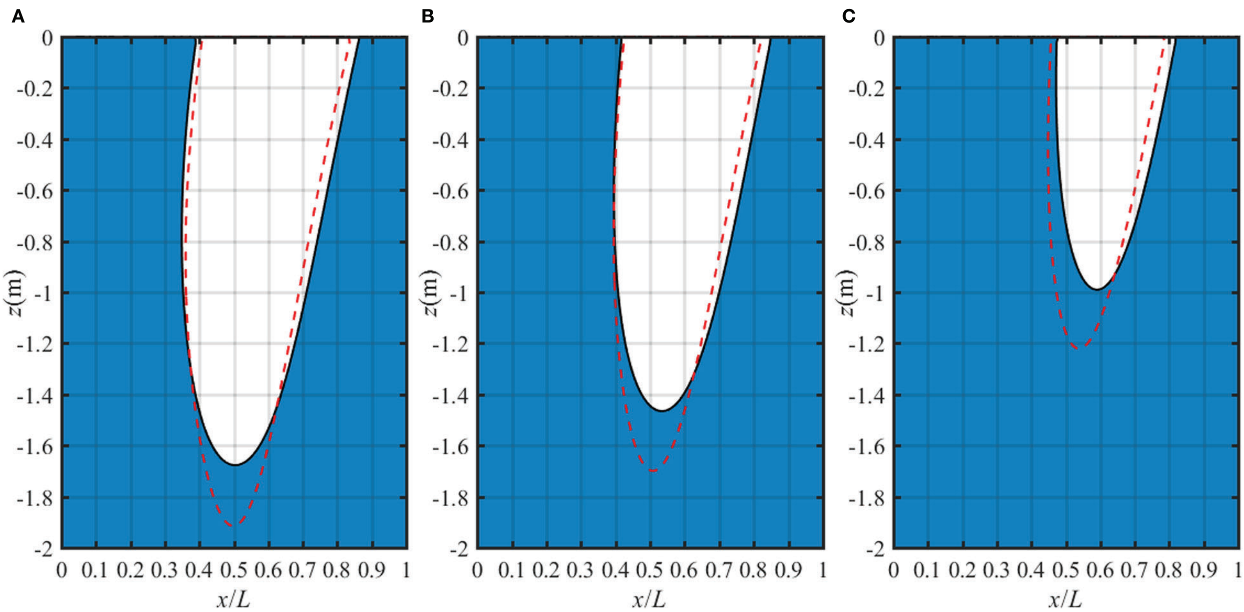

FIGURE 12
Liquefaction zone in a homogeneous isotropic poroelastic seabed for various degree of saturation: **(A)** S_r=0.95, **(B)** S_r=0.975 and **(C)** S_r=0.99.

10.3389/fmars.2022.1082337

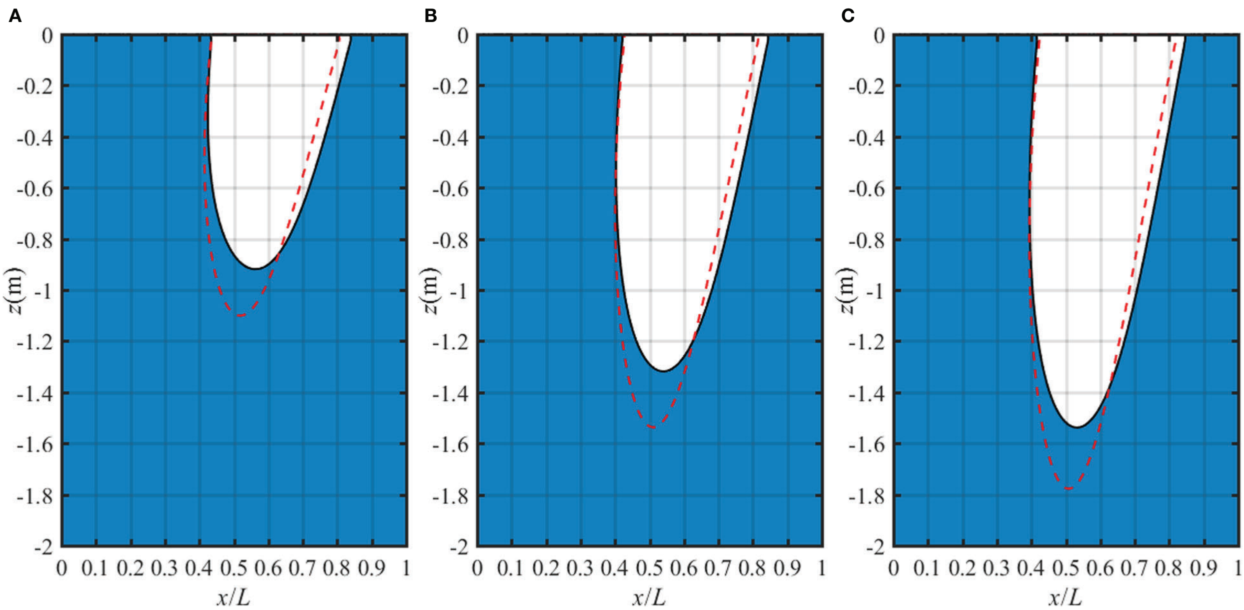

FIGURE 13
Liquefaction zone in a two-layer TI poroelastic seabed for various E_{v1}/E_{v2}: **(A)** E_{v1}/E_{v2} = 0.5, **(B)** E_{v1}/E_{v2} = 1 and **(C)** E_{v1}/E_{v2} = 1.5 with fixed E_{hi}/E_{vi}=0.8, G_{vi}/E_{vi}=0.6, k_{zi}/k_{xi}=1, E_{v2} = 1.4×10^{7} Pa.

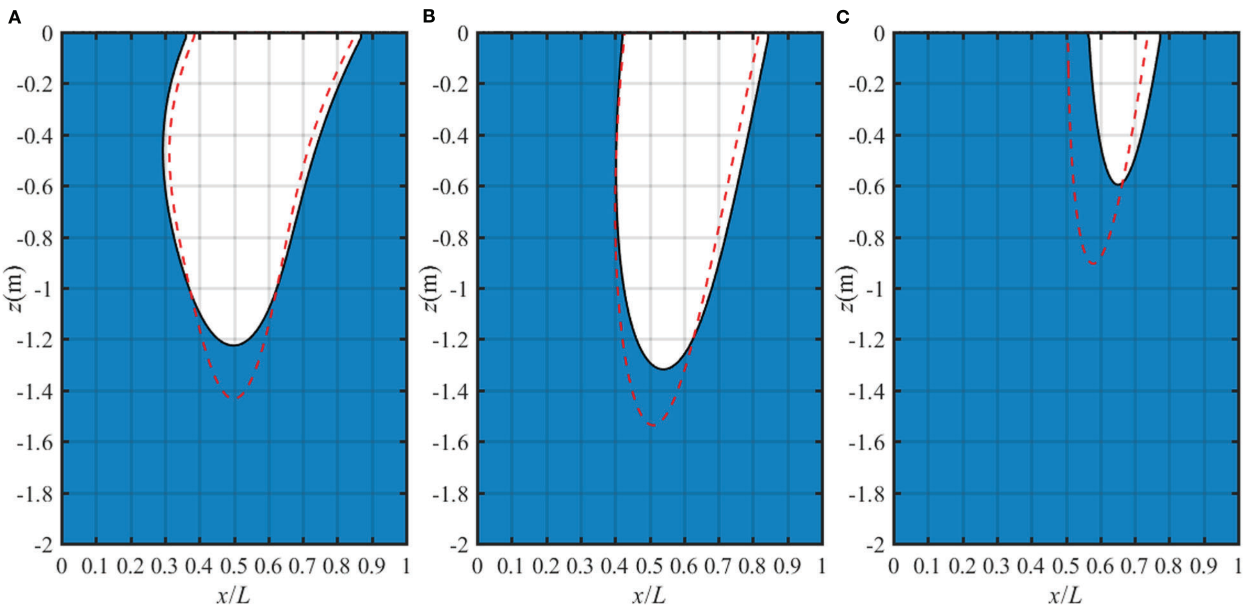

FIGURE 14
Liquefaction region in a two-layer TI poroelastic seabed for various k_{z1}/k_{z2}: **(A)** k_{z1}/k_{z2} = 0.1, **(B)** k_{z1}/k_{z2} = 1 and **(C)** k_{z1}/k_{z2} = 5 with fixed E_{hi}/E_{vi}=0.8, G_{vi}/E_{vi}=0.6, k_{zi}/k_{xi}=1, k_{z2} = 1×10^{-4} m/s.

liquefy (Jeng, 1996), while the seabed could liquefy at certain soil properties conditions (Chen et al., 2022). Hence, we present the results corresponding to S_r=0.95, 0.975 and 0.99. It is found that the maximum liquefaction depth decreases significantly with increasing S_r. When the seabed tends to be completely saturated, the probability of seabed liquefaction will be greatly reduced.

The liquefaction zone in a two-layer anisotropic seabed for various moduli ratio E_{v1}/E_{v2} is shown in Figure 13. The depth and width of the liquefaction zone in the seabed increase with the increase of E_{v1}/E_{v2}. In other words, when the other parameters are fixed, the stiff top layer makes the seabed much easier to liquefy. The liquefaction zone in a two-layer anisotropic seabed for various permeability ratio k_{z1}/k_{z2} is shown in Figure 14. The effect of k_{z1}/k_{z2} is similar to the effect of anisotropic permeability ratio k_z/k_x in the single-layer case. When the permeability of the first layer increases, the pore pressure is hard to accumulate, resulting in more vertical effective stress in the seabed and thus the lower liquefaction depth. Furthermore, it can be concluded from Figures 10–14 that the liquefaction depth and liquefaction width by the non-linear wave are lower than those by the linear wave for various soil properties. Hence, in order to accurately judge the liquefaction potential of the seabed, the anisotropic stiffness, anisotropic permeability, degree of saturation and stratification should be carefully considered.

5 Conclusions

In this study, the dynamic response of a TI multilayered poroelastic seabed under non-linear wave is established based on Biot's complete dynamic consolidation theory and second-order Stokes theory. The corresponding solution is derived by virtue of potential-function scheme and DVP method. After verifying the accuracy and reliability of the developed solution, the effects of main parameters on the dynamic response and liquefaction potential of single-layer and multilayered anisotropic poroelastic seabed are analyzed. The main conclusions can be summarized as follows:

1. Compared to the linear wave, the nonlinear wave shows higher/sharper wave crest and lower/flatter wave trough with the evident behavior of asymmetric distribution. The changing rule of pore pressure, normal effective stress and shear stress in the seabed induced by non-linear wave is similar with that by the linear wave, except for much higher induced amplitude by non-linear wave. For the liquefaction potential, the depth and width of liquefaction by the nonlinear wave are generally lower than those by linear wave for various soil properties.
2. Both anisotropic stiffness and permeability have significant influence on the dynamic response and liquefaction potential of the seabed to non-linear wave. The maximum liquefaction depth increases with increasing E_h/E_v or decreasing G_v/E_v, while the liquefaction zone by the nonlinear wave is wider than that by the linear wave. The influence of anisotropic permeability on the liquefaction depth is relatively complex.
3. The degree of saturation S_r of the seabed has a significant effect on the dynamic response and liquefaction potential of the seabed under non-linear wave. The maximum pore pressure (vertical effective stress) increase (decreases) with increasing S_r. The seabed soil is less susceptible to liquefy as the degree of saturation increases.
4. The stratification has remarkable influence on the dynamic response of the seabed subjected to non-linear wave. For a typical two-layer seabed, the depth and width of the liquefaction zone increase with increasing E_{v1}/E_{v2} (i.e., increasing Young's modulus in the top layer) and decrease with increasing k_{z1}/k_{z2} (i.e., increasing vertical permeability coefficient in the top layer). That is to say, when the top layer is stiff or the corresponding permeability is poor, the seabed is much easier to liquefy.

Data availability statement

The raw data supporting the conclusions of this article will be available by the corresponding authors upon request.

Author contributions

ZZ: Software, Writing original draft. BZ: Formal analysis, Writing original draft. XL: Methodology, Writing-review and editing, Supervision. ZW: Conceptualization, Methodology. All authors contributed to the article and approved the submitted version.

Funding

This research is supported by National Natural Science Foundation of China (Grant Nos. 52178367, 52078467), Natural Science Foundation of Zhejiang Province (Grant No. LHZ21E090001), and Research and Development Fund of Zhejiang A & F University (Grant No. 2020FR052).

Conflict of interest

The authors declare that the research was conducted in the absence of any commercial or financial relationships that could be construed as a potential conflict of interest.

Publisher's note

References

Biot, M. A. (1941). General theory of three-dimensional consolidation. *J. Appl. Phys.* 12, 155–164. doi: 10.1063/1.1712886

Biot, M. A. (1956). Theory of propagation of elastic waves in a fluid-saturated porous solid. i. low-frequency range. *J. Acoust. Soc Am.* 28, 168–178. doi: 10.1121/1.1908239

Biot, M. A. (1962). Mechanics of deformation and acoustic propagation in porous media. *J. Appl. Phys.* 33, 1482–1498. doi: 10.1063/1.1728759

Chen, W. Y., Chen, G. X., Chen, W., Liao, C. C., and Gao, H. M. (2019). Numerical simulation of the non-linear wave-induced dynamic response of anisotropic poro-elastoplastic seabed. *Mar. Georesour. Geotec.* 37, 924–935. doi: 10.1080/1064119X.2018.1507064

Cheng, A. H. D. (1997). Material coefficients of anisotropic poroelasticity. *Int. J. Rock Mech. Min. Sci.* 34, 199–205. doi: 10.1016/S0148-9062(96)00055-1

Chen, L. B., Wu, W. B., Liu, H., El Naggar, M. H., Wen, M. J., and Wang, K. H. (2022a). Influence of defects on the lateral dynamic characteristics of offshore piles considering hydrodynamic pressure. *Ocean Eng.* 260, 111894. doi: 10.1016/j.oceaneng.2022.111894

Chen, L. B., Wu, W. B., Liu, H., Li, J. X., Newson, T., and El Naggar, M. H. (2022b). Analytical solution for kinematic response of offshore piles under vertically propagating s-waves. *Ocean Eng.* 262, 112018. doi: 10.1016/j.oceaneng.2022.112018

Chen, X., Zhang, Q., Zheng, X. Y., and Lei, Y. (2022). Dynamic responses of a multilayered transversely isotropic poroelastic seabed subjected to ocean waves and currents. *J. Mar. Sci. Eng.* 10, 73. doi: 10.3390/jmse10010073

Gao, J. L., Ji, C. Y., Ma, X. J., Liu, Y. Y., and Gaidai, O. (2017). Numerical investigation of infragravity wave amplifications during harbor oscillations influenced by variable offshore topography. *Ocean Dynam.* 67, 1151–1162. doi: 10.1007/s10236-017-1081-0

Gao, J. L., Ma, X. Z., Dong, G. H., Chen, H. Z., Liu, Q., and Zhang, J. (2021). Investigation on the effects of Bragg reflection on harbor oscillations. *Coast. Eng.* 170, 103977. doi: 10.1016/j.coastaleng.2021.103977

Gao, J. L., Ma, X. Z., Zang, J., Dong, G. H., Ma, X. J., Zhu, Y. Z., et al. (2020). Numerical investigation of harbor oscillations induced by focused transient wave groups. *Coast. Eng.* 158, 103670. doi: 10.1016/j.coastaleng.2020.103670

Gatmiri, B. (1992). Response of cross-anisotropic seabed to ocean waves. *J. Geotech. Eng.* 118, 1295–1314. doi: 10.1061/(ASCE)0733-9410(1992)118:9(1295

He, R., Kaynia, A. M., Zheng, J., and Zhang, J. (2022a). Effect of gap and scour on dynamic behavior of monopiles and offshore wind structures. *Ocean Eng.* 243, 110336. doi: 10.1016/j.oceaneng.2021.110336

He, R., Zhang, J., and Zheng, J. (2022b). Vertical dynamic interaction factors for offshore thin-walled pipe piles. *Comput. Geotech.* 145, 104656. doi: 10.1016/j.compgeo.2022.104656

Hsu, C. J., Chen, Y. Y., and Tsai, C. C. (2019). Wave-induced seabed response in shallow water. *Appl. Ocean Res.* 89, 211–223. doi: 10.1016/j.apor.2019.05.016

Hsu, J. R. C., and Jeng, D. S. (1994). Wave-induced soil response in an unsaturated anisotropic seabed of finite thickness. *Int. J. Numer. Anal. Methods Geomech.* 18, 785–807. doi: 10.1002/nag.1610181104

Hsu, J. R. C., Jeng, D. S., and Lee, C. P. (1995). Oscillatory soil response and liquefaction in an unsaturated layered seabed. *Int. J. Numer. Anal. Methods Geomech.* 19, 825–849. doi: 10.1002/nag.1610191202

Hsu, J. R. C., Jeng, D. S., and Tsai, C. P. (1993). Short-crested wave-induced soil response in a porous seabed of infinite thickness. *Int. J. Numer. Anal. Methods Geomech.* 17, 553–576. doi: 10.1002/nag.1610170803

Jeng, D. S. (1996). Wave-induced liquefaction potential in a cross-anisotropic seabed. *J. Chin. Institute Engineers* 19, 59–70. doi: 10.1080/02533839.1996.9677765

Jeng, D. S. (2015). Review of liquefaction around marine structures by b. mutlu Sumer. *J. Waterw. Port Coast. Ocean Eng.* 141, 07515001. doi: 10.1061/(ASCE)WW.1943-5460.0000296

Jeng, D. S., and Cha, D. H. (2003). Effects of dynamic soil behavior and wave non-linearity on the wave-induced pore pressure and effective stresses in porous seabed. *Ocean Eng.* 30, 2065–2089. doi: 10.1016/S0029-8018(03)00070-2

Jeng, D. S., and Lee, T. L. (2001). Dynamic response of porous seabed to ocean waves. *Comput. Geotech.* 28, 99–128. doi: 10.1016/S0266-352X(00)00026-4

Jeng, D. S., and Rahman, M. S. (2000). Effective stresses in a porous seabed of finite thickness: inertia effects. *Can. Geotech. J.* 37, 1383–1392. doi: 10.1139/t00-063

Jeng, D. S., Rahman, M. S., and Lee, T. L. (1999). Effects of inertia forces on wave-induced seabed response. *Int. J. Offshore Polar Eng.* 9, 307–313. Available at: https://www.scopus.com/record/display.uri?eid=2-s2.0-0033496335&origin=inward.

Jeng, D. S., and Seymour, B. R. (1997). Wave-induced pore pressure and effective stresses in a porous seabed with variable permeability. *J. Offshore Mech. Arct. Eng.* 119, 226–233. doi: 10.1115/1.2829100

Jeng, D. S., and Zhang, H. (2005). An integrated three-dimensional model of wave-induced pore pressure and effective stresses in a porous seabed: II. breaking waves. *Ocean Eng.* 32, 1950–1967. doi: 10.1016/j.oceaneng.2005.01.005

Jouffray, J.-B., Blasiak, R., Norström, A. V., Österblom, H., and Nyström, M. (2020). The blue acceleration: The trajectory of human expansion into the ocean. *One Earth* 2, 43–54. doi: 10.1016/j.oneear.2019.12.016

Joydas, T. V., Qurban, M. A., Borja, A., Krishnakumar, P. K., and Al-Suwailem, A. (2017). Macrobenthic community structure in the northwestern Arabian gulf, twelve years after the 1991 oil spill. *Front. Mar. Sci.* 4. doi: 10.3389/fmars.2017.00248

Kitano, T., and Mase, H. (2001). Wave-induced porewater pressure in a seabed with inhomogeneous permeability. *Ocean Eng.* 28, 279–296. doi: 10.1016/S0029-8018(00)00010-X

Lauton, G., Pattiaratchi, C. B., and Lentini, C. A. D. (2021). Observations of breaking internal tides on the Australian north West shelf edge. *Front. Mar. Sci.* 8. doi: 10.3389/fmars.2021.629372

Le Méhauté, B. (1976). *An introduction to hydrodynamics and water waves* (Berlin Heidelberg: Springer). doi: 10.1007/978-3-642-85567-2

Liu, K. F., Zhang, Z. Q., and Pan, E. (2022). Dynamic response of a transversely isotropic and multilayered poroelastic medium subjected to a moving load. *Soil Dyn. Earthq. Eng.* 155, 107154. doi: 10.1016/j.soildyn.2022.107154

Li, X. B., Zhang, Z. Q., and Pan, E. (2020). Wave-induced dynamic response in a transversely isotropic and multilayered poroelastic seabed. *Soil Dyn. Earthq. Eng.* 139, 106365. doi: 10.1016/j.soildyn.2020.106365

Madsen, O. S. (1978). Wave-induced pore pressures and effective stresses in a porous bed. *Géotechnique* 28, 377–393. doi: 10.1680/geot.1978.28.4.377

Mei, C. C., and Foda, M. A. (1981). Wave-induced responses in a fluid-filled poro-elastic solid with a free surface — a boundary layer theory. *Geophys. J. Int.* 66, 597–631. doi: 10.1111/j.1365-246X.1981.tb04892.x

Okusa, S. (1985). Wave-induced stresses in unsaturated submarine sediments. *Géotechnique* 35, 517–532. doi: 10.1680/geot.1985.35.4.517

Pan, E. (2019). Green's functions for geophysics: a review. *Rep. Prog. Phys.* 82, 106801. doi: 10.1088/1361-6633/ab1877

Qi, H. F., Chen, Z. L., Li, Y. C., Feng, S. J., and Chen, H. X. (2020). Wave and current-induced dynamic response in a multilayered poroelastic seabed. *Bull. Eng. Geol. Environ.* 79, 11–26. doi: 10.1007/s10064-019-01553-8

Quiuqui, J. P. C., Tamayo, J. P., and Maghous, S. (2022). Closed-form solutions for wave-induced poroelastic response in seabed under dynamic and quasi-static regimes. *J. Braz. Soc Mech. Sci. Eng.* 44, 16. doi: 10.1007/s40430–021-03300-1.

Ryabinin, V., Barbière, J., Haugan, P., Kullenberg, G., Smith, N., McLean, C., et al. (2019). The UN decade of ocean science for sustainable development. *Front. Mar. Sci.* 6. doi: 10.3389/fmars.2019.00470

Sakai, T., Mase, H., and Matsumoto, A. (1988). "Effects of inertia and gravity on seabed response to ocean waves," in *Modeling soil-Water-Structure interactions*. Eds. P. A. Kolkman, J. Linderberg, K. Pilarczyk, A. Rotterdam and A. Balkema, Rotterdam. 61–66.

Soto, L. A., Botello, A. V., Licea-Durán, S., Lizárraga-Partida, M. L., and Yáñez-Arancibia, A. (2014). The environmental legacy of the ixtoc-I oil spill in campeche sound, southwestern gulf of Mexico. *Front. Mar. Sci.* 1. doi: 10.3389/fmars.2014.00057

Tsai, C. P., and Lee, T. L. (1995). Standing wave induced pore pressures in a porous seabed. *Ocean Eng.* 22, 505–517. doi: 10.1016/0029-8018(95)00003-4

Ulker, M. B. C. (2012a). Dynamic pore pressure response of two-layer seabed under non-linear waves. *AIP Conf. Proc.* 1479, 1480–1483. doi: 10.1063/1.4756443

Ulker, M. B. C. (2012b). Pore pressure, stress distributions, and instantaneous liquefaction of two-layer soil under waves. *J. Waterw. Port Coast. Ocean Eng.* 138, 435–450. doi: 10.1061/(ASCE)WW.1943-5460.0000155

Ulker, M. B. C., Rahman, M. S., and Jeng, D. S. (2009). Wave-induced response of seabed: Various formulations and their applicability. *Appl. Ocean Res.* 31, 12–24. doi: 10.1016/j.apor.2009.03.003

Verruijt, A. (1969). "Elastic storage of aquifers," in *Flow through porous media*. Eds. R. J. M. De Weist and J. Bear (New York: Academic Press), 331–376.

Wang, H. F. (2017). *Theory of linear poroelasticity with applications to geomechanics and hydrogeology* (New Jersey: Princeton University Press).

Wang, Z. T., Luan, M. T., Liu, T. G., and Wang, D. (2005). Studies on the effect of non-linear wave loading in shallow water region on dynamic response of sandy seabed. *Ocean Eng.* 23, 41–46.

Yamamoto, T. (1981). Wave-induced pore pressures and effective stresses in inhomogeneous seabed foundations. *Ocean Eng.* 8, 1–16. doi: 10.1016/0029-8018(81)90002-0

Yamamoto, T., Koning, H. L., Sellmeijer, H., and Hijum, E. V. (1978). On the response of a poro-elastic bed to water waves. *J. Fluid Mech.* 87, 193–206. doi: 10.1017/S0022112078003006

Ye, G. J., Leng, J., and Jeng, D. S. (2018). Numerical testing on wave-induced seabed liquefaction with a poro-elastoplastic model. *Soil Dyn. Earthq. Eng.* 105, 150–159. doi: 10.1016/j.soildyn.2017.11.026

Yuhi, M., and Ishida, H. (1998). Analytical solution for wave-induced seabed response in a soil-water two-phase mixture. *Coast. Eng. J.* 40, 367–381. doi: 10.1142/S0578563498000212

Yuhi, M., and Ishida, H. (2002). Simplified solutions for wave-induced response of anisotropic seabed. *J. Waterw. Port Coast. Ocean Eng.* 128, 46–50. doi: 10.1061/(ASCE)0733-950X(2002)128:1(46

Zhang, Y. P., El Naggar, M. H., Wu, W. B., Wang, Z. Q., Yang, X. Y., and Jiang, G. S. (2022). Dynamic torsional impedance of large-diameter pipe pile for offshore engineering: 3D analytical solution. *Appl. Math. Model.* 111, 664–680. doi: 10.1016/j.apm.2022.07.017

Zhang, Z. Q., and Pan, E. (2020). Time-harmonic response of transversely isotropic and layered poroelastic half-spaces under general buried loads. *Appl. Math. Model.* 80, 426–453. doi: 10.1016/j.apm.2019.11.035

Zhang, Z. Q., and Pan, E. (2023). Coupled horizontal and rocking vibrations of a rigid circular disc on the surface of a transversely isotropic and layered poroelastic half-space. *Appl. Math. Model.* 114, 270–290. doi: 10.1016/j.apm.2022.10.005

Zhou, J. C., Pan, E., and Bevis, M. (2021). Deformation due to surface temperature variation on a spherically layered, transversely isotropic and self-gravitating earth. *Geophys. J. Int.* 225, 1672–1688. doi: 10.1093/gji/ggab056

Zhou, X. L., Xu, B., Wang, J. H., and Li, Y. L. (2011). An analytical solution for wave-induced seabed response in a multi-layered poro-elastic seabed. *Ocean Eng.* 38, 119–129. doi: 10.1016/j.oceaneng.2010.10.003

Zienkiewicz, O. C., Chang, C. T., and Bettess, P. (1980). Drained, undrained, consolidating and dynamic behaviour assumptions in soils. *Gèotechnique* 30, 385–395. doi: 10.1680/geot.1980.30.4.385

Appendix A The relation between elastic constants and engineering parameters

According to Cheng (1997), the between elastic constants and engineering parameters can be expressed as

$$
\begin{aligned}
C_{11} &= \frac{E_h\left[1-(E_h/E_v)v_v^2\right]}{(1+v_h)[1-v_h-(2E_h/E_v)v_v^2]} \\
C_{12} &= \frac{E_h\left[v_h+(E_h/E_v)v_v^2\right]}{(1+v_h)[1-v_h-(2E_h/E_v)v_v^2]} \\
C_{13} &= \frac{E_h v_v}{1-v_h-(2E_h/E_v)v_v^2}; \quad C_{33} = \frac{E_v(1-v_h)}{1-v_h-(2E_h/E_v)v_v^2} \\
C_{44} &= G_v; C_{66} \equiv \frac{C_{11}-C_{12}}{2} = \frac{E_h}{2(1+v_h)} = G_h
\end{aligned} \tag{A.1}
$$

where v_h and v_v are the Poisson's ratio of the solid skeleton in horizontal and vertical directions, respectively.

Appendix B Coefficients $r_i^{(m)}$ (i=1-4)

$$
\begin{aligned}
r_1^{(m)} &= C_{33}C_{44}\delta_3^{(m)}; \\
r_2^{(m)} &= (a_4^{(m)}C_{44} + a_1^{(m)}C_{33} + a_2^{(m)}a_2^{(m)}k^2)\delta_3^{(m)} + (a_6^{(m)}C_{33} \\
&\quad + a_5^{(m)}a_5^{(m)})C_{44}; \\
r_3^{(m)} &= a_1^{(m)}a_4^{(m)}\delta_3^{(m)} + (a_4^{(m)}C_{44} + a_1^{(m)}C_{33} + a_2^{(m)}a_2^{(m)}k^2)a_6^{(m)} \\
&\quad + a_1^{(m)}a_5^{(m)}a_5^{(m)} + (2a_2^{(m)}a_3^{(m)}a_5^{(m)} - a_3^{(m)}a_3^{(m)}C_{33})k^2; \\
r_4^{(m)} &= a_4^{(m)}(a_1^{(m)}a_6^{(m)} - a_3^{(m)}a_3^{(m)}k^2)
\end{aligned} \tag{B.1}
$$

Appendix C Coefficients $\lambda_i^{(m)}$ (i=1-3)

$$
\begin{aligned}
\lambda_1^{(m)} &= \sqrt{\Delta_1^{(m)} - \frac{\Delta_2^{(m)}}{3\Delta_1^{(m)}} - \frac{r_2^{(m)}}{3r_1^{(m)}}}; \quad \lambda_2^{(m)} = \sqrt{\Delta_1^{(m)}\Delta_4^{(m)} - \frac{\Delta_2^{(m)}}{3\Delta_1^{(m)}\Delta_4^{(m)}} - \frac{r_2^{(m)}}{3r_1^{(m)}}}; \\
\lambda_3^{(m)} &= \sqrt{\Delta_1^{(m)}\left(\Delta_4^{(m)}\right)^2 - \frac{\Delta_2^{(m)}}{3\Delta_1^{(m)}\left(\Delta_4^{(m)}\right)^2} - \frac{r_2^{(m)}}{3r_1^{(m)}}}
\end{aligned} \tag{C.1}
$$

where

$$
\begin{aligned}
\Delta_1^{(m)} &= \left(-\frac{1}{2}\Delta_3^{(m)} + \frac{1}{2}\sqrt{\left(\Delta_3^{(m)}\right)^2 + 4\left(\Delta_2^{(m)}\right)^3/27}\right)^{1/3}; \\
\Delta_2^{(m)} &= -\frac{\left(r_2^{(m)}\right)^2}{3\left(r_1^{(m)}\right)^2} + \frac{r_3^{(m)}}{r_1^{(m)}} \\
\Delta_3^{(m)} &= \frac{2\left(r_2^{(m)}\right)^3}{27\left(r_1^{(m)}\right)^3} - \frac{3r_2^{(m)}r_3^{(m)}}{9\left(r_1^{(m)}\right)^2} + \frac{r_4^{(m)}}{r_1^{(m)}}; \quad \Delta_4^{(m)} = \frac{-1+\sqrt{3}\mathrm{i}}{2}
\end{aligned} \tag{C.2}
$$

Appendix D Coefficients $\chi_i^{(m)}$, $\varphi_i^{(m)}$, $\xi_i^{(m)}$ and $\eta_i^{(m)}$ (i=1-3)

$$
\begin{aligned}
\chi_i^{(m)} &= -\mathrm{i}k\lambda_i^{(m)}\left[a_2^{(m)}\left(a_6^{(m)} + \delta_3^{(m)}\lambda_i^{(m)}\lambda_i^{(m)}\right) + a_3^{(m)}a_5^{(m)}\right] \\
\varphi_i^{(m)} &= \left(a_6^{(m)} + \delta_3^{(m)}\lambda_i^{(m)}\lambda_i^{(m)}\right)\left(a_1^{(m)} + C_{44}\lambda_i^{(m)}\lambda_i^{(m)}\right) - a_3^{(m)}a_3^{(m)}k^2 \\
\xi_i^{(m)} &= \lambda_i^{(m)}\left[a_5^{(m)}\left(a_1^{(m)} + C_{44}\lambda_i^{(m)}\lambda_i^{(m)}\right) + a_2^{(m)}a_3^{(m)}k^2\right] \\
\eta_i^{(m)} &= \delta_3^{(m)}\left(\xi_i^{(m)}\lambda_i^{(m)} - \rho_f\omega^2\varphi_i^{(m)}\right)
\end{aligned} \tag{D.1}
$$

Appendix E Elements of constant coefficients $M^{(m)}$ (i=1-3)

$$
\begin{aligned}
M_{1i}^{(m)} &= \chi_i^{(m)}; M_{1(i+3)}^{(m)} = -\chi_i^{(m)}; \\
M_{2i}^{(m)} &= \varphi_i^{(m)}; M_{2(i+3)}^{(m)} = \varphi_i^{(m)}; \\
M_{3i}^{(m)} &= \eta_i^{(m)}; M_{3(i+3)}^{(m)} = \eta_i^{(m)}; \\
M_{4i}^{(m)} &= C_{44}(\mathrm{i}km\varphi_i^{(m)} + \lambda_i^m\chi_i^{(m)}) \\
M_{4(i+3)}^{(m)} &= C_{44}(\mathrm{i}km\varphi_i^{(m)} + \lambda_i^m\chi_i^{(m)}); \\
M_{5i}^{(m)} &= \mathrm{i}kmC_{13}\chi_i^{(m)} + C_{33}\lambda_i^m\varphi_i^{(m)} - \alpha_3\xi_i^{(m)}; \\
M_{5(i+3)}^{(m)} &= -(\mathrm{i}kmC_{13}\chi_i^{(m)} + C_{33}\lambda_i^m\varphi_i^{(m)} - \alpha_3\xi_i^{(m)}); \\
M_{6i}^{(m)} &= \xi_i^{(m)}; M_{6(i+3)}^{(m)} = -\xi_i^{(m)}
\end{aligned} \tag{E.1}
$$

frontiers | Frontiers in Marine Science

TYPE Original Research
PUBLISHED 02 February 2023
DOI 10.3389/fmars.2023.1097701

Check for updates

OPEN ACCESS

EDITED BY
Lian-Gang Lü,
First Institute of Oceanography (FIO), China

REVIEWED BY
Xianyan Wang,
Third Institute of Oceanography, China
Chao Sun,
Northwestern Polytechnical University, China

*CORRESPONDENCE
Xiao-Mei Xu
xmxu@xmu.edu.cn

SPECIALTY SECTION
This article was submitted to Ocean Observation, a section of the journal Frontiers in Marine Science

RECEIVED 14 November 2022
ACCEPTED 09 January 2023
PUBLISHED 02 February 2023

CITATION
Huang L-F, Xu X-M, Yang L-L, Huang S-Q, Zhang X-H and Zhou Y-L (2023) Underwater noise characteristics of offshore exploratory drilling and its impact on marine mammals.
Front. Mar. Sci. 10:1097701.
doi: 10.3389/fmars.2023.1097701

Underwater noise characteristics of offshore exploratory drilling and its impact on marine mammals

Long-Fei Huang[1], Xiao-Mei Xu[1*], Liang-Liang Yang[2,3], Shen-Qin Huang[1], Xin-Hai Zhang[1] and Yang-Liang Zhou[1]

[1]Key Laboratory of Underwater Acoustic Communication and Marine Information Technology of The Ministry of Education, College of Ocean and Earth Sciences, Xiamen University, Xiamen, Fujian, China, [2]Guangdong Provincial Key Laboratory of Marine Disaster Prediction and Prevention, Shantou University, Shantou, China, [3]Institute of Marine Science, Shantou University, Shantou, China

Geotechnical survey is an important prerequisite to the construction of offshore wind farms. However, the impact of underwater survey noises has not yet been studied in details. In this paper, we studied transmission of underwater noises from offshore exploratory drilling (OED) at the Xiamen port. The noises were categorized into three types: hammering noises (hammering down of casings, which were 180-mm diameter steel pipes), vibrating noises (vibration of casings that had been hammered down), and drilling noises (generated during the borehole drilling process). We considered the variation in intensity of these three noise types, and set up two fixed and one movable stations to measure and analyze the source and propagation characteristics of these noises. The results indicate that hammering noise is an impulsive sound with a dominant frequency below 10 kHz, and source levels (SL_s) of 197.1 dB re 1μPa @ 1 m (rms over 95% energy duration. 1–64,000 Hz) and 212.9 dB re 1μPa @ 1 m (peak). Vibrating and drilling noises are non-impulsive sounds with the fundamental frequencies of 41 Hz and 45 Hz, and SL_s of 158.9 dB re 1μPa rms @ 1 m and 155.9 dB re 1μPa rms @ 1 m, respectively. The impact assessment of OED noises on five groups of marine mammals with different audible frequency ranges (Low (LF), High (HF), and Very High (VHF) frequency cetaceans, sirenians (SI), and phocid pinnipeds (PW)) demonstrates that hammering noise can induce a high risk of hearing damage to their hearing, at as far as 300 meters for VHF group, while drilling noise can only induce hearing damage at about 40 meters. Marine mammals are susceptible to behavior alteration, with a detectable distance of 1.9 km from the source, and it is recommended to set a warning zone with a radius of 1.9 km during OED construction.

KEYWORDS

offshore wind farms, geotechnical survey, offshore exploratory drilling, underwater noise, marine mammals

1 Introduction

With the advantages of sufficient wind resources, no occupation of land resources, and proximity to power load centers (*e.g.*, megalopolis) along the coasts, offshore wind farms (OWFs) have become the treasure of energy market and rapidly developed across the globe. However, the development and operation of OWFs will generate a series of anthropogenic underwater noises, changing the ocean soundscape over a wide area. Most OWFs employ fixed-foundation wind turbines in the near-coastal within 50 m water depth, where inhabited kinds of marine mammals (Thomsen et al., 2006). Marine mammals, which mostly rely on sound for spatial orientation, communication, and predation, are very sensitive to changes in ocean soundscape (Wartzok and Ketten, 1999; Richardson et al., 2013; Haver et al., 2018). OWFs' noises may adversely affect marine mammals, including behavior alteration, hearing damage, physical injury, and even mortality (Ketten et al., 1993). In order to mitigate these potential effects, it is vital to measure and analyze the underwater noises during the OWFs lifecycle, and further assess the impacts of these noises on marine mammals (Díaz and Soares, 2020).

The lifecycle of an OWF can be split into four phases: pre-construction (geotechnical survey), construction, operation, and decommissioning (Nedwell and Howell, 2004; Popper et al., 2022). Underwater noises generated during the construction phase, such as pile driving noise (Herbert-Read et al., 2017; Branstetter et al., 2018; Guan and Miner, 2020) and power cable laying noise (Nedwell et al., 2003; Nedwell et al., 2012; Bald et al., 2015), and noises during the operation phase, such as the radiated underwater noise from wind turbines (Pangerc et al., 2016; Yang et al., 2018), have been monitored and analyzed. Additionally, concerns about the decommissioning noises have been heating up in recent years as more and more early-built OWFs reach their end of operational life (Fowler et al., 2018; Hall et al., 2020; Hall et al., 2022).

In contrast, research on underwater noises during the OWFs geotechnical survey phase is still scarce (Mooney et al., 2020; Popper et al., 2022). Offshore exploratory drilling (OED) is one of the most common methods in the phase, and the operating platform used for OED can be divided into two categories (Fugro Marine GeoServices, Inc 2017): standard vessel (use anchors or dynamic positioning systems to keep platforms on position) and jack-up platform (use three or four piles inserted into the seabed to lift and fix platforms above the sea surface). Jack-up platform has most machinery well above the water line, while the hull of standard vessel has good coupling with the water (Kyhn et al., 2014; Shonberg et al., 2017; Todd et al., 2020), which may result in different acoustic characteristics of OED noises. Jack-up platforms are primarily used on offshore oil (gas) exploration and exploitation projects (Erbe and McPherson, 2017; Jiménez-Arranz et al., 2020) measured the source level (*SL*) of geotechnical drilling noise on *Sideson II* jack-up rig is 142–145 dB re 1μPa rms @ 1 m (30–2000 Hz, 83 mm diameter drill rod), and Todd et al. (2020) measured the received level of underwater noises from *Noble Kolskaya* jack-up exploration drilling rig is 120 dB re 1μPa rms @ 41 m (2–1400 Hz). OWFs prefer to conduct OED on standard vessels because of the lower cost, deeper working depths and greater mobility (Maynard and Schneider, 2010). However, to date there has been no detailed analysis of underwater noises during OED on standard vessels.

In this paper, underwater survey noises of OED on a standard vessel were monitored in an offshore area of Xiamen, China. The OED noises were categorized into three types: hammering noise (generated by hammering down casings), vibrating noise (generated by vibrating down casings), and drilling noise (generated by borehole drilling). Considering the possible intensity variations of the three kinds of noise, two fixed and one movable measurement stations were set to obtain the accurate source intensity and propagation characteristics. Based on the measured data, the statistics [mean, standard deviation, and ranges (min–max)] of root-mean-square (rms) and zero-to-peak (peak) sound pressure levels, and sound exposure levels (SEL) were calculated, and the information on the time domains, frequency domains, and spectrograms were given in detail. Besides, by combining the auditory weighted SEL with the marine mammal noise exposure criteria, this paper further assessed the noise impacts (hearing damage and behavior alteration) on marine mammals (hearing groups of LF, HF, VHF, SI, and PW).

2 Materials and methods

2.1 Field operation

The study site was located in a sea area approximately 3 km from the coast of Xiamen, China. OED was conducted on a standard vessel of 45 m in length and 14 m in width (Figure 1A) that used 4-point anchor spread to remain in a stable location. A drilling platform of 2 m in length was welded to the deck on the middle side of the hull, and the rig derrick (Figure 1C3) was installed on the platform. OED rotated the drill rod to make the diamond bit (Figure 1C5), at the end of drill rod) grinding the soil and rock layer to obtain the cylindrical soil samples (Figure 1C6) and rock samples (Figure 1C7), and used steel casings (Figure 1C4) to protect the borehole. The specific steps are as follows (Figure 1B):

1. Hammering down casings with a hammer (Figure 1C1). After the drilling platform was in position, a 200 kg hammer was lifted to a height of 1.5–2 m and then released instantaneously to impact casings (180 mm diameter) at an interval of approximately 3 s, until the end of casings penetrated into the hard soil layer. This step was to prevent the borehole from collapsing in the loose soil layer during borehole drilling, and it lasted about 30 min in total (excluding the time to extend casings).
2. Vibrating down casings with a vibrator (Figure 1C2). The vibrator generated high-frequency vibrations to liquefy the soil structure and reduce the frictional resistance between the casing and soil, and then casings continued to be driven into the ground by the weight of casings and vibrator until the end of casings encountered the stiff fine-grained layer (about 3–5 m below the seabed). Switching from hammer to vibrator was to avoid damaging casings because of the strong instantaneous impact between the casing and hard soil. This step also lasted about 30 min.

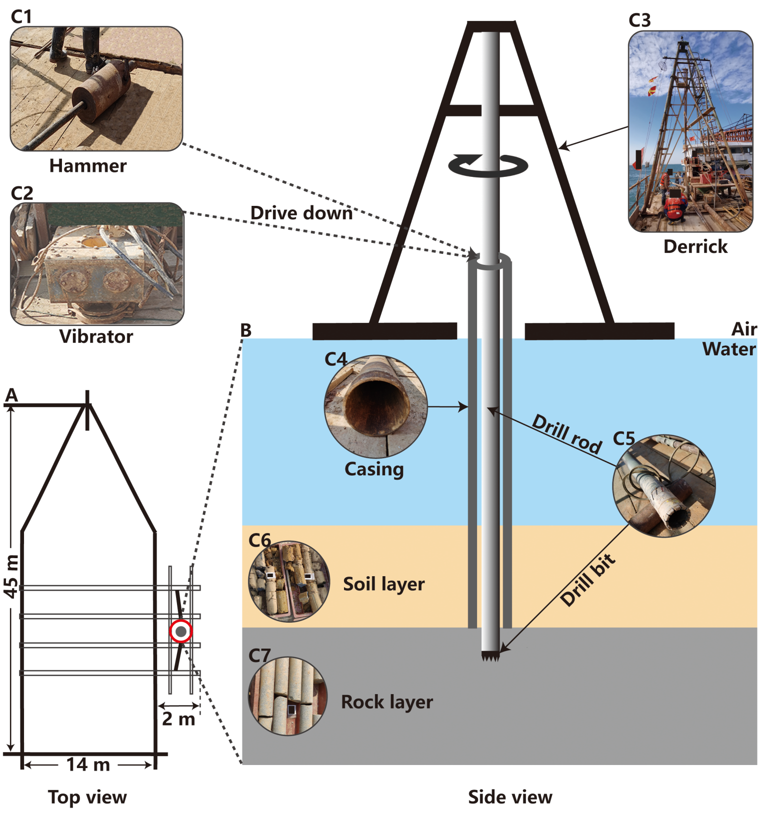

FIGURE 1
Schematic diagram of offshore exploration drilling (OED) on standard vessel [**(A)**: top view of OED platform; **(B)**: side view of OED construction]. **(C1, C2)**: the hammer and vibrator used to drive down the casing **(C4)**; **(C3)**: the derrick for fixing drilling machines; **(C5)**: the drill rod, which uses the drill bit at the end to obtain the samples of soil layer **(C6)** and rock layer **(C7)**.

3. Borehole drilling. A steel hollow drill rod (91 mm diameter) was lowered inside casings and driven by a motor to rotate advance along the soil and rock layers in 300 rpm. The diamond bit drilled and cut the soil (rock) layer to obtain cylindrical samples, until the bit reached the fixed depth (about 10 m below the bedrock). This step lasted approximately 20 hours because of the high hardness of the rock layer.

According to the field operation, underwater noises during OED on the anchored vessel were mainly categorized into three types: hammering noise (generated in step 1), vibrating noise (generated in step 2), and drilling noise (generated in step 3).

2.2 Noise recording

The noise monitoring was conducted on January 10, 2021, with the weather of sunny and the sea state of 2. The OED area's seafloor is flat, and the water depth was about 7 m (measured by Base X, a sound speed profiler made by Oceanographic AML, inc.) during monitoring. Two fixed measurement stations (station 1 and 2) and one movable measurement station (station 3) were set up to monitor the three kinds of noise, as illustrated in the measurement configuration diagram (Figure 2). Station 1 and 2 were set on the drilling vessel, with distances of 6 m and 18 m from the source, respectively. Station 3 was set on a movable boat with a distance of 280 m from the source during hammering and vibrating down casings, and 40 m during borehole drilling. The distances were measured by a laser rangefinder at the source. At station 1 and 3, underwater noises were recorded by a self-contained LoPAS-L recorder (Hangzhou Soniclnfo Technology Co., Ltd., China, the receiving voltage sensitivity is -192.6 dB re 1 V/µPa) at 3 m water depth, with a sampling frequency of 128,000 Hz. At station 2, noises were recorded by a B&K 8105 hydrophone at 3 m water depth (Brüel & Kjær, inc., the receiving voltage sensitivity ranges from -205.8 to -209.6 dB re 1V/µPa), and then collected by a USB 4431 multi-channel coherent data acquisition card (National Instrument, inc.), with a sampling frequency of 65,536 Hz. Additionally, background noise of the drilling area was monitored when the platform was silent.

2.3 Data analysis

The raw measured data (bin files) were converted into sound pressure time-series (time waveforms) in Pa and then analyzed using the custom written MATLAB (MathWorks Inc., Natick, MA, version R2022a) scripts.

In the first step, spectrum diagrams and spectrograms in sound pressure power spectral density (PSD) level (unit: dB re 1 $\mu Pa^2/Hz$) of OED noises were plotted. Spectrum diagrams can provide information on the distribution of noise energy in frequency, and

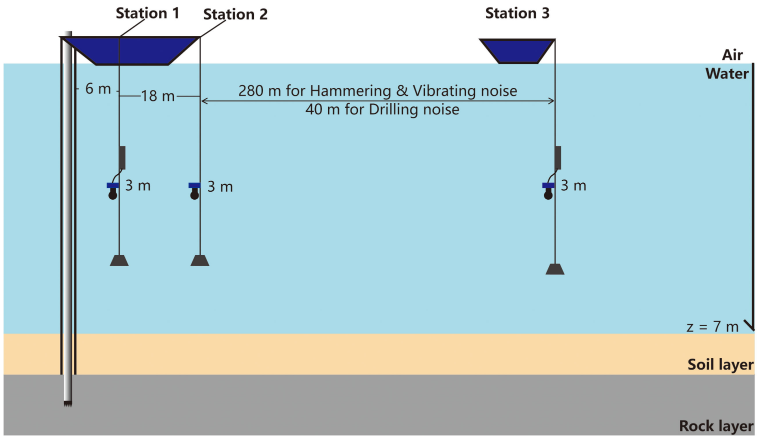

FIGURE 2
Schematic diagram of the measurement configuration for underwater noises during OED (distances shown are not to scale).

were generated with Welch's method of segment averaging (Welch, 1967), using 65,536 sample hamming windows with 80% overlap. Spectrograms can provide information on the distribution of noise energy in frequency and time, and were generated using a short-time Fourier transform size of 65,536 and a window size of 65,536 with 80% overlap.

In the second step, the root-mean-square and zero-to-peak sound pressure level (SPL_{rms} and SPL_{zp}) in dB re 1μPa, and the sound exposure level (SEL_s) in dB re 1μPa^2·s were calculated over 1-second-long segments of the sound pressure time-series (for hammering noise, the 0.5 s data before and after each pulse were selected as the 1-second segments). SPL_{rms}, SPL_{zp} and SEL_s were all recommended as the key metrics for analyzing and managing underwater soundscapes (Robinson et al., 2014), and SPL_{rms} is defined as follows (Madsen, 2005):

$$SPL_{rms} = 20\lg\left(\frac{\sqrt{\frac{1}{T}\int_T p_{(t)}^2 dt}}{p_{ref}}\right) \quad (1)$$

where $p(t)$ is the instantaneous sound pressure in Pa (Urick, 1983). T is the duration that comprises 95% of the acoustic energy. p_{ref} is the reference sound pressure, which equals 1 μPa .

SPL_{zp} provides the peak energy information of the noise (Hawkins et al., 2014; Merchant et al., 2015), and is defined as follows (ISO, 2017):

$$SPL_{zp} = 20\lg\left(\frac{max(|p(t)|)}{p_{ref}}\right) \quad (2)$$

SEL_s reflects the energy exposure level of a single signal (impulsive sound) or signal in unit time (non-impulsive sound), and is defined as follows (ISO, 2017):

$$SEL_s = 10\lg\left[\frac{1}{t_{ref}}\int_0^T \frac{p^2(t)}{p_{ref}^2} dt\right] \quad (3)$$

where T equals 1 s, t_{ref} is the reference time and equals 1 s.

The statistics including means, standard deviations (SD), and ranges (minimum–maximum values) of the three metrics were then calculated, and note that the means were calculated in Pa and then converted to dB.

In the third and final step, source levels (SL_s) in the three metrics were calculated. The propagation of underwater acoustic signals in marine environments is complex, especially in shallow water where OWFs are commonly located. Urick (1983) gives an equation to simplify the solution of SL_s:

$$SL_s = RSL_s + TL_s \quad (4)$$

where RSL_s are the received sound levels of each statistic at measurement stations, and TL_s are the transmission losses in dB, which can be defined by the equation:

$$TL_s = Alg(r) + \alpha r \quad (5)$$

where r is the propagation range in m. A is a distance-dependent factor, and it equaled 20 (spherical spreading) to estimate the SL_s (r = 1 m) based on the RSL_s at measurement station 1 (r = 6 m). ? is the frequency-depended absorption coefficient in dB/m, and it was ignored in this paper as the dominant frequencies of OED noises are lower than 10 kHz (Fisher and Simmons, 1977).

2.4 Impact assessment

This paper further evaluated the potential hearing damage and behavior alteration of OED noises on marine mammals. Hearing damage, also called noise-induced threshold shift (Finneran and Jenkins, 2012; Finneran, 2015), can be divided into temporary threshold shift (TTS) and permanent threshold shift (PTS). TTS means the animals' hearing thresholds return to normal when the noise exposure disappears, while PTS means the hearing thresholds remain elevated eventually (Southall, 2021). This paper assessed the PTS and TTS risk of OED noises with reference to the marine mammal noise exposure criteria (hereinafter referred to as the criteria) developed by Southall et al. (2019). The criteria divide marine mammals into six hearing groups: Low- (LF), High- (HF), and Very High- (VHF) frequency cetaceans, sirenians (SI), and otariid (OW) and phocid (PW) pinnipeds in water. OW group (sea lions, walruses, and polar bears) was not analyzed in this paper as relatively few conflicts have been reported between these animals and OWFs.

The criteria take the auditory weighted cumulative sound exposure level (SEL_w) in dB re 1μPa^{2}s as the main assessment metric. SEL_w is an important indicator for evaluating the overall energy exposure level of underwater noise on marine organisms (Martin et al., 2019), and can be expressed as follows:

$$SEL_w = 10lg\left(\frac{\int_0^{f_s/2} W_{aud}(f)S(f)df}{t_{ref}P_{ref}^2}\right) + 10lg\left(\frac{T_d}{t_{ref}}\right) \tag{6}$$

where f_s is the sampling frequency in Hz, and to measure the SEL_w for all marine mammal hearing groups, the f_s should be 64 kHz or higher. (f) is the mean PSD level of each 1-second-long segment data. T_d is the total exposure time (or called cumulative time) of underwater noises in s. $W_{aud}(f)$ is the auditory weighting function in dB/Hz, which aim to emphasize the frequencies where the animals are more sensitive and de-emphasize the frequencies where the animals are less sensitive, and it is expressed as follows (National Marine Fisheries Service, 2018):

$$W_{aud}(f) = C + 10\lg\left\{\frac{(f/f_1)^{2a}}{\left[1+(f/f_1)^2\right]^a\left[1+(f/f_2)^2\right]^b}\right\} \tag{7}$$

where f is the frequency in Hz. The values of gain parameter C in dB, cut-off frequencies f_1 and f_2 in kHz, and frequency exponents ? and b all vary with the hearing groups. *Eq.* (6) reduces to the unweighted cumulative *SEL* (*SELuw*) when W_{aud} (f) = 1.

The criteria establish different PTS and TTS risk thresholds for different hearing groups and noise types (impulsive sound and non-impulsive sound). This paper calculated the *SELw* for the five hearing groups, then evaluated the PTS and TTS risk of OED noises at three measurement stations referring to the corresponding thresholds. The potential ranges of PTS and TTS risk were estimated by calculating the distance from the source to the point where *SELw* attenuated to the thresholds.

To date no criteria have established behavior thresholds for different hearing groups to different underwater noises (Southall, 2021). Given the hearing capability of marine mammals' receiving system (hearing audiogram) is normally slightly higher than the background noise level, a simple method to assess the range of behavior alteration is turning to estimate the distance that the noise propagates from the source to the point where its energy attenuates to the background noise level (assume the animal responds to the noise once received). For instance, Wang et al. (2014) estimated the impact range of vibration piling noise on *Sousa chinensis* by this method. This paper combined *Eq.* (5) and the RSL_s in *SPLrms* at each measurement station to calculate the TL_s, then estimated the distances between the source and the points where the RSL_s attenuated to the background noise level, that are, the behavior reaction ranges of marine mammals to OED noises.

3 Results

After excluding the data with high background noise interference, a total of 8.2 GB noise data was acquired. Figure 3 illustrates the time waveforms, spectrum diagrams, and spectrograms of hammering noise, vibrating noise, and drilling noise that measured at station 1. It can be seen from Figures 3A1–C1 that hammering noise consists of a series of strikes with broadband and short duration, and is a typical impulsive sound (Hamernik and Hsueh, 1991). Figures 3A2–C2, and Figures 3A3–C3 illustrate that vibrating noise and drilling noise are continuous and the noise levels vary little with time, which are the typical characteristics of non-impulsive sound. It can be seen from Figures 3B1–B3 that the intensity of hammering noise is the highest among the three noise types, which is about 60 dB above the background level. In contrast, the intensity of vibrating and drilling noise is low and close to the background level. Besides, Figures 3C1–C3 illustrate that vibrating noise has two significant single-frequency components at 41 Hz and 124 Hz, and drilling noise has a significant single-frequency component at 45 Hz. Hammering noise and vibrating noise both have a high narrow-band component at the center frequency of 14 Hz with the bandwidth of 10 Hz.

Table 1 illustrates the source levels (SL_s) in the metrics of SPL_{zp}, SPL_{rms}, and SEL_s of the three noise types during OED, and the background noise in the table was measured at station 1. It can be seen from the Table that the intensity of hammering noise is the highest, followed by vibrating noise, and drilling noise is the lowest.

4 Discussions

4.1 Noise characterization

Hammering noise was generated during hammering down the casing. Since a large amount of gravitational potential energy (approximately 3000–4000 J) of the heavy hammer was instantaneously released on casings, hammering noise exhibits the significant characteristics of short duration and broadband, and is a typical impulsive sound (Figures 3A1–C1). Besides, repeated hammer strikes cause hammering noise appears in the form of pulse trains. The dominant frequency of hammering noise is below 10 kHz (take the PSD level of 100 dB re 1μPa^2/Hz at station 1 as the threshold), and its peak energy appears at 1 kHz with the PSD level of 140 dB re 1μPa^2/Hz. The intensity of hammering noise is the highest among the three kinds of noises, with the SL_s of 197.1 dB re 1μPa rms @ 1 m and 212.9 dB re 1μPa peak @ 1 m (Table 1). Hammering noise strongly resembles the noise of offshore impact piling during OWFs

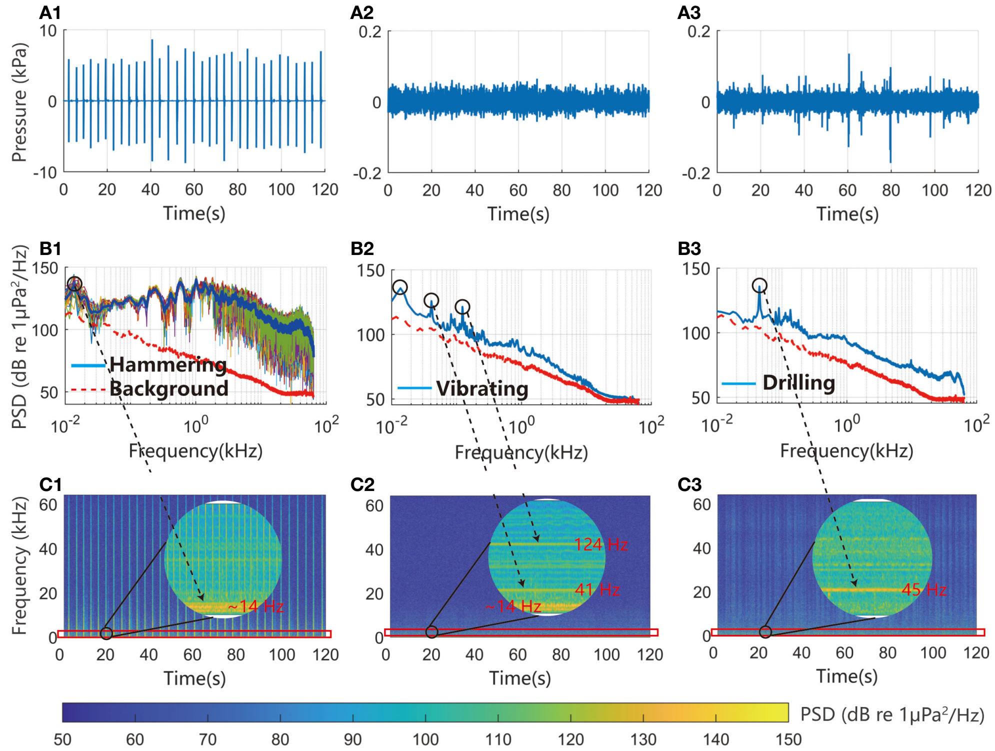

FIGURE 3
The time waveforms **(A1-A3)**, spectrum diagrams **(B1-B3)**, and spectrograms **(C1-C3)** of hammering noise, vibrating noise and drilling noise measured at the station 1 during OED. The spectrum diagrams in sound pressure power spectral density (PSD) level were generated with Welch's method (Welch, 1967), using 65,536 sample hamming windows with 80% overlap. The spectrograms in PSD level were generated using short-time Fourier transform (hamming window, window size: 65,536, overlap: 80%). The colored, thin lines in **(B1)** are single strikes of hammering noise, and the blue, thick line is the average. The circles in **(C1-C3)** are the local enlargements of spectrograms.

construction phase, and the diameter and material of pile (pipe) are the main factors affecting the noise levels (Reinhall and Dahl, 2011; Zampolli et al., 2013; Lippert and von Estorff, 2014). The pile (pipe) used in offshore impact piling is in various diameters, usually 0.3–2.0 m (Lippert et al., 2016), and in various materials, such as concrete, steel shell, and steel core (Guan and Miner, 2020), so the noise levels vary substantially with pile parameters. In contrast, the casing used in OED is usually steel pipe with a small and relatively fixed diameter, and the intensity of hammering noise normally does not change significantly due to casing parameters.

Vibrating noise was generated during vibrating down the casing. Because the vibration energy was released smoothly from the vibrator to casings, vibrating noise, as one of the products of the energy conversion, is a typical non-impulsive sound. The intensity of vibrating noise is low, with an *SL* of 158.9 dB re 1μPa rms @ 1 m (Table 1). Both vibrating noise and hammering noise have a strong narrow-band component at the center frequency of 14 Hz with the bandwidth of 10 Hz (Figures 2C1, 2C2). Considering the generation processes of the two noise types, the narrow-band component may be the low-frequency vibration generated by the interaction between the

TABLE 1 Source levels of hammering noise, vibrating noise, and drilling noise during OED.

Noise types	Statistics	SPL_{zp}	SPL_{rms}	SEL_s
Hammering	Mean ± SD	212.9 ± 1.4	197.1 ± 3.3	182.2 ± 1.5
	Range (min–max)	206.3–215.8	185.9–203.9	177.0–188.0
Vibrating	Mean ± SD	168.2 ± 1.8	158.9 ± 2.1	158.7 ± 2.1
	Range (min–max)	162.4–171.8	151.4–163.3	151.4–162.4
Drilling	Mean ± SD	168.3 ± 3.0	155.9 ± 1.4	155.8 ± 1.3
	Range (min–max)	161.6–180.3	150.5–161.8	150.4–161.2
Background	Mean ± SD	135.8 ± 2.1	123.1 ± 1.7	123.0 ± 1.6
	Range (min–max)	131.4–140.3	117.5–126.8	117.4–126.5

Units: dB re 1μPa for SPL_{zp} and SPL_{rms}, and dB re 1μPa^2· s for SEL_s. The background noise was measured at station 1.

casing and seabed when driving down casing. In addition, vibrating noise has two strong single-frequency components of 41 Hz and 124 Hz, which may be the resonance signals of casings that driven by vibrator and related to the inherent frequencies of casings. The noise of vibrating down piles during the OWFs construction phase is similar to vibrating noise, but the vibratory hammers used in vibrating down piles are generally heavier and oscillate at a much higher rate (Guan and Miner, 2020), which results in a higher noise level. For instance, the *SPLrms* of a typical noise during vibratory pile driving of a 1 m diameter steel pile is 175 dB re 1μPa @ 10 m (Buehler et al., 2015).

Drilling noise was generated during the drilling bit grinding the soil and rock layer, which is a non-impulsive sound. The noise came primarily from inside the seabed, and its energy would be greatly attenuated as it transmitted from the soil and rock layer into water. Besides, casings on the outside of drill rod acted as a sound barrier and further impeded the noise propagation. The *SL* of drilling noise is 155.9 dB re 1μPa rms @ 1 m (Table 1), and the peak energy appears at 45 Hz with a sound level of 136 dB re 1μPa^2/Hz. Unlike the vibrating noise, drilling noise still has a high energy in the frequency band above 1 kHz (Figure 3B3), and there is a series of clear irregular stripes with broadband on the spectrogram of drilling noise (Figure 3C3), which is likely to be generated by the collision of drilling rod with the inner wall of casing during rotation. The measured *SPLrms* of drilling noises on the jack-up platforms are 142–145 dB re 1μPa @ 1 m (Erbe and McPherson, 2017) and 120 dB re 1μPa @ 41 m (Todd et al., 2020), which are lower than the value of 155.9 dB re 1μPa rms @ 1 m measured in this study. The difference in the noise levels may be related to the platforms, the anchored vessel in this paper coupled well with the water and led to a good leakage of the equipment noise on the vessel into the water, while the jack-up platforms are well above the water line.

Figure 4 illustrates the spectrum diagrams of hammering noise, vibrating noise, and drilling noise that measured at the three measurement stations. It can be seen from the figure that the

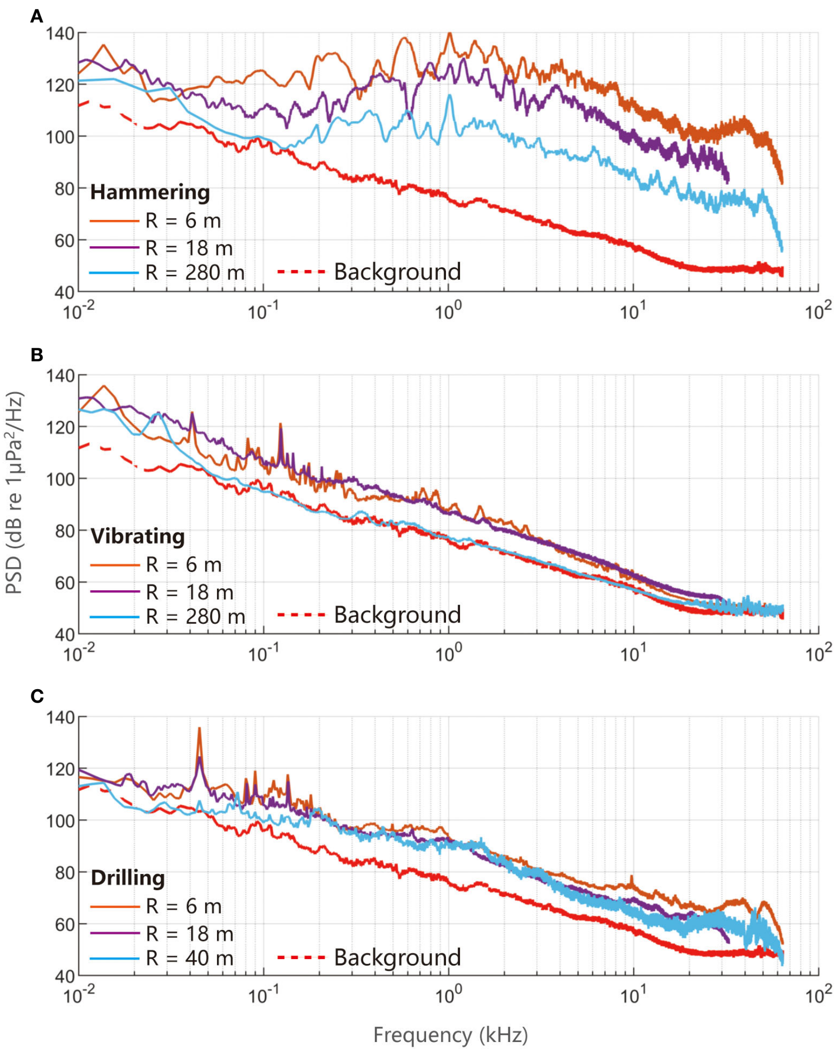

FIGURE 4
Spectrum diagrams of hammering noise **(A)**, vibrating noise **(B)**, and drilling noise **(C)** that measured at the station 1 (6 m from the source, R = 6 m), station 2 (R = 18 m) and station 3 (R = 280 m for hammering and vibrating noise, R = 40 m for drilling noise) during OED. The spectrum diagrams in sound pressure power spectral density (PSD) level were generated with Welch's method (Welch, 1967), using 65,536 sample hamming windows with 80% overlap.

energy of hammering noise decay significantly with the distance, and the decay rate is low in the frequency band below 40 Hz and high in the frequency band above 1 kHz. The energy decay rate of vibrating noise with distance is lower than that of hammering noise, but as the low SL_s, the energy of vibrating noise in the frequency band above 50 Hz would be closed to the background level before reaching station 3 (280 m from the source). Unlike hammering noise and vibrating noise, the energy decay rate in the frequency band below 200 Hz of drilling noise is significantly higher than that in the frequency band above 200 Hz (Figure 4C), which may be related to the noise sources and the propagation paths. Drilling noise has two sources: one was inside of seabed and transmitted through the soil (rock) layer to the water, and another was on the casing and transmitted directly into the water. The first source was in the low-frequency band and occupied the primary energy, and the second source was broadband with low energy, but its decay rate was lower than that of the first source. Besides, the decreased water depth (8.5 m depth during hammering down casings decreased to 6 m during borehole drilling because of the tide) was also expected to contribute to the difference in decay rate of the two frequency bands. Lower frequency acoustic signal with longer wavelength in relation to the water depth cannot propagate efficiently in shallower water, because of the "low-frequency" cut-off (Etter, 2018; Guan and Miner, 2020).

4.2 Impacts on marine mammals

Table 2 illustrates the auditory weighted cumulative *SEL* for the five hearing groups (*e.g.*, *SELw,LF* refers to the weighted cumulative *SEL* for the *LF* group), and the cumulative times (T_d in *Eq.* (6)) of hammering noise, vibrating noise, and drilling noise were 600 s, 1800 s, and 72,000 s according to the field operation. TL_s between the three measurement stations in the table were calculated based on the unweighted cumulative *SEL* (SEL_{uw}) at each station, and the *TL*

TABLE 2 The SEL_w of hammering noise, vibrating noise, and drilling noise that measured at the three stations during OED.

Measurement station	Acoustic parameters	Hammering	Vibrating	Drilling
	SEL_{uw}	195.4	174.3	187.5
Station 1 06 m from the Source	SEL_w,LF	194.5	163.0	179.6
	SEL_w,HF	184.1	138.9	163.4
	SEL_w,VHF	181.4	136.3	162.4
	SEL_w,SI	188.9	143.9	164.4
	SEL_w,PW	193.7	152.7	170.2
TL_s from the Source to Station **1**		15.6	15.6	15.6
	SEL_{uw}	190.6	173.6	185.8
Station 2 18 m from the source	SEL_w,LF	189.3	159.3	176.0
	SEL_w,HF	176.9	136.3	156.0
	SEL_w,VHF	173.1	133.7	153.6
	SEL_w,SI	182.7	140.8	159.8
	SEL_w,PW	186.8	148.5	167.5
TL_s from the Station **1** to Station **2**		4.8	0.7	1.7
	SEL_{uw}	168.3	173.4	176.5
Station 3 Hammering&Vibrating: 280 m from the source Drilling: 40 m from the source	SEL_w,LF	166.4	152.9	173.5
	SEL_w,HF	153.1	134.8	155.2
	SEL_w,VHF	151.0	134.1	153.0
	SEL_w,SI	156.9	136.0	158.0
	SEL_w,PW	162.5	141.8	166.8
TL_s from the Station **2** to Station **3**		22.3	–	9.3

Units: dB re 1μPa^{2}s for SEL, and dB re 1μPa for SPL_{rms}.
SELuw refers to the unweighted cumulative sound exposure level.
Hearing group of marine mammals: Low- (LF), High- (HF), and Very High- (VHF) frequency cetaceans, sirenians (SI), and phocid pinnipeds in water (PW).
SEL_w for impulsive Temporary Threshold Shift (TTS): LF = 168, HF = 170, VHF = 140, SI = 175, PW = 170.
SEL_w for impulsive Permanent Threshold Shift (PTS): LF = 183, HF = 185, VHF = 155, SI = 190, PW = 185.
SEL_w for non-impulsive TTS: LF = 179, HF = 178, VHF = 153, SI = 186, PW = 181.
SEL_w for non-impulsive PTS: LF = 199, HF = 198, VHF = 173, SI = 206, PW = 201.
Colored cells indicate: Above PTS.
Above TTS by 10–20 dB.
Above TTS less than 10 dB.

equations (*Eq.* (5)) for hammering noise and drilling noise from the station 2 to station 3 were modelled to $TL_1(r) = 9.1lg(r)$ and $TL_2(r) = 9.5lg(r)$, respectively.

It can be seen from Table 2 that hammering noise has a high hearing damage risk to marine mammals, and there is still a TTS risk to the VHF group at station 3. Based on the TL_1 equation and the thresholds of PTS and TTS risk, the hearing damage range of hammering noise to marine mammals (VHF group) was estimated to be up to a radius of 300 m from the source. Vibrating noise has low hearing damage risk, and its SEL_w at station 1 is already lower than the thresholds of PTS and TTS risk for each hearing group. Though the *SL* of drilling noise is lower than vibrating noise (Table 1), the cumulative time of 72,000 s resulted in a high SEL_w, and the maximum damage distance of drilling noise to marine mammals (VHF group) was estimated to be 40 m from the source.

The potential ranges of behavior alteration of OED noises on marine mammals exceeds that of hearing damage. Based on the *SPLrms* of the three kinds of noises and background noise (Table 1), hammering noise was estimated to be detected by marine mammals up to 1.9 km from the source, and drilling noise was estimated to be detected at a distance of 170 m. The risk of vibrating noise was ignored because its noise energy was likely to approach the ambient level before reaching station 3 (40 m from the source). Comprehensive analysis of the potential risk of hearing damage and behavior alteration, it is recommended to set up a warning zone with a radius of 1.9 km from the source to observe and avoid the presence of marine mammals during OED.

5 Conclusion

This study provides the first detailed analysis of underwater noises during OED on standard vessels, which are frequently generated in OWFs geotechnical surveys. The results indicate that OED noises mainly include three types: hammering noise, vibrating noise, and drilling noise. Hammering noise is a high-intensity impulsive sound with the source level (*SL*) of 197.1 dB re 1μPa rms @ 1 m, and its dominant frequency is below 10 kHz and peak energy appears at 1 kHz with the PSD level of 140 dB re $1\mu Pa^2/Hz$; Vibrating noise is a low-intensity non-impulsive sound with the *SL* of 158.9 dB re 1μPa rms @ 1 m. The noise has a significant single-frequency component at 41 Hz and 124 Hz, and has a same narrow-band signal with 14 Hz center frequency and 10 Hz bandwidth as hammering noise. Drilling noise is the lowest among the three noise types, with the *SL* of 155.9 dB re 1μPa rms @ 1 m and a significant single-frequency component at 45 Hz. The impact assessment of OED noises on marine mammals demonstrates that the potential range of hearing damage can reach a 300 m radius from the source, and the range of behavioral alteration is up to 1.9 km. Therefore, setting up a warning zone with a radius of 1.9 km during OED is recommended.

This study makes up for the lacking research on OWFs geotechnical survey noise, and improves the understanding of underwater noises and their ecological impacts during the whole OWFs' lifecycle. However, further research on noise levels and propagation characteristics during OED in different vessel size and different environmental conditions (*e.g.*, water depth and bedrock type) are needed to better understand OED noises characteristics and their impacts on marine life, including important fish species.

Data availability statement

The raw data supporting the conclusions of this article will be made available by the authors, without undue reservation.

Author contributions

LH: Conceptualization, investigation, data curation, formal analysis, writing – original draft, software, methodology and visualization. XX: Conceptualization, writing – review and editing, funding acquisition, methodology, project administration, and supervision. LY: Methodology. SH, XZ, and YZ: Investigation. All authors contributed to the article and approved the submitted version.

Funding

This work was supported by the National Natural Science Foundation of China (Grant number 41976178).

Acknowledgments

The authors are grateful to Fanggui Xiao, Chenhui Wang and Zhen Li for their help with the acoustic recordings in the measurement trials.

Conflict of interest

The authors declare that the research was conducted in the absence of any commercial or financial relationships that could be construed as a potential conflict of interest.

Publisher's note

References

Bald, J., Hernández, C., Uriarte, A., Castillo, J., Ruiz, P., and Ortega, N. (2015). Acoustic characterization of submarine cable installation in the Biscay marine energy platform (BIMEP). *Bilbao Mar. Energy Week.* 27, 20–24. Available at: https://tethys.pnnl.gov/sites/default/files/publications/Bald-et-al-2015c.pdf

Branstetter, B. K., Bowman, V. F., Houser, D. S., Tormey, M., Banks, P., Finneran, J. J., et al. (2018). Effects of vibratory pile driver noise on echolocation and vigilance in bottlenose dolphins (*Tursiops truncatus*). *J. Acoust. Soc. Am.* 143, 429–439. doi: 10.1121/1.5021555

Buehler, D., Oestman, R., Reyff, J., Pommerenck, K., and Mitchell, B. (2015). *Technical guidance for assessment and mitigation of the hydroacoustic effects of pile driving on fish* (Sacramento, CA: California Department of Transportation), 4–21. California Department of Transportation (Caltrans) Report No. CTHWANP-RT-15-306.01.01.

Díaz, H., and Soares, C. G. (2020). Review of the current status, technology and future trends of offshore wind farms. *Ocean Eng.* 209, 107381. doi: 10.1016/j.oceaneng.2020.107381

Erbe, C., and McPherson, C. (2017). Underwater noise from geotechnical drilling and standard penetration testing. *J. Acoust. Soc. Am.* 142, EL281–EL285. doi: 10.1121/1.5003328

Etter, P. C. (2018). *Underwater acoustic modeling and simulation. 4th ed* (Boca Raton: CRC Press).

Finneran, J. J. (2015). Noise-induced hearing loss in marine mammals: A review of temporary threshold shift studies from 1996 to 2015. *J. Acoust. Soc. Am.* 138, 1702–1726. doi: 10.1121/1.4927418

Finneran, J., and Jenkins, A. (2012). *Criteria and thresholds for US navy acoustic and explosive effects analysis* (Space and Naval Warfare Systems Center Pacific San Diego, CA). Available at: https://apps.dtic.mil/sti/citations/ADA561707

Fisher, F., and Simmons, V. (1977). Sound absorption in sea water. *J. Acoust. Soc. Am.* 62, 558–564. doi: 10.1121/1.381574

Fowler, A. M., Jørgensen, A. M., Svendsen, J. C., Macreadie, P. I., Jones, D. O., Boon, A. R., et al. (2018). Environmental benefits of leaving offshore infrastructure in the ocean. *Front. Ecol. Environ.* 16, 571–578. doi: 10.1002/fee.1827

Fugro Marine GeoServices, Inc (2017). *Geophysical and geotechnical investigation methodology assessment for siting renewable energy facilities on the Atlantic OCS* (Fugro Marine GeoServices, Inc). OCS Study BOEM 2017-049. Available at: https://tethys.pnnl.gov/publications/geophysical-geotechnical-investigation-methodology-assessment-siting-renewable-energy

Guan, S., and Miner, R. (2020). Underwater noise characterization of down-the-hole pile driving activities off biorka island, Alaska. *Mar. pollut. Bull.* 160, 111664. doi: 10.1016/j.marpolbul.2020.111664

Hall, R., João, E., and Knapp, C. W. (2020). Environmental impacts of decommissioning: Onshore versus offshore wind farms. *Environ. Impact. Asses.* 83, 106404. doi: 10.1016/j.eiar.2020.106404

Hall, R., Topham, E., and João, E. (2022). Environmental impact assessment for the decommissioning of offshore wind farms. *Renewable Sustain. Energy Rev.* 165, 112580. doi: 10.1016/j.eiar.2020.106404

Hamernik, R. P., and Hsueh, K. D. (1991). Impulse noise: some definitions, physical acoustics and other considerations. *J. Acoust. Soc. Am.* 90, 189–196. doi: 10.1121/1.401287

Haver, S. M., Gedamke, J., Hatch, L. T., Dziak, R. P., Van Parijs, S., McKenna, M. F., et al. (2018). Monitoring long-term soundscape trends in US waters: the NMFS/NPS ocean noise reference station network. *Mar. Policy.* 90, 6–13. doi: 10.1016/j.marpol.2018.01.023

Hawkins, A., Popper, A., Fay, R., Mann, D., Bartol, S., Carlson, T., et al. (2014). *Sound exposure guidelines for fishes and Sea turtles: A technical report* (Cham, Switzerland: Springer and ASA Press).

Herbert-Read, J. E., Kremer, L., Bruintjes, R., Radford, A. N., and Ioannou, C. C. (2017). Anthropogenic noise pollution from pile-driving disrupts the structure and dynamics of fish shoals. *Proc. R. Soc B* 284, 20171627. doi: 10.1098/rspb.2017.1627

ISO (2017). *Underwater acoustics–terminology* (Switzerland: International Organization for Standardization Geneva).

Jiménez-Arranz, G., Banda, N., Cook, S., and Wyatt, R. (2020). "Review on existing data on underwater sounds produced by the oil and gas industry," in *JIP topic - sound source characterisation and propagation* (Joint Industry Programme (JIP) on E&P Sound and Marine Life). Available at: https://gisserver.intertek.com/JIP/DMS/ProjectReports/Cat1/JIP-Proj1.4.2_Review_on_Noise_from_Industrial_Sources.pdf

Ketten, D., Lien, J., and Todd, S. (1993). Blast injury in humpback whale ears: Evidence and implications. *J. Acoust. Soc. Am.* 94, 1849–1850. doi: 10.1121/1.407688

Kyhn, L. A., Sveegaard, S., and Tougaard, J. (2014). Underwater noise emissions from a drillship in the Arctic. *Mar. pollut. Bull.* 86, 424–433. doi: 10.1016/j.marpolbul.2014.06.037

Lippert, S., Nijhof, M., Lippert, T., Wilkes, D., Gavrilov, A., Heitmann, K., et al. (2016). COMPILE–a generic benchmark case for predictions of marine pile-driving noise. *IEEE J. Oceanic Eng.* 41, 1061–1071. doi: 10.1109/JOE.2016.2524738

Lippert, T., and von Estorff, O. (2014). The significance of parameter uncertainties for the prediction of offshore pile driving noise. *J. Acoust. Soc. Am.* 136, 2463–2471. doi: 10.1121/1.4896458

Madsen, P. T. (2005). Marine mammals and noise: Problems with root mean square sound pressure levels for transients. *J. Acoust. Soc. Am.* 117, 3952–3957. doi: 10.1121/1.1921508

Martin, S. B., Morris, C., Bröker, K., and O'Neill, C. (2019). Sound exposure level as a metric for analyzing and managing underwater soundscapes. *J. Acoust. Soc. Am.* 146, 135–149. doi: 10.1121/1.5113578

Maynard, M. L., and Schneider, J. (2010). *Geotechnics for developing offshore renewable energy in the US. 1st ed* (CRC Press), 611–616. Frontiers in Offshore Geotechnics II. Available at: https://www.taylorfrancis.com/chapters/edit/10.1201/b10132-83/geotechnics-developing-offshore-renewable-energy-us-landon-maynard-schneider

Merchant, N. D., Fristrup, K. M., Johnson, M. P., Tyack, P. L., Witt, M. J., Blondel, P., et al. (2015). Measuring acoustic habitats. *Methods Ecol. Evol.* 6, 257–265. doi: 10.1111/2041-210X.12330

Mooney, T. A., Andersson, M. H., and Stanley, J. (2020). Acoustic impacts of offshore wind energy on fishery resources. *Oceanography.* 33, 82–95. Available at: https://www.jstor.org/stable/26965752

National Marine Fisheries Service (2018). *2018 revisions to: Technical guidance for assessing the effects of anthropogenic sound on marine mammal hearing (Version 2.0)* Vol. 167 (Silver Spring, MD: National Marine Fisheries Service). NOAA Tech. Memo. NMFS-OPR-59. Available at: https://www.fisheries.noaa.gov/resource/document/technical-guidance-assessing-effects-anthropogenic-sound-marine-mammal-hearing

Nedwell, J., Brooker, A., and Barham, R. (2012). Assesment of underwater noise during the installation of export power cables at the Beatrice offshore wind farm. *Subacoustech Environ. Rep. NE318R0106.* Available at: https://marine.gov.scot/datafiles/lot/bowl/ES/ES%20Volume%204%20-%20Annexes/7B%20OfTW%20Underwater%20Noise/Annex%207B%20OfTW%20Underwater%20Noise.pdf

Nedwell, J., and Howell, D. (2004). A review of offshore windfarm related underwater noise sources. *Cowrie Rep.* 544, 1–57.

Nedwell, J., Langworthy, J., and Howell, D. (2003). Assessment of sub-sea acoustic noise and vibration from offshore wind turbines and its impact on marine wildlife; initial measurements of underwater noise during construction of offshore windfarms, and comparison with background noise. *Subacoustech Rep. ref: 544R0423 published by COWRIE* 725. Available at: http://users.ece.utexas.edu/~ling/2A_EU1.pdf

Pangerc, T., Theobald, P. D., Wang, L. S., Robinson, S. P., and Lepper, P. A. (2016). Measurement and characterisation of radiated underwater sound from a 3.6 MW monopile wind turbine. *J. Acoust. Soc. Am.* 140, 2913–2922. doi: 10.1121/1.4964824

Popper, A. N., Hice-Dunton, L., Jenkins, E., Higgs, D. M., Krebs, J., Mooney, A., et al. (2022). Offshore wind energy development: Research priorities for sound and vibration effects on fishes and aquatic invertebrates. *J. Acoust. Soc. Am.* 151, 205–215. doi: 10.1121/10.0009237

Reinhall, P. G., and Dahl, P. H. (2011). Underwater Mach wave radiation from impact pile driving: Theory and observation. *J. Acoust. Soc. Am.* 130, 1209–1216. doi: 10.1121/1.3614540

Richardson, W. J., Greene, C. R.Jr., Malme, C. I., and Thomson, D. H. (2013). *Marine mammals and noise* (San Diego: Academic Press).

Robinson, S. P., Lepper, P. A., and Hazelwood, R. A. (2014). *Good practice guide for underwater noise measurement* (Technical report, National Measurement Office, Marine Scotland, The Crown Estate). doi: 10.25607/OBP-21

Shonberg, A., Harte, M., Aghakouchak, A., Brown, C., Andrade, M. P., and Liingaard, M. (2017). "Suction bucket jackets for offshore wind turbines: applications from *in situ* observations," in *Proc. TC209 Workshop, 19th International Conference on Soil Mechanics and Geotechnical Engineering*, Seoul, South Korea. p65–p77. Available at: https://scholar.google.com/scholar_lookup?title=Suction%20bucket%20jackets%20for%20offshore%20wind%20turbines%3A%20applications%20from%20in%20situ%20observations&author=A.%20Shonberg&publication_year=2017

Southall, B. L. (2021). Evolutions in marine mammal noise exposure criteria. *Acoustics Today* 17, 52–60. doi: 10.1121/AT.2021.17.2.52

Southall, B. L., Finneran, J. J., Reichmuth, C., Nachtigall, P. E., Ketten, D. R., Bowles, A. E., et al. (2019). Marine mammal noise exposure criteria: Updated scientific recommendations for residual hearing effects. *Aquat. Mamm.* 45, 125–232. doi: 10.1578/AM.45.2.2019.125

Thomsen, F., Lüdemann, K., Kafemann, R., and Piper, W. (2006). *Effects of offshore wind farm noise on marine mammals and fish* (Newbury, UK: Biola, Hamburg, Germany on behalf of COWRIE Ltd.), 62pp.

Todd, V. L., Williamson, L. D., Jiang, J., Cox, S. E., Todd, I. B., and Ruffert, M. (2020). Proximate underwater soundscape of a north Sea offshore petroleum exploration jack-up drilling rig in the dogger bank. *J. Acoust. Soc. Am.* 148, 3971–3979. doi: 10.1121/10.0002958

Urick, R. J. (1983). *Principles of underwater sound. 3rd ed* (Peninsula Publising Los Atlos, California: Academic Press), 23–24. Available at: https://books.google.co.jp/books/about/Principles_of_Underwater_Sound.html?id=MBBgQgAACAAJ&redir_esc=y

Wang, Z., Wu, Y., Duan, G., Cao, H., Liu, J., Wang, K., et al. (2014). Assessing the underwater acoustics of the world's largest vibration hammer (OCTA-KONG) and its potential effects on the indo-pacific humpbacked dolphin (*Sousa chinensis*). *PloS One* 9, e110590. doi: 10.1371/journal.pone.0110590

Wartzok, D., and Ketten, D. R. (1999). "Marine mammal sensory systems," in *Biology of marine mammals.* Eds. J. E. Reynolds II and S. A. Rommel (Washington, DC: Smithsonian Institute Press), 117–175.

Welch, P. (1967). The use of fast Fourier transform for the estimation of power spectra: a method based on time averaging over short, modified periodograms. *IEEE Trans. Audio Electroacoust.* 15, 70–73. doi: 10.1109/TAU.1967.1161901

Yang, C.-M., Liu, Z.-W., Lü, L.-G., Yang, G.-B., Huang, L.-F., and Jiang, Y. (2018). Observation and comparison of tower vibration and underwater noise from offshore operational wind turbines in the East China Sea bridge of shanghai. *J. Acoust. Soc. Am.* 144, EL522–EL527. doi: 10.1121/1.5082983

Zampolli, M., Nijhof, M. J., de Jong, C. A., Ainslie, M. A., Jansen, E. H., and Quesson, B. A. (2013). Validation of finite element computations for the quantitative prediction of underwater noise from impact pile driving. *J. Acoust. Soc. Am.* 133, 72–81. doi: 10.1121/1.4768886

frontiers | Frontiers in Marine Science

TYPE Original Research
PUBLISHED 03 February 2023
DOI 10.3389/fmars.2023.1106980

Check for updates

OPEN ACCESS

EDITED BY
Rui He,
Hohai University, China

REVIEWED BY
Michael L. Fine,
Virginia Commonwealth University,
United States
Zhongchang Song,
Xiamen University, China

*CORRESPONDENCE
Yanming Yang
yangyanming@tio.org.cn

SPECIALTY SECTION
This article was submitted to
Ocean Observation,
a section of the journal
Frontiers in Marine Science

RECEIVED 24 November 2022
ACCEPTED 16 January 2023
PUBLISHED 03 February 2023

CITATION
Niu F, Xie J, Zhang X, Xue R, Chen B, Liu Z and Yang Y (2023) Assessing differences in acoustic characteristics from impact and vibratory pile installation and their potential effects on the large yellow croaker (*Pseudosciaena crocea*).
Front. Mar. Sci. 10:1106980.
doi: 10.3389/fmars.2023.1106980

Assessing differences in acoustic characteristics from impact and vibratory pile installation and their potential effects on the large yellow croaker (*Pseudosciaena crocea*)

Fuqiang Niu[1,2,3], Jiarui Xie[1], Xuexin Zhang[4], Ruichao Xue[1,2], Benqing Chen[1,2,3], Zhenwen Liu[5] and Yanming Yang[1,2*]

[1]Third Institute of Oceanography, Ministry of Natural Resources, Xiamen, China, [2]Fujian Provincial Key Laboratory of Marine Physical and Geological Processes, Xiamen, China, [3]Observation and Research Station of Coastal Wetland Ecosystem in Beibu Gulf, Ministry of Natural Resources, Beihai, China, [4]Zhejiang Communications Construction Group Co. LTD., Hangzhou, China, [5]College of Harbour and Coastal Engineering, Jimei University, Xiamen, China

Underwater noise from anthropogenic activities can have negative behavioral and physical effects on marine life, including physical changes, injuries, and death. Impact pile driving and vibratory pile driving are generally used for the construction of ocean-based foundations. Based on the field data under the same marine engineering and marine environment, this paper addresses the characteristics of underwater noise from impact and vibratory pile driving, their differences, and the effects of noise on populations of the large yellow croaker (*Pseudosciaena crocea*). The impact pile driving pulse had a median peak-to-peak sound pressure source level (SPL_{pp}) of 244.7 dB re 1 μPa at 1 m and a median sound exposure source level (SEL_{ss}) of 208.1 dB re 1 $\mu Pa^2 s$ at 1 m by linear regression. The waveform of vibratory pile driving appears to be continuous with a low SPL_{pp}, but the cumulative SEL (SEL_{cum}) in 1 min is very high, reaching 207.5 dB re 1 $\mu Pa^2 s$ at 1 m. The range of behavioral response for adult large yellow croaker (20–23 cm) is predicted to be 4,798 m for impact pile driving and 1,779 m for vibratory pile driving. The study provides evidence of the comparative potential effects of vibratory and impact pile driving on the large yellow croaker and reference for the conservation of croaker.

KEYWORDS

underwater noise, impact pile driving, vibratory pile driving, sound characteristics, behavioral response, large yellow croaker (*Pseudosciaena crocea*)

Introduction

The increasing number of marine engineering construction, such as offshore wind farm projects, cross-sea bridges, and submarine tunnels, has attracted public attention to its environmental impact. In particular, the sound emanating from these anthropogenic activities has been shown to have a wide range of potential effects on marine life

(Nowacek et al., 2007; Kight and Swaddle, 2011; Southall et al., 2019). The impact of underwater noise generated in different construction periods of marine engineering projects on marine life cannot be ignored. To minimize the impact of underwater noise on marine life, it is essential to establish controls on the acoustic characteristics of noise sources to meet the exposure criteria for different animals. Sound exposure criteria are the sound levels, based on acoustic response thresholds, above which sounds may have negative effects on specified animals (Hawkins et al., 2020).

In the past decades, many studies have been carried out to address the impact of underwater noise on marine mammals (National Research Council [NRC], 2003; Southall et al., 2007; National Marine Fisheries Service [NMFS], 2018). There is growing concern about the effects of anthropogenic noise on fishes in recent years, and more studies are necessary to address the issue (Popper and Hawkins, 2016; Popper and Hawkins, 2019; Hawkins et al., 2020). Sound is used for communication, reproduction, the detection of prey and predators, orientation and migration, and habitat selection (Webb et al., 2008). Therefore, anything that biologically interferes with how fish live can have a negative effect on them. However, there are still substantial knowledge gaps in the potential effects of sound on some fishes, such as the large yellow croaker (*Pseudosciaena crocea*). The large yellow croaker, which has significant economic value, is one of the important aquaculture fish species in China. Large yellow croakers are known to produce sound, the acoustic characteristics of which have been widely studied in recent years (Ramcharitar et al., 2006; Ren et al., 2007; Zhou et al., 2022). Moreover, most croakers are sensitive to sound through their otoliths and swim bladder (Zhang et al., 2021). Wang et al. (2017) studied the noise field distribution of underwater blasting and evaluated its impact on the large yellow croaker. The results suggested that for a 155-kg charge, a juvenile yellow croaker requires a safe range of approximately 2,500 m, while young fish and adult fish require a range of 1,600 and 900 m, respectively. Lin et al. (2019) designed two laboratory experiments to study the impacts of ship noise on the growth and immunophysiological response in the juveniles of two Sciaenidae species, *Larimichthys crocea* and *Nibea albiflora*. The results showed that the physiological indices of both *L. crocea* and *N. albiflora* increased sharply within 3 h due to ship noise stimulation, but after a month of noise stimulation, the growth and immune indices decreased significantly. However, the effects of underwater noise on the species have rarely been investigated (Horodysky et al., 2008).

Pile driving is a construction method generally used to provide foundation support for buildings and structures including offshore wind turbines, bridges, harbor facilities, and offshore oil and gas production structures (Reyff, 2012). There are mainly two types of pile driving based on mechanical principle: impact and vibratory. Impact pile driving occurs during the installation in construction projects using high-energy impact hammers, which creates an intense, impulsive, and sharp sound that radiates into the surrounding environment (Amaral et al., 2020). Many studies indicated that impact pile driving noise has adverse effects on marine life, including marine mammals (Nehls et al., 2007; Kastelein et al., 2013; Leunissen and Dawson, 2018; Leunissen et al., 2019) and fish (Casper et al., 2013; Bagocius, 2015; Hawkins and Popper, 2017). Unlike impact pile driving, vibratory pile driving describes the process in which the pile is vibrated into the sediment rather than being hammered in (Popper et al., 2022). The sound produced by vibratory pile driving is nonimpulsive and continuous, which is different from impact pile driving (Dahl et al., 2015; Jiménez-Arranz et al., 2020). Vibratory pile driving has been recommended as a quieter alternative to impact pile driving in some cases. However, only a few studies have been conducted to investigate the effects of vibratory pile driving on marine life (Wang et al., 2014; Branstetter et al., 2018), which focused on cetaceans. No studies about the effects of vibratory pile driving on fish have been conducted. Assessments of the potential impacts of sound exposures are typically used to distinguish between continuous sounds and impulse sounds. Because different kinds of sounds have different attributes, they may have very different effects on animals. Assessments should consider the intensity of the sound at the moment of exposure, the duration of individual exposure events, the integration of all exposure events, and the time interval between repeated exposure events (Hawkins et al., 2020).

The acoustic characteristics of the pile driving noise may be related to the local ocean environment. Therefore, the sound features and differences between impact and vibratory pile driving noise produced during the same marine engineering and marine environment were investigated. The sound data on received levels at different sites were collected to fit noise propagation for the research area. Finally, the effects of pile driving noise on populations of the large yellow croaker are also evaluated in this paper by the field observation of the behavioral response of yellow croakers at each site.

Acoustic measurements

The study was conducted within the Sandu Bay, Ningde City, Fujian Province, China. The large yellow croaker is the largest sea-cage culture fish in China, and more than 80% of large yellow croakers are produced in Ningde City (Chen et al., 2018). Measurements of underwater noise, including impact and vibratory pile driving noise, were made during the construction of the Dong-Wu-Yang cross-sea bridge in April and September 2022 (26.66°N, 119.94°E; Figure 1A), at water depths of approximately 40–60 m. The measurement of impact pile driving noise was carried out simultaneously at six locations on two range transects (blue solid circles in Figure 1A) during the installation of a steel casing pile (blue five-pointed star in Figure 1A), with a diameter of 2.5 m and a length of 80 m, on 1 April 2022. The pile was driven into the seabed using a hydraulic impact hammer (IHC-800, IHC, Kinderdijk, Netherlands Figure 1B) with an energy rating of 800 kJ. Underwater acoustic measurement for vibratory pile driving was conducted simultaneously at five locations on two range directions (red solid circles in Figure 1A) during the installation of five steel casing piles (red five-pointed stars in Figure 1A) from 7 to 14 September 2022. The diameter and length of five steel piles were 4.4 and 79 m, respectively. The piles were driven using a hydraulic vibratory piling hammer (YZ-800B, Yongan, Wenzhou, China) with a centrifugal force of 11,000 kN. The distances from the steel piles to the measurement locations were measured using a GNSS equipment (Global Navigation Satellite System (GNSS) N6, Sino, Guangzhou, China). To investigate the propagation attenuation of sound levels with distance for impact and vibratory pile driving noise, measurements were made at 80, 598, 664, 1,530, 3,563,

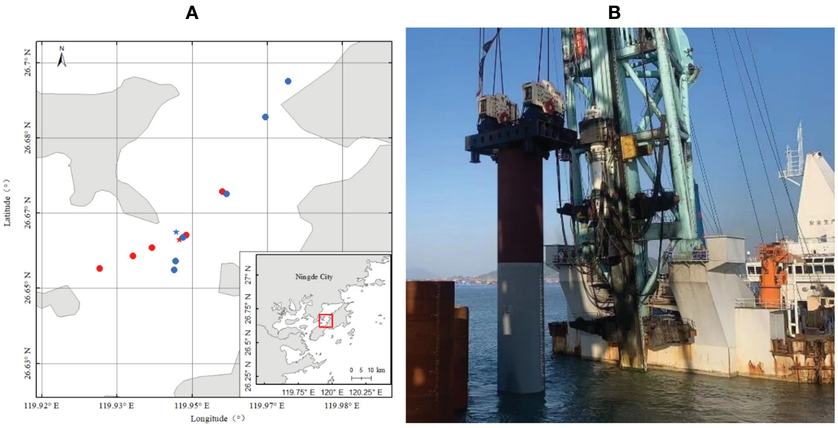

FIGURE 1
(A) Location of the steel casing piles and measurement sites. Five-pointed stars indicate the expected locations for pile driving. Solid circles represent the measurement sites. **(B)** Photograph of the cross-sea bridge construction.

and 4,573 m from the pile for impact pile driving and at 120, 717, 1,137, 1,484, and 1,933 m (averaged) for vibratory pile driving (Figure 1A).

All monitoring stations were equipped with the autonomous, low-power underwater acoustic recorders (USR2000, IOACAS) with hydrophones at a depth of 5 m. During the measurements, the deployment depth was recorded by a depth sensor (Duo-500, RBR) positioned 0.5 m above each hydrophone. The omnidirectional hydrophone has a flat frequency response (± 2 dB) between 20 Hz and 20 kHz. During the measurement of impact pile driving, recorders with a sampling frequency of 48 kHz were used in three stations with a distance of less than 1 km from each other, and the other three stations used hydrophones with an effective receiving sensitivity of −220 and −170 dB re 1 V/µPa. The recorders were sampled at 16 kHz and the hydrophones' effective receiving sensitivity was −170 dB re 1 V/µPa for vibratory pile driving. Prior to measurements, all hydrophones were calibrated by the Hangzhou Institute of Applied Acoustics in Hangzhou, China. Water column sound speed measured by SVP (Minos X, AML Oceanographic) during the two measurements were 1,498 and 1,540 m/s, respectively. A portable depth sounder (SM-5, Speedtech, Great Falls, America) was used to measure the bathymetry of the study area. The average water depth at the pile position was approximately 55 m, which decreased subtly to approximately 40 m at 4,500 m to the northeast and approximately 30 m at 2,000 m to the southwest. The sediment layer in the study area consists of coarse sand and clay *via* sample analysis. In the same area, 10 min of ambient noise was measured when no pile driving occurred.

During the entire pile driving duration, field observation of the behavioral response of yellow croakers in a normal aquaculture cage at each site was also conducted. The size of the cage is 5 m × 5 m, with a depth of 8 m, which contains approximately 100,000 adult fishes. The sound exposure level in the cage was recorded while the behavioral response of croakers in the cage was observed. The average sound exposure level in multiple observations was estimated as the behavioral response threshold of croakers in this paper. In this paper, behavioral response is defined as the substantial change in the behavior of an animal population (the croakers, in this case) such as fleeing quickly, moving away from the sound source, and jumping out of the water.

The pile driving signals were detected and calculated by custom analysis scripts written in MATLAB R2019a. For impact pile driving, it can be characterized by using peak-to-peak sound pressure level (SPL_{pp}) and sound exposure level (SEL), which indicate the maximum peak-to-peak pressure of the impulse signal and the total energy for the duration of a single pulse, respectively. The waveform of vibratory pile driving appears as a continuous signal with a low SPL_{pp}; thus, the cumulative SEL (SEL_{cum}) in 1 min is calculated to characterize exposure energy. These are given by the following formulas:

$$\mathbf{SPL_{pp}} = 20\mathbf{log}_{10}\left(\frac{|\mathbf{max}(p(t)) - \mathbf{min}(p(t))|}{p_{\mathbf{ref}}}\right) \tag{1}$$

$$\mathbf{SEL} = 10\mathbf{log}_{10}\left(\frac{\int_{t_1}^{t_2} p(t)^2 dt}{p_{\mathbf{ref}}^2 t_{\mathbf{ref}}}\right) \tag{2}$$

$$\mathbf{SEL_{cum}} = 10\mathbf{log}_{10}\left(\frac{\sum_{i=1}^{N} \int_{t_1}^{t_2} p_i(t)^2 dt}{p_{\mathbf{ref}}^2 t_{\mathbf{ref}}}\right) \tag{3}$$

where $p(t)$ is the measured pressure signal. p_{ref} is the reference value of sound pressure (equal to 1 µPa) and t_{ref} is the reference value of time (equal to 1 s). t_1 and t_2 are the start and end points of time window, respectively, for a single exposure duration. The time interval is bounded by the times when the cumulative signal energy exceeds 5% of the total signal energy and ends when it reaches 95% for impulse signals (Southall et al., 2007). N is the number of signals.

The frequency spectrum of pile driving noise and ambient noise can be expressed in pressure spectral density in units of $\mu Pa^2/Hz$, which is computed in constant-width bands of 1 Hz.

Results

Acoustic characteristics of impact and vibratory pile driving noise

To investigate the differences in impact and vibratory pile driving noise, the pressure time series of the two signals are given in Figure 2, which were measured at 598 and 717 m from the sound source, respectively. The waveform of ambient noise and an expanded signal of impact pile driving are also shown in Figure 2. The waveform of impact pile driving noise consists of several Mach waves called a Mach cone (Reinhall and Dahl, 2011). Because the study focuses on the difference in underwater noise from impact and vibratory pile driving and its effect on the large yellow croaker, the details of Mach waves were not measured in the paper.

Underwater noise from impact pile driving appeared in a time series of single impulse signals (Figures 2A, D). The mean duration of the impulse including 90% of the energy was approximately 121 ms. Figure 2A also shows that the sound pressure amplitudes of received signals in the same distance varied with the time series. SPL_{pp} increased from 187 to 191 dB. The cause of the variations in SPL_{pp} may be related to the energy per strike. Hammer strikes were repeated until the pile was driven to the desired depth. Impact pile driving is always initiated with a soft-start period in the early stages, in which the hammer energy was initially low and gradually increased to reach the required stroke strength. Data for the initial strikes corresponding to the soft-start period were excluded. During the measurements, the hammer strikes were repeated 160 times for 4 min. Figures 3A–C respectively depict the measured SPL_{pp}, SEL_{ss}, and strike energy as a function of the number of hammer strikes for 160 strikes. The range values of SPL_{pp} and SEL_{ss} were 162–166 dB with a mean value of 189.7 ± 1.2 dB and 189–195 dB with a mean value of 159.8 ± 1.2 dB, respectively. The strike energy increased from 150 to 350 kJ. The relation curve between SEL_{ss} and the strike energy of each hammer strike is shown in Figure 3D. With the increase in strike energy, SEL_{ss} increased correspondingly. When strike energy was increased from 150 to 350 kJ, SEL_{ss} was increased by approximately 4 dB. However, the difference in SEL_{ss} was little because of the slight variation in strike energy.

The SPL_{pp} of underwater noise generated from vibratory pile driving presented a continuous signal without a maximum value and a lower level than impact pile driving (Figure 2B). The mean-square pressure level reached over 1 s of averaging in the time series with a length of 1 min was 149.3 dB.

Figure 4 shows the averaged narrow-band (resolution, 1 Hz) pressure spectral densities for impact pile driving noise from 160 hammer strikes at the range of 598 m and for vibratory pile driving noise based on 3 min of sound data at the range of 717 m. To show contrast with pile driving noise, the pressure spectral densities of background ambient noise are also analyzed and presented in Figure 4. It can be seen from the figure that the noise spectrum of the two types of pile driving was different. The acoustic energy from impact pile driving concentrated between 100 and 1,000 Hz, which was approximately 40 dB higher than noise in the same frequency band from vibratory pile driving. In addition, the overall frequency band of sound levels for impact pile driving noise was also much higher than natural ambient sound levels. The spectral analysis also showed that the acoustic energy from vibratory pile driving was distributed below 100 Hz and decreased at a rate of approximately 6 dB/octave with increasing frequency in the bands. Although sound levels in some higher-frequency components (>700 Hz) had no difference between vibratory pile driving and natural ambient noise, the overall sound levels during vibratory pile driving were higher than ambient noise.

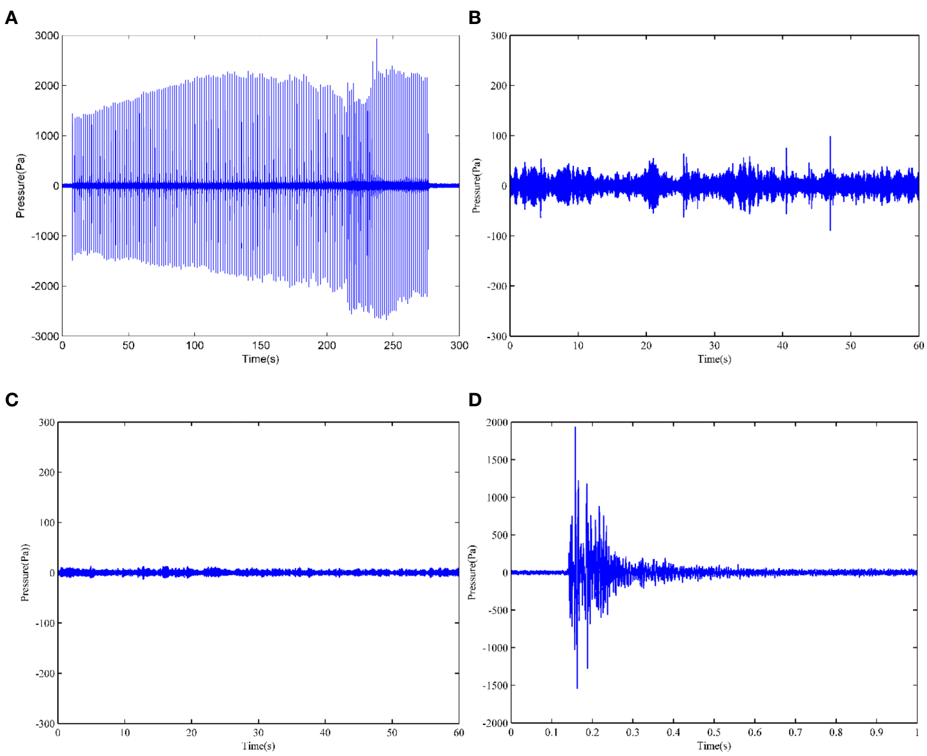

FIGURE 2
Sound pressure time series **(A)** and an expanded signal **(D)** of impact pile driving noise measured at 598 m from the pile. Sound pressure time series of vibratory pile driving noise **(B)** measured at 717 m from the pile. Waveform of ambient noise **(C)** measured at pile position.

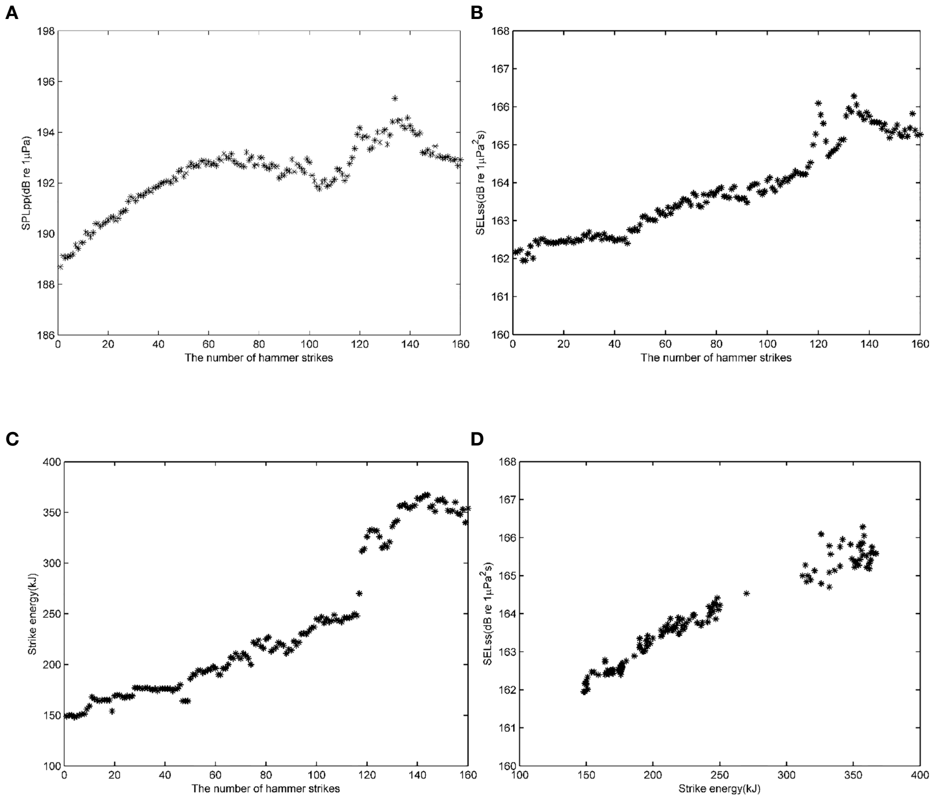

FIGURE 3
(A) Measured peak-to-peak sound pressure levels and **(B)** sound exposure levels at the range of 598 m as a function of the number of hammer strikes for impact pile driving noise. **(C)** Strike energy as a function of the number of hammer strikes for impact pile driving. **(D)** SEL_{ss} versus strike energy for each hammer strike for impact pile driving.

Variation of impact and vibratory pile driving noise with distance

Regression analysis is used to estimate the sound source levels based on the measured data. The commonly used measures of acoustic propagation loss in shallow water are the geometrical spreading laws for sound intensity, i.e., the spherical, intermediate, and cylindrical spreading laws, often called the 20 log *r*, 15 log *r*, and 10 log *r* laws, where *r* is the distance from the sound source. To begin with, the transition from 20 log *r* to 15 log *r* to 10 log *r* was a continuous one. The Marsh–Schulkin (M–S) equation used the concept of skip distance for acoustic propagation in shallow water (Urick, 1983). The M–S skip distance *R*, in kilometers, is

$$R = \left[\frac{(H + L)}{3}\right]^{1/2} \tag{4}$$

where *H*, in meters, is the depth of water and *L*, in meters, is the depth of the mixed layer. The mean depth of water in the study region is 44 m, and the depth of the mixed layer is approximately 5 m. *R* is calculated to be 4,041 m. Therefore, only data within a distance of 4,041 m were used for regression analysis.

Figures 5A–C show the mean of measured SPL_{pp}s, SEL_{ss}s (for impact pile driving), and SEL_{cum}s (for vibratory pile driving) as a function of distance and their comparisons with a regression curve based on the measured values. Because of the strong acoustic interaction with the seafloor due to a downward radiation of pile driving noise, the energy loss appeared to rapidly increase with increasing distance (Han and Choi, 2022). Sound transmission loss coefficients were calculated by the linear curve fitting of median values to estimate the sound levels with distance. The results of regression

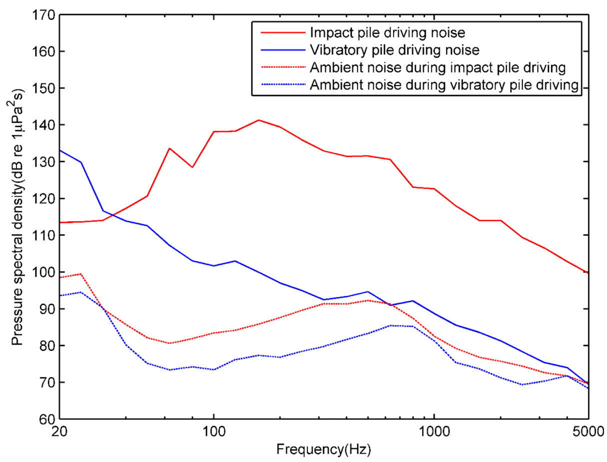

FIGURE 4
Comparison of the spectrum levels between impact and vibratory pile driving noise, and ambient noise. The red line represents the averaged Pressure spectral density (PSD) measured at the range of 598 m for 160 strikes. The blue line represents the PSD based on the 3-min time series of data measured at the range of 717 m for vibratory pile driving. The dashed lines display the PSD of ambient noise during impact and vibratory pile driving.

indicate that the best-fitting data were 20.4 log r (goodness of fit, R^2 = 0.97), 18.5 log r (R^2 = 0.93), and 19.2 log r (R^2 = 0.95), which were consistent with spherical spreading transmission loss (20 log r), where r is the distance in meters from the pile, in meters. The uncertainty of measured data excluded the difference caused by the depth of the pile penetrating the seabed. The average values and standard deviations are listed in Table 1.

The peak-to-peak pressure level versus the strike number and the sound exposure level are used to describe the pile driving noise. The results show that the mean peak-to-peak sound pressure source level and single-pulse sound exposure source level for impact pile driving are 244.7 and 208.1 dB, respectively, which are consistent with the calculation result of Wyatt's empirical formula (Wyatt, 2008). The waveform of vibratory pile driving appeared as a continuous signal with low SPL_{pp}, but the cumulative sound exposure source level in 1 min was also very high, approximately 207.5 dB.

Effects of pile driving noise on the behavior of the large yellow croaker

Before pile driving started, the large yellow croaker swam normally without any abnormal behavior. At the beginning of pile driving, the croaker showed a behavioral response (Figure 6). The degree of behavioral response varied at different distances. Table 2 shows the behavioral response of the croaker at different distances

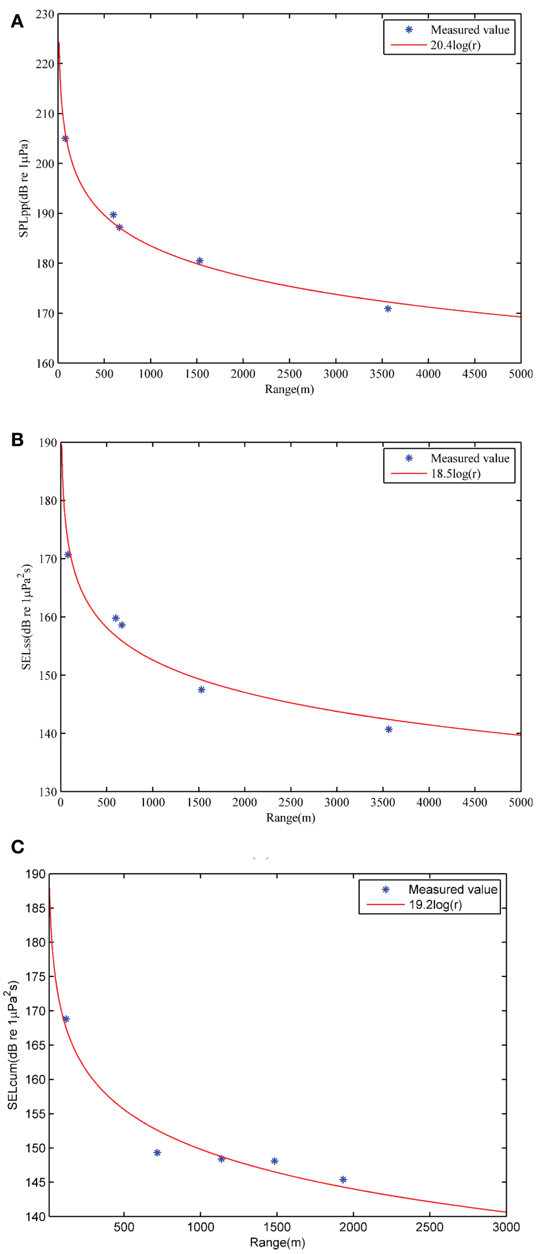

FIGURE 5
(A) The peak-to-peak sound pressure levels, **(B)** single sound exposure levels, and **(C)** cumulative sound exposure levels estimated as a function of distance and their comparisons with regression curves. The blue points represent the averaged measured values at different ranges. The red line represents the regression curve based on the measured values.

TABLE 1 Peak-to-peak pressure levels, single sound exposure levels, and cumulative sound exposure levels for pile driving as a function of distance.

Range (m)	80	598	664	1,530	3,563
SPL_{pp} (dB)	205.0 ± 1.3	189.7 ± 1.2	187.2 ± 1.8	180.5 ± 1.5	170.9 ± 1.5
SEL_{ss} (dB)	170.7 ± 1.5	159.8 ± 1.2	158.6 ± 1.8	147.5 ± 1.3	140.7 ± 1.7
Range (m)	120	717	1,137	1,484	1,933
SEL_{cum} (dB)	168.8 ± 8.6	149.3 ± 9.3	148.4 ± 8.0	148.1 ± 3.4	145.4 ± 4.8

The impulse number used in the analysis for impact pile driving was 160. The pile number used in the analysis for vibratory pile driving was 5.

during pile driving and the sound exposure values when behavioral response appeared. Within a few minutes after pile driving stopped, the croaker returned to normal behavior.

Based on the results of field observation of behavioral response of the large yellow croaker and corresponding sound measurement data at each site, the statistical onset of behavioral responses occurred in adult large yellow croakers (20–23 cm) exposed to a SEL_{ss} of 140 dB for impact pile driving and a SEL_{cum} in 1 min of 145 dB for vibratory pile driving. Therefore, based on attenuation coefficients of acoustic propagation and sound source levels obtained from measured data fitting and the behavioral response thresholds, the range of influence can be calculated by the following equation:

$$\mathbf{RL_{SEL}} = \mathbf{SL_{SEL}} - \boldsymbol{\alpha}\mathbf{log}_{10}(R) \tag{5}$$

When received sound levels are equal to the behavioral response thresholds, the calculated range values are the influence range. The range of behavioral response for adult large yellow croakers (20–23 cm) was calculated to be 4,798 m for impact pile driving and 1,779 m for vibratory pile driving, respectively. The impact of underwater noise on the large yellow croaker is obviously greater than that of vibratory pile driving (Figure 6).

Discussion and conclusion

Underwater noise from impact and vibratory pile driving was measured simultaneously at different distances during the construction of the Dong-Wu-Yang cross-sea bridge. The SPL_{pp}s and SEL_{ss}s of impact pile driving were measured at six positions at the range of 80–5,000 m, and the sound source levels were also estimated based on the measured values. In the same marine project, the measurements from vibratory pile driving were also taken simultaneously at five positions at the range of 120–2,000 m. The SPL_{pp}s values of underwater noise from vibratory pile driving were lower than those from impact pile driving; thus, cumulative sound exposure source levels in 1 min were calculated by linear regression analysis. Based on the linear regressions, the average SEL_{ss} of impact pile driving and SEL_{cum} in 1 min of vibratory pile driving were predicted to be approximately 208.1 dB re 1 μPa^2s at 1 m and 207.5 dB re 1 μPa^2s at 1 m, respectively. The frequency spectrum calculated over a given bandwidth, generally, 1 Hz or one-third octave is also important. As different animals have different frequency responses, it is important to indicate the frequency bandwidth (Popper and Hawkins, 2019). The averaged narrow-band (resolution, 1 Hz) pressure spectral densities for impact and vibratory pile driving

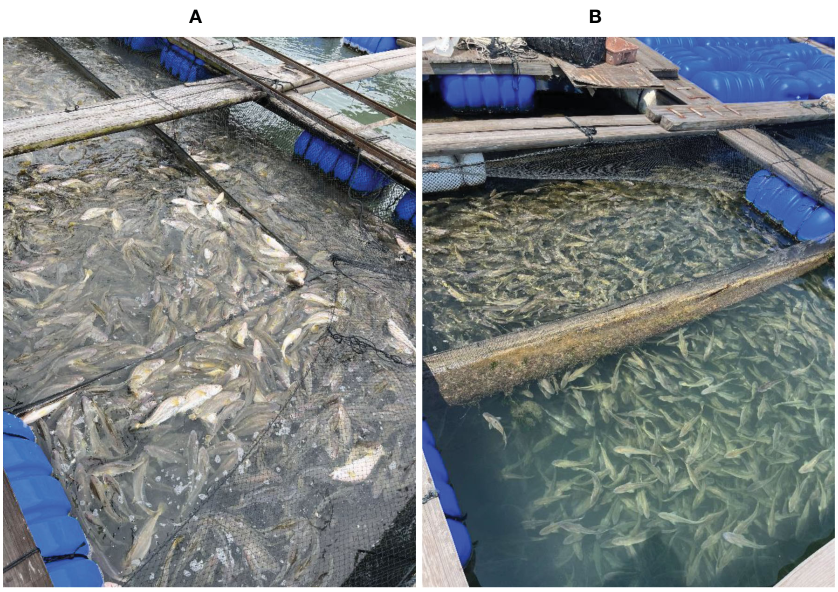

FIGURE 6
Picture of the behavioral response of the large yellow croaker at the range of 598 m for impact pile driving **(A)** and at the range of 717 m for vibratory pile driving **(B)** at the beginning of pile driving.

TABLE 2 Behavioral response of croakers at different distances and the sound exposure values when behavioral response appeared during pile driving.

	Range (m)	SEL_{ss} (dB)	Behavioral response
Impact pile driving	598	156.7	Strong changes in behavior, such as fleeing quickly, with some jumping out of the water and rolling their belly
	664	155.6	Strong changes in behavior, such as fleeing quickly, with some jumping out of the water and rolling their belly
	1,530	144.5	Substantial changes in behavior, such as fleeing quickly
	3,563	140.7	Some changes in behavior, such as emerging from the surface and swimming faster
	4,573	140.1	Minor changes in behavior, such as swimming faster
	5,100	138.9	Normal swimming, no obvious observed response
Vibratory pile driving	Range (m)	Averaged SEL_{cum} (dB)	Behavioral response
	717	148.9	Strong changes in behavior, such as fleeing quickly, with some jumping out of the water
	1,137	147.8	Some changes in behavior, such as emerging from the surface and swimming faster
	1,484	147.6	Some changes in behavior, such as emerging from the surface and swimming faster
	1,933	145.1	Minor changes in behavior, such as swimming faster
	2,837	143.2	Normal swimming, no obvious observed response

The pile number used in the analysis for vibratory pile driving was 5.

were different. The acoustic energy from impact and vibratory pile driving was concentrated between 100 and 1,000 Hz and below 100 Hz, respectively. The overall sound levels during impact and vibratory pile driving were higher than ambient noise levels.

The propagation properties of noise were determined by linear fitting regression to analyze the effect of underwater noise on marine animals. The propagation loss model is usually defined by $N \log r$, where N is the spreading loss constant and r is the distance in meters. The regressive results showed that N was 20.4 (SPL_{pp}) and 18.5 (SEL_{ss}) for impact pile driving, and 19.2 (SEL_{cum}) for vibratory pile driving, which were consistent with spherical spreading transmission loss ($20 \log r$). However, in the same marine construction project, the propagation attenuation coefficients of the two kinds of pile driving noise are different. The difference is reasonable because the coefficients are related to water column sound speed. During the measurement of vibratory pile driving, the sound speed is obviously higher than that of impact pile driving. For impact pile driving, although a previous study indicated that a relatively rapid energy loss with increasing distance was observed because of the strong acoustic interaction with the seafloor of Mach cone wave sequence radiating upwards and downwards (Han and Choi, 2022), the propagation attenuation in our study did not increase significantly with distance. The possible reason is that the hydrophone in measurements is close to the sea surface and far away from the seafloor. Three-dimensional (3D) effects can vastly affect acoustic propagation in a complex shallow water environment. Underwater sound wave is affected by a series of geological features and physical oceanographic processes and can produce horizontal reflection, refraction, and diffraction (Oliveira et al., 2021). Because variation in water depth and geological features in the study area is small, the 3D sound propagation effect is ignored in the present study. To improve the accuracy of sound source level prediction, an underwater sound propagation model should be selected to calculate transmission loss in the future.

Liu et al. (2014) investigated the peak sound pressure level safe threshold for the large yellow croaker through the acoustic stimulation experiment in the laboratory. However, sound exposure time and population effects were not considered in the experiment. Unlike marine mammals, it is more important to focus on population effects than individuals for fishes (Popper and Hawkins, 2016; Pirotta et al., 2018). The sound exposure level should be used to evaluate its effect on large yellow croaker populations. Based on field observation, the use of single-pulse SEL as assessment criteria for impact pile driving is suggested. The underwater noise from vibratory pile driving has a low sound pressure level; therefore, the SEL_{cum} over a given period of time is recommended. The accumulative period should be carefully detailed. The SEL_{cum} may be defined over a standard period or for the duration of an activity, or over the entire period that the animal will be exposed (Popper et al., 2014). In addition, the distribution and changes in the magnitude of sound events within that period also need to be considered. In the present study, the cumulative exposure time selected for the period with the highest amplitude is 1 min. However, choosing the cumulative time still needs to be investigated in the future when we can better understand the effects of anthropogenic noise on fishes.

Because not all anthropogenic noise can have a negative effect on fish, impact criteria must be regulated by how fishes respond to sound exposures. The effects on fishes mainly include death and injuries, physiological effects, and changes in behavior. Behavioral responses will be especially detrimental if fishes are more exposed to predators, are displaced from feeding or spawning grounds, have their migrations affected, or experience disruption of communication between individuals (Hawkins et al., 2020). However, these behavioral characteristics are difficult to observe for cage-cultured larger yellow croakers. It is more appropriate to consider the population effects. A criterion currently recommended by the National Marine Fisheries Service (NMFS) for behavioral response is 150 dB (Stadler and Woodbury, 2009); however, whether the value is a peak or root mean square (rms) level is not indicated. Through observation of the behavioral response in the field experiment, the criterion is not suitable to evaluate the effects on the larger yellow croaker. The sound exposure level should be used to evaluate its effect on the large yellow croaker.

Finally, based on sound propagation attenuation and the behavioral response thresholds, the range of behavioral response for adult large yellow croakers is calculated to be 4,798 m for impact pile driving and 1,779 m for vibratory pile driving. For noise due to underwater blasting of a 155-kg charge, adult large yellow croakers require a safe range of 900 m (Wang et al., 2017). The influence of pile driving noise on the large yellow croaker is larger than that of a small charge of underwater blasting. However, the influence of underwater blasting increased with increasing blasting charge. The accuracy of measurement and assessment results in the study is verified by simultaneous field observation of the behavior of the large yellow croaker. It is obvious that the influence range given in this paper was only used as a reference value for pile driving noise due to lack of sufficient test data. It is very difficult to set an acoustic response threshold for croakers because it is dependent on a suite of factors, such as individual differences, densities, and circumstances. As human activities in the ocean have increased, it is therefore important to assess the noise impact, including the measurements of pile driving noise levels, and investigate their propagation properties as a function of distance. The purpose of the present study is to enhance the understanding of the potential effect of pile driving on the large yellow croaker and provide reference for the conservation of croaker.

Data availability statement

The original contributions presented in the study are included in the article/supplementary material. Further inquiries can be directed to the corresponding author.

Ethics statement

Ethical review and approval was not required for the study of animals in accordance with the local legislation and institutional requirements. The study investigates the behavioral response of the large yellow croaker. No auditory or physical damage is caused to the large yellow croaker. Therefore, ethical approval is not required.

Author contributions

FN: investigation, methodology, formal analysis, and writing—original draft and review. JX and RX: data curation and acoustic data analysis. XZ, BC, and ZL: supervision, validation, and writing—review and editing. YY: methodology and writing—review and editing. All authors contributed to the article and approved the submitted version.

Funding

This research was supported by grants from the National Natural Science Foundation of China (41976175), the Scientific Research Foundation of the Third Institute of Oceanography, Ministry of Natural Resources (2020017), the Natural Science Foundation of Fujian Province (2020J01696), and the High Level Research and Cultivation Fund of Transportation Engineering of Jimei University (HHXY2020016).

Conflict of interest

Author XZ is employed by Zhejiang Communications Construction Group Co. Ltd.

The remaining authors declare that the research was conducted in the absence of any commercial or financial relationships that could be construed as a potential conflict of interest.

Publisher's note

References

Amaral, J. L., Miller, J. H., Potty, G. R., Vigness-Raposa, K. J., Frankel, A. S., Lin, Y. T., et al. (2020). Characterization of impact pile driving signals during installation of offshore wind turbine foundations. *J. Acoust. Soc. Am.* 147, 2323–2333. doi: 10.1121/10.0001035

Bagocius, D. (2015). Piling underwater noise impact on migrating salmon fish during Lithuanian LNG terminal construction (Curonian lagoon, Eastern Baltic Sea coast). *Mar. Pollut. Bull.* 92, 45–51. doi: 10.1016/j.marpolbul.2015.01.002

Branstetter, B. K., Bowman, V. F., Houser, D. S., Tormey, M., Banks, P., Finneran, J. J., et al. (2018). Effects of vibratory pile driver noise on echolocation and vigilance in bottlenose dolphins (*Tursiops truncatus*). *J. Acoust. Soc. Am.* 143, 429–439. doi: 10.1121/1.5021555

Casper, B. M., Smith, M. E., Halvorsen, M. B., Sun, H., Carlson, T. J., and Popper, A. N. (2013). Effects of exposure to pile driving sounds on fish inner ear tissues. *Comp. Biochem. Physiol. A. Mol. Integr. Physiol.* 166, 352–360. doi: 10.1016/j.cbpa.2013.07.008

Chen, S. X., Su, Y. Q., and Hong, W. S. (2018). "Aquaculture of the Large yellow croaker," in *Aquaculture in China: success stories and modern trends* (Wiley Blackwell), 297–308. doi: 10.1002/9781119120759.ch3_10

Dahl, P. H., Dall'Osto, D. R., and Farrell, D. M. (2015). The underwater sound field from vibratory pile driving. *J. Acoust. Soc. Am.* 137, 3544–3554. doi: 10.1121/1.4921288

Han, D. G., and Choi, J. W. (2022). Measurements and spatial distribution simulation of impact pile driving underwater noise generated during the construction of offshore wind power plant off the southwest coast of Korea. *Front. Mar. Sci.* 8. doi: 10.3389/fmars.2021.654991

Hawkins, A. D., Johnson, C., and Popper, A. N. (2020). How to set sound exposure criteria for fishes. *J. Acoust. Soc. Am.* 147, 1762–1777. doi: 10.1121/10.0000907

Hawkins, A. D., and Popper, A. N. (2017). A sound approach to assessing the impact of underwater noise on marine fishes and invertebrates. *ICES. J. Mar. Sci.* 74, 635–651. doi: 10.1093/icesjms/fsw205

Horodysky, A. Z., Brill, R. W., Fine, M. L., Musick, J. A., and Latour, R. J. (2008). Acoustic pressure and particle motion thresholds in six sciaenid fishes. *J. Exp. Biol.* 211, 1504–1511. doi: 10.1242/jeb.016196

Jiménez-Arranz, G., Banda, N., Cook, S., and Wyatt, R. (2020). *Review on existing data on underwater sounds from pile driving activities* (Seiche Ltd for the Joint Industry Programme (JIP) on E&P Sound and Marine Life). Available at: www.soundandmarinelife.org.

Kastelein, R. A., van Heerden, D., Gransier, R., and Hoek, L. (2013). Behavioral responses of a harbor porpoise (Phocoena phocoena) to playbacks of broadband pile driving sounds. *Mar. Environ. Res.* 92, 206–214. doi: 10.1016/j.marenvres.2013.09.020

Kight, C. R., and Swaddle, J. P. (2011). How and why environmental noise impacts animals: an integrative, mechanistic review. *Ecol. Lett.* 14, 1052–1061. doi: 10.1111/j.1461-0248.2011.01664.x

Leunissen, E. M., and Dawson, S. M. (2018). Underwater noise levels of pile-driving in a new Zealand harbor, and the potential impacts on endangered hector's dolphins. *Mar. Pollut. Bull.* 135, 195–204. doi: 10.1016/j.marpolbul.2018.07.024

Leunissen, E. M., Rayment, W. J., and Dawson, S. M. (2019). Impact of pile-driving on hector's dolphin in lyttelton harbour, new Zealand. *Mar. Pollut. Bull.* 142, 31–42. doi: 10.1016/j.marpolbul.2019.03.017

Lin, T. T., Wang, C. B., Liu, X., and Zhang, D. (2019). Impacts of ship noise on the growth and immunophysiological response in the juveniles of two sciaenidae species, *Larimichthys crocea* and *Nibea albiflora*. *J. Appl. Ichthyol.* 35, 1234–1241. doi: 10.1111/jai.13976

Liu, Z. W., Xu, X. M., Huang, E. H., and Yang, Y. M. (2014). Study on behavior of sound stimulation for large yellow croaker (*Pseudosciaena crocea*). *J. Appl. Oceanogr.* 33, 105–110. doi: 10.3969/J.ISSN.2095-4972.2014.01.014

National Marine Fisheries Service [NMFS] (2018). "Technical guidance for assessing the effects of anthropogenic sound on marine mammal hearing (Version 2.0)," in *Underwater thresholds for onset of permanent and temporary threshold shifts* (Washington, DC: NOAA Technical Memorandum NMFS-OPR-59), 167.

National Research Council [NRC] (2003). *Ocean noise and marine mammals* (Washington, DC: The National Academies Press).

Nehls, G., Betke, K., Eckelmann, S., and Ros, M. (2007). "Assessment and costs of potential engineering solutions for the mitigation of the impacts of underwater noise arising from the construction of offshore windfarms," in *COWRIE ENG-14-2007* (Windsor, CT: COWRIE Ltd).

Nowacek, D. P., Thorne, L. H., Johnston, D. W., and Tyack, P. L. (2007). Responses of cetaceans to anthropogenic noise. *Mamm. Rev.* 37, 81–115. doi: 10.1111/j.1365-2907.2007.00104.x

Oliveira, T. C. A., Lin, Y. T., and Porter, M. B. (2021). Underwater sound propagation modeling in a complex shallow water environment. *Front. Mar. Sci.* 8. doi: 10.3389/fmars.2021.751327

Pirotta, E., Booth, C. G., Costa, D. P., Fleishman, E., Kraus, S. D., Lusseau, D., et al. (2018). Understanding the population consequences of disturbance. *Ecol. Evol.* 8, 9934–9946. doi: 10.1002/ece3.4458

Popper, A. N., and Hawkins, A. (2016). *The effects of noise on aquatic life II* (New York, USA: Springer).

Popper, A. N., and Hawkins, A. (2019). An overview of fish bioacoustics and the impacts of anthropogenic sounds on fishes. *J. Fish Biol.* 94, 692–713. doi: 10.1111/jfb.13948

Popper, A. N., Hawkins, A. D., Fay, R. R., Mann, D. A., Bartol, S., Carlson, T. J., et al. (2014). *ASA S3/SC1. 4 TR-2014 sound exposure guidelines for fishes and Sea turtles: A technical report prepared by ANSI-accredited standards committee S3/SC1 and registered with ANSI* (New York, USA: Springer).

Popper, A. N., Hice-Dunton, L., Jenkins, E., Higgs, D. M., Krebs, J., and Mooney, A. (2022). Offshore wind energy development: Research priorities for sound and vibration effects on fishes and aquatic invertebrates. *J. Acoust. Soc. Am.* 151, 205–215. doi: 10.1121/10.0009237

Ramcharitar, J., Gannon, D. P., and Popper, A. N. (2006). Bioacoustics of fishes of the family sciaenidae (*croakers and drums*). *T. Am. Fish Soc.* 135, 1409–1431. doi: 10.1577/T05-207.1

Reinhall, P. G., and Dahl, P. H. (2011). Underwater mach wave radiation from impact pile driving: theory and observation. *J. Acoust. Soc. Am.* 130, 1209–1216. doi: 10.1121/1.3614540

Ren, X. M., Gao, D. Z., Yao, Y. L., Yang, F., Liu, J. F., and Xie, F. J. (2007). Occurrence and characteristic of sound in large yellow croaker (*Pseudosciaena crocea*). *J. Dalian. Ocean Univ.* 22, 123–128. doi: 10.3969/j.issn.1000-9957.2007.02.009

Reyff, J. A. (2012). "Underwater sounds from unattenuated and attenuated marine pile driving," in *The effects of noise on aquatic life*. Eds. A. N. Popper and A. D. Hawkins (LLC New York: Springer Science + Business Media), p 439–p 444.

Southall, B. L., Bowles, A. E., Ellison, W. T., Finneran, J. J., Gentry, R. L., Greene, C. R., et al. (2007). Marine mammal noise exposure criteria: initial scientific recommendations. *Aquat. Mamm.* 33, 411–414. doi: 10.1578/AM.33.4.2007.411

Southall, B. L., Finneran, J. J., Reichmuth, C., Nachtigall, P. E., Ketten, D. R., Bowles, A. E., et al. (2019). Marine mammal noise exposure criteria: updated scientific recommendations for residual hearing effects. *Aquat. Mamm.* 45, 125–232. doi: 10.1578/AM.45.2.2019.125

Stadler, J. H., and Woodbury, D. P. (2009). *). the effects of noise on aquatic life. inter-noise 2009* Inter-Noise:Ottawa, Ontario, Canada.

Urick, R. J. (1983). *Principles of underwater sound. 3rd edition* (USA: McGraw-Hill Education).

Wang, Z. T., Wu, Y. P., Duan, G. Q., Cao, H. J., Liu, J. C., Wang, K. X., et al. (2014). Assessing the underwater acoustics of the world's largest vibration hammer (OCTA-KONG) and its potential effects on the indo-pacific humpbacked dolphin (*Sousa chinensis*). *PloS One* 9, e110590. doi: 10.1371/journal.pone.0110590

Wang, R. W., Xu, X. M., Zou, Z. G., and Zhou, Y. L. (2017). "Prediction of underwater blasting safe range for Large yellow croaker (*Pseudosciaena crocea*)," in *2017 IEEE International Conference on Signal Processing, Communications and Computing (ICSPCC)*, Xiamen, China. doi: 10.1109/ICSPCC.2017.8242546

J. F. Webb, R. R. Fay and A. N. Popper (Eds.) (2008). *Fish bioacoustics* (New York, USA: Springer).

Wyatt, R. (2008). *Joint industry programme on sound and marine life review of existing data on underwater sounds produced by the oil and gas industry* (Great Torrington: Seiche Measurements Ltd).

Zhang, X. H., Tao, Y., Zhou, Y. L., Tang, L. G., Liu, M., and Xu, X. M. (2021). Acoustic properties of the otolith of the Large yellow croaker *Larimichthys crocea* (Perciformes: Sciaenidae). *Zool. Stud.* 60, e64. doi: 10.6620/ZS.2021.60–64

Zhou, Y. L., Xu, X. M., Zhang, X. ,. H., Huang, L. F., Xiao, F. G., and He, Y. W. (2022). Vocalization behavior differs across reproductive stages in cultured large yellow croaker *Larimichthys crocea* (Perciformes: *Sciaenidae*). *Aquaculture* 556, 738267. doi: 10.1016/j.aquaculture.2022.738267

frontiers | Frontiers in Marine Science

TYPE Methods
PUBLISHED 27 February 2023
DOI 10.3389/fmars.2023.1090132

Check for updates

OPEN ACCESS

EDITED BY
Xiaomei Xu,
Xiamen University, China

REVIEWED BY
Daniela Silvia Pace,
Sapienza University of Rome, Italy
Elena Bianca Papale,
Department of Earth System Sciences and Technologies for the Environment (CNR), Italy

*CORRESPONDENCE
Brandon L. Southall
Brandon.Southall@sea-inc.net

SPECIALTY SECTION
This article was submitted to Ocean Observation, a section of the journal Frontiers in Marine Science

RECEIVED 04 November 2022
ACCEPTED 03 February 2023
PUBLISHED 27 February 2023

CITATION
Southall BL, Tollit D, Amaral J, Clark CW and Ellison WT (2023) Managing human activity and marine mammals: A biologically based, relativistic risk assessment framework.
Front. Mar. Sci. 10:1090132.
doi: 10.3389/fmars.2023.1090132

Managing human activity and marine mammals: A biologically based, relativistic risk assessment framework

Brandon L. Southall[1,2*], Dominic Tollit[3], Jennifer Amaral[4], Christopher W. Clark[4,5] and William T. Ellison[4]

[1]Southall Environmental Associates, Inc., Aptos, CA, United States, [2]Institute of Marine Science, University of California, Santa Cruz, Santa Cruz, CA, United States, [3]Sea Mammal Research Unit Consulting, Vancouver, BC, Canada, [4]Marine Acoustics, Inc., Middletown, RI, United States, [5]K. Lisa Yang Center for Conservation Bioacoustics, Cornell Lab of Ornithology, Cornell University, Ithaca, NY, United States

Presented here is a broadly applicable, transparent, repeatable analytical framework for assessing relative risk of anthropogenic disturbances on marine vertebrates, with the emphasis on the sound generating aspects of the activity. The objectives are to provide managers and action-proponents tools with which to objectively evaluate drivers of potential biological risk, to identify data gaps that limit assessment, and to identify actionable measures to reduce risk. Current regulatory assessments of how human activities (particularly those that produce sound) influence the likelihood of marine mammal behavioral responses and potential injury, rely principally on generalized characterizations of exposure and effect using simple, threshold-based criteria. While this is relatively straightforward in regulatory applications, this approach fails to adequately address realistic site and seasonal scenarios, other potential stressors, and scalable outcome probabilities. The risk assessment presented here is primarily based on a common and broad understanding of the spatial-temporal-spectral intersections of animals and anthropogenic activities, and specific examples of its application to hypothetical offshore wind farms are given. The resulting species- and activity-specific framework parses risk into two discrete factors: a population's innate 'vulnerability' (potential degree of susceptibility to disturbance) and an 'exposure index' (magnitude-duration severity resulting from exposure to an activity). The classic intersection of these factors and their multi-dimensional components provides a relativistic risk assessment process for realistic evaluation of specified activity contexts, sites, and schedules, convolved with species-specific seasonal presence, behavioral-ecological context, and natural history. This process is inherently scalable, allowing a relativistic means of assessing potential disturbance scenarios, tunable to animal distribution, region, context, and degrees of spatial-temporal-spectral resolution.

KEYWORDS

marine mammals, noise, conservation, risk assessment, management, disturbance

1 Introduction

The science of marine mammals and noise has substantially progressed in recent decades with the rapid expansion of research and monitoring in this field (see: Southall, 2017). This has resulted in clear and increasing documentation of both the context-dependency of an animal's response (e.g., behavioral state, proximity, ecological context) in mediating exposure-response probability (Ellison et al., 2012; Pirotta et al., 2015; Ellison et al., 2018; Pirotta et al., 2022a; Southall et al., 2016; Erbe et al., 2018; Southall et al., 2019b; Erbe et al., 2022), and differences between taxa in auditory effects (Southall et al., 2019a) and behavioral responses (Southall et al., 2021a). Despite such progress, there have been limited developments in U.S. regulatory policy guidelines to track some of this complexity, and to move beyond the most simplistic threshold approaches in terms of auditory effects (NMFS, 2016). Approaches to ocean policies regarding management of human noise impacts on marine mammals have ranged from historically simplistic received level (RL) 'threshold' markers of behavioral or auditory impacts from both impulsive or continuous (non-impulsive) noise stressors (see Southall et al., 2007; Southall et al., 2019a; Southall, 2021; Southall et al., 2021a) to complex, statistically intensive population-level modeling approaches for discrete kinds of disturbance events (see: King et al., 2015; Pirotta et al., 2018; Booth et al., 2020; Pirotta et al., 2021) or multiple exposures (NAS, 2017). There is a need for a coherent assessment framework that addresses the inherent complexity of behavioral response to noise and provides managers and action-proponents tools with which to objectively evaluate and dissect the principal activities that drive potential biological risk, to identify data gaps limiting assessment, and to identify actionable measures to reduce risk. The objective of this paper is to present a broadly applicable, transparent, repeatable analytical tool for assessing relative risk of anthropogenic disturbances on marine species with the emphasis on the noise aspects of the activity.

Marine mammals include highly visible and iconic species of disproportionately greater attention in management, conservation, and litigation relative to most other marine taxa (e.g., Williams et al., 2014; Williams et al., 2015a; Erbe et al., 2018; Weilgart, 2019; Williams et al., 2020; Chou et al., 2021). Such attention often includes regulatory decisions and outcomes with major economic and/or national security implications (e.g., Gordon et al., 2003; Abate, 2010; Nowacek et al., 2015; Thomson and Binder, 2021). These factors illustrate the need for an effective, science-based, defensible means of managing impacts of human activities.

Adverse human impacts include a suite of possible outcomes. These include injury or mortality from direct harvesting, entanglement, vessel strike, or physiological disturbance (e.g., Knowlton et al., 2012; Rockwood et al., 2017; Carretta et al., 2020). They may also include habitat degradation, pollution, and myriad behavioral disturbances of variable severity. Substantial scientific and regulatory attention has focused on how intentional or incidental noise can negatively impact marine mammals (NRC, 2005; Williams et al., 2015a; Williams et al., 2015b; Southall, 2017; Southall et al., 2007; Southall et al., 2019a; Southall et al., 2021a; Erbe et al., 2022). The topic has drawn extensive national, regional, and international attention, resulting in legal and regulatory conflicts that have or are impacting every major ocean industry (e.g., Chou et al., 2021).

Early regulatory approaches in some jurisdictions used simplistic all-or-nothing thresholds for individual animals based on the predicted RL from a specified anthropogenic disturbance (Malme et al., 1984, HESS 1999). Such approaches, subsequently woven into U.S. regulatory decision-making, effectively treated noise like a single metric "speed limit" for predicting harm. This approach did not distinguish between taxa, species, individuals or biological context (e.g., foraging, migrating, mating) nor did it consider how animals perceive, respond to, or are disturbed or injured by sound exposure. Predicted impacts were then often integrated over the course of an activity to predict aggregate impacts, which were then evaluated with a binary assessment of potential 'jeopardy' to the population or species. Approaches generally considered that disturbance or injury would result from short-term (acute) exposures without consideration of long-term (chronic) impacts, including communication masking or habitat avoidance from a sustained activity.

Large-scale investments to measure impacts have yielded rapid advances in understanding how noise might disturb and/or harm marine mammals, while informing criteria to predict behavioral (Southall et al., 2021a), auditory (Southall et al., 2019a), and cumulative impacts (NAS, 2017). Broad-scale noise metrics targeted to maintain acceptable levels of environmental status have also been developed (EC, 2008), providing a unique perspective for managing human noise based on aggregate ambient noise levels from many sources. Energetic and demographic population-level models linking disturbance with metrics of species and ecological fitness have also opened new frontiers (NAS, 2017; Pirotta et al., 2018; Pirotta et al., 2021; Pirotta et al., 2022b; New et al., 2020). The energetic models predicting population trends, which assume the impacts of disturbance carry through to changes in fitness, survival, and ultimately population parameters, have yet to be systematically adopted into marine regulatory policy. This is, at least in part, because of what may be perceived as their general lack of transparency and ease of replicability given the inherent statistical complexities, as well as typically substantial limitations in empirical parameterization of key assumptions for most species and contexts of interest (but see recent substantial developments for key, data-rich species in Pirotta et al., 2018; Pirotta et al., 2021).

The relativistic, ecological risk assessment framework presented here was developed as a biologically based approach to provide regulatory decision-makers and industry planners an objective, transparent means of evaluating relative risk across species for specified scenarios of industrial activity. The framework evolved from a simpler and more subjective alternative approach to RL, threshold-based predictions of impacts, motivated by a proposed seismic survey off California (Wood et al., 2012). It was extended to considerations of multiple overlapping seismic surveys occurring dynamically in variable times and places in the Gulf of Mexico (Ellison et al., 2015; Southall et al., 2018; Southall et al., 2019b; Southall et al., 2021b) and then subsequently adapted and applied to the installation and operation of several stationary wind energy facilities off Massachusetts (Southall et al., 2021c).

The outcomes of the framework are intended to inform and target focused monitoring, mitigation, and impact assessment, potentially including subsequent population consequence modeling for strategic species and scenarios. The risk framework utilizes semi-quantitative approaches to evaluate both the inherent species-specific vulnerability based on population, natural history, and existing environmental stressors as well as the severity (magnitude) of potential impact. The exposure magnitude and duration of a noise-producing activity is related to population models of disturbance through a statistical framework and applied as a metric of exposure severity for acute exposures. A statistical framework relating exposure magnitude and duration to population models of disturbance was applied as a metric of exposure severity for acute exposures. For multiple (aggregate) human disturbances on broader spatial and temporal scales, a quantitative spatial-temporal-spectral 'index' for exposure severity was developed in which a higher risk index values indicate greater overlap in space, time, and the frequency of disturbing noise and hearing for each protected species.

Similar approaches integrating semi-quantitative risk assessment frameworks with expert elicitation have been increasingly applied in evaluating other potential impacts for a variety of contexts. For instance, expert elicitation has been applied in evaluating the relative safety of food in human and agricultural settings (European Food Safety Authority, 2014). Further, there has been a series of increasingly sophisticated structured risk assessments used in policy and management context that incorporating expert elicitation in evaluating vulnerability and impacts for a variety of marine fisheries contexts (e.g., Sethi, 2010; Morrison et al., 2015; Johnson and Welch, 2016) as well as evaluating risk associated with collision and displacement for seabirds associated with offshore wind energy development (Adams et al., 2017). Other examples of semi-quantitative risk assessment applications include evaluations of impacts on marine mammals from global warming (Albouy et al., 2020) and disease (Norman et al., 2022).

The novel approach to risk assessment synthesized here integrates species-specific population, life history, behavioral sensitivity, and spatio-temporal contextual aspects of potential disturbances into the assessment of response probability, species vulnerability at the population level, and impact severity. The overall goal is to provide resource managers from regulatory agencies and industry action proponents with an early-stage, sensible, objective, understandable, stepwise decision-making tool for evaluating relative risk to specified marine species from specified industrial activities. The approach applies a systematic, largely quantitative, transparent, repeatable, and simplistic method for evaluating potential biological risk to marine mammals from different operational scenarios based on common, broad assumptions across space, time, and different acoustic conditions.

2 Methods

The iteratively derived risk assessment framework is based on two discrete components, species-specific 'vulnerability' and species-specific and scenario-specific 'severity'. The assessment of potential vulnerability includes a systematic appraisal of species-specific population, life history, auditory communication systems, and environmental factors. The assessment of severity includes population modeling methods for acute (short-term, project specific) exposure events (*e.g.*, a seismic airgun survey or pile driving installation period, but not single shots or single pile strikes) and a spatial-temporal-spectral algorithm for estimating a disturbance magnitude metric (referred to as "exposure index") from aggregate events (long-term, multiple years and/or multiple projects). Each assessment is conducted discretely for specified species, area, and exposure period. This yields a vulnerability risk rating and a severity risk rating for each species and exposure scenario, which are then convolved to assess the overall relativistic risk rating for each scenario.

Given the inherent and varying degrees of uncertainty for many sources of requisite input data in the underlying steps of the assessment process, several different means of characterizing and accounting for uncertainty are applied. In the most extreme cases where critical data are entirely absent (e.g., species-specific spatial-temporal distribution), vulnerability or severity factor scores may not be possible to quantify or adequately assess, even with expert judgment. In such instances, while some factor scores can be judged and included, an overall risk assessment score cannot be determined; a situation that identifies a knowledge gap and could lead to recommendations for research. In some cases, with high levels of uncertainty or lack of information (e.g., population trends), vulnerability risk assessment factors may be explicitly assigned higher factor scores as a means of highlighting the higher risk as a result of the uncertainty. Finally, a subjective overall three-step consideration of confidence in scores is provided for each vulnerability assessment scenario; some degree of expert elicitation is required to determine this.

2.1 Quantifying species-specific vulnerability

A total species-specific vulnerability score is determined for each scenario based on four contextual factors: species population factor (3.1.1.); species habitat use and compensatory abilities factor (3.1.2.); potential masking factor (3.1.3.); and other environmental stressors factor (3.1.4.). Total factor scores resulting from a structured assessment of a factor's sub-elements are aggregated to determine an overall vulnerability risk rating score for each species-area-time disturbance scenario (3.1.5.). The maximum total species-specific vulnerability score is 30, with a five-point vulnerability rating determined as a proportion of this maximum score (as described in 3.1.5.).

2.1.1 Species population factor

Population parameters are a critical consideration in evaluating the potential vulnerability of a species to disturbance (e.g., Kraus et al., 2016; Nowacek and Southall, 2016) and are not explicitly considered in the RL, threshold-based framework. The Species Population risk factor (Table 1) incorporates relatively well-defined quantitative criteria (e.g., conservation status, population trend, and overall population size) such as those applied in U.S. regulatory policy for some jurisdictions. International conservation status lists (e.g., IUCN) can provide this information for other jurisdictions. A limitation of the species population factor assessment can be the lack of current or sufficiently precise population or stock assessments at a regional level. This limitation and resultant uncertainty have been taken into consideration by weighting the score. The inclusion of a population size element was deemed appropriate beyond simply protected or endangered status, as not all endangered or listed marine mammal

TABLE 1 Species population factor scoring criteria.

Population Factor Elements	Score (max 7)
Population status: • *Endangered* (U.S. Endangered Species Act (ESA)), *depleted* (U.S. Marine Mammal Protection Act (MMPA)), or comparable jurisdiction-dependent distinction = **3** • *Threatened* (U.S. MMPA), or comparable jurisdiction-dependent distinction = **1**	**max = 3**
Population trend: • *Decreasing* (last three stock assessment reports [SARs] for which new population estimates were updated) = **2** • *Unknown* (last three SARs) - no population trend analysis performed or data deficient = **1** • *Stable* (last three SARs) for which new population estimates were updated within 5%) = **0** • *Increasing* (last three SARs) = **-1**	**max = 2**
Population size: • *Small* (n< 2,500, as specified by International Union for the Conservation of Nature [IUCN] designation) = **2** • *Unknown* (last three SARs) but possibly below 2500 = **1** • *> 2500* = **0**	**max = 2**

species necessarily have low populations (e.g., sperm whales (*Physeter macrocephalus*), Steller sea lions (*Eumetopias jubatus*). The species population factor includes three discrete elements of a regional population and has a maximum score of seven.

2.1.2 Species habitat use and compensatory abilities factor

An essential component of risk assessment is identification of whether individuals will be exposed to a risk. This requires information on the proportion of the population exposed, for how long, and during what activity (i.e., feeding, migrating, and breeding) (Costa et al., 2016). This information is highly pertinent to the extent to which a species might be able to compensate for or offset the effect of the exposure. The species habitat use and compensatory abilities factor (Table 2) quantifies the species-specific, biological importance of an area in which potential disturbance will occur. The location of potential disturbance is considered on a zone-by-zone basis, which allows the risk framework to stay general and not conflict with detailed environmental assessments for specific activities. This factor considers how a species uses the zone in which the disturbance will occur and if the disturbance will overlap in time with key behaviors (i.e., breeding, migration, feeding). Within the Gulf of Mexico region, Southall et al. (2021b) defined nine zones, whereas Southall et al. (2021c) derived seven ecological zones for mid- and northern U.S. east coast regions. Relatively higher potential vulnerability is assessed for areas where a species has high site fidelity (e.g., Forney et al., 2017), or where there is a higher spatial overlap between anthropogenic, sound-generating activities and seasonally important biological activities (e.g., mating, rearing of offspring, foraging, migrating). Assessments in the Gulf of Mexico, where many species lack strong seasonal patterns, were conducted annually. Assessments off the U.S. east coast, where many species have distinct seasonal occurrences and behavioral context patterns, were calculated monthly. The species habitat use and compensatory abilities factor includes two discrete elements, the more heavily weighted being related to spatio-temporal habitat use and another that is specific to temporal overlap with key biological activities. This factor also has a maximum total score of seven.

2.1.3 Potential masking factor

The potential masking factor considers the potential for disruption of acoustically mediated behaviors such as communication, and spatial orientation and navigation. Masking potential depends on the location and nature of a potentially disruptive activity; the sound field generated by the activity; the existing ambient noise in the area; and the spectral overlap between the aggregate noise field and the hearing, behavior, and acoustic ecology of the species (see Southall, 2018). To determine the potential of an activity to acoustically mask biological important

TABLE 2 Species habitat use and compensatory abilities factor scoring criteria.

Species habitat and temporal factor elements	Score (max 7)
Habitat use: • Specified zone contains ≥ 30% of total regionwide or estimated population during specified period) = **5** • < 30% and ≥ 20% = **4** • < 20% and ≥ 10% = **3** • < 10% and ≥ 5% = **2** • < 5% and ≥ 1% = **1** • < 1% = **0**	**max = 5**
Temporal overlap: • *High probability* that activity will overlap with concentrated breeding/maternal care periods and/or key feeding or migration periods within specified area = **2** • *Low probability* that activity will overlap with concentrated breeding/maternal care periods and/or key feeding or migration periods within specified area = **1** • *No probability* = **0** (only when<0.1% of total regionwide or estimated population occurs within zone).	**max = 2**

behaviors of a species, the baseline ambient noise conditions in the area must be considered. Ideally the conditions are determined using ambient noise measurements collected over multiple seasons within the area being considered (as in Southall et al., 2021c). The potential masking factor is considered on the vulnerability side of the framework as a separate type of stressor rather than subsumed in the exposure severity calculation, which is intended to address potential behavioral response and thus a proxy for higher-order auditory effects (e.g., hearing loss).

The potential masking factor is calculated using derived frequency-weighted values ('M-weighted' filters; Southall et al., 2007) based on the species. This is done as a precautionary approach given the broader nature of these filters for lower-level exposures where masking may occur relative to narrower filters derived specifically for auditory damage from very high-intensity sound exposure (Southall et al., 2019a). 'Signal'-to-noise ratios (herein defined as ambient noise-to-noise ratio (ANNR) values) are calculated using an iterative series of calculations for LF (< 1 kHz), MF (1-10 kHz), and high frequency (HF; > 10 kHz) frequency bands within specified zones and time periods:

1. Aggregate (full bandwidth) noise spectra for each source are generated over specified resolution throughout the zone and period for each M-weighted condition.
2. The M-weighted, aggregate ambient noise (not including defined activity sources) spectrum is determined over defined sub-areas throughout the zone (e.g., for Southall et al., 2021c see Estabrook et al., 2022). This is a baseline, existing ambient noise condition that is based on empirical measurements (where available) or typical median noise conditions.
3. Relative spectrum level differences are determined between these two M-weighted, aggregate noise spectrum levels, which are then converted into ambient noise-to-noise ratio (ANNR) values for each respective band.

For each species of interest, the masking factor score for each relevant communication and spatial orientation frequency band is calculated based on frequency-band-specific criteria (Table 3).

TABLE 3 Potential masking factor scoring criteria. Each individual factor score is combined.

Masking Factor Elements	Score (max 9)
Communication masking factor: • Median ANNR (for all cells within zone in which species is predicted to occur) within primary species-specific communication (conspecific and auto-communication) band > 20 dB = **6** • 10–20 dB = **3** • 1–10 dB = **1** • < 1 dB = **0**	**max = 6**
Spatial orientation and navigation masking factor: • Median ANNR within LF band > 20 dB = **2** • 10–20 dB = **1** • < 10 dB = **0**	**max = 2**
Spatial orientation and navigation masking factor: • Median ANNR within MF band is > 20 dB = **1** • < 20 dB = **0**	**max = 1**

Communication bands are presumed as the LF band (< 1 kHz) for baleen whales and pinnipeds, the MF band (1-10 kHz) for odontocetes, and the HF band (> 10 kHz) for odontocetes (echolocation and conspecific signals for high frequency specialists; e.g., harbor porpoises). Given the assumption that passive listening can facilitate spatial orientation and navigation for any species that can detect and use the relatively low frequency signals that propagate and convey information on environmental factors over appreciable distances, weighted ANNR values are determined for LF and MF bands for all species. The potential masking factor includes three discrete elements related to communication and spatial orientation and navigation, which are added together and has a maximum score of nine. This higher maximum score reflects the critical importance of acoustic communication as well as the use of passive listening for other biological and environmental sounds in spatial orientation and navigation.

2.1.4 Other environmental stressors factor

The other environmental stressors factor considers other environmental and/or human stressors already impacting species prior to the specified potential disturbance. This has been a key element of the framework since Ellison et al. (2016), although quantitative distinctions and reference points (e.g., potential biological removal; see Wade, 1998), and uncertainty within species-specific mortality estimates) have been subsequently added. Sub-factors consider the relative levels of all types of ongoing human activity, which considers existing current and likely future uses and is distinguished from masking associated with the specific disturbance being assessed. Another sub-factor evaluates the existence and severity of biological (non-anthropogenic) risk factors such as disease, climate change or nutritional stress (Table 4). The other environmental stressors factor is applied on an annual basis given the nature of the associated stressors and typical reporting of data for each. The other environmental stressors factor includes a maximum possible score of seven.

2.1.5 Total vulnerability score rating method

A vulnerability score is the percentage of the aggregate of the four factor scores relative to the maximum possible score (30). Vulnerability scores are assigned a relative risk probability and a vulnerability rating using quintiles (Table 5). It is important to note that these ratings are intended to represent relativistic values for distinct species, time periods, and areas considered within the same context. Consequently, relative terms (e.g., lowest, highest) are used rather than absolute terms that might become misused to compare risks between very different combinations of species, time, area, and context, which is not the intention here.

2.2 Quantifying exposure severity

Throughout the advancement of these risk assessment methods, separate approaches for quantifying the potential magnitude of severity have been developed for discrete, project specific, disturbance events (acute approach) and multiple overlapping events (aggregate approach) (see: Southall et al., 2018). We focus

TABLE 4 Other environmental stressors factor scoring criteria.

Other Stressors Factor Elements	Score (max 7)
Chronic anthropogenic noise: Species subject to variable levels of current or known future chronic anthropogenic noise (i.e., dense or overlapping concentrations of industrial activity such as shipping lanes, sonar testing ranges, areas of regular seismic surveys)	**Up to 2**
Chronic anthropogenic risk factors (non-noise direct anthropogenic impacts): Species subject to variable degrees of current or known future risk from other chronic, non-noise anthropogenic activities (e.g., regular documented cases of fisheries interactions, whale-watching, research activities, ship-strike). Total annual known or estimated direct anthropogenic mortality, as documented in last SARs, evaluated relative to species-specific potential biological removal (PBR). • Annual mortality ≥ PBR: **3** • Annual mortality ≥ 50% PBR or mortality unknown/unreliable: **2** • Annual mortality ≥ 25% PBR: **1**	**Up to 3**
Chronic biological risk factors (non-noise environmental impacts): Variable presence of disease, parasites, prey limitation (including indirect climate change related), or high predation pressure (recent SARs as reference). • Documented instances of multiple such stressors in last three SARs: **2** • Documented instance of one such stressor in last three SARs: **1** (also assigned when insufficient data for the species is present). • No documented instances of such stressors where species are sufficiently monitored: **0**	**Up to 2**

here on the aggregate approach most fully developed in Southall et al. (2021c), while recognizing that this approach can also be applied to discrete events. A detailed description of the earlier acute approach method for exposure risk assessment is provided in the associated Supplementary Materials.

Aggregate exposure risk assessment: "Exposure Index"

Ellison et al. (2015) built upon and conceptually integrated general principles and aspects of the acute exposure assessment framework to develop new approaches for application to broader scales (larger than single activity) and multiple overlapping activities. The assessment method presented here was developed in Southall et al. (2019c) and enhanced by Southall et al. (2021b; 2021c). It uses an algorithmic approach to calculate the spatial-temporal-spectral quantitative intersection of potential disturbance and marine species distribution and hearing capabilities, yielding a non-dimensional "exposure index" for each disturbance scenario across all species considered. The intent is to provide systematic, quantitative methods that enable the relative evaluation of potential aggregate effects across various specified operational scenarios. The spatial-temporal-spectral basis of the exposure index renders it both modular and inherently scalable. The output is a straightforward, relativistic index and risk rating process by which to assess variable scenarios in which a single or multiple potential disturbances might occur (e.g., periods of time, areas, types of sound generating activities.)

TABLE 5 Normalized species-, time-, area- context-specific vulnerability score, and associated risk probability and relative vulnerability rating.

Total Vulnerability Score (from all factors)	Total Risk Probability (% of total possible)	Relative Vulnerability Rating
24–30	**80–100%**	**Highest**
18–23	**60–79%**	**High**
12–17	**40–59%**	**Moderate**
6–11	**20–39%**	**Low**
0–5	**0–19%**	**Lowest**

Unlike the acute risk assessment where specific "takes" are estimated for defined impacts (injury = MMPA level A; behavioral disturbance = MMPA level B), the aggregate risk assessment framework makes no such distinction. Rather, the probability of these and other adverse effects of disturbance are presumed to co-occur spatially, temporally, and spectrally. As such, the exposure index serves as a relative proxy across species and contexts for all forms of potential acoustic harassment. It is designed to broadly identify the conditions under which the overall severity of disturbance is relatively lower or higher based on the overlaps between the spatial, temporal, and spectral features of sound fields from aggregate activities and the species-specific attributes of exposed animals. The exposure index metric can thus be quantified as the relative exposure severity and a proxy for the presumed impact as a proportion of the local population within either a defined geographic 'zone' or an entire defined 'region'. The exposure index has the following characteristics:

- Spatial resolution for calculations is modular. Recent applications (Southall et al., 2021c) applied 10 x 10 km grid cells for all species other than species of particular interest (e.g., North Atlantic right whales) where finer (5 x 5 km) grid resolution was provided by Roberts et al. (2020).
- Temporal windowing is also modular in that exposure index values can be calculated at variable (monthly, seasonal, annual) resolution.
- The exposure index is calculated for individual elements of compound operations (e.g., piles driven in an offshore wind farm) or of multiple overlapping operations (e.g., multiple seismic surveys) and combined to determine an aggregate risk.
- Exposure index calculations are determined in a relativistic sense in terms of the percentage of the populations affected of the total number for that species within specified geographic zones and regions (not necessarily the entire population).
- The exposure index is comprised of an *activity index* and a *spectral index*. These indices characterize the temporal and spatial extent of potential disturbance in relation to species-specific distribution and acoustic communication.

Below we introduce the concepts behind the activity and spectral indices. The equations provided are examples that have been specifically tuned to assess the installation and operation of offshore wind farms off the U.S. east coast. The spatial-temporal-spectral concept of this framework is applicable to any sound generating activity (i.e., seismic surveys, offshore wind, vessel operations), but the specific equations require tuning based on the values of the parameters associated with the activity (e.g., duration, source movement).

2.2.1 Activity index

The activity index (AI) quantifies the spatial and temporal extent of a sound generating activity into a single metric. AI is calculated by using species-specific limits associated with the presumed onset of behavioral responses to a specified sound at specified geographic ranges. It is calculated for each specified period during which an operational activity, and thus potential disturbance, is assumed to occur. AI (Eqn 1) is composed of two discrete terms, $AI_{spatial}$ and $AI_{temporal}$, that quantify the spatial and temporal activity.

$$AI = AI_{spatial} * AI_{temporal} \tag{1}$$

The *spatial activity index* ($AI_{spatial}$) component (units: km^2) is derived from the spatial area within which the RL from a known activity is thought or known to be high enough to elicit a species-specific behavioral response 50% of the time (i.e., 50% response probability). It is calculated for each active source type (e.g., turbine in a wind farm; seismic airgun array) for each defined temporal period. The 50% response probability and associated impact area differ based on the species being considered since different species react at different RLs (see Southall et al., 2007; Southall et al., 2021a). In this analysis, a 50% response probability of 120 dB (root mean square; RMS) is used for harbor porpoise and beaked whales and 160 dB (RMS) for all other species and behavioral contexts. When evaluating turbine construction or operation at an offshore wind farm, the spatial activity index (Eqn 2) is calculated for each source component individually for each specified period, where r is the range (km) to the 50% response probability RL isopleth, which can be adjusted based on species or taxa-specific empirical data related to source-specific response probability.:

$$AI_{spatial} = \pi r^2 * N_t \tag{2}$$

This term is determined separately for each discrete condition (based on direct measurements of identical or similar operations and/or acoustic propagation modeling evaluation). N_t is a daily unitless metric of activity defined for different activities (e.g., offshore wind turbine installation, operation). When evaluating potential risk to a marine mammal due to vessel activity in an area, the spatial index term represents the area around a vessel within which the 50% response probability occurs. It is calculated for the vessel activity occurring within a defined area and period (Eqn 3), where r is the max range to estimated behavioral response (km); S_v is the average speed of a vessel (km/hr) within the defined area; and T_v is the average length of time of a vessel trip (hours).

$$AI_{spatial} = 2r * S_v * T_v \tag{3}$$

The *temporal activity index* ($AI_{temporal}$) represents the percentage of days within a specific time period that disturbance will occur. It is calculated for each type of activity for each period within which the activity occurs. In the case of evaluating turbine and vessel activity at an offshore wind farm, similar equations are used for turbine and vessel activity and a monthly resolution was used to assess both activity types. To quantify turbine installation and operation, the temporal index (Eqn 4) is defined where N_{td} is the total number of days when turbines are being installed or operating in a month, and N_d is the total number of days in the month being evaluated.

$$AI_{t-temporal} = \frac{N_{td}}{N_d} \tag{4}$$

To quantify the temporal extent of vessel operations, the temporal index (Eqn 5) is defined where N_v is the number of vessel trips occurring in an individual wind farm in a month and N_d is the total number of days in the month being evaluated.

$$AI_{v-temporal} = \frac{N_v}{N_d} \tag{5}$$

2.2.2 Spectral index

The *Spectral Index* (SI) is dependent on the hearing capability of a marine mammal of interest given its species abundance in the operational area for a given period. It serves to quantify the spectral difference between the unweighted spectrum of the sound source under assessment and the M-weighted functional hearing group for the species of interest (Southall et al., 2007). The M-weighting was selected as a deliberately wider frequency range than subsequent narrower auditory filters (Southall et al., 2019a) given that the predominant consideration for nearly all contexts relate to behavioral response. SI (Eqn 6) is calculated where $E_{weighted}$ is the amount of acoustic energy in a spectrum weighted by the M-weighting, $E_{unweighted}$ is the amount of acoustic energy in the unweighted spectrum, and $N_{animals\ buffered\ WF}$ is the total species abundance within a buffered region around the area of activity (i.e. buffer the lease area when evaluating offshore wind farms), within the range that encompasses contextual behavioral reactions from animals.

$$SI = \frac{E_{weighted}}{E_{unweighted}} * N_{animals\ buffered\ WF} \tag{6}$$

2.2.3 Exposure index calculation and risk rating

The *exposure index* (EI; Eqn 7) is calculated separately for each wind farm, month, and species. Calculating separately for each active source allows for evaluation of operations that are in different phases (i.e., one wind farm could be in construction and the other could be in operation) and their noise conditions are different.

$$EI = AI * SI \tag{7}$$

The exposure index from all sources is summed to yield an aggregate exposure index ($EI_{aggregate}$; Eqn 8) for each defined period.

$$EI_{aggregate} = \sum\nolimits_{Sources} EI \tag{8}$$

The total number of animals within a broader zone or region, whichever is of interest, is then used ($N_{total\ animals}$) to determine an aggregate, normalized exposure index (Eqn 9).

$$EI_{aggregate,\ normalized} = \frac{EI_{aggregate}}{N_{total\ animals}} \tag{9}$$

$EI_{aggregate,\ normalized}$ is a non-dimensional value that is related as the percentage of the species within a zone or region during which activities occur for a specified period. Given that $\mathrm{EI}_{\mathrm{aggregate,\ normalized}}$ is normalized by total animals, it can be compared across species provided the same geographic area (zone or region) was used to determine the $N_{total\ animals}$ term. $\mathrm{EI}_{\mathrm{aggregate,\ normalized}}$ is calculated for each noise source unit independently such that the index of source will inform the user as to which source is of higher relative impact to the species under consideration. When calculating the EI for compound source conditions with multiple discrete activities (e.g., vessel activity and operational turbine noise in a wind farm), the activity yielding the highest EI is used as the representative EI for the overall operation.

Once species-specific EI values for a period and geographic area of interest are calculated, several processes are required to determine a risk assessment rating. Zone-wide representations of EI results are calculated from the most representative scenarios to serve as references for comparing relative species-specific exposure risk within and between different scenarios. Quintile values at the 20^{th}, 40^{th}, 60^{th}, and 80^{th} percentile indices of this distribution are determined, yielding five equally distributed proportions of the total EI values (Table 6). These values serve as a means of quantitatively assessing relative risk based on the distribution of EI results for representative scenarios across all species of interest. It is important to note that this process is entirely dependent upon the selection of species, the geographic area considered, and the context of the base distribution used to determine these percentile breakpoints. This process is emphasized to be a transparent, consistent tool used to evaluate relative risk in defined scenarios for assessing species and scenario differences and/or in contingency and scenario planning rather than an absolute quantification of risk or severity of impact.

2.3 Integrated, species-specific risk assessment rating

The final step in the risk assessment process for a specified scenario is to integrate the vulnerability and EI ratings. This involves merging the species-specific vulnerability rating (Table 5) and EI risk rating (Table 6) into a 5x5 matrix in which resultant risk in evaluated on a five-step relative scale from lowest (blue) to highest (red) (Figure 1). This matrix yields a species-specific relative risk assessment for defined scenarios of industrial activities for the zones, region, and time periods specified.

TABLE 6 Exposure Index (EI) value percentile breakpoints and corresponding risk ratings.

EI Value (percentile values of % of zone population)	EI Relative Risk Rating
> 80^{th} percentile	Highest (5)
> 60^{th} to 80^{th} percentile	Higher (4)
> 40^{th} to 60^{th} percentile	Moderate (3)
> 20^{th} to 40^{th} percentile	Lower (2)
< 20^{th} percentile	Lowest (1)

3 Modeled results for wind farms and seismic survey examples

During the evolution of our approach, various disturbance scenarios have been evaluated in extensive detail, including modeled and actual seismic airgun surveys off California (Wood et al., 2012) and in the Gulf of Mexico (Ellison et al., 2018; Southall et al., 2019a; Southall et al., 2021b), as well as modeled offshore wind energy facility installation and operation (Southall et al., 2021c). The focus here is on the development, adaptation, and utility of the risk assessment paradigm within the context of marine policy applications. Results presented are illustrative examples of the assessment process and outcomes based on several different scenarios rather than a comprehensive assessment of an individual scenario across all contexts and species. Examples are given to demonstrate how results within and across scenarios could be evaluated in making informed and strategic management decisions. These strategic management decisions are considered a primary mitigation tool. For example, avoiding a particularly sensitive time period or area, reducing the overall time period of disturbance by allowing night-time or co-occurring activities, or adopting enhanced operational mitigation measures for species that are identified as highest risk.

3.1 Vulnerability risk assessment

Species-specific vulnerability to disturbance is evaluated relative to factors that are both fixed at the time of the analysis (e.g., population status/trend, anthropogenic stressors other than the disturbance being considered) and important aspects of natural history and behavior (e.g., seasonal distribution and behavior, auditory masking in the context of seasonal differences of ambient noise). The degree of seasonal variance in biological systems can determine the selection of temporal periods for vulnerability assessments. For many of the Gulf of Mexico species considered for risk assessment from seismic survey operations, there is relatively little seasonality so an annual vulnerability assessment was considered appropriate (Southall et al., 2019a; Southall et al., 2021a), so an annual vulnerability assessment was considered appropriate. In contrast, many of the marine mammals considered in risk assessment from offshore wind farm construction and operations on the U.S. east coast (Southall et al., 2021c) have highly seasonal occurrence and behavioral patterns, so vulnerability was assessed on a monthly basis. Example results of vulnerability assessments for different species in each context (Table 7) illustrate how different factors drive the relativistic nature of the risk assessment across species and contexts.

3.2 Exposure severity risk assessments

An example of exposure severity results is provided for five marine mammal species (selected for their management relevance and taxonomic representation of local taxa; see Southall et al., 2021c) evaluated with the risk assessment paradigm for selected offshore wind energy facility installation scenarios in locations within actual

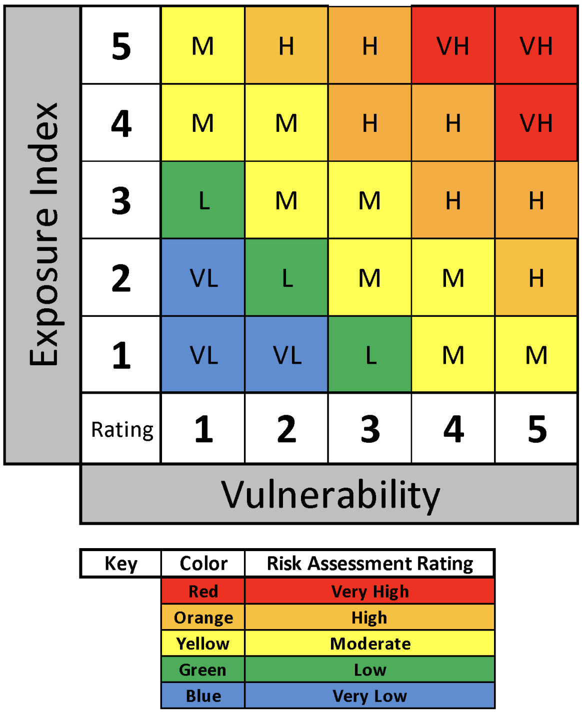

FIGURE 1
Example of a risk assessment rating matrix based on species-specific and scenario-specific vulnerability and exposure index rating scores.

wind energy lease areas off the U.S. east coast. These scenarios include the installation of a single windfarm of 120 piles starting in three different months (March, May, or July) with a single pile driven per day for four months. Monthly EI scores and their corresponding risk ratings (relativistic within this specific application as they are based on quintile values for EI scores across all species and contexts) in which operations were presumed to occur are given (Table 8).

An additional utility of the EI calculation process is that it provides the means by which to comparatively evaluate risk over different temporal periods associated with variable scenarios. (e.g., individual months as in Table 8 or aggregated over multiple months during which potential disturbance could occur). For instance, Southall et al. (2021c) evaluated scenarios in which a single monopile per day would be driven in the installation of a single windfarm, which is the more typically expected scenario involving daytime-only piling operations. As noted in the above example, at one pile per day, this would nominally require four months of installation for 120 piles. However, scenarios were considered where nighttime piling would be allowed, meaning two piles per day could be driven and the overall disturbance would occur over two months. This more concentrated piling scenario resulted in higher EI scores within the 2-month piling period relative to the 4-month piling period scenario. However, aggregate EI scores (the overall integrated predicted disturbance) were actually lower in some scenarios for conditions involving two piles per day versus one pile per day despite the monthly differences, simply because the disturbance occurs for half the total overall time during months when densities are relatively low. Example results showing aggregate EI values for two baleen whale species evaluated in the 2-month and 4-month piling scenarios are given below (Figure 2). This aggregate difference, represented as negative difference scores, is not observed in all periods, but rather only in the later (1 July) start date scenario. These results suggest that for some whale species with high seasonal variability of occurrence, concentrating installation into periods with lowest occurrence can result in a tangible (10-15%) reduction in aggregate risk to those species.

These risk framework results highlight key data needs given the required assumptions for the timescale of baleen whale disturbance effects post-piling. We conservatively assume disturbance of a second piling event in a day is identical to the first, although, in reality, the two disturbance events could spatially overlap. If effective disturbance wanes during sustained operations, the relative differences between extended, intermittent disturbance and concentrated, sustained disturbance be more pronounced.

3.3 Integrated risk assessments

Risk assessment results for potential disturbance in different offshore windfarm installation scenarios for selected key U.S. east coast species (Southall et al., 2021c) are shown for four different temporal scenarios (Table 9). These scenarios include the installation of a single windfarm starting in three different months of the year (March, May, July) and lasting for a comparable period and the installation of two windfarms in wind lease areas (~60 km from one another) with differential degrees of temporal overlap. Where two wind farms were presumed to be installed in the same year, three different temporal scenarios were considered:

(1) Sequential Installation = two separate installation periods, two months (July-Aug) at first site followed by two months (Sept-Oct) at second site;
(2) Partial overlap = installation at one site in Aug-Sept and Sept-Oct at the second site, such that both sights are active in Sept;
(3) Total overlap = installation of both site in Aug-Sept.

Additional examples of integrated risk assessment results for selected key species from the Gulf of Mexico exposed to seismic surveys from Southall et al. (2021b) are given in Supplementary Materials.

4 Discussion and conclusions

We present a transparent, objective, and simple means of assessing relative overall relative evaluated risk to marine mammals from human disturbance in defined scenarios. It is intended as an early-stage strategic assessment tool for identifying key species, locations, time periods, and disturbance scenarios that identify key areas of uncertainty and inform the implementation of marine policies and effective management. The methodology is based principally on a spatially and temporally explicit framework for integrating general biological vulnerability with the potential exposure to industrial activity. It allows a practical means of considering the optimal timing of an activity at a specific location, identifying locations of high risk to particular species, or assessing cumulative risk of multiple activities over time. Notably, the derived risk assessment framework was designed to be inherently modular and scalable, allowing it to be tuned to key questions, areas, or degrees of spatial and/or temporal resolution and even adapted to non-acoustic impacts (*e.g.*, vessel-strike, entanglement). The precision of

TABLE 7 Vulnerability factor scores and risk assessment ratings for selected Gulf of Mexico and east coast marine mammal species evaluated relative to potential impacts of seismic surveys and offshore windfarm installation, respectively.

Gulf of Mexico Marine Mammal Species		Vulnerability Factor				Seismic Survey Vulnerability Risk Rating (of 30)
		1	2	3	4	
Rice's whale		7	4	8	4	**23 - Higher**
Sperm whale		7	2	3	4	**16 - Moderate**
Pygmy sperm whale		4	2	2	4	**12 - Moderate**
Bottlenose dolphin		-1	0	3	4	**6 - Lower**
Spinner dolphin		0	2	3	4	**6 – Lower**
U.S. East Coast Marine Mammal Species	Installation Start Month	Vulnerability Factor				Offshore Windfarm Vulnerability Risk Rating (of 30)
		1	2	3	4	
N. Atlantic Right Whale	March	7	7	5	7	**26 - Highest**
	May	7	5	5	7	**24 - Highest**
	July	7	2	7	7	**23 - Higher**
Humpback Whale	March	1	5	5	5	**16 - Moderate**
	May	1	3	5	5	**14 - Moderate**
	July	1	3	8	5	**17 - Moderate**
Common Dolphin	March	1	2	0	4	**7 - Lower**
	May	1	2	0	4	**7 - Lower**
	July	1	3	0	4	**8 - Lower**
Harbor Porpoise	March	1	5	0	5	**11 - Lower**
	May	1	4	0	5	**10 - Lower**
	July	1	3	0	5	**9 - Lower**
Gray Seal	March	1	6	1	4	**12 - Moderate**
	May	1	6	1	4	**12 - Moderate**
	July	1	3	1	4	**9 - Lower**

the results may be limited in resolution based on the type and confidence of the underlying input data, this scalability was intended to provide a means of evaluating relative risk for multiple species over defined areas and time periods. This tool is intended to allow managers to evaluate multiple kinds of development or operational scenarios using common assumptions and evaluate the relative pros and cons of different scenarios across many different species that may co-occur in order to make strategic choices based on management priorities and requirements. The risk framework is not intended to replicate or supersede current regulatory guidelines for auditory injury or behavioral impacts, or modeling approaches to evaluate long-term assessments of population consequences of disturbance. Rather, it is intended as a complementary, practical, early-stage approach that can provide relative assessments of specific scenarios compared to more complex and intensively data-dependent, model-based evaluations.

TABLE 8 EI scores and associated relative risk ratings for selected marine mammal species off the U.S. east coast evaluated for hypothetical offshore wind energy facility installation scenarios (single windfarm).

Marine Mammal Species	Installation EI Score (% zone population) - Relative Risk Rating		
	March Start	May Start	July Start
N. Atlantic Right Whale	**0.281% - Higher**	**0.2874% - Higher**	**0.1226% - Lower**
Humpback Whale	**0.079% - Lower**	**0.058% - Lowest**	**0.050% - Lowest**
Common Dolphin	**0.006% - Lowest**	**0.014% - Lowest**	**0.014% - Lowest**
Harbor Porpoise	**0.233% - Moderate**	**0.148% - Lower**	**0.141% - Lower**
Gray Seal	**0.079% - Lower**	**0.043% - Lowest**	**0.005% - Lowest**

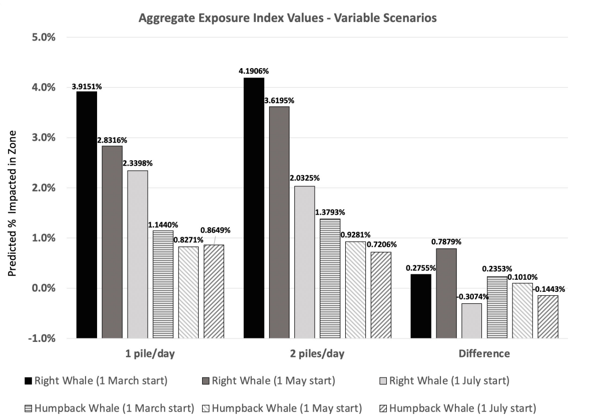

FIGURE 2
Aggregate EI values for two baleen whale species evaluated relative to potential impacts from pile driving either 1 pile/day or 2 piles/day for a 120 turbine offshore wind farm.

The risk assessment approach specifically recognizes the critical factors regarding the regional and seasonal species population cohorts and their natural history, hearing, and behavior; and integrates the potential vulnerability posed by these factors with the temporal, spectral and contextual exposure introduced by coincident anthropogenic activities. By scoring and convolving the relative level of species vulnerability factor and severity factor (quantified as an exposure index), a relative risk or overall impact assessment can be constructed and evaluated in a classic X-Y trade space paradigm. Managers can evaluate relative risk with a standardized approach and common assumption, using this 'trade-space' approach to evaluate various operational scenarios related to proposed industrial activity. For instance, relative risk in different scenarios may be assessed by varying the assumptions of disturbance contexts (e.g., start times, temporal overlap, operational parameters including nighttime operations). Such an approach will allow managers and action proponents a way of more objectively implementing and comparing adaptive strategies to reduce risk across species that may have very

TABLE 9 Assessed relative risk derived from vulnerability and severity ratings for selected marine mammal species off the U.S. east coast from installation of one or two offshore wind farms in different scenarios for start month (March, May, July) for a single installation location or for variable temporal overlap (sequential, partial, total) of two installations.

Marine Mammal Species	Temporal Scenario	EI (Severity) Risk Rating	Vulnerability Risk Rating	Overall Assessed Relative Risk
N. Atlantic Right Whale	1 March Start	Higher	Highest	Highest
	1 May Start	Higher	Highest	Highest
	1 July Start	Lower	Higher	Moderate
	Sequential Instal.	Highest	Higher	Highest
	Partial Overlap	Highest	Highest	Highest
	Total Overlap	Highest	Highest	Highest
Humpback Whale	1 March Start	Lower	Moderate	Lower
	1 May Start	Lowest	Moderate	Lower
	1 July Start	Lowest	Moderate	Lower
	Sequential Instal.	Moderate	Moderate	Moderate
	Partial Overlap	Moderate	Moderate	Moderate
	Total Overlap	Highest	Moderate	Higher
Common Dolphin	1 March Start	Lowest	Lower	Lowest
	1 May Start	Lowest	Lower	Lowest
	1 July Start	Lowest	Lower	Lowest
	Sequential Instal.	Lowest	Lower	Lowest
	Partial Overlap	Lowest	Lower	Lowest
	Total Overlap	Lower	Lower	Lower
Harbor Porpoise	1 March Start	Moderate	Lower	Moderate
	1 May Start	Lower	Lower	Lower
	1 July Start	Lower	Lower	Lower
	Sequential Instal.	Moderate	Lower	Moderate
	Partial Overlap	Moderate	Lower	Moderate
	Total Overlap	Higher	Lower	Moderate

(Continued)

TABLE 9 Continued

Marine Mammal Species	Temporal Scenario	EI (Severity) Risk Rating	Vulnerability Risk Rating	Overall Assessed Relative Risk
Gray Seal	1 March Start	Lower	Lower	Lower
	1 May Start	Lowest	Lower	Lowest
	1 July Start	Lowest	Lower	Lowest
	Sequential Instal.	Lowest	Lower	Lowest
	Partial Overlap	Lowest	Lower	Lowest
	Total Overlap	Lower	Lower	Lower

HESS (1999). High energy seismic survey review process report AND Interim operational guidelines for high-energy seismic surveys off Southern California.
Malme, C. I., P. R. Miles, C. W. Clark, P. L. Tyack and J. E. Bird (1984). Investigations of the potential effects of underwater noise from petroleum industry activities on migrating gray whale behavior, Phase II., Bolt, Beranek and Newman: **var.**
For each scenario installation would occur for a total of four months.

different management priorities. This process also enables comparative evaluation of critical data needs and thus investment to support future assessments and effective mitigation.

In developing the modeled results (Section 3) for both seismic survey and wind farm installation scenarios, several key insights emerged in terms of the application and generalizability of the risk assessment framework. The spatially static nature of disturbance associated with wind farm construction relative to mobile sources considered previously (seismic surveys) required different considerations and assumptions, including the relative potential disturbance zones around individual turbines during installation. We also evaluated the relative impacts of mitigation measures (e.g., bubble curtains) that reduce the acoustic footprint of impact pile driving and used smaller potential disturbance zones in calculating EI values for unmitigated versus mitigated conditions. Thus, the modular nature of our assessment framework allows for relatively easy comparative testing of different disturbance radii values and mitigation assumptions. This motivates empirical evaluation of ways to test and improve mitigation methods. Data limitations in the underlying quality and nature of animal distribution data as well as data and analyses conducted (or missing) from the NMFS SARs imposed higher levels of uncertainty that required more precautionary conclusions. Additional distinctions were made throughout the evolution of the framework, specifically in the vulnerability scoring where data were deficient.

Several revealing insights evolved from the application of the risk assessment framework to offshore windfarms for different species. The relative density and abundance of species within the focal zone for a specified time period are the primary drivers of the exposure index scores and influence the habitat use factor in the vulnerability assessment. Scenarios considering the installation of piles during different seasonal time periods yielded several important insights regarding potential risk. Most notably, for species with more temporally ephemeral distributions in areas where operations were presumed to occur, the highest predicted risk values logically occurred when installation overlapped with relatively higher species occurrence. Considering these patterns across species, certain periods (installation in late summer and early fall off Massachusetts) were clearly associated with lower risk for multiple focal species, including critically endangered North Atlantic right whales. This assessment provides a clear management strategy that might have initially been presumed for one or a few species but can now be extended to a suite of species. Logical associated mitigation measures to reduce potential risk of disturbance may be to employ seasonal mitigation measures. For seasonally occurring species, this can be accomplished by conducting the activity during times of year when key species are at their lowest rates of occurrence. For resident species, however, this may be more challenging given they may have little ability to move to alternative habitats (Forney et al., 2017). The framework enables the assessment of which are at greater relative risk for different periods and a relativistic comparison of the efficacy of certain mitigation approaches, such as targeting a window of activity to avoid a certain important species. Where approaches are selected to minimize risk to selected species, they may result in increased risk for other species although in a transparent manner that would identify mitigation approaches tailored to those other species.

Similar messages emerged relative to the potential concentration of installation periods. While it may not be possible or common for multiple monopiles to be installed on the same day, this would likely require low-visibility and/or nighttime piling. The mitigation and monitoring requirements for such operations notwithstanding, we evaluated potential risk differences between driving a single versus two piles a day and differences between variable amounts of temporal overlap for multiple windfarm installations. While additional consideration of other mitigation and practicality considerations are required, the risk assessment conducted for the contexts considered here clearly suggests that there could be conservation benefits (i.e., lower risk) by strategically concentrating potential disturbance activities into shorter periods, particularly during seasons when key species are relatively scarce (see Figure 2).

We acknowledge that there are limitations to the overall approach presented here. Firstly, it is only as applicable and reliable as the underlying data. The fundamental spatial, temporal. and spectral nature of the underlying model, intersecting these features with potential disturbance, requires as much detailed information on the spatial and temporal distribution and density of protected species, characteristics of their sound production and reception characteristics, and the behavioral ecological context as possible. Such data are continuously increasing and improving but remain limited in many areas and are also rapidly changing due to changes in ocean climate. Additional details on operational aspects of offshore wind energy facilities (e.g., service vessel types and modes of operations) are needed in subsequent analyses, as are potential ecological and physical interactions with offshore facilities. It should also be clearly noted that, given the 'tuning' required for application in different contexts, this framework is intended to provide relative risk assessment within the scenario, area, and species considered rather than an absolute assessment of impact that could be compared to a dissimilar context or species group. Finally, we acknowledge that subjective aspects of the framework remain. Substantial progress was made for instance in the quantitative methods for the calculation of the auditory masking factor from earlier iterations of the framework. Yet key aspects of the vulnerability rating (e.g., species habitat factor) still do and likely will continue to require expert-elicitation and assessment, including the possible assignment of scores where uncertainty is high.

In summary, the framework offers a structured, straightforward means of assessing relative risk due to anthropogenic sound generating activities for many possible scenarios. It provides resource managers an objective decision-making tool to strategically assess relative biological risk and overall negative impact at a regional marine species population level. It is intended to provide a systematic method by which to evaluate relative risks from different operational scenarios using common, broad assumptions across space, time, and differing levels of received sounds. Further developments and adaptations of this risk assessment paradigm are needed to advance its applicability and generalizability. Further quantitative metrics for additional aspects of species-specific vulnerability are needed, including more explicit metrics for temporal aspects of habitat use and more consistent measures of other environmental stressors. Further clarification is also needed on the extent to which species vulnerability might change over time when considering scoring criteria for other stressors (e.g., future noise effects, changes in habitat utilization, food chain disruption, potential beneficial aspects (e.g., reef effects)). Another substantial opportunity to improve the process relates to the integration of dynamic environmental covariates (e.g., concentrating oceanographic conditions, prey layers) that could result in more heterogeneous distribution of key species than may be reflected in density databases. This could allow scenario testing of dynamic variables using ecosystem model forecasts. Further efforts to quantify uncertainty in key parameters could include developing quantitative means of assessing certainty/quality of underlying density data within areas of operations in order to put potential error bounds on exposure index calculations (i.e., risk) and to derive uncertainty around exposure index point estimates. Finally, refined methods to partition risk rating breakpoints could be evaluated, to possibly move beyond discrete risk categories (lowest, lower, moderate, high, and higher) so as to develop risk as a continuous variable. Recent and future policy changes are driving intensive offshore wind developments, while conventional energy developments continue. We believe this early-stage, multi-species relativistic risk assessment framework can play a useful role in strategic ocean planning needed by resource managers and industry action proponents.

Data availability statement

The original contributions presented in the study are included in the article/Supplementary Material. Further inquiries can be directed to the corresponding author.

Author contributions

BS: Conceptualization, Methodology, Formal Analysis, Investigation, Writing – original draft, Writing – Review and Editing, Visualization, Supervision, Project Administration, Funding Acquisition. DT: Conceptualization, Methodology, Formal Analysis, Investigation, Writing – Review and Editing, Visualization. JA: Conceptualization, Methodology, Formal Analysis, Investigation, Writing – Review and Editing, Visualization. CC: Conceptualization, Methodology, Formal Analysis, Investigation, Writing – Review and Editing. WE: Conceptualization, Methodology, Formal Analysis, Investigation, Writing – Review and Editing, Supervision. All authors contributed to the article and approved the submitted version.

Funding

The development of this article was supported under award 140M0120C0007 by the Bureau of Ocean Energy Management (BOEM). The funder was not involved in the study design, collection, analysis, interpretation of data, the writing of this article or the decision to submit it for publication.

Acknowledgments

We acknowledge the support provided by a number of colleagues who substantially contributed to this effort, including Stan Laback, Jill Lewandosky, Erica Staaterman, Louis Brzuzy, Koen Bröker, Cynthia Pyc, David Mann, Adam Frankel, Kathy Vigness-Raposa, Jason Wood, Dmitri Ponirakis, Jolie Harrison, Ben Laws, and Shane Guan.

Conflict of interest

Author BS was and is employed by Southall Environmental Associates, Inc. Author DT was and is employed by Sea Mammal Research Unit, Consulting. Authors JA, CC, and WE were and are employed by Marine Acoustics, Inc. The remaining authors declare that the research was conducted in the absence of any commercial or financial relationships that could be construed as a potential conflict of interest.

Publisher's note

Supplementary material

The Supplementary Material for this article can be found online at: https://www.frontiersin.org/articles/10.3389/fmars.2023.1090132/full#supplementary-material

References

Abate, R. S. (2010). NEPA, national security, and ocean noise: the past, present, and future of regulating the impact of navy sonar on marine mammals. *J. Int. Wildlife Law Policy* 13 (4), 326–356. doi: 10.1080/13880292.2010.524588

Adams, J., Kelsey, E. C., Felis, J. J., and Pereksta, D. M. (2017). *Collision and displacement vulnerability among marine birds of the California current system associated with offshore wind energy infrastructure* (Reston, VA: U.S. Geological Survey), 116. doi: 10.3133/ofr20161154

Albouy, C., Delattre, V., Donati, G., Frölicher, T. L., Albouy-Boyer, S., Rufino, M., et al. (2020). Global vulnerability of marine mammals to global warming. *Sci. Rep.* 10 (1), 1–12. doi: 10.1038/s41598-019-57280-3

Booth, C. G., Sinclair, R. R., and Harwood, J. (2020). Methods for monitoring for the population consequences of disturbance in marine mammals: a review. *Front. Mar. Sci.* 7, 115. doi: 10.3389/fmars.2020.00115

Carretta, J. V., Delean, B., Helker, V., Muto, M. M., Greenman, J., Wilkinson, K., et al. (2020). Sources of human-related injury and mortality for U.S. pacific West coast marine mammal stock assessment-2018. *NOAA Tech. Memorandum* 631, 147. doi: 10.25923/j73c-6q78

Chou, E., Southall, B. L., Robards, M., and Rosenbaum, H. C. (2021). International policy, recommendations, actions and mitigation efforts of anthropogenic underwater noise. *Ocean Coast. Manage.* 202, 105427. doi: 10.1016/j.ocecoaman.2020.105427

Costa, D. P., Schwarz, L., Robinson, P., Schick, R. S., Morris, P. A., Condit, R., et al (2016). A bioenergetics approach to understanding the population consequences of disturbance: elephant seals as a model system. In *The effects of noise on aquatic life II* (pp. 161–169). Springer New York.

Ellison, W. T., Clark, C. W., Mann, D. A., Southall, B., and Tollit, D. J. (2015). "A risk assessment framework to assess the biological significance of noise exposure on marine mammals," in *21st Biennial Conference on the Biology of Marine Mammals*, San Francisco, CA, USA, 13-18 December.

Ellison, W. T., Racca, R., Clark, C. W., Streever, B., Frankel, A. S., Fleishman, E., et al. (2016). Modeling the aggregated exposure and responses of bowhead whales balaena mysticetus to multiple sources of anthropogenic underwater sound. *Endangered Species Res.* 30, 95–108. doi: 10.3354/esr00727

Ellison, W. T., Southall, B. L., Clark, C. W., and Frankel, A. F. (2012). A new context-based approach to assess marine mammal behavioral responses to anthropogenic sounds. *Conserv. Biol.* 26, 21–28. doi: 10.1111/j.1523-1739.2011.01803.x

Ellison, W. T., Southall, B. L., Frankel, A. S., Vigness-Raposa, K., and Clark., C. (2018). An acoustic scene perspective on spatial, temporal, and spectral aspects of marine mammal behavioral response to noise. *Aquat. Mammals* 44, 239–243. doi: 10.1578/AM.44.3.2019.239

Erbe, C., Dent, M. L., Gannon, W. L., McCauley, R. D., Römer, H., Southall, B. L., et al. (2022). "The effects of noise on animals," in *Exploring animal behavior through sound*, vol. 1 . Eds. C. Erbe and J. A. Thomas, 459–506. doi: 10.1007/978-3-030-97540-1_13

Erbe, C., Dunlop, R., and Dolman, S. (2018). "Effects of noise on marine mammals," in *Effects of anthropogenic noise on animals* (New York, NY: Springer), 277–309.

Estabrook, B. J., Tielens, J. T., Rahaman, A., Ponirakis, D. W., Clark, C. W., and Rice, A. N. (2022). Dynamic spatiotemporal acoustic occurrence of north Atlantic right whales in the offshore Rhode island and Massachusetts wind energy areas. *Endangered Species Res.* 49, 115–133. doi: 10.3354/esr01206

European Commission (EC) (2008). Marine strategy framework directive (MSFD) 2008/56/EC, descriptor 11, energy including underwater noise.

European Food Safety Authority (2014). Guidance on expert knowledge elicitation in food and feed safety risk assessment. *EFSA J.* 12 (6), 3734. doi: 10.2903/j.efsa.2014.3734

Forney, K. A., Southall, B. L., Slooten, E., Dawson, S., Read, A. J., Baird, R. W., et al. (2017). Nowhere to go: noise impact assessments for marine mammal populations with high site fidelity. *Endangered species Res.* 32, 391–413. doi: 10.3354/esr00820

Gordon, J., Gillespie, D., Potter, J., Frantzis, A., Simmonds, M. P., Swift, R., et al. (2003). A review of the effects of seismic surveys on marine mammals. *Mar. Technol. Soc. J.* 37 (4), 16–34. doi: 10.4031/002533203787536998

High Energy Seismic Survey (HESS) (1999). *High energy seismic survey review process and interim operational guidelines for marine survey offshore southern california. camarillo, California: High energy seismic survey team for California state lands commission and U.S* Vol. 39 (Reston, VA: Mineral Management Service).

Johnson, J. E., and Welch, D. J. (2016). Climate change implications for Torres strait fisheries: assessing vulnerability to inform adaptation. *Climatic Change* 135 (3), 611–624. doi: 10.1007/s10584-015-1583-z

King, S. L., Schick, R. S., Donovan, C., Booth, C. G., Burgman, M., Thomas, L., et al. (2015). An interim framework for assessing the population consequences of disturbance. *Methods Ecol. Evol.* 6 (10), 1150–1158. doi: 10.1111/2041-210X.12411

Knowlton, A. R., Hamilton, P. K., Marx, M. K., Pettis, H. M., and Kraus, S. D. (2012). Monitoring north Atlantic right whale eubalaena glacialis entanglement rates: A 30 year retrospective. *Mar. Ecol. Prog. Ser.* 466, 293–302. doi: 10.3354/meps09923

Kraus, S. D., Kenney, R. D., Mayo, C. A., McLellan, W. A., Moore, M. J., and Nowacek, D. P. (2016). Recent scientific publications cast doubt on north Atlantic right whale future. *Front. Mar. Sci.* 3, 137. doi: 10.3389/fmars.2016.00137

Malme, C. I., Miles, P. R., Clark, C. W., Tyack, P. L., and Bird, J. E. (1984). Investigations of the potential effects of underwater noise from petroleum industry activities on migrating gray whale behavior, phase II., bolt, beranek and Newman: var.

Morrison, W. E., Nelson, M. W., Howard, J. F., Teeters, E. J., Hare, J. A., Griffis, R. B., et al. (2015). Methodology for assessing the vulnerability of marine fish and shellfish species to a changing climate. *U.S. Department of Commerce - NOAA. NOAA Technical Memorandum NMFS-OSF-3*, 48p. doi: 10.7289/V54X55TC

National Academies of Sciences and Medicine (NAS) (2017). "Approaches to understanding the cumulative effects of stressors on marine mammals," (Washington DC: The National Academies Press).

National Marine Fisheries Service (NMFS) (2016). *Technical guidance for assessing the effects of anthropogenic sound on marine mammal hearing: Underwater acoustic thresholds for onset of permanent and temporary threshold shifts* (Silver Spring, MD: US Department of Commerce, NOAA), 178.

National Research Council (NRC) (2005). "Marine mammal populations and ocean noise: Determining when noise causes biologically significant events," (Washington, DC: The National Academies Press).

New, L., Lusseau, D., and Harcourt, R. (2020). Dolphins and boats: when is a disturbance, disturbing?. *Frontiers in Marine Science* 7, 353.

Norman, S., Huggins, J. L., Lambourn, D. M., Rhodes, L. D., Garner, M. M., Bolton, J., et al. (2022). Risk factor determination and qualitative risk assessment of mucormycosis in harbor porpoise, an emergent fungal disease in salish Sea marine mammals. *Front. Mar. Sci.* 1420. doi: 10.3389/fmars.2022.962857

Nowacek, D. P., Clark, C. W., Mann, D., Miller, P. J., Rosenbaum, H. C., Golden, J. S., et al. (2015). Marine seismic surveys and ocean noise: time for coordinated and prudent planning. *Front. Ecol. Environ.* 13 (7), 378–386. doi: 10.1890/130286

Nowacek, D. P., and Southall, B. L. (2016). "Effective planning strategies for managing environmental risk associated with geophysical and other imaging surveys," in *International union for the conservation of nature (IUCN)*(Gland, Switzerland: International Union for the Conservation of Nature (IUCN)), 42.

Pirotta, E., Booth, C., Cade, D. E., Calambokidis, J., Costa, D. P., Fahlbusch, J. A., et al. (2021). Context-dependent variability in the predicted daily energetic costs of disturbance in blue whales. *Conserv. Physiol.*, coaa137. doi: 10.1093/conphys/coaa137

Pirotta, E., Booth, C. G., Calambokidis, J., Costa, D. P., Fahlbusch, J. A., Friedlaender, A. S., et al. (2022b). From individual responses to population effects: Integrating a decade of multidisciplinary research on blue whales and sonar. *Anim. Conserv.*, 1367–9430. doi: 10.1111/acv.12785

Pirotta, E., Booth, C. G., Costa, D. P., Fleishman, E., Kraus, S. D., Lusseau, D., et al. (2018). Understanding the population consequences of disturbance. *Ecol. Evol.* 8 (19), 9934–9946. doi: 10.1002/ece3.4458

Pirotta, E., Merchant, N. D., Thompson, P. M., Barton, T. R., and Lusseau, D. (2015). Quantifying the effect of boat disturbance on bottlenose dolphin foraging activity. *Biol. Conserv.* 181, 82–89. doi: 10.1016/j.biocon.2014.11.003

Pirotta, E., Thomas, L., Costa, D. P., Hall, A. J., Harris, C. M., Harwood, J., et al. (2022a). Understanding the combined effects of multiple stressors: A new perspective on a longstanding challenge. *Sci. Total Environ.*, 153322. doi: 10.1016/j.scitotenv.2022.153322

Roberts, J. J., Schick, R. S., and Halpin, P. N. (2020). "Final project report: Marine species density data gap assessments and update for the AFTT study area 2018-2020 (Option year 3)," in *Document version 1.4. report prepared for naval facilities engineering command, Atlantic* (Durham, NC: Duke University Marine Geospatial Ecology Lab).

Rockwood, R. C., Calambokidis, J., and Jahncke, J. (2017). High mortality of blue, humpback and fin whales from modeling of vessel collisions on the US West coast suggests population impacts and insufficient protection. *PloS One* 12 (8), e0183052. doi: 10.1371/journal.pone.0183052

Sethi, S. A. (2010). Risk management for fisheries. *Fish Fisheries* 11 (4), 341–365. doi: 10.1111/j.1467-2979.2010.00363.x

Southall, B. L. (2017). "Noise," in *Encyclopedia of marine mammals, 3rd Edition*. Eds. B. Würsig and H. Thiewesson (New York: Academic Press), 699–707.

Southall, B. L. (2021). Evolutions in marine mammal noise exposure criteria. *Acoustics Today* 17 (2), 52–60. doi: 10.1121/AT.2021.17.2.52

Southall, B. L., Amaral, J., Clark, C. W., Ellison, W., Joy, R., Tollit, D., et al. (2018). "A risk assessment framework to evaluate the potential relative effects of noise on marine mammals," in *6th conference on the effects of sound on marine mammal*(Den Haag, Netherlands), 10–14.

Southall, B. L., Bowles, A. E., Ellison, W. T., Finneran, J. J., Gentry, R. L., Greene, C. R.Jr., et al. (2007). Marine mammal noise exposure criteria: initial scientific recommendations. *Aquat. Mammals* 33, 411–521. doi: 10.1578/AM.33.4.2007.411

Southall, B. L., DeRuiter, S. L., Friedlaender, A., Stimpert, A. K., Goldbogen, J. A., Hazen, E., et al. (2019b). Behavioral responses of individual blue whales (*Balaenoptera musculus*) to mid-frequency military sonar. *J. Exp. Biol.* 222, jeb190637. doi: 10.1242/jeb.190637

Southall, B., Ellison, W., Clark, C., and Tollit, D. (2019c). *Aggregate (chronic) noise exposure risk assessment report (task 5, part 1)* (Aptos (CA: US Department of the Interior, Bureau of Ocean Energy Management), . 66.

Southall, B., Ellison, W., Clark, C., Tollit, D., and Amaral, J. (2021b). "Marine mammal risk assessment for gulf of Mexico G&G activities," (Sterling (VA: US Department of the Interior, Bureau of Ocean Energy Management), 99.

Southall, B., Ellison, W., Clark, C., Tollit, D., and Amaral, J. (2021c). *Marine mammal risk assessment for new England offshore windfarm construction and operational scenarios* (Sterling (VA: US Department of the Interior, Bureau of Ocean Energy Management), 94.

Southall, B. L., Finneran, J. J., Reichmuth, C., Nachtigall, P. E., Ketten, D. R., Bowles, A. E., et al. (2019a). Marine mammal noise exposure criteria: Updated scientific recommendations for residual hearing effects. *Aquat. Mammals* 45, 125–232. doi: 10.1578/AM.45.2.2019.125

Southall, B. L., Nowacek, D. P., Bowles, A. E., Senigaglia, V., Bejder, L., and Tyack, P. L. (2021a). Marine mammal noise exposure criteria: Assessing the severity of marine mammal behavioral responses to human noise. *Aquat. Mammals* 47 (5), 421–464. doi: 10.1578/AM.47.5.2021.421

Thomson, M. D. J., and Binder, C. M. (2021). Recalibrating the department of national defence approach to active sonar impact management. *Mar. pollut. Bull.* 173, 113044. doi: 10.1016/j.marpolbul.2021.113044

Wade, P. R. (1998). Calculating limits to the allowable human-caused mortality of cetaceans and pinnipeds. *Mar. Mammal Sci.* 14, 1–37. doi: 10.1111/j.1748-7692.1998.tb00688.x

Weilgart, L. (2019). "Keeping the noise down: Approaches to the mitigation and regulation of human-caused ocean noise," in *The future of ocean governance and capacity development* (Brill Nijhoff), 298–302.

Williams, R., Ashe, E., Blight, L., Jasny, M., and Nowlan, L. (2014). Marine mammals and ocean noise: future directions and information needs with respect to science, policy and law in Canada. *Mar. pollut. Bull.* 86 (1-2), 29–38. doi: 10.1016/j.marpolbul.2014.05.056

Williams, R., Cholewiak, D., Clark, C. W., Erbe, C., George, J. C. C., Lacy, R. C., et al. (2020). Chronic ocean noise and cetacean population models. *J. Cetacean Res. Manage.* 21, 85–94. doi: 10.47536/jcrm.v21i1.202

Williams, R., Erbe, C., Ashe, E., and Clark, C. W. (2015b). Quiet(er) marine protected areas. *Mar. pollut. Bull.* 100(1), 154–161. doi: 10.1016/j.marpolbul.2015.09.012

Williams, R., Wright, A. J., Ashe, E., Blight, L. K., Bruintjes, R., Canessa, R., et al. (2015a). Impacts of anthropogenic noise on marine life: Publication patterns, new discoveries, and future directions in research and management. *Ocean Coast. Manage.* 115, 17–24. doi: 10.1016/j.ocecoaman.2015.05.021

Wood, J., Southall, B. L., and Tollit, D. J. (2012). PG&E offshore 3-d seismic survey project EIR – marine mammal technical report. *Sea Mammal Research Unit Ltd.*

frontiers | Frontiers in Marine Science

TYPE Original Research
PUBLISHED 27 March 2023
DOI 10.3389/fmars.2023.1118286

Check for updates

OPEN ACCESS

EDITED BY
Yuxing Li,
Xi'an University of Technology, China

REVIEWED BY
Ying Jiang,
First Institute of Oceanography, China
Zhongchang Song,
Xiamen University, China

*CORRESPONDENCE
Timo Molenkamp
t.molenkamp@tudelft.nl

SPECIALTY SECTION
This article was submitted to Ocean Observation, a section of the journal Frontiers in Marine Science

RECEIVED 07 December 2022
ACCEPTED 16 February 2023
PUBLISHED 27 March 2023

CITATION
Molenkamp T, Tsouvalas A and Metrikine A (2023) The influence of contact relaxation on underwater noise emission and seabed vibrations due to offshore vibratory pile installation.
Front. Mar. Sci. 10:1118286.
doi: 10.3389/fmars.2023.1118286

The influence of contact relaxation on underwater noise emission and seabed vibrations due to offshore vibratory pile installation

Timo Molenkamp*, Apostolos Tsouvalas and Andrei Metrikine

Department of Civil Engineering and Geosciences, Delft University of Technology, Delft, Netherlands

The growing interest in offshore wind leads to an increasing number of wind farms planned to be constructed in the coming years. Installation of these piles often causes high underwater noise levels that harm aquatic life. State-of-the-art models have problems predicting the noise and seabed vibrations from vibratory pile driving. A significant reason for that is the modeling of the sediment and its interaction with the driven pile. In principle, linear vibroacoustic models assume perfect contact between pile and soil, i.e., no pile slip. In this study, this pile-soil interface condition is relaxed, and a slip condition is implemented that allows vertical motion of the pile relative to the soil. First, a model is developed which employs contact spring elements between the pile and the soil, allowing the former to move relative to the latter in the vertical direction. The developed model is then verified against a finite element software. Second, a parametric study is conducted to investigate the effect of the interface conditions on the emitted wave field. The results show that the noise generation mechanism depends strongly on the interface conditions. Third, this study concludes that models developed to predict noise emission from impact pile driving are not directly suitable for vibratory pile driving since the pile-soil interaction becomes essential for noise generation in the latter case.

KEYWORDS
underwater noise, offshore pile driving, vibratory pile driving, soil-structure interaction, particle motion, seabed vibrations

1 Introduction

In the transition to renewable energy sources, the interest in wind energy grows significantly as a renewable clean energy source. The EU Offshore Renewable Energy Strategy recommends up-scaling of offshore wind. The aim is to install 60 GW of offshore wind capacity by 2030 and 300 GW by 2050 (European Commission, 2020) compared to the 25 GW in 2020. The achievement of this goal should take place with minimal environmental impact.

The wind power generators in shallow waters, like the European North Sea, are generally founded on hollow cylindrical foundation piles. Traditionally, the foundation piles are installed by impact piling, causing potential harm and behavioral disturbances to marine life because of the high underwater noise levels at large distances from the construction sites (Madsen et al., 2006). Direct physical harm and, ultimately, death are at risk in the first few hundred meters near a pile driving site (Southall et al., 2019). Additionally, behavioral changes of various kinds of mammals are observed at distances over 100 km from the noise source (Benhemma-Le Gall et al., 2021; Fernandez-Betelu et al., 2021).

Various vibratory pile driving methods are currently under development, promising reduced noise levels during installation. There are principally two ways to reduce underwater noise pollution. On the one hand, noise can be mitigated at the path to the receiver by various principles, such as air bubble curtains (Peng et al., 2021b) or piles surrounded by a double-walled steel tube (Reinhall and Dahl, 2011a). On the other hand, the noise levels can be reduced at the source. Potentially more silent driving methods, such as vibratory pile driving, belong to the latter category.

Reinhall and Dahl (2011b) show that in impact piling, the Mach wave radiation in the fluid, caused by the supersonic waves that propagate through the pile following the hammer impact, is the primary noise generation mechanism. Thus, the waves radiating from the pile directly into the water constitute the so-called primary noise path. Since then, several contributions have been considered to improve noise predictions. Fricke and Rolfes (2015) add a module that derives the force on top from an impact hammer, while Lippert and von Estorff (2014b) conducted a Monte Carlo analysis to quantify the significance of parameter uncertainties. The COMPILE benchmark case compares noise predictions of various models for a simplified case (Lippert et al., 2016). The COMPILE benchmark case is widely accepted to benchmark various solution techniques for underwater noise predictions in offshore pile driving. The models align well in the near field, but predictions deviate with increasing distance from the source. All models use separate modules for near- and far-field calculations. The near-field models are based on the finite element or the finite difference method. The far-field models are based on wavenumber integration, the parabolic equation, or normal modes (MacGillivray, 2013; Lippert and von Estorff, 2014a; Schecklman et al., 2015).

The COMPILE case treats the sediment as an acoustic fluid, which is common in early noise prediction models. The representation of the sediment by an acoustic fluid reduces the computation time significantly (Wood, 2016). However, all information on shear and seabed-water interface waves is lost. Next-generation models represent the soil by an elastic medium (Zampolli et al., 2013; Tsouvalas and Metrikine, 2014), which introduces a secondary noise path, i.e., noise generated via the Scholte interface waves traveling along the seabed-water interface. Peng et al. (2021a) developed an improved noise propagation model, including an elastic layered half-space for the description of the seabed. Wood (2016) builds further on noise generation models with elastic soil and underlines the significance of an accurate description of the soil in noise predictions. Wood (2016) states that significant acoustic pressures are associated with the slow-traveling interface waves and that the description of the interface between pile and soil is essential. The interface condition affects the shape of the traveling pulse along the pile and, subsequently, the wave radiation pattern. An extension of the wave equation analysis of piles (WEAP) method is used to solve this problem. The WEAP method describes the vertical displacement field in a pile following a single blow. After including radial pile displacements in the model, the pile is straightforwardly modeled as the noise source. The benefits of the model come with the cost of additional parametric assumptions (Wood and Humphrey, 2013; Heitmann et al., 2015).

Few attempts are reported to model vibratory pile driving. Tsouvalas and Metrikine (2016) compare the wave field emitted between an impact-driven and a vibratory-driven pile. They observe that the highest noise levels are just above the seabed; this phenomenon is more substantial in vibratory pile driving due to the presence of the Scholte waves. The Scholte waves are even more dominant under low-frequency excitation, consistent with the primary driving frequency in vibratory pile driving (10~40 Hz). Furthermore, Tsouvalas and Metrikine note that the system almost reaches a steady state during vibratory pile driving. Consequently, pile-soil interaction is critical to accurately describe the dynamic behavior in this steady state.

Dahl et al. (2015) discuss results from an experimental campaign on underwater noise from vibratory pile driving and propagate the measured field with an acoustic propagation model. Though the pile vibrations, as a noise source, are not directly measured, the acoustic measurements clearly show the presence of the primary driving frequency and several super-harmonics. In a review paper, Tsouvalas (2020) addresses the development of noise prediction models for vibratory pile driving as one of the five open challenges in state-of-the-art noise prediction. Other challenges include noise mitigation modeling, improvement of computational efficiency for uncertainty analysis, incorporation of the three-dimensional domain, and knowledge integration with marine biologists for a unified environmental impact assessment.

The concept of (non-linear) pile-soil interaction is not novel. Various related fields note the importance of pile-soil interaction during dynamic loading, for example, post-installation modeling of wind and wave loads (Markou and Kaynia, 2018), piles in earthquake analysis (Nogami and Konagai, 1987; Novak, 1991), pile bearing capacity under vertical vibration (Nogami and Konagai, 1987) and onshore vibratory pile driving (Holeyman, 2002). Cui et al. (2022) introduce a Winkler spring connection between the pile and surrounding soil to study the effect of incomplete pile-soil bonding on the vibrations of a floating pile. All cases justify further research in pile-soil interaction for vibratory pile driving. The abovementioned cases mainly focus on pile vibrations, though the emitted wave field is specifically interested in noise predictions.

State-of-the-art models in impact pile driving are not directly suitable for vibratory installation because sufficiently accurate modeling of the pile-soil slip is essential for predicting underwater noise in the latter case. In vibratory pile driving, the system reaches a quasi-steady state where pile-soil interaction plays an essential role in describing the state. On the contrary, a wave traveling through the pile governs the motion in impact pile driving and the associated primary noise emission, while pile-soil interaction mainly affects the amplitude of the wave reflections and a short-lived transient slip. Thus, relative motion between pile and soil and the resulting soil dynamics should be modeled to improve the accuracy of noise predictions. In addition, improved accuracy should not cost significant computational power since computational efficiency is a substantial challenge in noise prediction models (Tsouvalas, 2020).

This paper introduces a model that allows for relative motion between pile and soil in acoustic predictions of vibratory pile driving. It relaxes the perfect contact, i.e., monolithic, interface conditions between pile and soil, that is standard in acoustic pile driving models, by introducing a contact stiffness element comparable as done by Cui et al. (2022). Friction is essential in vibratory pile installation but is strongly non-linear by definition. Regardless, the contact stiffness element allows for relative motion linearly between pile and soil, which is assumed sufficient for acoustic predictions. The model separates pile and fluid-soil substructures; a summation of the in-vacuo eigenmodes describes the pile vibration. The fluid-soil reaction to thepile is modeled via an indirect boundary element method. This model that allows for relative motion between pile and soil is the first novel contribution of the paper. The model is then validated based on the COMPILE benchmark case (Lippert et al., 2016) with the finite element software 'COMSOL Multiphysics®' (COMSOL, 2019). Hereafter, a realistic case study is developed to analyze the noise and seabed vibrations based on the contact element stiffness variation. The stiffness is varied between two extreme cases; the case of perfect contact and the case of no frictional force, i.e., perfect slip, between pile and soil. Last, the effect of the interface condition on the noise generation mechanism is highlighted. The analysis confirms that models that do not account for pile slip are not directly applicable to the vibratory installation. To the authors' knowledge, this influence is for the first time discussed in scientific knowledge.

This paper introduces a new model with the governing equations and mathematical considerations discussed in Section 2. The Green's functions of ring sources in the fluid and soil domain are vital for the developed model and are derived in Section 3. The model is verified for a limit case in Section 4. Section 5 investigates the effect of pile-soil slip on noise generation mechanisms, noise pollution, and seabed vibrations. Finally, conclusions are drawn in Section 6.

2 Noise and seabed vibrations

2.1 Model description

The problem at hand considers a pile driven offshore. A thin shell theory describes the motion of the pile. The shell occupies the domain $0< z< L_p$, having constant thickness h_p and diameter $2r_p$. The constants E_p, ν_p, and ρ_p correspond to the modulus of elasticity, Poisson's ratio, and density of the pile, respectively. The seawater is described as an acoustic fluid, and the soil is modeled as an elastic continuum. The fluid occupies the domain $z_1< z< z_2$ anddepends on constants c_f and ρ_f, the fluid wave speed and density, respectively. The soil half-space at $z_2< z$ is defined by Lamé constants λ_s and μ_s and density ρ_s. The model geometry and sub-structuring approach are visualized in Figure 1. The problem is modeled in a cylindrical coordinate system, assuming symmetry over the azimuth (r, z). The pile and fluid-soil domains are first considered individually, i.e., a substructuring approach, and subsequently coupled via kinematic and dynamic interface conditions at the pile surface, i.e., $r = r_p$.

The interface conditions between the pile and soil are crucial in the modeling approach. The present model allows for relative motion between pile and soil via a contact stiffness element that varies in stiffness between the ultimate cases of perfect contact (PC), and no friction (NF), i.e. frictionless sliding. The authors believe that introducing the contact stiffness element improves noise prediction without computationally expensive non-linear time-domain calculations because it allows for limited relative motion

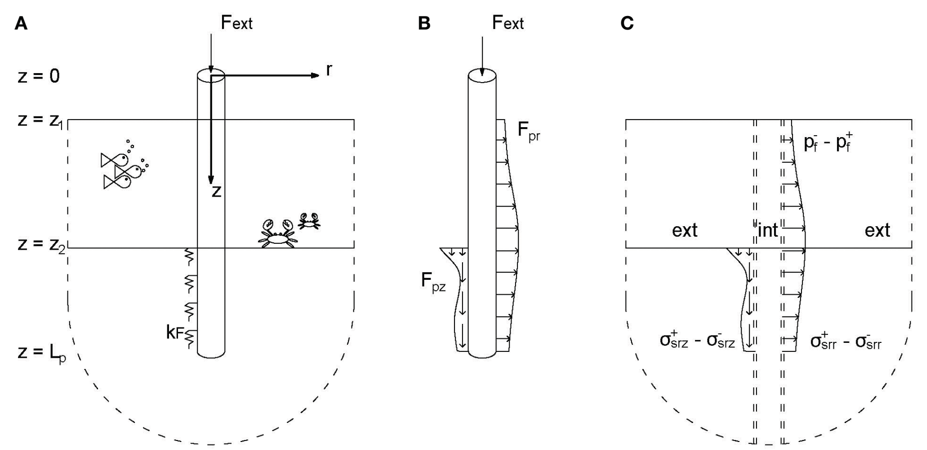

FIGURE 1
The sub-structuring approach of the model: **(A)** the model geometry, **(B)** the in-vacuo pile substructure with an external load on top and distributed loads representing the fluid and soil response, and **(C)** the internal and external fluid-soil substructures with the pile load acting on the boundaries at $r = r_p$.

between pile and soil, which is considered necessary for noise emission modeling. This study considers a frequency- and depth-independent contact spring element, though the element can theoretically contain both spring and damper and can be depth- and frequency-dependent. The idea behind this approach is that the pile is considered around a particular equilibrium state, i.e., the penetration depth is fixed. The contact spring element can be calibrated further based on a driveability model, i.e., (Tsetas et al., 2023b) or experimental data.

2.2 Governing equations

The analysis in this study is performed in the frequency domain, making use of the following Fourier transform pair:

$$f(t) = \frac{1}{2\pi}\int_{-\infty}^{\infty}\tilde{f}(\omega)e^{\mathrm{i}\omega t}\mathrm{d}\omega, \qquad \tilde{f}(\omega) = \int_{-\infty}^{\infty} f(t)e^{-\mathrm{i}\omega t}\mathrm{d}t \quad (1)$$

The pile, fluid, and soil domains are referred to by subscript p, f, and s, respectively. Subscripts r and z refer to the radial and the vertical direction, respectively. The equations of motion of the pile read:

$$\boldsymbol{L}_{\mathrm{p}}\tilde{\boldsymbol{u}}_{\mathrm{p}}(z) - \rho_{\mathrm{p}}h_{\mathrm{p}}\omega^2\tilde{\boldsymbol{u}}_{\mathrm{p}}(z) = \tilde{\boldsymbol{f}}_{\mathrm{p}}(z) + \tilde{f}_{\mathrm{ext}}\delta(z)\hat{\mathrm{e}}_{\mathrm{z}} \quad (2)$$

where $\boldsymbol{L}_{\mathrm{p}}$ represents the stiffness components of Flügge's thin shell theory (Leissa, 1973) and depends on the shell material and geometrical properties. $\tilde{\boldsymbol{u}}_{\mathrm{p}}(z) = [\tilde{u}_{\mathrm{p,r}}(z), \tilde{u}_{\mathrm{p,z}}(z)]^T$ contains the displacements of the pile. The hammer force is modeled as a distributed load on top of the pile via $\tilde{f}_{\mathrm{ext}}\delta(z)\hat{\mathrm{e}}_{\mathrm{z}}$, while the fluid and soil reactions are lumped in $\tilde{\boldsymbol{f}}_{\mathrm{p}}(z) = [\tilde{f}_{\mathrm{p,r}}(z), \tilde{f}_{\mathrm{p,z}}(z)]^T$. The interaction with fluid and soil can be written as a convolution over the length of the pile of the effective dynamic stiffness of the fluid-soil domain and the pile displacements: $\tilde{\boldsymbol{f}}_{\mathrm{p}}(z) = -(\tilde{\boldsymbol{K}}_{\mathrm{fs}}^{\mathrm{F}} * \tilde{\boldsymbol{u}}_{\mathrm{p}})(z)$. $\tilde{\mathbf{K}}_{\mathrm{fs}}^{\mathrm{F}}(z)$ is the analytical description of the effective dynamic stiffness, including the contact spring element, coupling the radial and the vertical direction. This convolution is later evaluated numerically and substituted by the boundary element matrix. The fluid and soil media are modeled as acoustic and linearly elastic continua. The equations of motion read:

$$\left(\nabla^2 + \frac{\omega^2}{c_{\mathrm{f}}^2}\right)\tilde{\phi}_{\mathrm{f}}(r,z) = -\tilde{s}_{\mathrm{f}}(z)\delta(r - r_{\mathrm{p}}) \quad (3)$$

$$(\lambda_{\mathrm{s}} + 2\mu_{\mathrm{s}})\,\nabla\,\nabla\cdot\tilde{\boldsymbol{u}}_{\mathrm{s}}(r,z) - \mu_{\mathrm{s}}\,\nabla\times\nabla\times\tilde{\boldsymbol{u}}_{\mathrm{s}}(r,z) + \rho_{\mathrm{s}}\omega^2\tilde{\boldsymbol{u}}_{\mathrm{s}}(r,z) = -\tilde{\boldsymbol{f}}_{\mathrm{s}}(z)\delta(r - r_{\mathrm{p}}) \quad (4)$$

The fluid equation of motion is written as a function of the displacement potential ϕ_{f} (r, z), with $\tilde{u}_{\mathrm{f}}(r,z) = \nabla\tilde{\phi}_{\mathrm{f}}(r,z)$ and fluid pressure $\tilde{p}_{\mathrm{f}}(r,z) = \rho_{\mathrm{f}}\omega^2\phi_{\mathrm{f}}(r,z)$, including $\tilde{s}_{\mathrm{f}}(z)$ as volume injection source at the location of the pile (Jensen et al., 2011). The soil equation of motion contains displacements vector $\tilde{\boldsymbol{u}}_{\mathrm{s}}(r,z) = [\tilde{u}_{\mathrm{s,r}}(r, z), \tilde{u}_{\mathrm{s,z}}(r,z)]^T$ and body forces vector $\tilde{\boldsymbol{f}}_{\mathrm{s}}(z) = [\tilde{f}_{\mathrm{s,r}}(z), \tilde{f}_{\mathrm{s,z}}(z)]^T$ at the radius of the pile. The boundary value problem for the fluid-soil substructure is composed of a single fluid layer overlaying a soil half-space. The accompanying interface conditions read:

$$\tilde{p}_{\mathrm{f}}(r, z_1) = 0 \quad (5)$$

$$\tilde{p}_{\mathrm{f}}(r, z_2) + \tilde{\sigma}_{\mathrm{s,zz}}(r, z_2) = 0 \quad (6)$$

$$\tilde{u}_{\mathrm{f,z}}(r, z_2) - \tilde{u}_{\mathrm{s,z}}(r, z_2) = 0 \quad (7)$$

$$\tilde{\sigma}_{\mathrm{s,zr}}(r, z_2) = 0 \quad (8)$$

Next to the interface conditions, the Sommerfeld radiation condition is applied at the infinite boundaries. Last, the two substructures are coupled via the interface conditions on the pile's interior and exterior surfaces. The interior surface is indicated with superscript '-' and the exterior with '+'. The interface conditions read:

$$\tilde{u}_{\mathrm{p,r}}(z) = \tilde{u}_{\mathrm{f,r}}(r_{\mathrm{p}}, z) \qquad z_1 < z < z_2 \quad (9)$$

$$\tilde{F}_{\mathrm{p,r}}(z) = -\tilde{p}_{\mathrm{f}}(r_{\mathrm{p}}^+, z) + \tilde{p}_{\mathrm{f}}(r_{\mathrm{p}}^-, z) \qquad z_1 < z < z_2 \quad (10)$$

$$\tilde{u}_{\mathrm{p,r}}(z) = \tilde{u}_{\mathrm{s,r}}(r_{\mathrm{p}}, z) \qquad z_2 < z < L_{\mathrm{p}} \quad (11)$$

$$\tilde{F}_{\mathrm{p,r}}(z) = \tilde{\sigma}_{\mathrm{s,rr}}(r_{\mathrm{p}}^+, z) - \tilde{\sigma}_{\mathrm{s,rr}}(r_{\mathrm{p}}^-, z) \qquad z_2 < z < L_{\mathrm{p}} \quad (12)$$

$$\tilde{F}_{\mathrm{p,z}}(z) = \tilde{k}_{\mathrm{F}}(2\tilde{u}_{\mathrm{p,z}}(z) - \tilde{u}_{\mathrm{s,z}}(r_{\mathrm{p}}^+, z) - \tilde{u}_{\mathrm{s,z}}(r_{\mathrm{p}}^-, z)) \qquad z_2 < z < L_{\mathrm{p}} \quad (13)$$

$$\tilde{\sigma}_{\mathrm{s,rz}}(r_{\mathrm{p}}^+, z) - \tilde{\sigma}_{\mathrm{s,rz}}(r_{\mathrm{p}}^-, z) = \tilde{k}_{\mathrm{F}}(2\tilde{u}_{\mathrm{p,z}}(z) - \tilde{u}_{\mathrm{s,z}}(r_{\mathrm{p}}^+, z) - \tilde{u}_{\mathrm{s,z}}(r_{\mathrm{p}}^-, z)) \; z_2 < z < L_{\mathrm{p}} \quad (14)$$

in which $\tilde{k}_{\mathrm{F}}$ is the introduced contact stiffness element that allows for relative motion between pile and soil in the vertical direction. The limit cases of PC and NF are approached by the limits of $\tilde{k}_{\mathrm{F}} \to \infty$ and $\tilde{k}_{\mathrm{F}} \to 0$, respectively. In all cases, the continuity of displacements in the radial direction and equilibrium of stresses are satisfied.

2.3 Solution method

A solution for the pile and fluid-soil substructure is found independently and coupled via the interface conditions. A summation of in-vacuo modes describes the pile substructure, and an indirect boundary element approach defines the fluid-soil domain. Green's functions for a layered medium are obtained in the wavenumber domain (Section 3), and retrieved in space by the wavenumber integration technique (Jensen et al., 2011). A boundary element matrix for the interior and exterior fluid-soil domainsis first obtained and subsequently substituted into the interface conditions: Eqs. (9) to (14). From the interface conditions, an effective boundary element matrix is derived based on the pile displacements, which is then substituted back into the equation of motion of the pile. Last, the orthogonality relation of the structural modes is applied to find the complex-valued modal coefficients.

First, the equation of motion of the pile is rewritten:

$$\boldsymbol{L}_{\mathrm{p}}\tilde{\boldsymbol{u}}_{\mathrm{p}}(z) - \rho_{\mathrm{p}}h_{\mathrm{p}}\omega^2\tilde{\boldsymbol{u}}_{\mathrm{p}}(z) + (\tilde{\boldsymbol{K}}_{\mathrm{fs}}^{\mathrm{F}} * \tilde{\boldsymbol{u}}_{\mathrm{p}})(z) = \tilde{f}_{\mathrm{ext}}\delta(z)\hat{\mathrm{e}}_{\mathrm{z}} \quad (15)$$

Then the displacement field of the pile is decomposed into a summation of structural modes, i.e.:

$$\tilde{\boldsymbol{u}}_{\mathrm{p}}(z) = \sum_{k=1}^{\infty} \tilde{\eta}_k \boldsymbol{U}_{\mathrm{p},k}(z) \tag{16}$$

The mode shapes $\boldsymbol{U}_{\mathrm{p},k}(z)$ are found by solving the eigenvalue problem of the in-vacuo pile with free-end boundary conditions. The modal amplitudes $\tilde{\eta}_k$ are obtained after pre-multiplying Eq. (15) with another mode l once expressed in the modal domain, and subsequently, integrating over the length of the pile:

$$\tilde{\eta}_k = \sum_l \left[(\omega_k^2 - \omega^2) N_k \delta_{lk} + \int_{z_1}^{L_{\mathrm{p}}} \boldsymbol{U}_{\mathrm{p},l}^T(z) (\tilde{\boldsymbol{K}}_{\mathrm{fs}}^{\mathrm{F}} \star \boldsymbol{U}_{\mathrm{p},k})(z) \mathrm{d}z \right]^{-1} U_{pz,l}(0) f_{\mathrm{ext}} \tag{17}$$

in which δ_{lk} is the Kronecker delta function, and N_k is expressed as:

$$N_k = \rho_{\mathrm{p}} h_{\mathrm{p}} \int_0^{L_{\mathrm{p}}} \boldsymbol{U}_{\mathrm{p},k}^T(z) \boldsymbol{U}_{\mathrm{p},k}(z) \mathrm{d}z \tag{18}$$

The boundary element matrix of the fluid-soil substructure is derived based on the indirect boundary element method. The indirect boundary integral for a field ϕ at p and a source σ at q reads (Kirkup, 2019):

$$\phi(\boldsymbol{p}) = \int_{\Gamma} G(\boldsymbol{p}, \boldsymbol{q}) \sigma(\boldsymbol{q}) \mathrm{d}\Gamma_q \tag{19}$$

$$\frac{\partial}{\partial n_p} \phi(\boldsymbol{p}) = \int_{\Gamma} \frac{\partial}{\partial n_p} G(\boldsymbol{p}, \boldsymbol{q}) \sigma(\boldsymbol{q}) \mathrm{d}\Gamma_q + c_p \sigma(\boldsymbol{p}) \tag{20}$$

with n_p being the normal vector and the constant $c_p = \frac{1}{2}$ when p is on Γ_q and $c_p = 0$ otherwise. The boundary element matrix is found after substituting Eq. (20) in Eq. (19) and eliminating the sources $\sigma(\boldsymbol{q})$. The boundary element matrices for the interior and exterior domains are found based on the same Green's function, though the normal vector n_p changes direction. Since the problem is cylindrically symmetric with sources at the pile radius $r = r_{\mathrm{p}}$, Green's functions are derived for ring sources in both domains. The displacements and stress fields in fluid and soil are expressed in terms of Green's functions. The displacements, pressure, and stresses are expressed as integrals over all sources on the pile surface.

$$\begin{aligned} \tilde{u}_{\mathrm{f,f}}^{\pm}(z) = & \int_{z_1}^{z_2} \tilde{T}_{\mathrm{f,f}}(z, z_s) \tilde{s}_{\mathrm{f}}(z_s) \mathrm{d}z_s \pm \frac{\tilde{s}_{\mathrm{f}}(z)}{2} \\ & + \int_{z_2}^{\infty} \tilde{T}_{\mathrm{f,sr}}(z, z_s) \tilde{f}_{\mathrm{s,r}}(z_s) + \tilde{T}_{\mathrm{f,sz}}(z, z_s) \tilde{f}_{\mathrm{s,z}}(z_s) \mathrm{d}z_s \end{aligned} \tag{21}$$

$$\begin{aligned} p_{\mathrm{f,f}}(z) = & \int_{z_1}^{z_2} \tilde{G}_{\mathrm{f,f}}(z, z_s) \tilde{s}_{\mathrm{f}}(z_s) \mathrm{d}z_s + \int_{z_2}^{\infty} \tilde{G}_{\mathrm{f,sr}}(z, z_s) \tilde{f}_{\mathrm{s,r}}(z_s) \\ & + \tilde{G}_{\mathrm{f,sz}}(z, z_s) \tilde{f}_{\mathrm{s,z}}(z_s) \mathrm{d}z_s \end{aligned} \tag{22}$$

$$\begin{aligned} \tilde{u}_{\mathrm{s}\alpha,\mathrm{f}}(z) = & \int_{z_1}^{z_2} \tilde{G}_{\mathrm{s}\alpha,\mathrm{f}}(z, z_s) \tilde{s}_{\mathrm{f}}(z_s) \mathrm{d}z_s + \int_{z_2}^{\infty} \tilde{G}_{\mathrm{s}\alpha,\mathrm{sr}}(z, z_s) \tilde{f}_{\mathrm{s,r}}(z_s) \\ & + \tilde{G}_{\mathrm{s}\alpha,\mathrm{sz}}(z, z_s) \tilde{f}_{\mathrm{s,z}}(z_s) \mathrm{d}z_s \end{aligned} \tag{23}$$

$$\begin{aligned} \tilde{\sigma}_{\mathrm{sr}\alpha,\mathrm{f}}^{\pm}(z) = & \int_{z_1}^{z_2} \tilde{T}_{\mathrm{s}\alpha,\mathrm{f}}(z, z_s) \tilde{s}_{\mathrm{f}}(z_s) \mathrm{d}z_s \\ & + \int_{z_2}^{\infty} \tilde{T}_{\mathrm{s}\alpha,\mathrm{sr}}(z, z_s) \tilde{f}_{\mathrm{s,r}}(z_s) + \tilde{T}_{\mathrm{s}\alpha,\mathrm{sz}}(z, z_s) \tilde{f}_{\mathrm{s,z}}(z_s) \mathrm{d}z_s \pm \frac{\tilde{f}_{\mathrm{s},\alpha}(z)}{2} \end{aligned} \tag{24}$$

in which α = r, z, corresponds to the radial and vertical direction. The frequency domain Green's functions and Green's tensors are given by $\tilde{G}_{\dots,\mathrm{f}}(z, z_s)$ and $\tilde{T}_{\dots,\mathrm{f}}(z, z_s)$, respectively. The superscript and operator ± in Eqs. (21) and (24) corresponds to the exterior (+) and interior (-) domain and originates from the direction of the normal vector n_p in Eq. (20). Numerical integration of Eqs. (21) to (24) results in a discrete matrix relating displacements, pressure, and stresses to the ring sources, both in the exterior and the interior domain, indicated with ± respectively. Because Green's functions are singular at the source, it is chosen to have a source of constant amplitude over the height of an element to circumvent the singularity; i.e., the integrals are evaluated by the midpoint rule. Additionally, the integration scheme positively affects the convergence rate of the inverse Hankel transforms addressed later. The Green's functions and Green's tensor functions are derived in Section 3.

$$\begin{bmatrix} \bar{\boldsymbol{u}}_{\mathrm{fr}}^{\pm} \\ \bar{\boldsymbol{u}}_{\mathrm{sr}} \\ \bar{\boldsymbol{u}}_{\mathrm{sz}} \\ \bar{\boldsymbol{p}}_{\mathrm{f}} \\ \bar{\boldsymbol{\sigma}}_{\mathrm{srr}}^{\pm} \\ \bar{\boldsymbol{\sigma}}_{\mathrm{srz}}^{\pm} \end{bmatrix} = \begin{bmatrix} \bar{\boldsymbol{T}}_{\mathrm{f,f}} \pm \frac{1}{2}\boldsymbol{I} & \bar{\boldsymbol{T}}_{\mathrm{f,sr}} & \bar{\boldsymbol{T}}_{\mathrm{f,sz}} \\ \bar{\boldsymbol{G}}_{\mathrm{sr,f}} & \bar{\boldsymbol{G}}_{\mathrm{sr,sr}} & \bar{\boldsymbol{G}}_{\mathrm{sr,sz}} \\ \bar{\boldsymbol{G}}_{\mathrm{sz,f}} & \bar{\boldsymbol{G}}_{\mathrm{sz,sr}} & \bar{\boldsymbol{G}}_{\mathrm{sz,sz}} \\ \bar{\boldsymbol{G}}_{\mathrm{f,f}} & \bar{\boldsymbol{G}}_{f,\mathrm{sr}} & \bar{\boldsymbol{G}}_{\mathrm{f,sz}} \\ \bar{\boldsymbol{T}}_{\mathrm{sr,f}} & \bar{\boldsymbol{T}}_{\mathrm{sr,sr}} \pm \frac{1}{2}\boldsymbol{I} & \bar{\boldsymbol{T}}_{\mathrm{sr},sz} \\ \bar{\boldsymbol{T}}_{\mathrm{sz,f}} & \bar{\boldsymbol{T}}_{\mathrm{sz,sr}} & \bar{\boldsymbol{T}}_{\mathrm{sz,sz}} \pm \frac{1}{2}\boldsymbol{I} \end{bmatrix} \begin{bmatrix} \bar{\boldsymbol{s}}_{\mathrm{f}} \\ \bar{\boldsymbol{f}}_{\mathrm{sr}} \\ \bar{\boldsymbol{f}}_{\mathrm{sz}} \end{bmatrix} \tag{25}$$

with $\boldsymbol{I}$ being the identity matrix and the overhead bar indicating that the variables are discretized. After some standard linear algebra, stresses and displacements are related via the dynamic stiffness matrix of the fluid-soil domain:

$$\begin{bmatrix} -\bar{\boldsymbol{p}}_{\mathrm{f}} \\ \bar{\boldsymbol{\sigma}}_{\mathrm{srr}} \\ \bar{\boldsymbol{\sigma}}_{\mathrm{srz}} \end{bmatrix} = \bar{\boldsymbol{K}}_{\mathrm{fs}} \begin{bmatrix} \bar{\boldsymbol{u}}_{\mathrm{fr}} \\ \bar{\boldsymbol{u}}_{\mathrm{sr}} \\ \bar{\boldsymbol{u}}_{\mathrm{sz}} \end{bmatrix} \tag{26}$$

The effective fluid-soil stiffness matrix in Eq. (17) is a function of the pile displacements and therefore includes the description of the pile-soil interface condition. Thus, the convolution integral $(\tilde{\boldsymbol{K}}_{\mathrm{fs}}^{\mathrm{F}} \star \tilde{\boldsymbol{u}}_{\mathrm{p}})(z)$ is numerically evaluated by substituting Eq. (26) into Eqs. (9) to (14). In the PC case, the effective stiffness fluid-soil matrix is equal to the matrix found in Eq. (26), i.e., $(\tilde{\boldsymbol{K}}_{\mathrm{fs}}^{\mathrm{F}} \star \tilde{\boldsymbol{u}}_{\mathrm{p}})(z) \rightarrow \bar{\boldsymbol{K}}_{\mathrm{fs}} \bar{\boldsymbol{u}}_{\mathrm{p}}$

3 Fluid-soil Green's functions

The Green's functions for a layered medium are derived in two steps. First, Green's functions for the infinite space are derived from a ring source in both fluid and soil media. Second, the infinite space Green's functions are substituted in the boundary value problem. Since the problem is cylindrically symmetric with sources at $r = r_{\mathrm{p}}$, Green's functions are derived for ring sources in both domains. First, the soil displacements are decomposed into potentials:

$\tilde{u}_s(r,z) = \nabla\tilde{\phi}_s(r,z) + \nabla \times \nabla \times \tilde{\psi}_s(r,z)\hat{e}_z$. Hereafter, the problem is transformed to the frequency-wavenumber domain by making use of the following Hankel transform pair:

$$\tilde{\phi}(r,z) = \int_0^\infty \hat{\Phi}(k,z)\mathrm{J}_0(kr)k\mathrm{d}k \leftrightarrow \hat{\Phi}(k,z) = \int_0^\infty \tilde{\phi}(r,z)\mathrm{J}_0(kr)r\mathrm{d}r \quad (27)$$

The fluid-soil domain is split into an interior and an exterior domain at the position of the pile, $r = r_\mathrm{p}$. The applied indirect boundary method includes Green's functions of ring sources at the pile's location and derives the displacement and stress field at the boundary as a function of the sources. The potential solution is sought for in the form of a homogeneous solution and a particular solution:

$$\hat{\Phi}_\mathrm{f}(k,z) = A_1 e^{-\alpha_\mathrm{f} z} + B_1 e^{\alpha_\mathrm{f} z} + \hat{\Phi}_\mathrm{f}^\mathrm{P}(k,z) \quad (28)$$

$$\hat{\Phi}_\mathrm{s}(k,z) = A_2 e^{-\alpha_s z} + \hat{\Phi}_\mathrm{s}^\mathrm{P}(k,z) \quad (29)$$

$$\hat{\Psi}_\mathrm{s}(k,z) = A_3 e^{-\beta_s z} + \hat{\Psi}_\mathrm{s}^\mathrm{P}(k,z) \quad (30)$$

The particular solutions in Eqs. (28) to (30) are derived from the infinite space Green's functions introduced in Sections 3.1 and 3.2. The homogeneous part is based on the boundary value problem, given by Eqs. (5) to (8). The problem is transformed to the wavenumber domain by applying Eq. (27):

$$\rho_\mathrm{f}\omega^2\hat{\Phi}_\mathrm{f}(k,\ z_1) = 0 \quad (31)$$

$$\rho_\mathrm{f}\omega^2\hat{\Phi}_\mathrm{f}(k,z_2) + \hat{S}_{\mathrm{s},3}(k,z_2) = 0 \quad (32)$$

$$\frac{\mathrm{d}}{\mathrm{d}z}\hat{\Phi}_\mathrm{f}(k,z_2) - \hat{U}_{\mathrm{s},3}(k,z_2) = 0 \quad (33)$$

$$\hat{S}_{\mathrm{s},1}(k,z_2) = 0 \quad (34)$$

which can be expressed in potentials via:

$$\hat{U}_{\mathrm{s},1}(k,z) = \left(\hat{\Phi}_\mathrm{s}(k,z) + \frac{\mathrm{d}}{\mathrm{d}z}\hat{\Psi}_\mathrm{s}(k,z)\right)k \quad (35)$$

$$\hat{U}_{\mathrm{s},3}(k,z) = \frac{\mathrm{d}}{\mathrm{d}z}\hat{\Phi}_\mathrm{s}(k,z) + \hat{\Psi}_\mathrm{s}(k,z)k^2 \quad (36)$$

$$\hat{S}_{\mathrm{s},1}(k,z) = \mu_\mathrm{s}\left(\frac{\mathrm{d}}{\mathrm{d}z}\hat{U}_{\mathrm{s},1}(k,z) + k\hat{U}_{\mathrm{s},3}(k,z)\right) \quad (37)$$

$$\hat{S}_{\mathrm{s},3}(k,z) = -k\lambda_\mathrm{s}\hat{U}_{\mathrm{s},1}(k,z) + (\lambda_\mathrm{s} + 2\mu_\mathrm{s})\frac{\mathrm{d}}{\mathrm{d}z}\hat{U}_{\mathrm{s},3}(k,z) \quad (38)$$

The Green's functions and Green's tensors in Eqs. (21) to (24) are found by substituting the potential in the displacements and stresses and by applying the inverse Hankel transform.

3.1 Fluid source

The ring source in the fluid is introduced in the form of a ring volume injection $\tilde{s}_\mathrm{f}(z_s)$, of which the wavenumber counterpart is designated as $\hat{S}_\mathrm{f}(z_s)$. Equation (3) is transformed to the wavenumber domain by applying Eq. (27) to give:

$$\left(\frac{\mathrm{d}^2}{\mathrm{d}z^2} - \alpha_\mathrm{f}^2\right)\hat{\Phi}_\mathrm{f}(k,z) = \hat{S}_\mathrm{f}(z_s)\mathrm{J}_0(kr_\mathrm{p})r_\mathrm{p}\delta(z - z_s) \quad (39)$$

with $\alpha_\mathrm{f} = \sqrt{k^2 - \frac{\omega^2}{c_\mathrm{f}^2}}$ and z_s the source position. The infinite space Greens function for a ring load in the wavenumber domain is given by Peng et al. (2021a):

$$\hat{\Phi}_\mathrm{f}^\mathrm{P}(k,z) = -\frac{\hat{S}_\mathrm{f}(z_s)}{2\alpha_\mathrm{f}}\mathrm{J}_0(kr_\mathrm{p})r_\mathrm{p}\begin{cases} e^{\alpha_\mathrm{f}(z-z_s)} & z < z_s \\ e^{-\alpha_\mathrm{f}(z-z_s)} & z > z_s \end{cases} \quad (40)$$

The Green's functions for a layered medium are obtained after substituting the free field particular solution given by Eq. (40) into Eq. (28) and the boundary value problem: Eqs. (31) to (34), and applying the inverse Hankel transform.

3.2 Soil source

Similarly to the fluid source, a distributed ring load at $r = r_\mathrm{p}$ excites the infinite space. The force is directed either in the radial or the vertical direction. Equation (4) is first transformed to the wavenumber domain resulting in the following coupled equations:

$$\left(\mu_\mathrm{s}\frac{\mathrm{d}^2}{\mathrm{d}z^2} - (\lambda_\mathrm{s} + 2\mu_\mathrm{s})\alpha_\mathrm{s}^2\right)\hat{U}_{\mathrm{s},1}(k,z) + k(\lambda_\mathrm{s} + \mu_\mathrm{s})\frac{\mathrm{d}}{\mathrm{d}z}\hat{U}_{\mathrm{s},3}(k,z) = \hat{F}_{\mathrm{s,r}}(z_s)\mathrm{J}_1(kr_\mathrm{p})r_\mathrm{p}\delta(z - z_s) \quad (41)$$

$$\left((\lambda_\mathrm{s} + 2\mu_\mathrm{s})\frac{\mathrm{d}^2}{\mathrm{d}z^2} - \mu_\mathrm{s}\beta_\mathrm{s}^2\right)\hat{U}_{\mathrm{s},3}(k,z) - k(\lambda_\mathrm{s} + \mu_\mathrm{s})\frac{\mathrm{d}}{\mathrm{d}z}\hat{U}_{\mathrm{s},1}(k,z) = -\hat{F}_{\mathrm{s,z}}(z_s)\mathrm{J}_0(kr_\mathrm{p})r_\mathrm{p}\delta(z - z_s) \quad (42)$$

with $\alpha_\mathrm{s} = \sqrt{k^2 - \frac{\omega^2}{c_\mathrm{L}^2}}$, $\beta_\mathrm{s} = \sqrt{k^2 - \frac{\omega^2}{c_\mathrm{T}^2}}$, $c_\mathrm{L} = \sqrt{\frac{\lambda_\mathrm{s}+2\mu_\mathrm{s}}{\rho_\mathrm{s}}}$, and $c_\mathrm{T} = \sqrt{\frac{\mu_\mathrm{s}}{\rho_\mathrm{s}}}$. The potentials for a ring load in the radial direction in an infinite elastic space read:

$$\hat{\Phi}^\mathrm{P}_{\mathrm{s}\hat{\mathrm{F}}_{\mathrm{sr}}}(k,z) = \frac{\hat{F}_{\mathrm{s},r}(z_s)k}{2\mu_\mathrm{s}\alpha_\mathrm{s}k_\mathrm{s}^2}\mathrm{J}_1(kr_\mathrm{p})r_\mathrm{p}\begin{cases} e^{\alpha_\mathrm{s}(z-z_s)} & z < z_s \\ e^{-\alpha_\mathrm{s}(z-z_s)} & z > z_s \end{cases} \quad (43)$$

$$\hat{\Psi}^\mathrm{P}_{\mathrm{s}\hat{\mathrm{F}}_{\mathrm{sr}}}(k,z) = \frac{\hat{F}_{\mathrm{s},r}(z_s)}{2\mu_\mathrm{s}kk_\mathrm{s}^2}\mathrm{J}_1(kr_\mathrm{p})r_\mathrm{p}\begin{cases} -e^{\beta_\mathrm{s}(z-z_s)} & z < z_s \\ e^{-\beta_\mathrm{s}(z-z_s)} & z > z_s \end{cases} \quad (44)$$

Similarly, the potentials for a vertical load read:

$$\hat{\Phi}^\mathrm{P}_{\mathrm{s}\hat{\mathrm{F}}_{\mathrm{sz}}}(k,z) = \frac{\hat{F}_{\mathrm{s},z}(z_s)}{2\mu_\mathrm{s}k_\mathrm{s}^2}\mathrm{J}_0(kr_\mathrm{p})r_\mathrm{p}\begin{cases} e^{\alpha_\mathrm{s}(z-z_s)} & z < z_s \\ -e^{-\alpha_\mathrm{s}(z-z_s)} & z > z_s \end{cases} \quad (45)$$

$$\hat{\Psi}^\mathrm{P}_{\mathrm{s}\hat{\mathrm{F}}_{\mathrm{sz}}}(k,z) = -\frac{\hat{F}_{\mathrm{s},z}(z_s)}{2\mu_\mathrm{s}\beta_\mathrm{s}k_\mathrm{s}^2}\mathrm{J}_0(kr_\mathrm{p})r_\mathrm{p}\begin{cases} e^{\beta_\mathrm{s}(z-z_s)} & z < z_s \\ e^{-\beta_\mathrm{s}(z-z_s)} & z > z_s \end{cases} \quad (46)$$

Again, the displacement and stress field at boundary $r = r_\mathrm{p}$ are found in terms of Green's functions and Green's tensor functions by substitution of the particular solutions in the boundary value problem.

4 Model verification

The model developed in this paper is verified against a finite element model in 'COMSOL Multiphysics®' (COMSOL, 2019), with input data from the COMPILE benchmark case (Lippert et al., 2016), together with the near-field responses in the companion paper (Lippert et al., 2016). In the COMPILE case, the soil domain is represented by an acoustic fluid though. Therefore, soil parameters are adapted from Peng et al. (2021a) to validate the elastic soil case, and all properties are summarized in Table 1. The verification is performed under perfect contact conditions in which no sliding is allowed between the pile and the soil.

For the validation of the near field model, a harmonic load on top of the pile is considered at frequencies up to 500 Hz. Boundary elements of 0.05 m are used; the mesh is sufficiently small compared to the shortest wavelength of 0.34 m. The upper limit in the inverse Hankel transform is fixed at k = 500 m^{-1} which is sufficiently large because it guarantees that all integrands are smaller than 0.2% of the maximum amplitude. The truncation might seem unnecessarily high compared to the Scholte wavenumber at f = 500 Hz, i.e., $k_{\mathrm{scholte}} \approx 20.5$ m^{-1}, however, it is deemed necessary when source and receiver are positioned at close distance. Pile, fluid, and soil transfer functions are validated for a load amplitude of 1 MN on top of the pile throughout the frequency range. Figure 2 shows the pile displacements at three frequencies distributed within the frequency domain of interest for vibratory pile driving (~15 → 500 Hz). The pile displacements predicted by Comsol and the present model are in excellent agreement.

The sound pressure level (L_p) in the fluid is calculated by (ISO, 2017):

$$L_p = 20 \log \left(\frac{p_{\mathrm{rms}}}{p_{\mathrm{ref}}} \right) \tag{47}$$

in which the real mean square in the frequency domain is found by $p_{\mathrm{rms}}^2 = \frac{1}{2} |\tilde{p}^2|$ and the reference pressure in underwater acoustics is p_{ref} = 1μPa. The sound pressure levels in the near field are in excellent agreement between Comsol and the present model, both in the center of the fluid layer (z = 5 m) and at one meter above the seabed surface (z = 9 m) as shown in Figure 3.

5 Effect of pile-soil interface conditions

A realistic case study is considered hereafter to examine the effect of varying pile-soil interface conditions based on the geometry and material parameters described in Dahl et al. (2015) and measurements of a representative vibratory force by Tsetas et al. (2023a). The data can be used together since both campaigns used piles with an equal diameter of 0.762 m and comparable driving depths into the soil. Table 2 includes all parameters used in the case study.

The applied force at the top of the pile is derived from actual strain measurements as shown in Figure 4. The force is periodic and consists of a primary driving frequency of 25 Hz and strong super-harmonics every 25 Hz. The super-harmonics play a major role in noise emission because at these frequencies sound radiation is more efficient than the main driving frequency. This is confirmed by Dahl et al. (2015) (Figure 3), where the measured sound pressure levels at the super-harmonics are of higher amplitude than the sound pressure level at the main driving frequency.

The Scholte wave often plays a significant role in underwater noise at relatively low frequencies. The intensity of this wave is often overestimated if the pile and soil are assumed in perfect contact. Hereafter, relative motion is allowed between pile and soil via a linear spring element introduced at the pile-soil interface. Four cases are evaluated; a case with perfect contact between pile and soil (PC), a case of no frictional forces (NF), and two cases with relaxed pile-soil contact via the interface element. The interface element relaxes the static (f = 0 Hz) vertical soil stiffness to 75% and 5% of its original stiffness. The cases are abbreviated to k_F 75% and k_F 5%, and correspond to values of $\tilde{k}_F = 5 \times 10^6$ Nm^{-1} and $\tilde{k}_F = 5 \times 10^8$Nm^{-1}, respectively.

TABLE 1 Model properties for model verification in Section 4.

Parameter		unit	Parameter		unit
Sea surface depth [z_1]	0	m	Structural damping	0.001	-
Seabed depth [z_2]	10	m	Fluid wavespeed [c_f]	1500	m s^{-1}
Final penetration depth	25	m	Fluid density [ρ_f]	1025	kg m^{-3}
Pile length [L_p]	25	m	Compression wavespeed soil [c_L]	1800	m s^{-1}
Pile thickness [t_p]	0.05	m	Shear wavespeed soil [c_T]	170	m s^{-1}
Pile radius [r_p]	1	m	Soil density [ρ_s]	2000	kg m^{-3}
Pile Poisons ratio [ν_p]	0.30	-	Compressional wave attenuation [α_L]	0.469	dB/λ
Pile Youngs modulus [E_p]	210	GPa	Shear wave attenuation [α_T]	1.69	dB/λ
Pile density [ρ_p]	7850	kg m^{-3}			

Parameters adapted from Lippert et al. (2016) and Peng et al. (2021a).

5.1 Pile vibrations

Allowing for relative motion between pile and soil affects the pile vibrations and the energy transferred to the surrounding domain. Figure 5 shows the amplitude of the pile displacements at 25 Hz and 125 Hz for varying values of $\tilde{k}_F$. The frequencies are chosen specifically at the driving frequency and the fourth superharmonic. Figure 5A shows that the rigid body motion governs the pile vibrations at low frequencies. For k_F 5%, the radial pile and soil displacements are amplified. This is counterintuitive, but because the system has reduced soil stiffness and low damping, the resonance amplitude of the rigid body mode is amplified significantly. At higher frequencies, the dynamic response of the pile is strongly influenced by the pile-soil interface as shown in Figure 5B; altering the noise source significantly in the fluid domain.

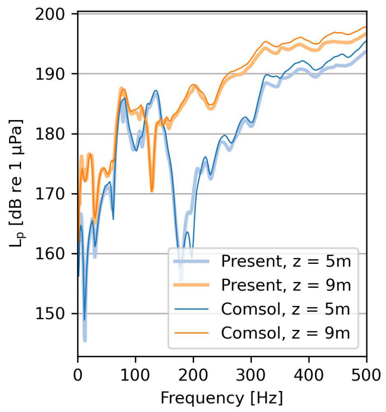

FIGURE 3
Comparison of the sound pressure levels in the water at a radius of 10 m between Comsol (dark colors) and the present model (light colors) for a harmonic load of 1 MN.

5.2 Underwater noise field and seabed vibrations

The change in pile dynamics affects the soil displacements and pressure levels in the fluid. The traveling waves in fluid and soil are visualized in Figure 6. The figure shows snapshots of the fluid pressure and vertical soil displacement in the surroundings. Figure 6A shows that the Scholte waves govern the wavefield because the excitation frequency is below the cut-off frequency of this shallow fluid waveguide ($f_{cut\text{-}off}$ ≈ 37.5 Hz). The cut-off frequency linearly depends on water depth; thus, a pressure wave can exist at the driving frequency in the case of deeper waters. The Scholte wave is visible in the soil and fluid, though the amplitude is negligible in case of perfect sliding conditions (NF case). The soil motion is amplified at k_F 5% because the main driving frequency is close to the eigenfrequency of the rigid body mode. It is debatable if this resonance is an artifact or physical. Experimental data should justify if it is indeed physical or that the artifact disappears with more realistic interface modeling, e.g. including damping. Contrary, Figure 6B clearly shows bulk pressure waves propagating through the fluid, while the Scholte waves influence a narrow zone close to the seabed. Next, the Scholte wave becomes visible with increasing pile-soil stiffness, though the penetration zone in the fluid reduces at higher frequencies due to the shorter wavelength of the Scholte waves. Figure 6 confirms the expectation that the interface conditions strongly affect both primary and secondary noise paths.

Figure 7 shows the sound pressure levels as a function of range and depth for varying cases. The pressure levels are highest above the seabed both from the primary and secondary noise path and decay with distance. With increasing contact stiffness k_F, the interference of pressure waves in the fluid and Scholte waves is clearly visible in Figure 7B. Negligible noise is generated in the case of NF at 25 Hz because this frequency is below the cut-off frequency of propagating body modes in the fluid and almost no energy is transferred to the Scholte waves due to the lack of shear excitation.

The transfer functions or frequency response functions for a unit 1 MN harmonic load on top of the pile at a receiver point at a radius of 20 m are shown in Figures 8A, B. The sound pressure level

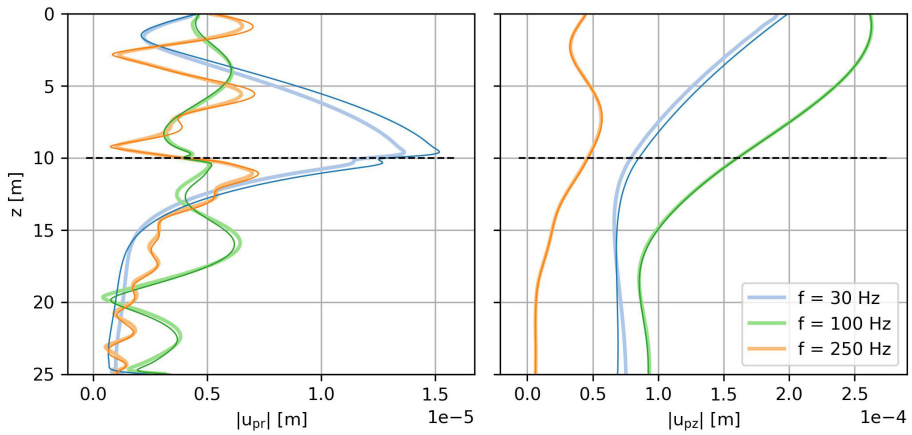

FIGURE 2
Comparison of the amplitudes of the pile vibrations between Comsol (dark colors) and the present model (light colors) for a harmonic load of 1 MN on top of the pile at 30, 100 and 250 Hz.

10.3389/fmars.2023.1118286

TABLE 2 Model properties used to examine the effect of pile-soil interface conditions based on parameters in Section 5.

Parameter		unit	Parameter		unit
Sea surface depth [z_1]	1.4	m	Structural damping	0.001	-
Seabed depth [z_2]	8.9	m	Fluid wavespeed [c_f]	1475	m s^{-1}
Final penetration depth	16	m	Fluid density [ρ_f]	1000	kg m^{-3}
Pile length [L_p]	17.4	m	Compression wavespeed soil [c_L]	1850	m s^{-1}
Pile thickness [t_p]	2.54	m	Shear wavespeed soil [c_T]	400	m s^{-1}
Pile radius [r_p]	0.762	m	Soil density [ρ_s]	1900	kg m^{-3}
Pile Poisons ratio [ν_p]	0.28	-	Compressional wave attenuation [α_L]	0.03	dB/λ
Pile Youngs modulus [E_p]	210	GPa	Shear wave attenuation [α_T]	0.20	dB/λ
Pile density [ρ_p]	7850	kg m^{-3}			

Parameters adapted from Dahl et al. (2015).

transfer functions depend strongly on the contact stiffness element. The sound pressure levels are significantly higher at 0.5 m above the seabed than in the middle of the fluid column for cases with Scholte waves. Scholte waves are most dominant at low frequencies (<200 Hz). At approximately 150, 300, and 450 Hz, the first in-vacuo eigenfrequencies of the pile are indicated with a black dotted vertical line. The sound pressure level amplifies around these frequencies if soil and pile are loosely coupled and the system experiences low

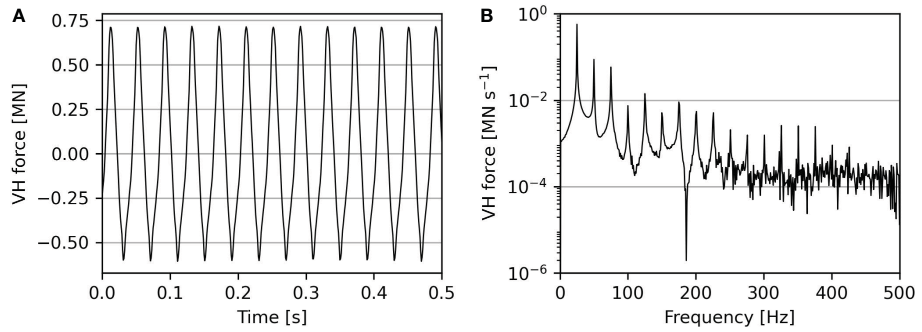

FIGURE 4
Estimated vibratory force exerted by the installation tool at the pile head as a function. **(A)** shows the time signature and **(B)** the amplitude spectrum of the force (Tsetas et al., 2023a).

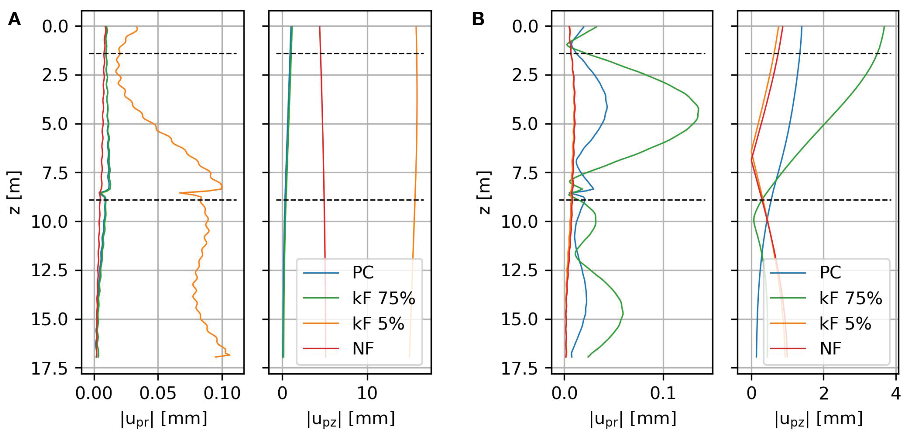

FIGURE 5
The amplitudes of the pile displacements in radial (u_{pr}) and vertical (u_{pz}) direction for a 1 MN harmonic force on top of the pile at 25 Hz and 125 Hz in **(A, B)**, respectively.

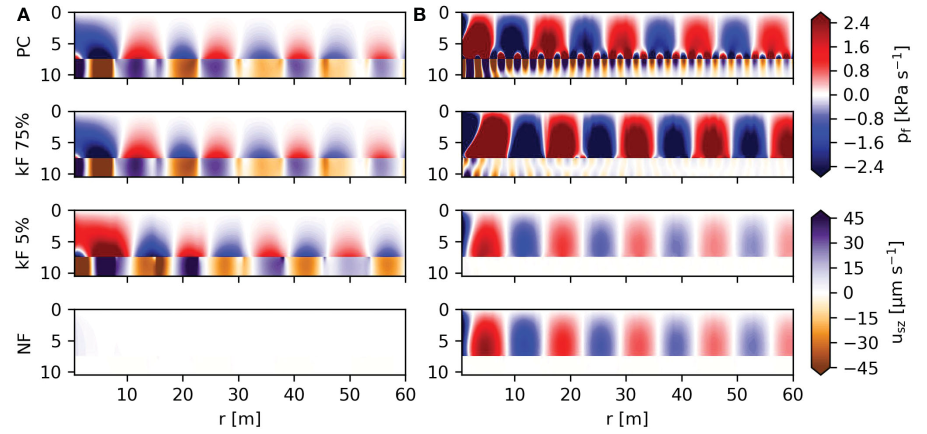

FIGURE 6
(A, B) show the real part of the fluid pressure and vertical soil displacement for a harmonic 1 MN force at 25 Hz and 125 Hz respectively.

damping. Thus, eigenfrequencies play an increasingly important role in the case of reduced resistance. The resonance of the rigid body mode, as discussed in Section 5.1, is visible at 23 Hz for k_F 5%. It is debatable whether this mode is physical or not. One might say that, in reality, this mode can exist at low frequencies with reduced soil resistance. On the other hand, it can be argued that frictional damping limits this resonance behavior. Damping at the pile-soil surface via an imaginary part in k_F can represent the interface damping.

The importance of the sound pressure level transfer functions becomes evident when the actual force is applied at the top of the pile by multiplying the transfer functions with the spectrum of the force plotted in Figure 4B. Figures 8C, D shows the periodicity of the peaks related to the force spectrum. The surface waves at low frequencies govern the noise field above the seabed except for the NF case as shown in Figure 8D. In the middle of the fluid layer, the peaks are of similar amplitude for most super-harmonics. In the case of NF and k_F 5%, the in-vacuo eigenfrequencies of the pile amplify the sound pressure level next to the peaks enforced by the external force.

Applying the inverse Fourier transform gives the periodic time domain response of the fluid and soil. Figure 9 shows a snapshot of the time domain pressure field in the fluid and vertical displacements in the soil. The Scholte waves at the driving frequency govern the wavefield in all cases except for the case of NF. In the upper part of the fluid layer, interference patterns are visible in fluid pressure waves of varying wavelengths. The predominant pressure wave pattern in the case of NF corresponds to a frequency of approximately 150 Hz i.e., the first eigenfrequency of the pile, in line with expectations from the earlier analysis.

To examine the accumulative noise pollution over a time interval, the sound exposure levels (L_E) are calculated. The sound exposure level shows the time-integrated squared sound pressure in decibels and are calculated via (ISO, 2017):

$$L_E = 10\log\left(\frac{E_p}{E_{ref}}\right), \quad E_p = \int_{t_1}^{t_2} p^2 dt = \int_0^{\infty} 2|\tilde{p}|^2 df \qquad (48)$$

with the reference value for sound pressure in fluids $E_{ref} = 1\mu\ \mathrm{Pa}^2\mathrm{s}$. Figure 10 shows the sound exposure levels in the fluid domain

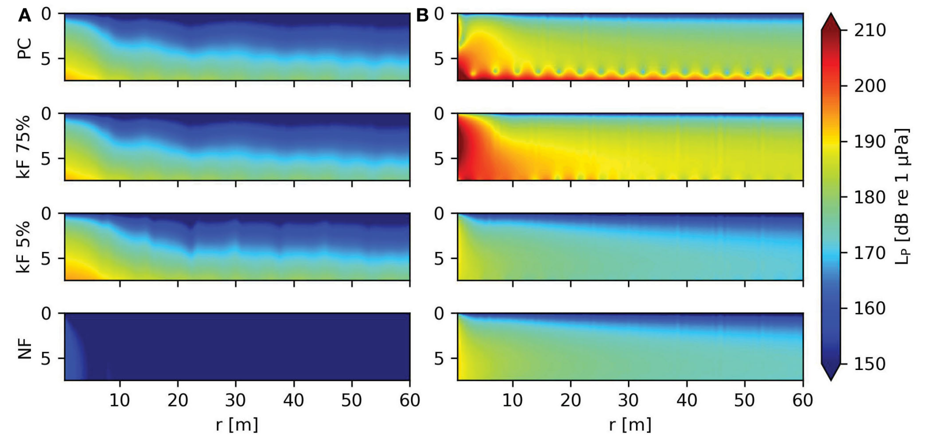

FIGURE 7
Figure **(A, B)** show the sound pressure levels in dB versus depth and height in the fluid for a harmonic 1 MN force at 25 Hz and 125 Hz respectively.

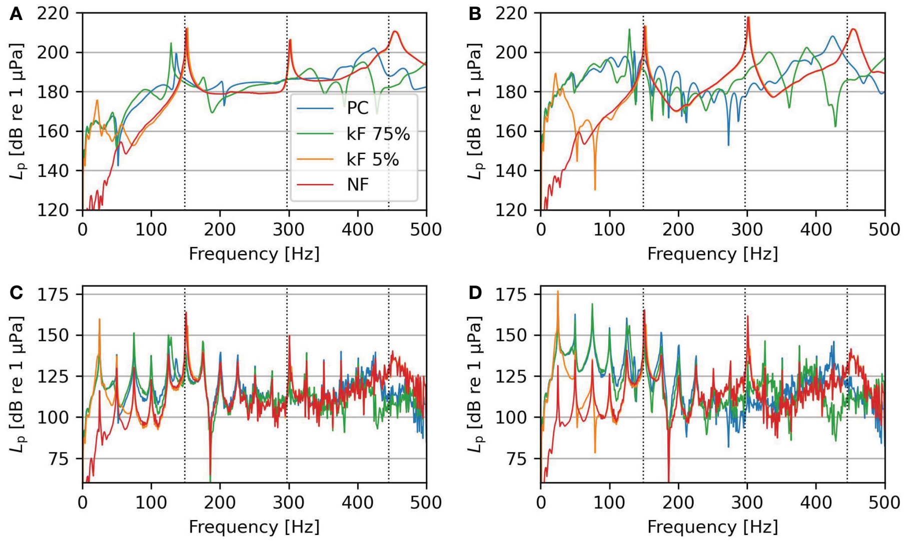

FIGURE 8
(A, B) show the sound pressure level transfer functions for a 1 MN harmonic load on top of the pile at a 20 m radius and z = 3 m and z = 7 m, respectively. **(C, D)** show the sound pressure levels resulting from the vibratory force from Figure 4 at a 20 m radius and z = 3 m and z = 7 m, respectively. The dotted vertical lines indicate the eigenfrequencies of the pile.

throughout 1 second of the forced response. The amplitude of the sound exposure levels varies strongly with the various cases with no particular trend. In the NF case, the sound exposure is governed by the bulk pressure waves, while in the PC case, the Scholte waves contribute significantly. This shows that the sound exposure level above the seabed is highest in the Scholte waves' presence. In the case of NF, the bulk pressure wave causes lower sound exposure levels above the seabed but relatively higher levels in the middle and upper part of the fluid column.

Biologists are additionally interested in particle velocity of fluid and seabed for environmental assessment. Figure 11 shows the particle velocity norm and directionality at a snapshot in time. The figure shows that the predominant particle motion is along the vertical direction at the seabed-water interface. However, in the absence of the Scholte waves, the particle motion direction is governed by the radial direction due to the bulk pressure waves alone.

5.3 Reduced soil shear stiffness

The experimental campaign in Dahl et al. (2015) consists of soil with high shear wave speed. In many known cases, the shear wave speed is significantly lower. Since the shear wave speed strongly influences the amplification of the Scholte waves, the analysis is repeated for a reduced shear wave speed of 150 ms^{-1}, which is

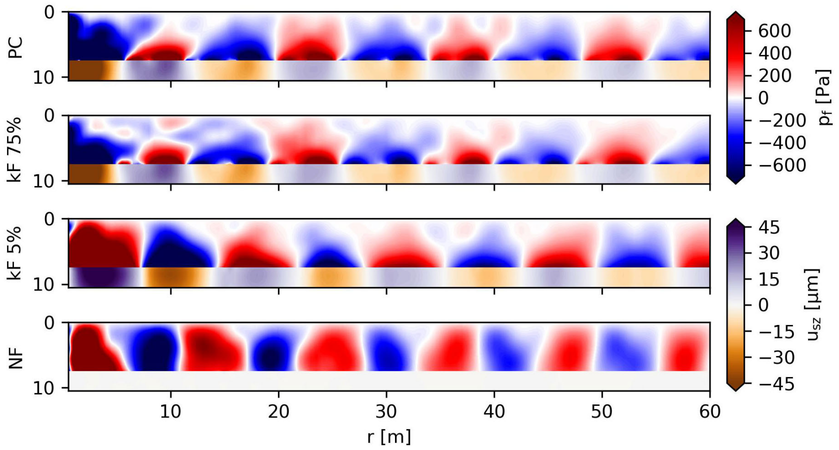

FIGURE 9
Snapshot of the time domain pressure field for the periodic force for varying interface conditions.

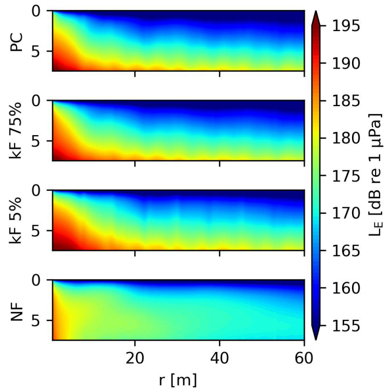

FIGURE 10
Sound exposure levels in dB versus depth and height in the fluid throughout 1 second forcing.

typical in marine environments with sandy sediments in the North Sea in Europe (Peng et al., 2021a). The rest of the parameters are given in Table 2. This results in a relative reduction of the stiffness to 95% and 20% compared to the static stiffness for the rigid body mode, for a contact spring element k_F of 5×10^8 N m^{-1} and 5×10^6 N m^{-1}, respectively.

Figure 12 shows the transfer functions of the pressure field, similarly to Figures 8A, B. Both figures show similar behavior, though the differences in pressure levels between the cases in sound pressure levels are smaller with lower shear wave speed at frequencies between 100 Hz and 350 Hz.

Figure 13 shows a snapshot of the time domain fluid pressures and the vertical soil displacements. The Scholte waves visible differ significantly compared to Figure 9. The Scholte wave is of a shorter wavelength due to the lower shear wave speed and has a reduced penetration into the fluid zone. Thus, the primary noise path becomes more pronounced. The reduced penetration of the Scholte waves also explains the reason why the Scholte waves contribute less to the sound pressure levels in Figure 12 compared to the case shown earlier. Contrary, the vertical displacements in the soil are of larger amplitude compared to Figure 9. Otherwise, the principles of noise generation align with the original case. Even for soil with lower shear wave speeds, the role of the interface waves in the noise generation remains significant, causing dominant pressure levels and seabed vibrations.

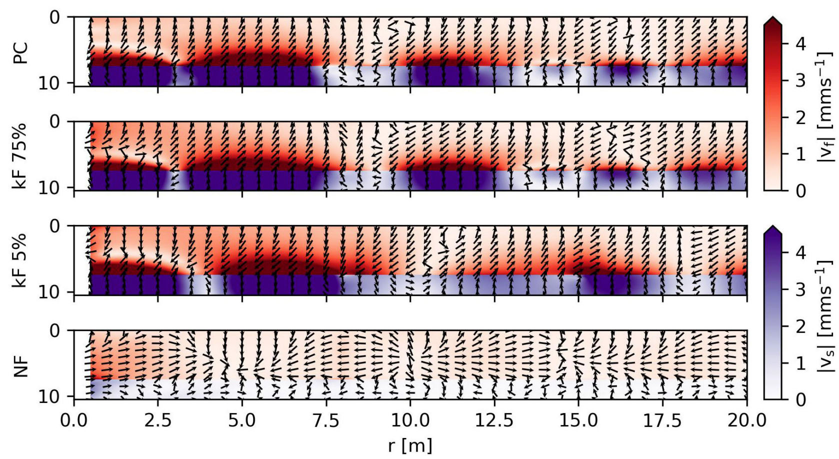

FIGURE 11
Snapshot of particle velocity norm in mm s^{-1} in fluid and soil domains including velocity directionality.

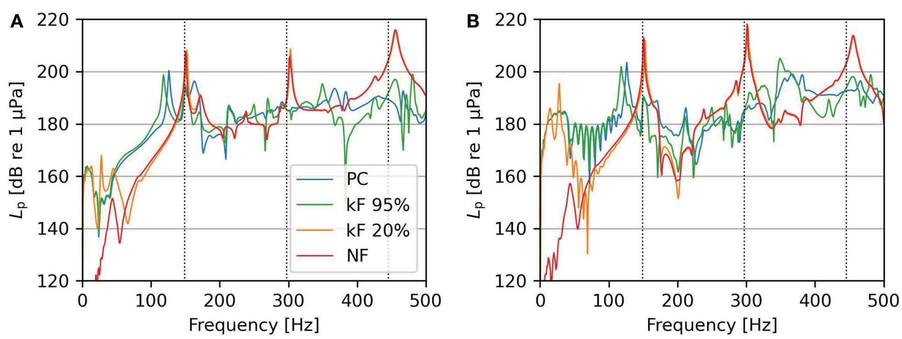

FIGURE 12
(A, B) show the sound pressure level transfer functions for a 1 MN harmonic load on top of the pile at 20 m radius and soil with a low shear modulus.

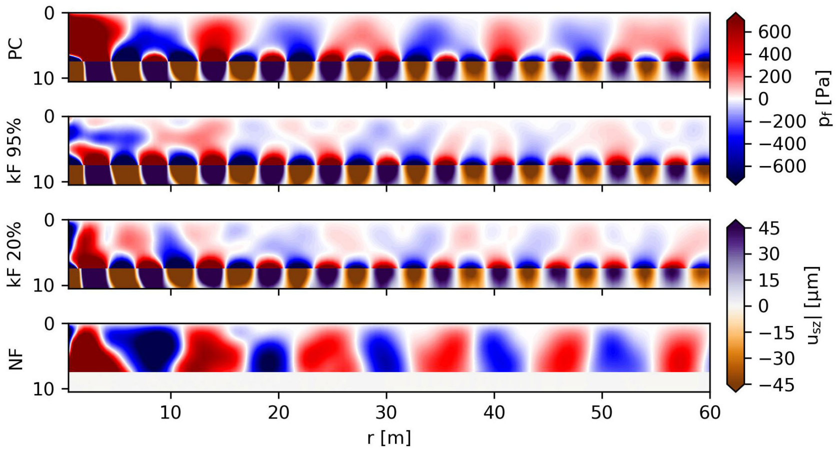

FIGURE 13
Snapshot of time domain pressure field for the periodic force for varying interface conditions with soil with a low shear modulus.

6 Conclusion

This paper concludes that models for impact pile driving are not directly applicable in vibratory pile driving because a more advanced description of pile-soil interaction is essential for predicting noise and vibrations accurately. The pile-soil interface condition strongly influences the dynamic response of the pile and the energy transfer mechanism in the surrounding domain. More specifically:

- The dynamic response of the pile depends strongly on the coupling to the soil, which, in turn, influences the primary noise and secondary noise paths.
- In case pile and soil are loosely coupled, the in-vacuo eigenfrequencies of the pile play an increasingly important role in noise generation. The reduced damping and stiffness in the system cause amplification of the structural vibrations around the eigenfrequencies of the coupled system.
- In the case of strong pile-soil coupling, Scholte interface waves are amplified and contribute significantly to the fluid pressures. The Scholte waves govern the seabed vibrations for high and low shear speeds. Due to the possible intense seabed vibrations, marine life on or above can potentially be harmed. The Scholte waves are significant at low frequencies and, therefore, more important in vibratory installation compared to impact pile driving.
- The pile-soil interface conditions strongly influence the particle velocity field.

Even with a relaxation of the pile-soil interface condition, the presence of the Scholte wave affects the sound field due to the relatively low primary excitation frequency. Therefore, models representing the soil by an acoustic fluid are insufficient invibratory pile driving. This study shows the noise generation mechanisms qualitatively in the case of piles installed with vibratory tools. Future research in describing the interface condition and experimental data to validate the model is needed for a fully quantitative investigation.

Data availability statement

The original contributions presented in the study are included in the article/supplementary material. Further inquiries can be directed to the corresponding author.

Author contributions

TM, AT, and AM contributed to the concept of the study. TM built the model and ran the analysis. AT and AM gave important feedback on the results, and all discussed the interpretation of the results. TM wrote the first draft of the manuscript; AT significantly directed the manuscript's content. All authors contributed to the manuscript revision and read and approved the submitted version.

Funding

This research is funded in the framework of the Grow joint research program by "Topsector Energiesubsidie van het Ministerie van Economische Zaken" under grant number TE-HE117100.

Acknowledgments

This research is associated with the GDP project in the framework of the GROW joint research program. Funding from "Topsector Energiesubsidie van het Ministerie van Economische Zaken" under grant number TE-HE117100 and financial/technical support from the following partners is gratefully acknowledged: Royal Boskalis Westminster N.V., CAPE Holland B.V., Deltares, Delft Offshore Turbine B.V., Delft University of Technology, ECN, EnecoWind B.V., IHC IQIP B.V., SHL Offshore Contractors B.V., Shell Global Solutions International B.V., Sif Netherlands B.V., TNO, and Van Oord OffshoreWind Projects B.V.

Conflict of interest

The authors declare that the research was conducted in the absence of any commercial or financial relationships that could be construed as a potential conflict of interest.

Publisher's note

All claims expressed in this article are solely those of the authors and do not necessarily represent those of their affiliated organizations, or those of the publisher, the editors and the reviewers. Any product that may be evaluated in this article, or claim that may be made by its manufacturer, is not guaranteed or endorsed by the publisher.

References

Benhemma-Le Gall, A., Graham, I. M., Merchant, N. D., and Thompson, P. M. (2021). Broad-scale responses of harbor porpoises to pile-driving and vessel activities during offshore windfarm construction. *Front. Mar. Sci.* 8. doi: 10.3389/fmars.2021.664724

COMSOL (2019). *Comsol multiphysics® v. 5.6* (stockholm, sweden: comsol ab). Available at: www.comsol.com.

Cui, C., Meng, K., Xu, C., Wang, B., and Xin, Y. (2022). Vertical vibration of a floating pile considering the incomplete bonding effect of the pile-soil interface. *Comput. Geotechnics* 150, 104894. doi: 10.1016/j.compgeo.2022.104894

Dahl, P. H., Dall'Osto, D. R., and Farrell, D. M. (2015). The underwater sound field from vibratory pile driving. *J. Acoustical Soc. America* 137, 3544–3554. doi: 10.1121/1.4921288

European Commission (2020). *Communication from the commission to the European parliament, the council, the European economic and social committee and the committee of the regions: An EU strategy to harness the potential of offshore renewable energy for a climate neutral future* (Brussels, Belgium: Tech. rep).

Fernandez-Betelu, O., Graham, I. M., Brookes, K. L., Cheney, B. J., Barton, T. R., and Thompson, P. M. (2021). Far-field effects of impulsive noise on coastal bottlenose dolphins. *Front. Mar. Sci.* 8. doi: 10.3389/fmars.2021.664230

Fricke, M. B., and Rolfes, R. (2015). Towards a complete physically based forecast model for underwater noise related to impact pile driving. *J. Acoustical Soc. America* 137, 1564–1575. doi: 10.1121/1.4908241

Heitmann, K., Mallapur, S., Lippert, T., Ruhnau, M., Lippert, S., and von Estorff, O. (2015). Numerical determination of equivalent damping parameters for a finite element model to predict the underwater noise due to offshore pile driving. *Euronoise* 2015, 605–610.

Holeyman, A. E. (2002). Soil behaviour under vibratory driving. *Proceedings of the International Conference on Vibratory Pile Driving and Deep Soil Compaction, Transvib 2002*. 3–20.

ISO. (2017). *ISO 18405:2017 underwater acoustics — terminology* (Geneva, Switzerland).

Jensen, F. B., Kuperman, W. A., Porter, M. B., and Schmidt, H. (2011). *Computational ocean acoustics. 2nd ed.* (New York, NY: Springer New York). doi: 10.1007/978-1-4419-8678-8

Kirkup, S. (2019). The boundary element method in acoustics: A survey. *Appl. Sci. (Switzerland)* 9, 1642. doi: 10.3390/app9081642

Leissa, A. W. (1973). *Vibration of shells* (Washington, D.C: Tech. rep., Scientific and Technical Information Office National Aeronautics and Space Administration).

Lippert, S., Nijhof, M., Lippert, T., Wilkes, D., Gavrilov, A., Heitmann, K., et al. (2016). COMPILE–a generic benchmark case for predictions of marine pile-driving noise. *IEEE J. Oceanic Eng.* 41, 1061–1071. doi: 10.1109/JOE.2016.2524738

Lippert, T., and von Estorff, O. (2014a). On a hybrid model for the prediction of pile driving noise from offshore wind farms. *Acta Acustica united Acustica* 100, 244–253. doi: 10.3813/AAA.918717

Lippert, T., and von Estorff, O. (2014b). The significance of parameter uncertainties for the prediction of offshore pile driving noise. *J. Acoustical Soc. America* 136, 2463–2471. doi: 10.1121/1.4896458

MacGillivray, A. O. (2013). A model for underwater sound levels generated by marine impact pile driving. *J. Acoustical Soc. America* 134, 4024–4024. doi: 10.1121/1.4830689

Madsen, P., Wahlberg, M., Tougaard, J., Lucke, K., and Tyack, P. (2006). Wind turbine underwater noise and marine mammals: Implications of current knowledge and data needs. *Mar. Ecol. Prog. Ser.* 309, 279–295. doi: 10.3354/meps309279

Markou, A. A., and Kaynia, A. M. (2018). Nonlinear soil-pile interaction for offshore wind turbines. *Wind Energy* 21, 558–574. doi: 10.1002/we.2178

Nogami, T., and Konagai, K. (1987). Dynamic response of vertically loaded nonlinear pile foundations. *J. Geotechnical Eng.* 113, 147–160. doi: 10.1061/(ASCE)0733-9410(1987)113:2(147

Novak, M. (1991). "Piles under dynamic loads," in *Second International Conference on Recent Advances In Geotechnical Earthquake Engineering and Soil Dynamics*, Vol. 2. 2433–2456. Saint Louis, United States.

Peng, Y., Tsouvalas, A., Stampoultzoglou, T., and Metrikine, A. (2021a). A fast computational model for near- and far-field noise prediction due to offshore pile driving. *J. Acoustical Soc. America* (Saint Louis, United States) 149, 1772–1790. doi: 10.1121/10.0003752

Peng, Y., Tsouvalas, A., Stampoultzoglou, T., and Metrikine, A. (2021b). Study of the sound escape with the use of an air bubble curtain in offshore pile driving. *J. Mar. Sci. Eng.* 9, 232. doi: 10.3390/jmse9020232

Reinhall, P. G., and Dahl, P. H. (2011a). An investigation of underwater sound propagation from pile driving. *Tech. Rep*.

Reinhall, P. G., and Dahl, P. H. (2011b). Underwater Mach wave radiation from impact pile driving: Theory and observation. *J. Acoustical Soc. America* 130, 1209–1216. doi: 10.1121/1.3614540

Schecklman, S., Laws, N., Zurk, L. M., and Siderius, M. (2015). A computational method to predict and study underwater noise due to pile driving. *J. Acoustical Soc. America* 138, 258–266. doi: 10.1121/1.4922333

Southall, B. L., Finneran, J. J., Reichmuth, C., Nachtigall, P. E., Ketten, D. R., Bowles, A. E., et al. (2019). Marine mammal noise exposure criteria: Updated scientific recommendations for residual hearing effects. *Aquat. Mammals* 45, 125–232. doi: 10.1578/AM.45.2.2019.125

Tsetas, A., Tsouvalas, A., Gómez, S. S., Pisanò, F., Kementzetzidis, E., Molenkamp, T., et al. (2023a). Gentle driving of piles (GDP) at a sandy site combining axial and torsional vibrations: Part I - installation tests. *Ocean Eng.* 270, 113453. doi: 10.1016/j.oceaneng.2022.113453

Tsetas, A., Tsouvalas, A., and Metrikine, A. V. (2023b). A non-linear three-dimensional pile-soil model for vibratory pile installation in layered media. *Int. J. Solids Structures (Under review)*.

Tsouvalas, A. (2020). Underwater noise emission due to offshore pile installation: A review. *Energies* 13, 3037. doi: 10.3390/en13123037

Tsouvalas, A., and Metrikine, A. V. (2014). A three-dimensional semi-analytical model for the prediction of underwater noise generated by offshore pile driving. *J. Sound Vibrationn* 333, 259–264. doi: 10.1007/978-3-642-40371-2_38

Tsouvalas, A., and Metrikine, A. V. (2016). Structure-borne wave radiation by impact and vibratory piling in offshore installations: From sound prediction to auditory damage. *J. Mar. Sci. Eng.* 4, 44. doi: 10.3390/jmse4030044

Wood, M. A. (2016). *Modelling and prediction of acoustic disturbances from off-shore piling* (Southampton, United Kingdom: Phd thesis, University of Southampton).

Wood, M. A., and Humphrey, V. F. (2013). "Modelling of offshore impact piling acoustics by use of wave equation analysis," in *1st Underwater Acoustics Conference*, Corfu, Greece. 171–178.

Zampolli, M., Nijhof, M. J. J., de Jong, C. A. F., Ainslie, M. A., Jansen, E. H. W., and Quesson, B. A. J. (2013). Validation of finite element computations for the quantitative prediction of underwater noise from impact pile driving. *J. Acoustical Soc. America* 133, 72–81. doi: 10.1121/1.4768886

frontiers | Frontiers in Marine Science

TYPE Original Research
PUBLISHED 29 March 2023
DOI 10.3389/fmars.2023.1146095

Check for updates

OPEN ACCESS

EDITED BY
Apostolos Tsouvalas,
Delft University of Technology, Netherlands

REVIEWED BY
Vanesa Magar,
Center for Scientific Research and Higher Education in Ensenada (CICESE), Mexico
Yaxi Peng,
Delft University of Technology, Netherlands

*CORRESPONDENCE
Peter H. Dahl
dahl97@uw.edu

SPECIALTY SECTION
This article was submitted to Ocean Observation, a section of the journal Frontiers in Marine Science

RECEIVED 17 January 2023
ACCEPTED 13 March 2023
PUBLISHED 29 March 2023

CITATION
Dahl PH, MacGillivray A and Racca R (2023) Vector acoustic properties of underwater noise from impact pile driving measured within the water column. *Front. Mar. Sci.* 10:1146095. doi: 10.3389/fmars.2023.1146095

Vector acoustic properties of underwater noise from impact pile driving measured within the water column

Peter H. Dahl[1]*, Alexander MacGillivray[2] and Roberto Racca[2]

[1]Applied Physics Laboratory, University of Washington, Seattle, WA, United States, [2]JASCO Applied Sciences, Victoria, BC, Canada

Vector acoustic properties of the underwater noise originating from impact pile driving on steel piles has been studied, including the identification of features of Mach wave radiation associated with the radial expansion of the pile upon hammer impact. The data originate from a 2005 study conducted in Puget Sound in the U.S. state of Washington, and were recorded on a four-channel hydrophone system mounted on a tetrahedral frame. The frame system measured the gradient of acoustic pressure in three dimensions (hydrophone separation 0.5 m) from which estimates of kinematic quantities, such as acoustic velocity and acceleration exposure spectral density, were derived. With frame at a depth of 5 m in waters 10 m deep, the data provide an important look at vector acoustic properties from impact pile driving within the water column. Basic features of the Mach wave are observed in both dynamic (pressure) and kinematic measurements, most notably the delay time T leading to spectral peaks separated in frequency by $1/T \sim$ 106 Hz, where T equals the travel time of the pile radial deformation over twice the length of the pile. For the two piles studied at range 10 and 16 m, the strike-averaged sound exposure level (SEL) was $\sim$ 177 dB re 1μPa^2-s and the acceleration exposure level (AEL) was 122-123 dB re $\mu m^2/s^4$ s. The study demonstrates an approximate equivalence of observations based on dynamic and kinematic components of the underwater acoustic field from impact pile driving measured within the water column.

KEYWORDS
impact pile driving, underwater sound, Mach wave, acoustic pressure, acoustic velocity

1 Introduction

Impact (also referred to as percussive) pile driving is a marine construction method for installing steel piles forming the basis of offshore wind farm platforms, or piles for the foundation of shoreline piers and ferry docks in inland waters. Over the past decade, considerable knowledge on properties of the underwater acoustic field associated with impact pile driving has emerged (Reinhall and Dahl, 2011; Dahl and Reinhall, 2013;

Tsouvalas and Metrikine, 2013; Zampolli et al., 2013; Tsouvalas, 2020). Much of this research has been motivated by the effects of the acoustic field on marine life, e.g., (Halvorsen et al., 2012).

The majority of studies have focused on the dynamic properties of the underwater sound, as governed by the acoustic pressure field. In contrast, this study presents an analysis of both dynamic and kinematic properties of the underwater sound field from impact pile driving, the latter governed by the acoustic velocity field (or acoustic acceleration and displacement fields); hence the term *vector acoustic* will be used in this paper. The two forms are, of course, linked in a manner fundamental to the mechanical wave nature of sound.

The data originate from a 2005 study conducted at a ferry dock construction site on Bainbridge Island, Puget Sound in the U.S. state of Washington. Of particular interest to these data is that the measurements were made at a depth of 5 m, in waters 10 m deep. There exists few vector acoustic measurements from impact pile driving similar to these made within the water column. One exception is a report[1] that summarizes measurements from off-shore driving involving a geophone deployed on the seabed along with a tetrahedral array of hydrophones deployed 1 m above the seabed from which the acoustic velocity field is estimated through finite difference methods. Although not associated with pile driving, Dahl and Dall'Osto (2020) measured the vector acoustic field of similarly broad-band waveforms originating from underwater explosive sources, using a measurement system deployed on the seafloor with the accelerometer-based sensor located within a neutrally buoyant sphere positioned 1.25 m above the seafloor.

The paper is arranged as follows: Section (2) outlines the basic framework of the Mach wave, a hallmark of the underwater sound field from impact pile driving particularly for observations made at close range (defined as ratio of measurement range to water depth less than about 3) as in this case. Section (3) provides a broad overview of the original 2005 measurement series along with the finite difference approximation that is essential to these data. A justification for the frequency range used in this 2022 analysis is also provided here.

In Section (4) the results of the new analysis are conveyed in three sections: overview of time series, analysis of arrival angles, and evaluation and comparison of pressure-based and velocity-based spectral densities. Section (5) concludes with a summary and discussion.

2 The Mach wave feature of impact pile driving

The Mach wave feature associated with impact pile driving of hollow steel piles has been demonstrated both theoretically and experimentally (Reinhall and Dahl, 2011; Dahl and Reinhall, 2013; Zampolli et al., 2013; MacGillivray, 2018) and, as will be shown, is a feature of the observations in this study. Briefly, the hammer impact on the pile produces a deformation on the surface of the pile (Figure 1) as a consequence of the Poisson effect. This deformation acts as a source of sound traveling initially downward on the pile surface. The speed of travel along the pile surface of this source, c_s, is approximately equal to the longitudinal wave speed of the steel pile material, or about 5000 m/s. As a consequence, the ensuing acoustic field will exhibit a quasi-planar wave front characterized by grazing angle $\theta_m = \sin^{1} \frac{c_w}{c_s}$ where c_w is water sound speed.

The deformation or radial expansion continues traveling to the end of the pile where it reflects, and now acts as a sound source traveling upward on the pile surface. Upon reaching the top of the pile, a further reflection generates a second downward traveling source. This downward source is in effect approximately T s after the first, where T is twice the travel time of the deformation over the length of the pile. Although this is an idealized description, we show subsequently that key features of the Mach wave in terms of θ_m and time delay T are observable.

3 Overview of measurement geometry and conditions

The measurements were made at the Washington State Ferries Eagle Harbor maintenance facility, located on Bainbridge Island (Puget Sound) in Washington State on October 31, 2005, to assess the effectiveness of a bubble curtain attenuation protocol for potential use in impact pile driving at ferry docks and other marine construction sites within Puget Sound. Further details on the study are summarized in the report by MacGillivray and Racca (2005), which determined that the attenuation protocol produced a reduction of approximately 10 dB in both acoustic pressure and velocity fields when mitigation was applied.

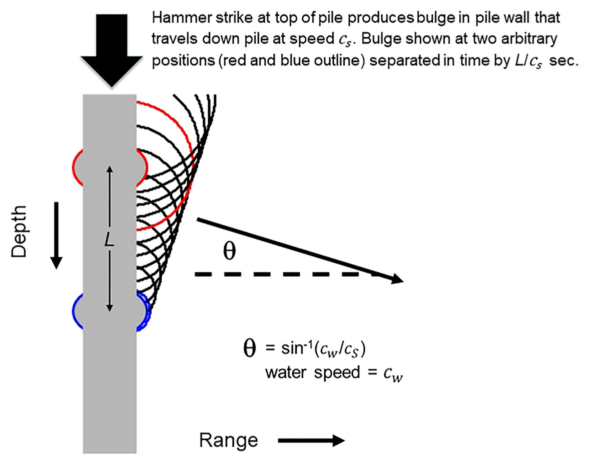

FIGURE 1
Bulge in the pile wall (red outline) as result of impact hammer strike (symbolized by large arrow) and subsequent compression of pile material. The bulge, which acts as a source of sound, travels down the pile at speed c_s and is shown again having traveled a distance L (blue outline). Wave fronts from the earlier emission (red) and later emission (blue) are shown with all prior emissions (black); these adding to form a quasi-planar wave front characterized by angle θ_m. Modified from Dahl et al. (2015) with permission of the Acoustical Society of America, Copyright 2015, Acoustical Society of America.

1 https://www.boem.gov/environment/underwater-acoustic-monitoring-data-analyses-block-island-wind-farm-rhode-island

The 2005 study was based on measurements made from 10 piles (Figure 2), all piles being in place during the measurements, having been pre-inserted and extending approximately 5 m above the water line (the stated water depth of 10 m is assumed to apply to the entire area in Figure 2). The piles were typical steel piles frequently used in Puget Sound marine construction, of length ~ 23.5 m, outer diameter 0.762 m, and wall thickness 0.019 m. The 2005 acoustic measurements covered the phase of impact pile driving used to drive the piles into the final ~ 1.5 m of seabed substrate using a Delmag 62 single-action diesel impact hammer with a 14,600 lbs (6620 kg) hammer piston. This new study is limited to the two piles at range 10 m (T8) and 16 m (T5) during which the bubble attenuation protocol was not applied, as analyzing the effects of bubble mitigation is beyond the scope of this work.

It is evident that the measurement geometry for piles T5 and T8 likely admitted multiple reflection and scattering from other piles and dock structures; the geometry is nevertheless representative of the kind of marine construction zone where often environmental monitoring must be undertaken. An additional complexity applies to pile T8 insofar as the bubble curtain apparatus surrounding the pile, though not operating, was in place for this measurement. The apparatus consisted of a 1 in. thick cylindrical PVC sleeve, 44 ft. long and 47 in. outside diameter, into which air was injected through two internally mounted aerating tubes.

Puget Sound archival shallow-water data for this time of year places water temperature[2] and salinity at ~ 10° C and 28.5 ppt [3], respectively, from which sea water sound speed c_w is estimated to be 1482 m/s. A sea water density ρ_w of 1027 kg/ m^3 will be assumed.

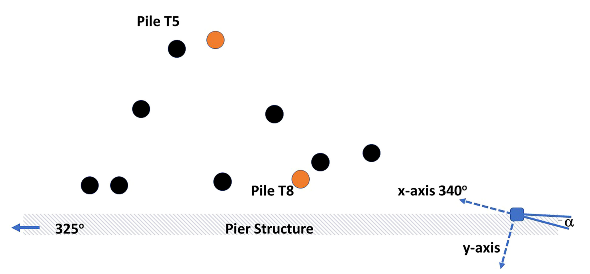

FIGURE 2
Location of the two piles T5 and T8 (orange circles) with respect to the acoustic measurement system (blue square) and the pier structure. For length scale reference the range from T8 to measurement system is 10 m. Bearing of T5 is 355° and that of T8 is 335°. Other pile structures (black circles) shown in approximate relative position. The x-axis of the measurement system is pointing the direction 340°, z- axis (not shown) points upward. The angle α as shown is defined as positive with respect to the x-axis.

2 https://www.seatemperature.org/north-america/united-states/bainbridge-island-october.htm

3 www.eopugetsound.org

3.1 Vector acoustic measurements

The acoustic pressure and velocity was measured by the pressure gradient method using a custom built, multi-component hydroacoustic sensor. The pressure gradient sensor was composed of a tetrahedral frame (Figure 3) supporting four Reson TC4043 hydrophones of sensitivity -201 dB re V/μPa, along with an attitude/depth sensor. The hydrophones were cross-calibrated before and after the field measurements using a swept reference signal (from 100 Hz to 2 kHz) from an underwater loudspeaker. The four hydrophone channels were coherently sampled at individual channel sampling frequency of 25,000 Hz.

The tetrahedral frame system was free to move but stable for the measurements from T5 and T8 (taken within an hour), for which the important orientation of the horizontal x-axis was determined by the attitude sensor to be ~ 340°, and thus y-axis was ~ 250° (Figure 2), and the x, y plane was at a depth 5 m.

To obtain kinematic quantities (acoustic acceleration and velocity) from this system, the finite difference approximation is used to estimate the acoustic pressure gradient. For example, the x -component of acoustic acceleration a_x is derived from the x -component of the gradient as result of Euler's equation,

$$a_x = -\frac{1}{\rho_w}\frac{\partial p}{\partial x}, \tag{1}$$

where ρ_w is sea water density.

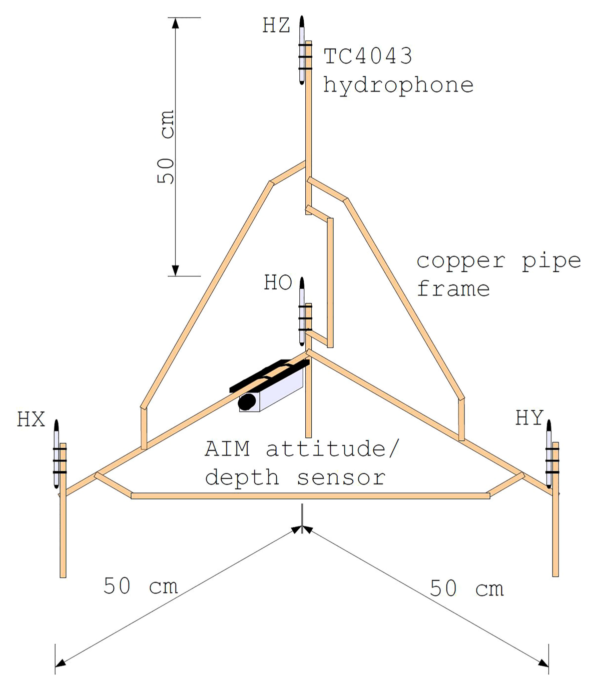

FIGURE 3
Schematic diagram of the pressure gradient sensor shown in isometric projection. Four Reson TC4043 hydrophones are located at the positions indicated HO (origin) HX(x-axis) HY(y-axis) and HZ(z-axis). The JASCO AIM attitude/depth sensor is oriented in the x-direction. The axial hydrophones HX, HY and HZ are all located 50 cm from the origin hydrophone HO.

The finite difference approximation [5] yields an estimate of the acoustic pressure gradient through subtraction of pressure signals between the closely spaced hydrophones in Figure 3 labeled HX, HY, HZ, all separated from hydrophone $H0$ by $\Delta = 0.5$m. Thus an approximation to the acoustic pressure gradient in the x-direction, and hence a_x, is obtained from the difference of pressure signals $H0$ and HX,

$$a_x \approx -\frac{1}{\rho_w}\frac{H0 - HX}{\Delta} \tag{2}$$

where it is important that these signals are expressed in MKS units of Pa. The analogous operation yields estimates of the y- and z-components of acoustic acceleration a_y and a_z, respectively, and corresponding estimates of acoustic velocity $v_{x,y,z}$ are obtained through time integration of $a_{x,y,z}$. For acoustic pressure p the average (finite sum) of the four hydrophones is used, where

$$p = (H0 + HX + HY + HZ)/4. \tag{3}$$

All quantities in Eqs. (1-3) are assumed to be a function of time t.

Systematic errors arise from applying the finite difference (and sum) approximation to obtain both kinematic and dynamic (pressure) fields, stemming primarily from the length scale of the sensor separation Δ with respect to the acoustic wavelength λ Fahy (1995); Jacobsen and Juhl (2013), with both described by the parameter $k\Delta$, where k is the acoustic wavenumber.

Importantly, the normalized error in pressure p ultimately becomes greater than that for velocity $v_{x,y,z}$, with direction for both quantities being such that approximate values (finite difference and finite sum) are less than true counterparts. This translates to estimates of velocity-based kinetic energy being greater than pressure-based potential energy for either frequency ranges or separations Δ that put $k\Delta$ above an acceptable value.

Small errors are also associated with the fact that the geometrical center of this 3D probe, where acoustic pressure p is to be identified, is not co-located with the velocity components $v_{x,y,z}$. Nevertheless, simple formulas in Fahy (1995) for 1D probes give approximate guidance. To mitigate this error we limit the upper frequency range of the analysis to 710 Hz, representing a normalized separation of $k\Delta < 1.5$. At the upper end of this frequency range the kinetic energy level is expected to be approximately 1.5 dB greater than potential energy, for otherwise equal energies. This high-frequency limit is somewhat more conservative than that imposed in the original 2005 study. However, there remain additional tradeoffs that are specifically identified in Section 4.3. Additionally, for very low frequencies there can be errors in realizing the proper phase relation between pressure and velocity (Thompson and Tree, 1981) particularly if the measurements are from sources more complex than a single point source or monopole. We thus limit the low frequency range to $k\Delta >$ 0.1, which translates to a low-frequency limit of $\sim$ 50 Hz. Imposing this limit does not produce further tradeoffs.

4 Analysis and results

4.1 Basic overview of time series

A summary of the 10-m (pile T8) and 16-m (pile T5) range measurements is presented in Figures 4 and 5. The pile strikes occur almost precisely every 1 s, and a short time series (0.075 s) $p_n(t)$ representing the n^{th} strike in the series of N is extracted by thresholding the pressure data to establish the onset time of a single strike arrival above background. The same onset time is applied to the velocity data for the corresponding time series $v_{(x,y,z)_n}(t)$ to maintain coherency between pressure and velocity channels. For pile T8 N = 13 strikes, and for pile T5 N = 24 strikes.

The coherent average of pressure, $\bar{p}(t)$, of the extracted time series over the N-strikes is

$$\bar{p}(t) = \frac{1}{N}\sum_{n=1}^{N} p_n(t) \tag{4}$$

(black curves, Figures 4A and 5A). The same coherent average over the N strikes is carried out for the three components of acoustic velocity yielding $\bar{v}_{x,y,z}(t)$ (black curves, Figures 4B–D and 5B–D). Individual strike time series (i.e., $p_n(t)$ and $v_{(x,y,z)_n}(t)$) are displayed by light gray lines and give a sense of the variation of strike arrival structure that tends to increase with time, presumably owing to the multiple scattering and reflection processes that are expected in this busy marine construction environment with nearby pier support structures, standing piles and floating construction barges.

The first arrival of approximately 4 ms displays less variation and is identified within a box (Figures 4A, 5A). This arrival is used subsequently for an analysis of the arrival angle, expected to be negative relative to horizontal and associated with the Mach wave. For pile T8 (Figure 4A) a second, 4 ms box is placed $T \sim 9.4$ ms after the first arrival, which we postulate is associated with a second Mach wave characterized by the same arrival angle. The estimate of T corresponds to the round-trip travel time of the deformation/source given a pile length of 23.5 m and speed $c_s \sim 5000$ m/s. Such a second arrival for pile T5 is more difficult to identify owing to the longer range (16 m) although the delay time $T \sim 9.4$ ms is still manifested in the spectrum as is shown subsequently. That the first arrival for pile T5 is not of the highest amplitude is also noteworthy. The influence of the Mach wave is lessened [10] when the observation depth is less than $R\tan\theta_m$, where R is horizontal range from the pile source. Taking θ_m as approximately 17° puts the measurement depth of 5 m on the edge of this bound.

For both piles the x-axis of the tetrahedral frame system was oriented most closely with the primary propagation path between pile source and receiver. It is thus of interest to plot acoustic velocity $\bar{v}_x(t)$ scaled by $\rho_w c_w$ (magenta line, Figures 5A and 6A). Note that the sign of $\bar{v}_x(t)$ is flipped in this display to facilitate a comparison in overlap between scaled velocity and pressure time series, but otherwise does not change the fact that the pressure and velocity are closely locked in phase and the acoustic field is primarily an

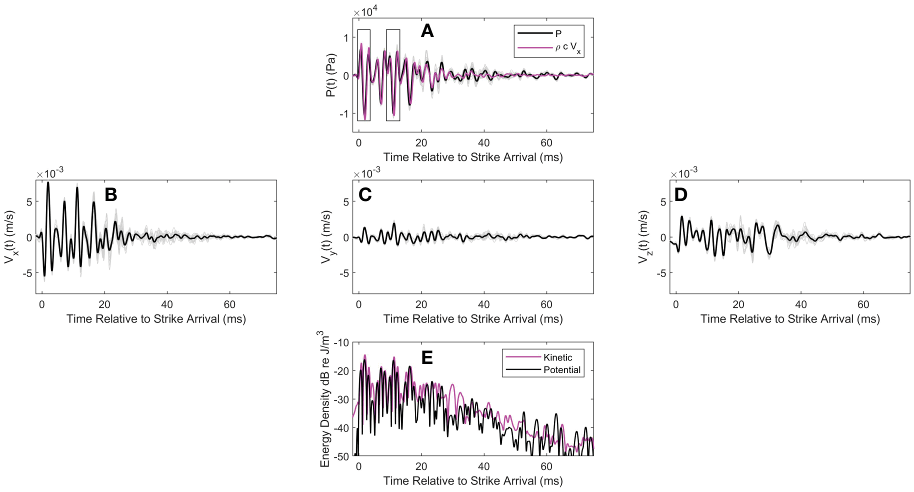

FIGURE 4
(A) coherent average of pressure over N strikes $\bar{p}(t)$ (black line) and individual strike time series $p_n(t)$ (gray lines). Measurements are from pile T8 at range 10 m. Magenta line shows coherent average of the x -component of acoustic velocity $\bar{v}_x(t)$ scaled by $\rho_w c_w$. For this display the sign of $\bar{v}_x(t)$ is flipped. Data shown within the two boxes (duration 4-ms) are used in subsequent analysis. Time is relative to the pile strike arrival. **(B)** Coherent average of $\bar{v}_x(t)$ along with individual strike time series $v_{x_n}(t)$ (gray lines); **(C, D)** provide similar display of $\bar{v}_y(t)$ and $\bar{v}_z(t)$, respectively, together with the individual strike time series (gray lines). **(E)** Time varying potential (black line) and kinetic (magenta line) energy density averaged over N strikes.

active one. Looking ahead, the original sign of acoustic velocity will be important to preserve the correct direction of acoustic vector intensity.

A final view is that of the ensemble average over N strikes of potential $E_p(t)$ and kinetic $E_k(t)$ energy densities, where

$$E_p(t) = 0.5\frac{1}{N}\sum_{n=1}^{N}\frac{p_n^2(t)}{\rho_w c_w^2} \quad (5)$$

and

$$E_k(t) = 0.5\frac{1}{N}\sum_{n=1}^{N}\rho_w(v_{x_n}^2(t) + v_{y_n}^2(t) + v_{z_n}^2(t))\,. \quad (6)$$

The time varying potential (black line) and kinetic (magenta line) energy densities (Figures 4E, 5E) are expressed in dB re J/m^3, where it is evident that the majority of the energy arrives within the first 20 ms. For pile T8 (Figure 4E) a time-average of $E_k(t)$ and $E_p(t)$

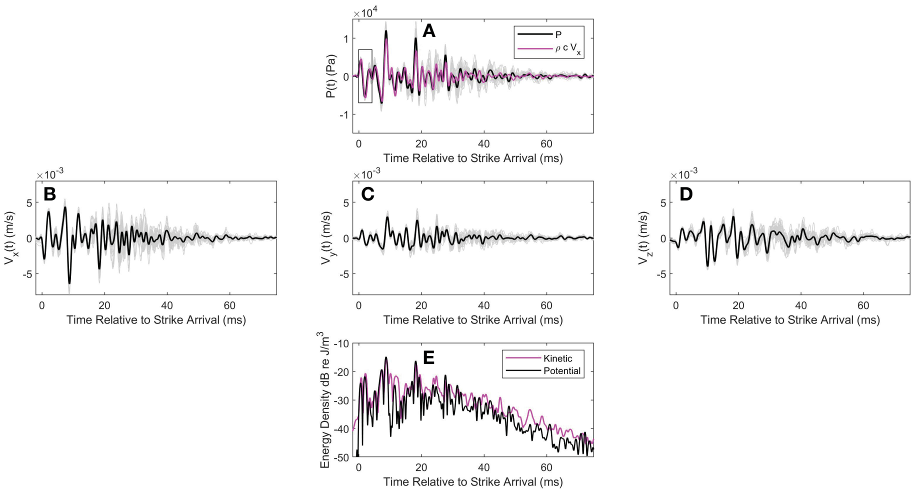

FIGURE 5
(A) coherent average of pressure over N strikes $\bar{p}(t)$ (black line) and individual strike time series $p_n(t)$ (gray lines). Measurements are from pile T5 at range 16 m. Magenta line shows coherent average of the x-component of acoustic velocity $\bar{v}_x(t)$ scaled by $\rho_w c_w$. For this display the sign of $\bar{v}_x(t)$ is flipped. Data shown within the box (duration 4-ms) are used in subsequent analysis. **(B)** Coherent average of $\bar{v}_x(t)$ along with individual strike time series $v_{x_n}(t)$ (gray lines); **(C, D)** provide similar display of $\bar{v}_y(t)$ and $\bar{v}_z(t)$, respectively, together with the individual strike time series (gray lines). **(E)** Time varying potential (black line) and kinetic (magenta line) energy density averaged over N strikes.

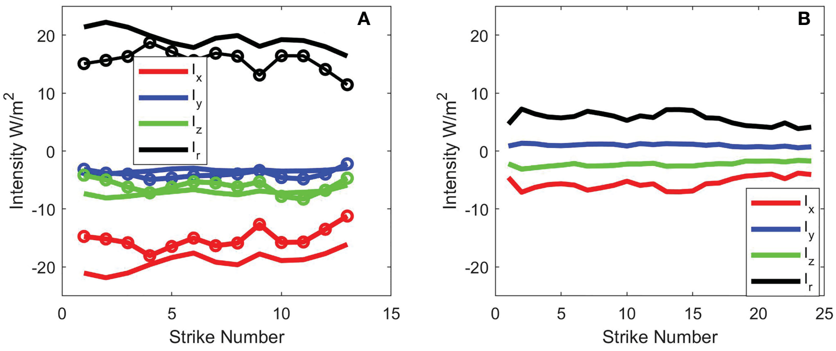

FIGURE 6
(A) Vector intensity Cartesian components $I_{(x,y,z)_n}$ and I_{r_n} versus strike number n derived from two selected arrival segments of the data from pile T8 at a range 10 m (see Figure 4A). First arrival identified by solid lines, and second (delayed by 9.4 ms) identified with same color code but with added symbols. **(B)** Same results corresponding to pile T5 range at 16 m (see Figure 5A), where only the first arrival is studied.

over the first 20-ms equals – 22.2 and – 23.6 dB, respectively, and for pile T5 (Figure 5E) this same time-average equals – 23.3 and – 24.2 dB, respectively. In each case the kinetic exceeds the potential counterpart by 1 to 1.5 dB, which is in part consistent with chosen upper bound for $k\Delta$ in applying finite difference approximation (Section 3.1). The notable excess in $E_k(t)$ over $E_p(t)$ near relative time 30 ms (Figure 4E) is very likely due to scattering from structures in close proximity of the receiving system, forming a near-field contribution. However, for both piles the average energy density in the remaining period from relative time 20 to 75 ms is approximately 10 dB less than that during the first 20 ms.

4.2 Vector intensity and arrival angles

The initial 4 ms of data denoted by the box (Figures 4A, 5A) represents a short-duration wavelet with initial positive-going pressure amplitude, and approximate center frequency $\sim$ 500 Hz. Let us denote a portion of the $p_n(t)$ and $v_{(x,y,z)_n}(t)$ time series over this same duration as $p_n(t_s)$ and $v_{(x,y,z)_n}(t_s)$, respectively. The active intensity in the x-direction (as defined by the reference frame Figure 2) for the n^{th} strike, I_{x_n}, corresponding to this segment of the data equals the time average over duration t_s

$$I_{x_n} = \langle p_n(t_s) v_{x_n}(t_s) \rangle . \tag{7}$$

The same operation involving $v_{y_n}(t_s)$ and $v_{z_n}(t_s)$ yields the active intensity in the y and z-directions, or I_{y_n} and I_{z_n}, respectively. For pile T8 this operation is also repeated on the second portion of data identified by the box delayed by 9.4 ms (Figure 4A).

The intensities $I_{(x,y,z)_n}$ estimated in this manner (Figure 6) tend to confirm the basic measurement geometry and are also approximately consistent with the Mach wave feature of impact pile driving. For pile T8 (Figure 6A), the sequence of I_{x_n} and I_{y_n} estimates for the first arrival are both negative, with the magnitude of I_{x_n} being greatest; a result anticipated by inspecting the line-of-sight between T8 and the receiving system (Figure 2). Taking I_x and I_y as the average of the N-strike ensemble, the ratio $I_y/I_x \sim 0.18$ defines an angle $\alpha \sim 10^\circ$ (Figure 2) and we infer the bearing of pile T8 is $\sim$ 330°, with the direction of the active intensity vector in the horizontal plane being towards $\sim$150°. For the second arrival delayed by 9.4 ms, (Figure 6A, same color code with added symbols) the ratio I_y/I_x is slightly higher at ~ 0.26 indicating the T8 bearing is $\sim$ 325°, but there is also considerably more variation. For pile T5 (Figure 6B), the sequence of I_{y_n} estimates for the first arrival is positive, and that for I_{x_n} is negative, with ratio $I_y/I_x \sim -0.18$ putting angle $\alpha \sim -10^\circ$. This is also consistent with the line-of-sight between pile T5 and the receiving system, and we infer the bearing of T5 is $\sim$350° with direction of the active intensity vector in the horizontal plane being towards $\sim$170°.

For pile T8 (Figure 6A) I_{z_n} is negative for both the first and second arrival, which is also the case for the first arrival with pile T5 (Figure 6B), which we interpret as the correct sense of a downward propagating Mach wave along the lines suggested by Figure 1. Defining a mean horizontal intensity I_r as $\sqrt{I_x^2 + I_y^2}$ the ratio I_z/I_r is similar, ~ -0.38, for all arrivals (first and second in Figure 5A and first in Figure 5B). This translates to an angle $\sim$ 21° below the horizontal, versus a theoretically expected angle θ_m given by $\sin^{-1}\frac{c_w}{c_s}$ or $\sim 17^\circ$ characterizing the arrival of the quasi-planar Mach wave (Figure 1). The discrepancy may be attributed to uncertainty in the vertical alignment of the z-axis of the measurements, which is not resolvable retrospectively from this 17-year old data set. Notably though, the observed angle is the same for the two ranges of 10 and 16 m.

4.3 Exposure levels and spectral densities

In this section the time series (Figures 4 and 5) are assessed in terms of both dynamic (pressure-based) and kinematic (velocity-based) measurements. The single-strike sound exposure level (SEL) is defined as the time integral of $|p_n(t)|^2$ expressed in dB re 1μ Pa^2-s, for which the time integral for these data is from relative time 0 to 75 ms. For both piles the strike-averaged SEL equals 176.8 dB, based on the more restrictive band-pass filtering (50-710 Hz) mentioned previously. Removing this filtering increases the SEL by only $\sim$ 0.5 dB, with 90% of the energy carried by frequencies between 50 and 710 Hz, changing to 95% with upper bound at 1000 Hz, and to 98% with upper bound at 2000 Hz.

Two spectral densities are next defined, sharing the common property that the integral of the (one-sided) spectral density over frequency equals the time integral of the squared-magnitude of corresponding time-domain quantity. Define first a squared magnitude spectrum $|P_n(f)|^2$ corresponding to each $p_n(t)$ (expressed for this purpose in μPa), computed *via* FFT and normalized so that the integral of $|P_n(f)|^2$ equals the single strike SEL in linear units, where f is frequency ($\Delta f = 14$ Hz). The SEL spectral density $S_p(f)$ is an average spectrum defined as

$$S_p(f) = \frac{1}{N}\sum_{n=1}^{N} |P_n(f)|^2 . \tag{8}$$

The SEL spectral densities for the two piles (Figures 7A, 8A) each show peaks separated notionally by $1/T = 106$ Hz (within the available spectral resolution), where $T \sim 9.4$ ms represents the travel time of the deformation over twice the length of the pile. Integrating $S_p(f)$ over frequency recovers the strike-averaged SEL values listed above upon conversion to dB.

Somewhat analogous to $S_p(f)$ (with exception that MKS units are maintained) let us define $S_k(f)$ based on the velocity data, which is composed of three additive components $S_{k_x}(f)$, $S_{k_y}(f)$ and $S_{k_z}(f)$. A one-sided magnitude spectrum $|V_{xn}(f)|^2$ is first computed corresponding to $v_{x_n}(t)$ and normalized so that the frequency integral of $|V_{xn}(f)|^2$ equals the time integral of $|v_{x_n}(t)|^2|$ of dimension $(\text{m/s})^2$-s. An average spectrum based on N strikes associated with the $x-$ component $S_{k_x}(f)$ is defined as

$$S_{k_x}(f) = \frac{1}{N}\sum_{n=1}^{N} |V_{xn}(f)|^2 . \tag{9}$$

The analogous computation is performed for the y- and z-components producing $S_{k_y}(f)$ and $S_{k_z}(f)$, respectively.

The two spectral forms based on pressure and velocity data are next converted to acoustic acceleration exposure spectral density expressed in units of m^2/s^4 s/Hz, defining this spectral density derived from the kinematic data as $A_k(f)$ and that from pressure or dynamic data as $A_p(f)$. In terms of the kinematic data let $A_{k_x}(f)$ be the component of spectral density covering the exposure associated with the x-direction, where

$$A_{k_x}(f) = S_{k_x}(f)(2\pi f)^2 . \tag{10}$$

The analogous conversion is made for the y- and z-components, $A_{k_y}(f)$ and $A_{k_z}(f)$, respectively, with three components summed to yield an estimate of $A_k(f)$. For the spectrum $A_p(f)$ using the pressure data, the conversion is

$$A_p(f) = 10^{-12}\frac{S_p(f)}{(\rho_w c_w)^2}(2\pi f)^2 \tag{11}$$

where 10^{-12} is used to restore $S_p(f)$ to units of Pa^2/Hz.

The two versions of these spectra (Figures 7B, 8B) again show peaks separated notionally by $1/T$ Hz. Note that the spectra are plotted with 120 dB offset to correspond to units of dB re $\mu m^2/s^4$ s/Hz, representing usage that is consistent with published studies on the effects of underwater noise on marine life, e.g., as in the work by Davidsen et al. (2019) on the effects of sound exposure from a seismic airgun. Analogous to SEL, the frequency integral of $A_k(f)$ yields an acceleration exposure level (AEL) in dB re $\mu m^2/s^4$s. The strike-averaged AEL is 122.9 dB for pile T8 at range 10 m and is 121.9 dB for pile T5 at range 16 m. Upon using the corresponding pressure-derived $A_p(f)$ the AEL reduces by ~ 1.5 dB for pile T8 and ~ 1 dB for pile T5.

Although agreement between the two AEL measures is satisfactory to within any reasonable calibration uncertainty, it is important in this case to consider the effect of limiting the upper frequency range to 710 Hz, necessary to realize the $k\Delta < 1.5$ bound. The factor $(2\pi f^2)$ in Eqs. (10) and (11) will amplify higher frequencies, which increases AEL if higher frequencies are included in the frequency integral. The effect can be assessed with the pressure data and $A_p(f)$. For example, using the same 95% energy criterion, AEL increases by 1 dB upon inclusion of frequencies up to 1000 Hz, and by 2 dB using 98% energy criterion involving frequencies up to 2000 Hz.

5 Discussion and summary

Vector acoustic properties of the underwater noise measured within the water column and originating from impact pile driving on steel piles has been studied, including the identification of features of Mach wave radiation associated with the radial

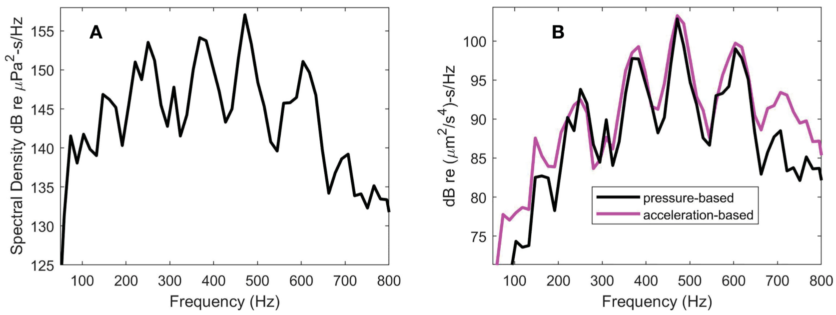

FIGURE 7
Spectral densities for pile T8, range 10 m **(A)** Sound exposure level (SEL) spectral density $S_p(f)$ **(B)** Acceleration exposure spectral density as derived with pressure data $A_p(f)$ (black line) and velocity data $A_k(f)$ (magenta line).

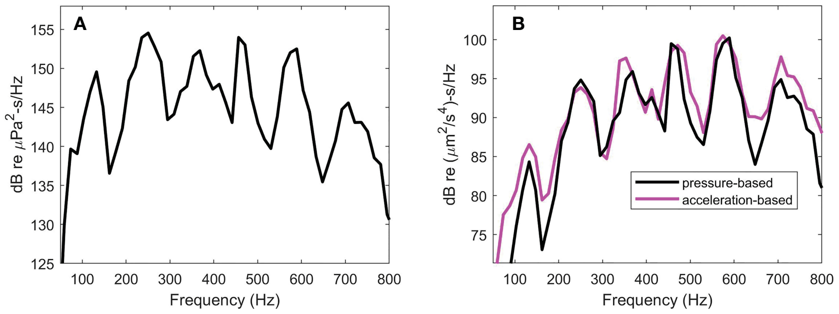

FIGURE 8
Spectral densities for pile T5, range 16 m **(A)** Sound exposure level (SEL) spectral density $S_p(f)$ **(B)** Acceleration exposure spectral density as derived with pressure data $A_p(f)$ (black line) and velocity data $A_k(f)$ (magenta line).

expansion of the pile upon hammer impact. The data were recorded on a four-channel hydrophone system mounted on a tetrahedral frame at a depth of 5 m in waters 10 m deep. The system measured acoustic pressure and, using the finite difference approximation, measured the gradient of acoustic pressure in three dimensions (hydrophone separation Δ =0.5 m) from which estimates of kinematic quantities, such as acoustic velocity and acceleration exposure spectral density, were derived.

The 2005 study from which these data originate was conducted at a marine construction site in Puget Sound with the primary purpose to assess effectiveness of a bubble curtain attenuation protocol. The two piles, T8 at range 10 m and T5 at range 16 m (Figure 2), selected for this study were not subjected to the bubble-mediated mitigation; however, a bubble curtain apparatus consisting of a cylindrical PVC sleeve (though not operational) still surrounded the closer T8 pile. It is likely for this reason that the strike-averaged SEL measured at the closer T8 pile was approximately identical to that estimated at the more distant T5 pile, both $\sim$ 177 dB re 1μ Pa^2-s.

To mitigate errors associated with use of the finite difference approximation, the data were band-passed filtered between 50 and 710 Hz, equivalent to placement of $k\Delta$ between 0.1 and 1.5, where k is acoustic wavenumber. The upper bound ka was chosen to limit to 1.5 dB the discrepancy between otherwise equivalent dynamic (pressure based) and kinematic quantities. In terms of the pressure-only data, removal of such filtering increased SEL by approximately 0.5 dB.

For each pile the initial 4 ms segment of pressure and velocity waveform data (boxes starting at relative time 0, Figures 4A, 5A) was selected for more detailed analysis. Evidence of the fidelity of the estimated 3-component acoustic velocity was shown by the accuracy with which the pile bearing with respect to the receiver location (Figure 2), was recovered from the ratio of active intensities in the x and y directions. For pile T8 a second data segment, delayed by T = 9.4 ms, was selected from which the approximate bearing was also reliably recovered. The 9.4 ms delay equals the travel time of the deformation (radial expansion) over twice the length of the pile.

The time varying potential $E_p(t)$ and kinetic $E_k(t)$ energy densities over the entire 75 ms of waveform time series data (Figures 4E, 5E) was also studied with results showing that the majority of the energy arrives within the first 20 ms. Time-averages of $E_k(t)$ over the first 20-ms for piles T8 range 10 m and T5 range 16 m yielded values – 22.2 and – 23.3 dB re J/m^3, respectively, with the corresponding time averages of $E_p(t)$ being $\sim$ 1 to 1.5 dB less. These differences are reasonably consistent with the expected energy difference (1.5 dB) based on the chosen upper bound for $k\Delta$ used in the finite difference approximation. Some degree of excess of $E_k(t)$ over $E_p(t)$ was observed particularly in later portions of the time series (beyond 20 ms) that is likely the result of near field effects due to secondary (scattering) sources such as other piles and dock structures in close proximity to the receiving system, although the average kinetic energy density over the remainder of the time series from 20 to 75 ms is approximately 10 dB less than that computed over the initial 20 ms.

Using the same selection of waveform data (boxes Figures 4A, 5A) the ratio of active vertical (in the z direction) to horizontal intensity yielded a notionally correct angle, directed downward with respect to horizontal and indicative of the expected quasi-planar Mach wave produced in impact pile driving. The accuracy of this angle is limited owing to instrumental uncertainty in the vertical orientation of the measurement frame; importantly, however, the determined angle was approximately the same for the two ranges, which is consistent with an expected property of the Mach wave. It is also worth noting that, unlike the case for pile T8 at range 10 m, the initial 4 ms of data for pile T5 at range 16 m did not have the highest amplitude relative to the remainder of the time series. A plausible reason is that amplitude of the downward Mach cone diminishes for depths less than $R \tan\,\theta_m$ where R is range (see (Reinhall and Dahl (2011)). The 5-m measurement depth begins to satisfy this criterion at range 16 m. More definitive interpretation of the time series data in Figures 4 and 5 beyond these basic observations is made difficult by the likely presence of multiple reflection and scattering of the acoustic field from other piles and dock structures, which is not uncommon for the type of busy marine construction zone where often environmental acoustic monitoring must be undertaken.

Of greater interest, however, are two variations of spectral densities (Figures 7 and 8) each based on the full extent of waveform data displayed in Figures 4 and 5. Evident in each spectra are peaks separated by ~ 106 Hz, or $1/T$, representing a clearly observable manifestation of the Mach wave embodied in the spectra. Furthermore the active, propagating nature of the acoustic field, such as evidenced by the $\rho_w c_w$ scaling in Figures 4A,5A, motivated comparisons between the pressure-based and velocity-based spectra.

From a comparison of acceleration exposure spectral density (Figures 7B, 8B), it is evident that the two forms $A_p(f)$ based on pressure, and $A_k(f)$ based on the three components of acoustic velocity, are in notional agreement. Computing from these, the acceleration exposure level (AEL) in dB re $\mu \quad m^2 \quad /s^4$-s yielded a strike-averaged AEL of 122.9 dB for pile T8 at range 10 m and 121.9 dB for pile T5 at range 16 m; the corresponding pressure-derived AEL estimates were 1 to 1.5 dB lower, and also consistent with the chosen upper bound for $k\Delta$. However, AEL does increase upon including higher frequencies, and assessing this effect using the pressure data showed that using the same 95% energy criterion, AEL increases by 1 dB upon inclusion of frequencies up to 1000 Hz, and by 2 dB using 98% energy criterion involving frequencies up to 2000 Hz.

It is worth emphasizing that from the standpoint of environmental monitoring, vector acoustic measurements within the water column such as those discussed here are inherently more difficult to make than scalar sound pressure measurements. Apart from the additional data analysis requirements, the calibration effort for a vector sensing system is four times that of a single hydrophone, and likelihood for systematic errors necessarily expands. This effort does not include the additional collection of metadata to monitor the equipment's orientation for resolving direction of the vector fields.

To study effects on marine life, acoustic data must be used as some measure of *dosage* from which a response is to be found. As a practical matter, any dose metric involving kinematic quantities (acoustic velocity, acceleration, displacement) must be in magnitude form as for example, in the AEL measure, and necessarily involve a degree of averaging. Here we have demonstrated, insofar as the finite difference approximation allows, the equivalence of observations based on dynamic (pressure) and kinematic components of the underwater acoustic field from impulse pile driving measured within the water column. The result should not be surprising given that such an acoustic field from impact pile driving is active and propagating energy, as distinct from a reactive field. This study nonetheless provides experimental evidence that may inform the choice of instrumentation in planning acoustic monitoring of pile driving operations.

Data availability statement

The data analyzed in this study is subject to the following licenses/restrictions: The raw data were gathered more than 17 years ago. Metadata is that identified only in this article. Information on processing of the raw data is that given only in this article. Requests to access these datasets should be directed to dahl@apl.washington.edu.

Author contributions

PD carried out the 2022 retrospective analysis contained herein on vector acoustic properties and produced the original draft of this manuscript along with figures associated data display and analysis. AM and RR conducted the original measurements in 2005 in cooperation with Washington State Department of Transportation (WSDOT), data analysis including the effects of bubble mitigation as documented in their 2005 report, and delivered the fully calibrated pressure and velocity data base to WSDOT archives used by PD, and contributed in the review and revision of the original draft. AM also evaluated and interpreted essential metadata used by PD. All authors contributed to the article and approved the submitted version.

Funding

The original data collection in 2005 was performed under a contract from the WSDOT. PD's efforts were funded by the U.S. Office of Naval Research.

Acknowledgments

The efforts of Jim Laughlin of WSDOT are appreciated for his help in coordinating the WSDOT funded study and recovery of the 2005 data from WSDOT data archives.

Conflict of interest

Authors AM and RR are employed by JASCO Applied Sciences Canada Ltd.

The remaining author declares that the research was conducted in the absence of any commercial or financial relationships that could be construed as a potential conflict of interest.

Publisher's note

References

Dahl, P. H., and Dall'Osto, D. R. (2020). Vector acoustic analysis of time-separated modal arrivals from explosive sound sources during the 2017 seabed characterization experiment. *IEEE J. Oceanic Eng.* 45, 131–143. doi: 10.1109/JOE.2019.2902500

Dahl, P. H., de Jong, C. A. F., and Popper, A. N. (2015). The underwater sound field from impact ple driving and its potential effects on marine life. *Acoustics Today* 11, 18–25.

Dahl, P. H., and Reinhall, P. G. (2013). Beam forming of the underwater sound field from impact pile driving. *J. Acoustical Soc. America* 134, EL1–EL6. doi: 10.1121/1.4807430

Davidsen, J. G., Dong, H., Linné, M., Andersson, M. H., Piper, A., Prystay, T. S., et al. (2019). Effects of sound exposure from a seismic airgun on heart rate, acceleration and depth use in free-swimming Atlantic cod and saithe. *Conserv. Physiol.* 7. doi: 10.1093/conphys/coz020

Fahy, F. (1995). *Sound intensity*. *2nd Ed* (London, U.K: Chapman and Hall).

Halvorsen, M. B., Casper, B. M., Woodley, C. M., Carlson, T. J., and Popper, A. N. (2012). Threshold for onset of injury in chinook salmon from exposure to impulsive pile driving sounds. *PloS One* 7. doi: 10.1371/journal.pone.0038968

Jacobsen, F., and Juhl, P. M. (2013). *Fundamentals of general linear acoustics* (Chichester, West Sussex, U.K: Wiley).

MacGillivray, A. (2018). Underwater noise from pile driving of conductor casing at a deep-water oil platform. *J. Acoustical Soc. America* 143, 450–459. doi: 10.1121/1.5021554

MacGillivray, A., and Racca, R. (2005). *Technical report: Sound pressure and particle velocity measurements from pile driving at Eagle Harbor maintenance facility, bainbridge island, WA* (Olympia, WA: Washington State Department of Transportation). Available at: https://wsdot.wa.gov/sites/default/files/2021-10/EnvNoiseMonRptEagleHarborPileDriving.pdf.

Reinhall, P. G., and Dahl, P. H. (2011). Underwater mach wave radiation from impact pile driving: Theory and observation. *J. Acoustical Soc. America* 130, 1209–1216. doi: 10.1121/1.3614540

Thompson, J., and Tree, D. (1981). Finite difference approximation errors in acoustic intensity measurements. *J. Sound Vibration* 75, 229–238. doi: 10.1016/0022-460X(81)90341-2

Tsouvalas, A. (2020). Underwater noise emission due to offshore pile installation: A review. *Energies* 13, 872–879. doi: 10.3390/en13123037

Tsouvalas, A., and Metrikine, A. V. (2013). A semi-analytical model for the prediction of underwater noise from offshore pile driving. *J. Sound Vib* 332, 3232–3257. doi: 10.1016/j.jsv.2013.01.026

Zampolli, M., Nijhof, M. J. J., de Jong, C. A. F., Ainslie, M. A., Jansen, E. H. W., and Quesson, B. A. J. (2013). Validation of finite element computations for the quantitative prediction of underwater noise from impact pile driving. *J. Acoustical Soc. America* 133, 72–81. doi: 10.1121/1.4768886

frontiers | Frontiers in Marine Science

TYPE Original Research
PUBLISHED 19 June 2023
DOI 10.3389/fmars.2023.1005374

Check for updates

OPEN ACCESS

EDITED BY
Lijun Dong,
Chinese Academy of Sciences (CAS), China

REVIEWED BY
Chongwei Peng,
Beibu Gulf University, China
Zhongchang Song,
Xiamen University, China
Ghulam Nabi,
Hebei Normal University, China

*CORRESPONDENCE
Tao Chen
chent@scsfri.ac.cn

RECEIVED 28 July 2022
ACCEPTED 05 June 2023
PUBLISHED 19 June 2023

CITATION
Fang L, Li M, Wang X, Chen Y and Chen T (2023) Indo-Pacific finless porpoises presence in response to pile driving on the Jinwan Offshore Wind Farm, China. *Front. Mar. Sci.* 10:1005374.
doi: 10.3389/fmars.2023.1005374

Indo-Pacific finless porpoises presence in response to pile driving on the Jinwan Offshore Wind Farm, China

Liang Fang[1,2], Min Li[1,2], Xinxing Wang[1,2], Yujian Chen[1,2] and Tao Chen[1,2]*

[1]Guangdong Provincial Key Laboratory of Fishery Ecology and Environment, Guangzhou, South China Sea Fisheries Research Institute, Chinese Academy of Fishery Sciences, Guangzhou, China, [2]Scientific Observation and Research Field Station of Pear River Estuary Ecosystem, Guangdong, Guangzou, China

The Jinwan Offshore Wind Farm project in the Pearl River Estuary (PRE) is a new stressor for the resident marine mammals there, especially for the Indo-Pacific finless porpoise. A broadband recording system was deployed in the Jinwan Offshore Wind Farm, before and during the construction period, in order to determine how the finless porpoise responded to pile driving activity. The results showed that the wind farm area was an important habitat for the finless porpoise during the monitoring period. The finless porpoise also showed avoidance behavior of pile driving activity. There was a significant negative correlation between porpoise detection and pile driving detection, and the time between porpoise's acoustic detections increased during pile driving compared to periods without pile driving. Our results indicated that acoustic protection measures are strongly recommended in future offshore wind farm developments in order to protect finless porpoises.

KEYWORDS

off shore wind farm, pile driving noise, finless porpoise, passive acoustic monitoring, habitat

1 Introduction

Anthropogenically accelerated climate change as a consequence of burning fossil fuels has led to many governments investing heavily in renewable energy sources (Gallagher, 2013; White et al., 2013; Dwyer and Teske, 2018; Johnsson et al., 2019; Sharif et al., 2019). This has been particularly noticeable in China, where the government has been rapidly constructing offshore wind farms with a potential total output of 600 GW (Yang et al., 2017). Installed wind energy capacity in China is said to be increasing at a rate of 9.56% through to 2025, including both on- and offshore wind farms (Yang et al., 2017). However, while the global benefits of offshore wind farms are not in question, the potential effects on marine mammals locally do need to be considered. This is because offshore wind farms are often constructed in shallow environments with high biodiversity and cover large areas. As such, there is often considerable physical overlap between offshore wind farms and core marine mammal habitats around China, particularly in the Pearl River Estuary (PRE)—leading to a range of potential impacts (Gill, 2005; OSPAR Commission, 2008; Bailey et al., 2014; Bergström et al., 2014). Public and stakeholder concerns about the potential impacts of the construction, operation and maintenance of offshore wind farms on marine mammals are therefore warranted.

Underwater noise from construction activities is well documented, and is a commonly listed contributor to habitat-use changes by marine mammals (Tyack, 2008; Richardson et al., 2013). Noise impacts relating to offshore wind farms are predominately associated with their installation, while increased vessel activity in the area, pile driving, dredging, blasting, and vibrations are the main sources of noise potentially impacting marine mammals (Madsen et al., 2006; Thomsen et al., 2006; Matuschek and Betke, 2009; Bailey et al., 2010; Thompson et al., 2010; Cheesman, 2016). Marine mammals are sensitive to underwater noise because they are heavily reliant on sound for communication, prey detection and capture, group cohesion, and navigation, and have evolved highly sensitive hearing to enable these diverse biological functions(Au et al., 2000; Au and Hastings, 2008). Therefore, underwater noise pollution can often affect the behavior, communications, acute physiology (such as hearing loss), and habitat-use of marine mammals(Weilgart, 2007a; Weilgart, 2007b).

The Indo-Pacific finless porpoise (*Neophocaena phocaenoides*) is a small and timid cetacean, occurring mainly in the shallow coastal waters (less than 50 m depth) of the Persian Gulf eastward to the Taiwan Strait and southward to Indonesia (Wang and Reeves, 2017). However, since it is difficult to survey this species in the wild by visual means, it has only been studied in a few areas (Wang and Reeves, 2017). The Pearl River Estuary (PRE) is an important habitat for the Indo-Pacific finless porpoise; however, nearly all of the surveys in the wild have been carried out in the waters around Hong Kong, which is located within the Pearl River Delta (Jefferson et al., 2002; Jefferson and Moore, 2020). The status of the finless porpoise population in the PRE is still controversial. Recently, a study of the abundance and population trends of this cetacean in the waters around Hong Kong suggested that there has been no significant change in population over the past 23 years (Jefferson and Moore, 2020), whereas an analysis of the population dynamics of the same species in the PRE region suggests that the population is fluctuating, which relates to the changing of fishery management (Lin et al., 2019). Offshore wind farm development in the PRE might therefore prove to be a new and serious challenge to finless porpoises in this area. Thus, it is critical to determine how the finless porpoise responds to underwater noise during wind farm construction.

Passive acoustic monitoring (PAM) of cetaceans is now a widely used and continuously evolving method due to its economic viability in providing detailed information on whale and dolphin activity (Zimmer, 2011; Sousa-Lima et al., 2013). The technology is also widely used in assessing the impacts of offshore wind farms on marine mammals (Brandt et al., 2009; Thompson et al., 2010; Scheidat et al., 2011; Brandt et al., 2018) and general habitat use by humpback dolphins within the PRE (Wang et al., 2015; Munger et al., 2016; Pine et al., 2016; Pine et al., 2017; Munger et al., 2018; Fang et al., 2020). Through the use of PAM, this study investigated the Indo-Pacific finless porpoise's presence in response to pile driving activity during the construction of the Jinwan Offshore Wind Farm. The results of our study and the recommendations outlined below are also relevant to the future management of offshore wind farm developments elsewhere globally.

2 Methods

2.1 Study area and acoustic measuring device

The Jinwan Offshore Wind Farm is the second wind farm to be constructed in the PRE, located to the southeast of Zhuhai Jinwan Airport and northeast of Gaolan Island, a distance of 10.5 km to the nearest point of land (Figure 1A). The wind farm consists of 55 5.5 MW wind turbines arranged in five rows, with spacings of 1912 m between the rows and 512 m between the wind turbines. The wind farm covers an area of 44.5 km^2, with the water depth ranging from 14 to 22 m. The foundations for the wind turbines were installed between August 2019 and May 2020. The turbine foundation piles are 7.5 m in diameter and 93.2 m in length. The pile driving for constructing the foundations was performed using an IHC S-3000 (IHC IQIP, USA) hydraulic hammer for steel piles.

To determine how the Indo-Pacific finless porpoise responded to the pile driving activity, a broadband acoustic recording system, Soundtrap 300 HF (Ocean Instruments Ltd, New Zealand), was used to record the sounds from the finless porpoises as well as the pile driving activity. The Soundtrap 300 HF is a compact autonomous unit with a frequency range between 20 Hz and 150 kHz. The duration of each deployment was dependent on the unit's battery and memory, as well as the weather conditions prevailing at the time of measurement, but usually lasted between 40 and 60 days. The series number and sensitivities of soundtraps, gain setting and recording time were show in Table 1.

During recording, the anemometer tower was used as the passive acoustic monitoring station (N21°52′33.17″, E 113°26′1.97″), where the distances were 780 m to the nearest and 6800 m to the furthest wind farm foundation (Figure 1A). The Soundtrap HF 300 was tied to the leg of the anemometer tower, 4 m below the water surface. The acoustic equipment was set to record for 5 min per hour, and the sampling rate was set at 288 kHz with high gain. The acoustic equipment was changed nearly two month once time to download data by diver.

2.2 Data analysis

All acoustic data were analyzed manually using Adobe Audition 3.0 (Adobe, Inc) digital audio workstation software. Finless porpoises emit narrow-band and high-frequency echolocation clicks, with a peak frequency higher than 120 kHz and barely have energy distributed less than 70 kHz. These special characteristics allow the clicks of finless porpoises to be easily

10.3389/fmars.2023.1005374

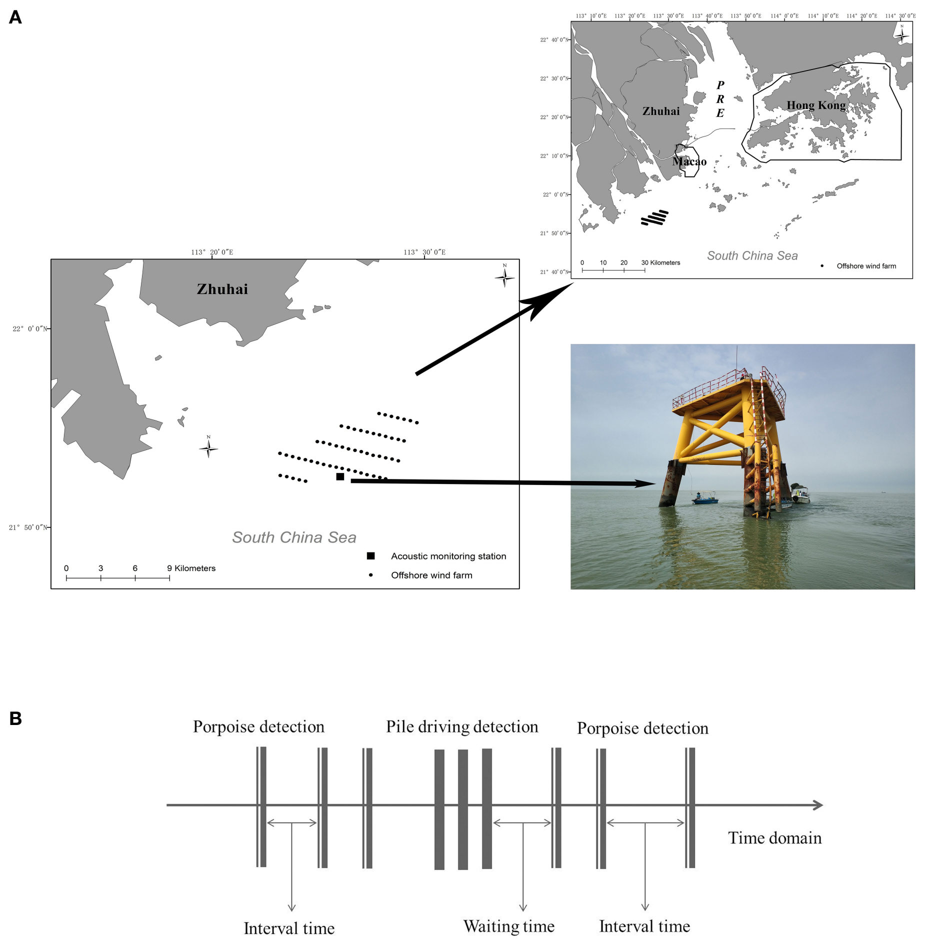

FIGURE 1
(A) Locations of the Jinwan Offshore Wind Farm turbine and the acoustic monitoring station; **(B)** Schematic of porpoise detection, pile driving detection, interval time of porpoise detection, and porpoise waiting time to pile driving.

distinguished in spectrograms from the background ocean noise (Li et al., 2005; Fang et al., 2015).

To better understand the effects of the offshore wind farm construction on the habitat used by the Indo-Pacific finless porpoise, several parameters were defined, including porpoise detection, pile driving activity detection, waiting time, and interval time. Porpoise detection was defined as the detection of echolocation clicks by finless porpoises in the acoustic file containing 5 min of recording time per hour, and pile driving detection was defined as the detection of pile driving sounds in the acoustic file of 5 min recording time. The detection rates in each month for finless porpoises and pile driving were calculated from the number of detections and the total number of recorded files (Fang et al., 2020). Waiting time was defined as the time interval between a pile driving detection and the first time of an acoustic occurrence from a finless porpoise, which is an important piece of data to show how long of the porpoise occurrence after the wind farm pile driving activity. The interval time was defined as the time between adjacent porpoise detections without the pile driving detection (Figure 1B).

TABLE 1 The information of the recording instruments, including the series mumber of soundtrap, sensitivities, gain setting and recording time of each period.

Series number of soundtrap	Sensitivity (dB)	Gain (dB)	Start time	End time
5324	176.8	High	2019-5-13	2019-7-15
5523	174.6	High	2019-8-6	2019-10-31
671399973	176.3	High	2019-11-2	2019-12-11
5324	176.8	High	2019-12-13	2020-3-25
5523	174.6	High	2020-3-25	2020-5-31

The porpoise clicks and pile driving were analyzed visually. The peak-to-peak sound pressure level (SPL) of pile driving detected by the acoustic measuring equipment was expressed as a peak-to-peak level given by Eq. (1):

$$SPL = 20 \quad \log 10(P_{peak}/P_0) \qquad (1)$$

Where SPL is the highest observed peak to peak sound pressure level from the acoustic recorder and P_0 is the reference sound pressure, which is 1μPa. An example of pile driving activities with the waveform and spectrum of a single pulse was presented on Figure 2.

The data were analyzed by SPSS software (version 16.0; SPSS Inc., Chicago, Illinois). Significant difference between the waiting times and the interval times was tested using Mann-Whitney U-test with the given significant level P<0.01 and the relationship between the acoustic detection rates of finless porpoises and of pile driving in each month was described by Pearson correlation.

3 Results

From May 13, 2019 to May 31, 2020, a total of 13 months of continuous acoustic recording was conducted (Figure 3A) and a total of 8631 sound files were collected, including 1072 files of finless porpoise sounds and 92 files of pile driving activities.

Histograms of the finless porpoise and pile driving detection rates in different months throughout the entire monitoring period are presented in Figure 3B. The results indicate the occurrence of finless porpoises in the monitoring area throughout the entire monitoring period. The highest detection rate of finless porpoises was 23% in July 2019, and the lowest rate was 4.7% in March 2020. Pile driving activity was first detected in November 2019 and continued until May 2020. The greatest number of occurrences was in March 2020, with a detection probability of 3.8%, while the lowest number of occurrences was in November 2019, with a detection probability of 0.4%.

A histogram of the SPL values of pile driving is presented in Figure 4. The SPL values ranged from 141.3 to 183.1 dB, nearly 41% of the SPL values were distributed between 170 and 180 dB, 17.85% were higher than 180 dB, and 28.21% were distributed between 160 and 170 dB.

A significant negative correlation between the detection rates of finless porpoises and pile driving activity was also observed (Pearson correlations, P = 0.025, R^2 = 0.69, Figure 5). The interval time of porpoise occurrence without pile driving activity is presented in Figure 6A. Nearly 89.2% of the interval times of porpoise occurrence were less than 20 h, and 73.9% of interval times were less than 10 h. The waiting times of finless porpoises to pile driving events are also presented in Figure 6A. A total of 45.9% of waiting times were distributed between 0 and 10 h and 29.7% between 10 and 20 h. The median interval time of porpoise occurrence and the average waiting time are presented in Figure 6B, and these showed a significant difference (P< 0.01).

4 Discussion

Our results for the detections of finless porpoises both before and during wind farm construction demonstrate for the first time that these waters are an important habitat for Indo-Pacific finless porpoises. However, there has been almost no consideration of the possible adverse effects of wind farm construction on the finless porpoise. Moreover, in recent years, offshore wind farm projects have been increasing rapidly in number in Pacific Ocean regions. Passive acoustic monitoring surveys, as a low-cost method, are strongly recommended for monitoring the activity of Indo-Pacific

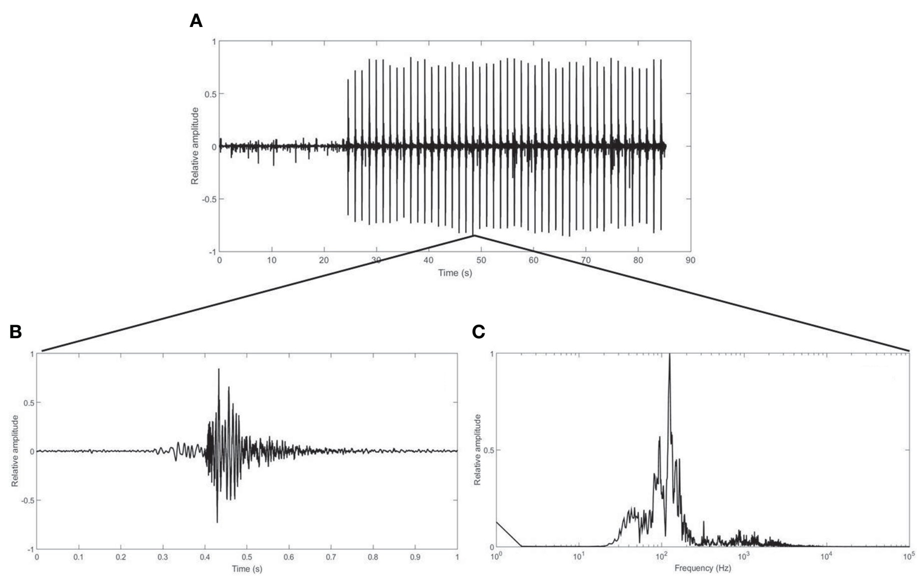

FIGURE 2
(A) Example of the high sound pressure level of pile driving activity; **(B)** waveform; **(C)** spectrum of a single pile driving pulse.

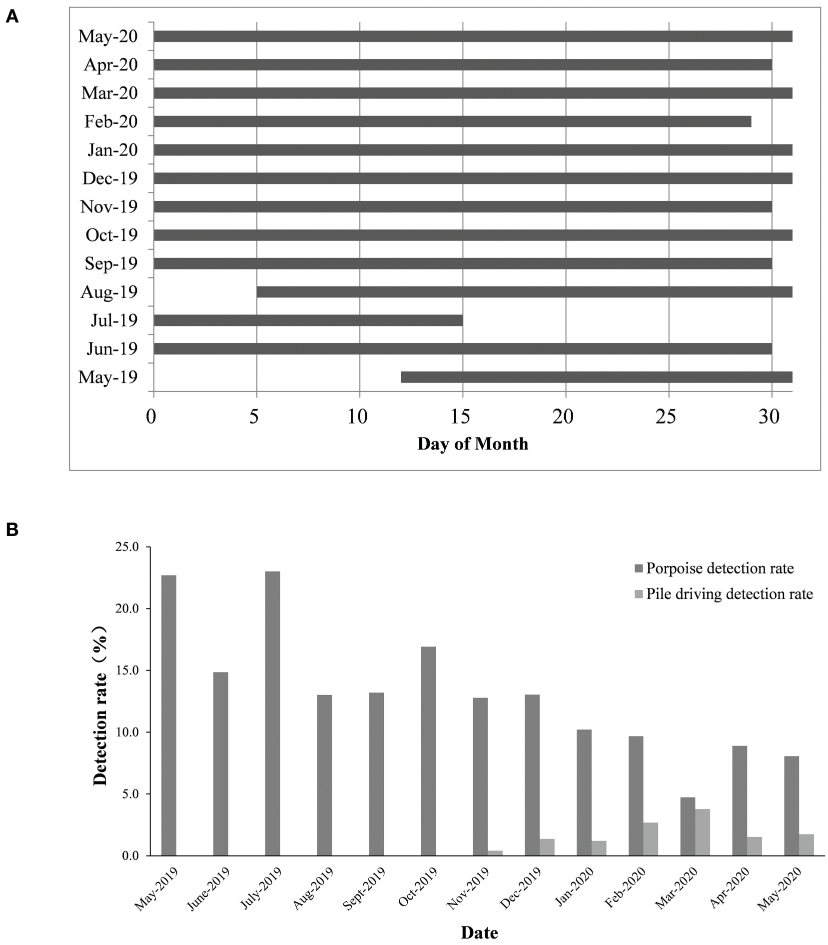

FIGURE 3
(A) The acoustic monitoring days of each month from May 2019 to May 2020; **(B)** histogram of detection rates of Indo-Pacific finless porpoises and pile driving activity in each month of monitoring.

finless porpoises in the candidate areas for offshore wind farms, which has been found to be effective in numerous studies of the environmental impacts of wind farm construction on marine mammals (Brandt et al., 2009; Thompson et al., 2010; Brandt et al., 2011; Brandt et al., 2012; Graham et al., 2017; Graham et al., 2019).

Pile driving is one of the major activities taking place during wind farm construction, and the high noise levels created by it can result in a series of adverse impacts on marine organisms, especially marine mammals (Madsen et al., 2006). Over short distances, the loud noise from pile driving may cause a direct disturbance or a hearing injury, such as temporary damage to hearing thresholds

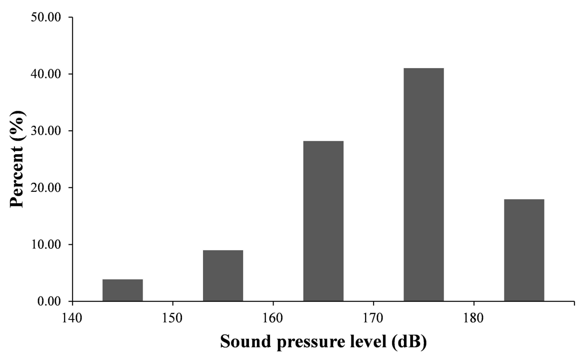

FIGURE 4
Distribution of sound pressure level (SPL) values of pile driving (peak-to-peak) detected by the passive acoustic measuring equipment.

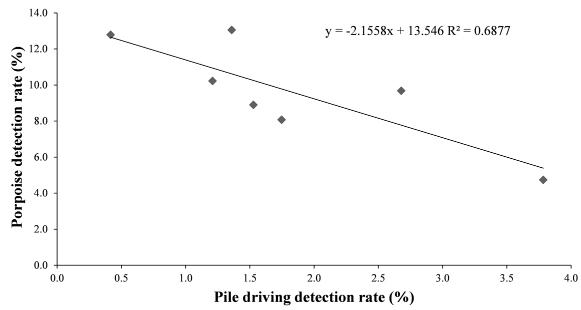

FIGURE 5
Relationship between the monthly detection rate of finless porpoises and pile driving activity (R^2 = 0.69).

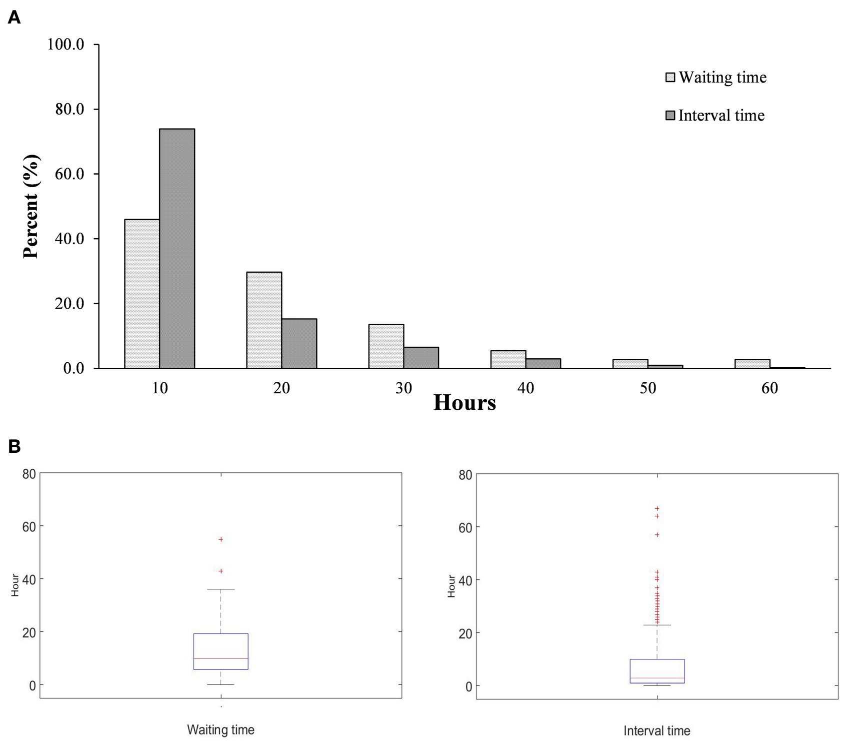

FIGURE 6
(A) Histograms of waiting time and interval time; **(B)** median waiting time and average interval time.

(Finneran, 2015; Southall et al., 2019). The source level (SL) of pile driving activity was given by equation SL= SPL +TL=SPL+20log10 (R)+ αR, TL is the transmission loss and R is the distance between pile driving site and acoustic equipment, α is the absorption coefficient of 0.0004dB (Bailey et al., 2010). In the present study, the highest peak-to-peak SPL received by the acoustic recorder was as much as 183.34 dB. Considering that the nearest turbine foundation was a distance of 780 m from the acoustic recorder, the actual noise level of the source pile driving activity was estimated to have been higher than 241.3 dB, which is much higher than the criterion 202 dB (unweight peak SPL) for the onset of permanent threshold shift (PTS) and 196 dB (unweight peak SPL) for the onset of temporary threshold shift (TTS) for very high-frequency cetaceans (Southall et al., 2019). The 241.3 dB pile driving sounds could induce the finless porpoise temporary and permanent hearing loss within range of 92.3 and 184.1 m. This means that there is quite a high risk of hearing damage to finless porpoises in close range to pile driving activities.

A significant negative correlation between the monthly detection rate of finless porpoises and pile driving activity was found, which suggests that finless porpoises reduce their use of their regular habitat in response to pile driving activity. In addition, the median waiting time 10 hour was significant longer than the median interval time 3 hour meant that harbor porpoises took more time to return to the wind farm habitat following completion of pile driving. This is probably because such a high-pressure level of pile driving noise can affect porpoises over a large spatial range. Pile driving can affect a quite large range of habitat for porpoises, which was observed in several studies. Brandt et al. (2011) found a clear negative effect on harbor porpoise acoustics at a distance of 17.8 km (Brandt et al., 2011). Dähne et al. (2013) showed a negative impact on harbor porpoise detection by pile driving at a distance of less than 10.8 km (Dähne et al., 2013). Even more, it has been reported as being more than 20 km by several studies (Tougaard et al., 2009; Thompson et al., 2010; Brandt et al., 2011). Our results show direct evidence for the porpoise avoidance of the pile driving activities and finless porpoise would reduce using this habitat in several months. It is unclear the effects of the porpoise away its habitat in several months, more work should be done during the construction, like monitoring the number of population and distribution of finless porpoise. In addition, continued concern for finless porpoises how to response and adapt the operation phase of off shore wind farm.

5 Conclusion and recommendations

Our results indicate that the waters surrounding the Jinwan Offshore Wind Farm are an important habitat for Indo-Pacific finless porpoises, which were found there both before and during the construction period. The frequency of finless porpoise detections was reduced after pile driving was detected, which correlated strongly with pile driving activity. Due to the noise level at the source of the pile driving being estimated to have been more than 240 dB, there was a high risk of temporary or even permanent hearing damage over short distances to finless porpoises according to the sound exposure criteria issued by the US Department of Commerce's National Oceanic and Atmospheric Administration (NOAA). Offshore wind farms, as a new energy industry, are growing rapidly in China and Southeast Asia in general. However, little attention has been paid to their impact on marine mammals, especially the Indo-Pacific finless porpoise. The following recommendations are based on the lessons learned from this study, which are hoped will help to reduce the impact of further offshore wind farm developments on the finless porpoise in unsurveyed waters:

1. Passive acoustic monitoring was successfully used to show the porpoise acoustic presence in response to pile driving activity. We strongly recommend the use of passive and stationary acoustic monitoring methods for surveying candidate waters for offshore wind farms where there is limited funding support. Such data are urgently required for assessing the impact of offshore wind farms on finless porpoises in order to take appropriate action to ease the effects on the porpoise population in these areas. Furthermore, to better know how the finless porpoise response to the pile driving activity, multiple acoustic recorders should be deployed before and during the construction period in different distances to the pile driving sites.
2. Because of unknown the distance between the acoustic recorder and the pile driving sites, we can't calculate the source level of pile driving. However, there is a need to monitor noise events and noise levels throughout the entire construction period, especially pile driving activities. The intensity of noise from pile driving is a key factor for evaluating the effects of offshore wind farm construction on marine mammals. Pile driving was always with multiple pulses. Analyzing the pile driving noise should also include the parameter of sound exposure level, which can provide the indication of pile driving energy with different number of pulses. Marine mammals show different acoustic activities to the pile driving noise in different distances, knowing the range of finless porpoise response to the pile driving noise can help the government making protect area for finless porpoies during the construction period.
3. High pile driving noise pressure level was observed in present study. The high intensity noise could damage the porpoise hearing system directly (Richardson et al., 2013; Southall et al., 2019). Noise mitigation measures should be developed during offshore wind farm construction. The principal source of noise coming from offshore wind farms during construction is foundation installation, including pile driving. Numerous measures are recommended for reducing noise and acoustic disturbance during construction, including bubble curtains, isolation casings, cofferdams, pingers, soft-start pile driving, and the use of low-noise pile driving equipment.
4. Until now, most studies of the noise from offshore wind farms have focused on construction activity, while the effects of noise from the actual operation of offshore wind farms has been ignored. Since the operating times of offshore wind farms are much longer than their construction periods, the short-term and long-term noise impacts on marine mammals during operation period of offshore wind farms should remain a concern.

Data availability statement

The raw data supporting the conclusions of this article will be made available by the authors, without undue reservation.

Ethics statement

Ethical review and approval was not required for the animal study because There is no negative effect on marine mammals by a station passive acoustic monitoring.

Author contributions

LF conceived the study, carried out field work, analyzed data, and wrote the majority of the manuscript. ML,XW, YJC carried out filed work TC conceived the study, analyzed data and revised the manuscript All authors contributed to the article and approved the submitted version.

Funding

This research was supported by the grant of Central Public-interest Scientific Institution Basal Research Fund, South China Sea Fisheries Research Institute, CAFS (NO. 2019TS27, 2019ZD0202, 2021SD18), CAS Key Laboratory of Science and Technology on Operational Oceanography (No.OOST2021-06) and Special Foundation for National Science and Technology Basic Research Program of China (2019FY101905).

Acknowledgments

We grateful thank the captain Jianxiong Ruan and stuff of Haiyang diving company Changqing Luo.

Conflict of interest

The authors declare that the research was conducted in the absence of any commercial or financial relationships that could be construed as a potential conflict of interest.

Publisher's note

References

Au, W. W. L., and Hastings, M. C. (2008). *Principles of marine bioacoustics* (New York: Springer Verlag).

Au, W. W. L., Popper, A. N., and Fay, R. R. (2000). *Hearing by whales and dolphins* (New York: Springer).

Bailey, H., Brookes, K. L., and Thompson, P. M. (2014). Assessing environmental impacts of offshore wind farms: lessons learned and recommendations for the future. *Aquat. Biosyst.* 10 (1), 8. doi: 10.1186/2046-9063-10-8

Bailey, H., Senior, B., Simmons, D., Rusin, J., Picken, G., and Thompson, P. M. (2010). Assessing underwater noise levels during pile-driving at an offshore windfarm and its potential effects on marine mammals. *Mar. pollut. Bull.* 60 (6), 888–897. doi: 10.1016/j.marpolbul.2010.01.003

Bergström, L., Kautsky, L., Malm, T., Rosenberg, R., Wahlberg, M., Capetillo, N.Å., et al. (2014). Effects of offshore wind farms on marine wildlife–a generalized impact assessment. *Environ. Res. Lett.* 9 (3), 34012. doi: 10.1088/1748-9326/9/3/034012

Brandt, M. J., Diederichs, A., Betke, K., and Nehls, G. (2011). Responses of harbour porpoises to pile driving at the horns rev II offshore wind farm in the Danish north Sea. *Mar. Ecol. Prog. Ser.* 421, 205–216. doi: 10.3354/meps08888

Brandt, M. J., Diederichs, A., Betke, K., and Nehls, G. (2012). "Effects of offshore pile driving on harbor porpoises (Phocoena phocoena)," in *The effects of noise on aquatic life* (New York: Springer), 281–284.

Brandt, M. J., Diederichs, A., and Nehls, G. (2009). *Harbour porpoise responses to pile driving at the Horns Rev II offshore wind farm in the Danish North Sea* (Husum, Germany: BioConsult SH).

Brandt, M. J., Dragon, A. C., Diederichs, A., Bellmann, M. A., Wahl, V., Piper, W., et al. (2018). Disturbance of harbour porpoises during construction of the first seven offshore wind farms in Germany. *Mar. Ecol. Prog.* 596, 213–232. doi: 10.3354/meps12560

Cheesman, S. (2016). Measurements of operational wind turbine noise in UK waters. *Adv. Exp. Med. Biol.* 875, 153–160. doi: 10.1007/978-1-4939-2981-8_18

Dähne, M., Gilles, A., Lucke, K., Peschko, V., Adler, S., Krügel, K., et al. (2013). Effects of pile-driving on harbour porpoises (Phocoena phocoena) at the first offshore wind farm in Germany. *Environ. Res. Lett.* 8 (2), 279–288.

Dwyer, S., and Teske, S. (2018). *Renewables 2018 Global Status Report* (Paris, France: Ren21).

Fang, L., Lin, W., Guo, L., Cai, H., Pine, M. K., and Wu, Y. (2020). Monitoring indo-pacific humpback dolphin occurrences in a highly urbanized estuary for informing conservation and management. *Aquat. Conservation: Mar. Freshw. Ecosyst.* 31 (3), 685–696. doi: 10.1002/aqc.3475

Fang, L., Wang, D., Li, Y., Cheng, Z., Pine, M. K., Wang, K., et al. (2015). The source parameters of echolocation clicks from captive and free-ranging Yangtze finless porpoises (*Neophocaena asiaeorientalis asiaeorientalis*). *PloS One* 10 (6), e0129143. doi: 10.1371/journal.pone.0129143

Finneran, J. J. (2015). Noise-induced hearing loss in marine mammals: a review of temporary threshold shift studies from 1996 to 2015. *J. Acoustical Soc. America* 138 (3), 1702–1726. doi: 10.1121/1.4927418

Gallagher, K. S. (2013). Why & how governments support renewable energy. *Daedalus* 142 (1), 59–77. doi: 10.1162/DAED_a_00185

Gill, A. B. (2005). Offshore renewable energy: ecological implications of generating electricity in the coastal zone. *J. Appl. Ecol.* 42 (4), 605–615. doi: 10.1111/j.1365-2664.2005.01060.x

Graham, I. M., Merchant, N. D., Farcas, A., Barton, T. R., Cheney, B., Bono, S., et al. (2019). Harbour porpoise responses to pile-driving diminish over time. *R. Soc. Open Sci.* 6 (6), 190335. doi: 10.1098/rsos.190335

Graham, I. M., Pirotta, E., Merchant, N. D., Farcas, A., Barton, T. R., Cheney, B., et al. (2017). Responses of bottlenose dolphins and harbor porpoises to impact and vibration piling noise during harbor construction. *Ecosphere* 8 (5), e01793. doi: 10.1002/ecs2.1793

Jefferson, T. A., Hung, S. K., Law, L., Torey, M., and Tregenza, N. (2002). Distribution and abundance of finless porpoises in Hong Kong and adjacent waters of China. *Raffles Bull. Zool* 50, 43–56.

Jefferson, T. A., and Moore, J. E. (2020). Abundance and trends of indo-pacific finless porpoises (*Neophocaena phocaenoides*) in Hong Kong water 1996–2019. *Front. Mar. Sci.* 7. doi: 10.3389/fmars.2020.574381

Johnsson, F., Kjärstad, J., and Rootzén, J. (2019). The threat to climate change mitigation posed by the abundance of fossil fuels. *Climate Policy* 19 (2), 258–274. doi: 10.1080/14693062.2018.1483885

Li, S., Wang, K., Wang, D., and Akamatsu, T. (2005). Echolocation signals of the free-ranging Yangtze finless porpoise (*Neophocaena phocaenoides asiaeorientialis*). *J. Acoustical Soc. America* 117 (5), 3288–3296. doi: 10.1121/1.1882945

Lin, W., Karczmarski, L., Li, J., Chan, S. C., Guo, L., and Wu, Y. (2019). Differential population dynamics of a coastal porpoise correspond to the fishing effort in a large estuarine system. *Aquat. Conservation: Mar. Freshw. Ecosyst.* 29 (2), 223–234. doi: 10.1002/aqc.2998

Madsen, P. T., Wahlberg, M., Tougaard, J., Lucke, K., and Tyack, P. (2006). Wind turbine underwater noise and marine mammals: implications of current knowledge and data needs. *Mar. Ecol. Prog. Ser.* 309, 279–295. doi: 10.3354/meps309279

Matuschek, R., and Betke, K. (2009). "Measurements of construction noise during pile driving of offshore research platforms and wind farms," in *Proc. NAG/DAGA int. conference on acoustics* (Rotterdam, Netherlands) 262–265.

Munger, L., Lammers, M. O., Cifuentes, M., Würsig, B., Jefferson, T. A., and Hung, S. K. (2016). Indo-pacific humpback dolphin occurrence north of lantau island, Hong Kong, based on year-round passive acoustic monitoring. *J. Acoustical Soc. America* 140 (4), 2754–2765. doi: 10.1121/1.4963874

Munger, L., Piwetz, S., Lammers, M. O., and Wursig, B. (2018). Passive acoustic monitoring and concurrent theodolite observations of indo-pacific humpback dolphins (*Sousa chinensis*) in Hong Kong: a case study. *Aquat. Mammals* 44 (6), 729–735. doi: 10.1578/am.44.6.2018.729

OSPAR Commission (2008). Assessment of the environmental impact of offshore windfarms. OSPAR commission biodiversity series.

Pine, M. K., Wang, K., and Wang, D. (2016). "Monitoring rising ambient sound levels from vessels and impacts on indo-pacific humpback dolphin (Sousa chinensis) occurrences," in *Proceedings of meetings on acoustics 4ENAL: acoustical society of America* (Dublin, Ireland), vol. 27. 070003.

Pine, M. K., Wang, K., and Wang, D. (2017). Fine-scale habitat use in indo-pacific humpback dolphins, Sousa chinensis, may be more influenced by fish rather than vessels in the pearl river estuary, China, *Mar. Mammal Sci.* 33 (1), 291–312. doi: 10.1111/mms.12366

Richardson, W. J., Greene, C. R.Jr., Malme, C. I., and Thomson, D. H. (2013). *Marine mammals and noise* (San Diego, CA: Academic Press).

Scheidat, M., Tougaard, J., Brasseur, S., Carstensen, J., Petel, T. V. P., Teilmann, J., et al. (2011). Harbour porpoises (*Phocoena phocoena*) and wind farms: a case study in the Dutch north Sea. *Environ. Res. Lett.* 6 (2), 025102. doi: 10.1088/1748-9326/6/2/025102

Sharif, A., Raza, S. A., Ozturk, I., and Afshan, S. (2019). The dynamic relationship of renewable and nonrenewable energy consumption with carbon emission: a global study with the application of heterogeneous panel estimations. *Renewable Energy* 133, 685–691. doi: 10.1016/j.renene.2018.10.052

Sousa-Lima, R. S., Norris, T. F., Oswald, J. N., and Fernandes, D. P. (2013). A review and inventory of fixed autonomous recorders for passive acoustic monitoring of marine mammals. *Aquat. Mammals* 39 (1), 23–53. doi: 10.1578/AM.39.1.2013.23

Southall, B. L., Finneran, J. J., Reichmuth, C., Nachtigall, P. E., Ketten, D. R., Bowles, A. E., et al. (2019). Marine mammal noise exposure criteria: updated scientific recommendations for residual hearing effects. *Aquat. Mammals* 45 (2), 125–232. doi: 10.1578/AM.45.2.2019.125

Thompson, P. M., Lusseau, D., Barton, T., Simmons, D., Rusin, J., and Bailey, H. (2010). Assessing the responses of coastal cetaceans to the construction of offshore wind turbines. *Mar. Pollut. Bull.* 60 (8), 1200–1208. doi: 10.1016/j.marpolbul.2010.03.030

Thomsen, F., Lüdemann, K., Kafemann, R., and Piper, W. (2006). "Effects of offshore wind farm noise on marine mammals and fish," in *Biola, Hamburg, Germany on behalf of COWRIE Ltd* (Biola, Hamburg, Germany on behalf of COWRIE Ltd), 62.

Tougaard, J., Carstensen, J., Teilmann, J., Skov, H., and Rasmussen, P. (2009). Pile driving zone of responsiveness extends beyond 20 km for harbor porpoises (*Phocoena phocoena* (L.)). *J. Acoustical Soc. America* 126 (1), 11–14. doi: 10.1121/1.3132523

Tyack, P. L. (2008). Implications for marine mammals of Large-scale changes in the marine acoustic environment. *J. Mammal* 89 (3), 549–558. doi: 10.1644/07-MAMM-S-307R.1

Wang, Z.-T., Nachtigall, P. E., Akamatsu, T., Wang, K.-X., Wu, Y.-P., Liu, J.-C., et al. (2015). Passive acoustic monitoring the diel, lunar, seasonal and tidal patterns in the biosonar activity of the indo-pacific humpback dolphins (*Sousa chinensis*) in the pearl river estuary, China. *PloS One* 10 (11), e0141807. doi: 10.1371/journal.pone.0141807

Wang, J., and Reeves, R. (2017). "Neophocaena phocaenoides," in *IUCN red list of threatened species 2017-2013.*

Weilgart, L. S. (2007a). A brief review of known effects of noise on marine mammals. *Int. J. Comp. Psychol.* 20 (2), 159–168. doi: 10.46867/IJCP.2007.20.02.09

Weilgart, L. S. (2007b). The impacts of anthropogenic ocean noise on cetaceans and implications for management. *Can. J. Zool* 85 (11), 1091–1116. doi: 10.1139/Z07-101

White, W., Lunnan, A., Nybakk, E., and Kulisic, B. (2013). The role of governments in renewable energy: the importance of policy consistency. *Biomass Bioenergy* 57, 97–105. doi: 10.1016/j.biombioe.2012.12.035

Yang, J., Liu, Q., Li, X., and Cui, X. (2017). Overview of wind power in China: status and future. *Sustainability* 9 (8), 1454. doi: 10.3390/su9081454

Zimmer, W. M. (2011). *Passive acoustic monitoring of cetaceans* (Cambridge: Cambridge University Press).

TYPE Original Research
PUBLISHED 14 July 2023
DOI 10.3389/fmars.2023.1153843

OPEN ACCESS

EDITED BY
Apostolos Tsouvalas,
Delft University of Technology,
Netherlands

REVIEWED BY
Giuseppa Buscaino,
National Research Council (CNR), Italy
Chongwei Peng,
Beibu Gulf University, China
Zhongchang Song,
Xiamen University, China

*CORRESPONDENCE
Jee Woong Choi
choijw@hanyang.ac.kr

†PRESENT ADDRESS
Dong-Gyun Han,
Oceansounds Inc., Ansan,
Republic of Korea

RECEIVED 30 January 2023
ACCEPTED 22 June 2023
PUBLISHED 14 July 2023

CITATION
Yoon YG, Han D-G and Choi JW (2023) Measurements of underwater operational noise caused by offshore wind turbine off the southwest coast of Korea.
Front. Mar. Sci. 10:1153843.
doi: 10.3389/fmars.2023.1153843

Measurements of underwater operational noise caused by offshore wind turbine off the southwest coast of Korea

Young Geul Yoon[1], Dong-Gyun Han[1†] and Jee Woong Choi[2,3*]

[1]Research Center for Ocean Security Engineering and Technology, Hanyang University ERICA, Ansan, Republic of Korea, [2]Department of Marine Science and Convergence Engineering, Hanyang University ERICA, Ansan, Republic of Korea, [3]Department of Military Information Engineering, Hanyang University ERICA, Ansan, Republic of Korea

As interest in the development of renewable energy increases, a large number of offshore wind farms are being built worldwide. Accordingly, the potential impacts of underwater operational noise on marine ecosystems have become an issue, and thus it is necessary to understand the mechanisms and acoustic characteristics of underwater operational noise for the environmental impact assessment. For this paper, underwater noise was measured for about 10 days near a 3-MW wind turbine off the southwest coast of Korea, and the acoustic characteristics of the operational noise and its relationship with rotor speed were investigated. The tonal frequencies of the underwater operational noise varied with rotor speed, and particularly the peak level at a frequency of ~198 Hz increased by ~20 dB or more at the rated rotor speed. Additional experiments were conducted to determine the relationship between underwater noise and wind turbine tower vibration, and finally, the underwater noise correlated highly with the tower vibration acceleration signal, wind speed, and rotor speed, with correlation coefficients of 0.95 or higher.

KEYWORDS

offshore wind turbine, underwater noise, operational noise, tower vibration, wind speed, rotor speed, acoustic characteristics

1 Introduction

Offshore wind power is playing an increasingly important role in the transition to sustainable green energy (Cranmer and Baker, 2020; Stöber and Thomsen, 2021; Popper et al., 2022). Offshore wind power has many advantages, such as stronger wind conditions than onshore, virtually no restrictions on the scale, limited visual pollution, and no noise issues for onshore residents (Bilgili et al., 2011; Oh et al., 2012). However, one major environmental issue caused by offshore wind power is underwater noise generated during the whole life cycle of a wind farm, from positioning and site surveys through construction, operation, and decommissioning (Tougaard et al., 2009; Kastelein et al., 2017; Mooney et al.,

10.3389/fmars.2023.1153843

2020; Galparsoro et al., 2022). Underwater noise from each of these phases has the potential to negatively impact aquatic life in several ways (Pangerc et al., 2016; Mooney et al., 2020; Tougaard et al., 2020; Han and Choi, 2022; Popper et al., 2022). Recently, several studies have been reported on the effects of environmental changes caused by the construction and operation of offshore wind farms on the marine ecosystem (Vaissière et al., 2014; Hall et al., 2020). Of these, most studies reported negative impacts from offshore wind farms, mostly related to birds, marine mammals, and ecosystem structure (Galparsoro et al., 2022). On the other hand, positive effects related to reef effects on fish and macroinvertebrates were less reported (Wilhelmsson et al., 2006; Bergström et al., 2013; Bray et al., 2016; Dannheim et al., 2020; Galparsoro et al., 2022).

Since pile-driving noise has an extremely high sound pressure level, studies on underwater noise have mostly focused on pile-driving noise generated during construction (Reinhall and Dahl, 2011; Dahl et al., 2015; Tsouvalas, 2020; Han and Choi, 2022). On the other hand, the underwater noise generated during wind turbine operation is relatively lower than that generated during pile installation, and thus fewer studies have examined its effects on marine ecosystems (Madsen et al., 2006; Thomsen et al., 2006; Gill et al., 2012; Thomsen et al., 2015; Mooney et al., 2020; Tougaard et al., 2020; Stöber and Thomsen, 2021). However, advances in offshore wind power technology enable the construction of taller wind turbines with larger blades. This can increase the mechanical forces acting on the gears and bearings, which increases underwater noise during operation (Marmo et al., 2013; Mooney et al., 2020; Tougaard et al., 2020; Stöber and Thomsen, 2021). In fact, it has been reported that the operational noise tends to increase in noise level with a nominal power of 13.6 dB/decade (Tougaard et al., 2020).

The operational noise mainly originates from vibrations caused by the movement of the various mechanical parts of a wind-turbine nacelle. The mechanical vibrations, which are generated continuously during turbine operation, are transmitted downward through the tower and radiate into the water (Tougaard et al., 2009; Amaral et al., 2020; Tougaard et al., 2020). It was reported that operational noise consists of tonal components with frequencies lower than 1 kHz, which typically correspond to the gear mesh frequencies of the gearbox and their harmonics (Pangerc et al., 2016; Tougaard et al., 2020). The gear mesh frequency is determined by multiplying the number of teeth by the rotational speed of the gear, and the properties of operational noise depend on the specifications of the gear and the turbine operation parameters.

A few studies have been conducted to quantify operational noise, but only Pangerc et al. (2016) have investigated operational noise over a wide range of operational conditions. In this study, we report the acoustic properties of underwater noise generated by a jacket-type wind turbine during operation based on measurements performed over 10 days at a wind-speed range from 0 to 20 m/s. The measured underwater noise is converted into a power spectral density (PSD) to analyze the frequencies and levels of the peak components relative to the wind speed and rotor speed. In addition, we investigated the correlation between underwater operational noise and the tower vibration acceleration signal of the wind turbine by simultaneously measuring those two signals for an additional 24 hours.

2 Field measurements

The underwater operational noise from the offshore wind turbine at the Southwest Offshore Wind Farm off the southwest coast of Korea (Figure 1) was measured twice. This wind farm contains 20 3-MW wind turbines: 19 with jacket-type foundations and 1 with a suction-type foundation. Underwater operational noise was first measured from turbine #16, located on the northernmost edge of the wind farm, for about 10 days, from February 24 to March 5, 2021. The bathymetry in the wind farm was relatively flat. The nominal water depth at the measurement site was 12 m, but it was measured to fluctuate up to ±3.6 m due to the tidal difference during the measurement period.

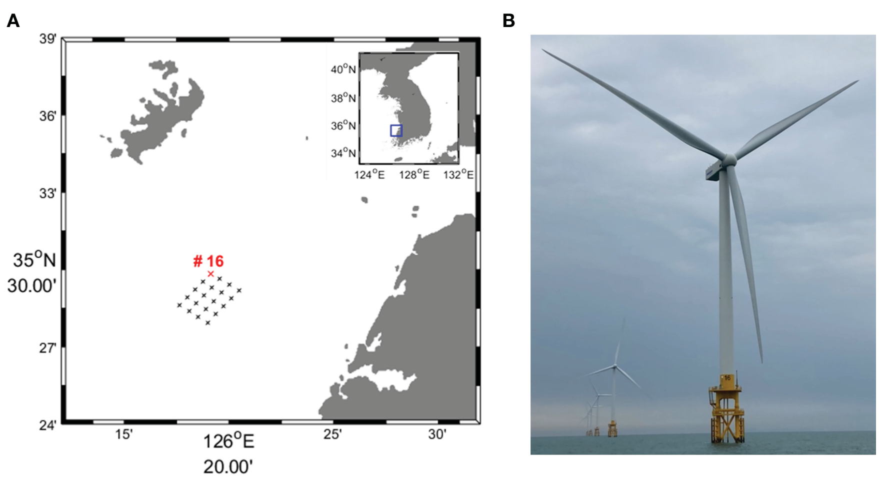

FIGURE 1
(A) Location of the Southwest Offshore Wind Farm, consisting of 20 offshore wind turbines (cross). The red cross indicates the location of turbine #16. **(B)** Photograph of wind turbine #16.

Acoustic data were received at a sampling frequency of 96 kHz using a self-recording hydrophone (SM3M, Wildlife Acoustics, USA) that was moored about 4 m above the seabed. The recorder was installed approximately 70 m away from turbine #16 (35° 29′ 53.13″N 126° 19′ 7.80″E) in the north direction of the wind farm where there are no other wind turbines to avoid noise interference from other wind turbines. The receiving voltage sensitivity of the hydrophone (standard, High Tech Inc., USA) was −164.4 5 dB re 1 V/μPa over the frequency band from 2 Hz to 48 kHz. A depth recorder (U20-001-03, Onset, USA) was installed on the hydrophone frame to monitor the deployment depth.

The acoustic data received for about 10 days were divided into time segments of 597 seconds, with a time interval of 3 seconds between each time segment. From each segment, 1,193 PSDs in dB re 1 $\mu Pa^2/Hz$ using Welch's method (Welch, 1967) with 1 second, 50% overlapping, and a Hanning window was calculated. And then the PSDs were intensity-averaged to represent the PSD for 10 minutes. The receiving voltage sensitivity of the hydrophone was then corrected. Among all the intensity-averaged PSDs, those estimated to contain noise other than the operational noise of offshore wind turbine, such as ship noise, were removed. Therefore, 1,095 PSDs were finally used for operational noise analysis. In addition, to investigate the correlation between the pressure level of operational turbine noise and the rotor speed of the wind turbine, the band pressure levels were estimated, which can be obtained by summing the PSDs estimated over the frequency band of interest (Yang et al., 2018). The frequency band of 60 to 500 Hz was selected in our case. A detailed description will be given in section 3.1.

The 10-minute averaged wind speed and rotor speed of the wind turbine during acoustic measurements were obtained from the supervisory control and data acquisition (SCADA) system attached to the wind turbine and provided by the Korea Offshore Wind Power Co., Ltd. The cut-in speed of the wind turbine was 3 m/s, the cut-out speed to protect the wind turbine from damage was 20 m/s, and the rated wind speed was 10 m/s. At or above the rated wind speed, the rotor speed is fixed at 10.7 rpm, producing a nominal maximum power output of 3 MW.

As mentioned in the Introduction, the operational noise is reported to be caused by tower vibration, which was not measured directly from the tower during the first measurement window. Therefore, a second measurement of underwater operational noise was performed along with tower vibration measurement at approximately the same location (35° 29′ 53.08″ N 126° 19′ 8.18″E) as the first measurement. The configuration and settings for the acoustic receiver system were the same as for the first measurement. On November 17, 2021, tower vibration was measured for 24 hours, beginning at 14:00 local time, using a vibrometer system, consisting of a miniature triaxial IEPE accelerometer (141A100, YMC Piezotronics Inc, China) and a data acquisition system (DT9837A, Data Translation Inc, USA) that was mounted on the inner wall of the tower. The frequency range of the accelerometer provided by the manufacturer was 0.5 to 5,000 Hz with ±10% accuracy. However, to accommodate the maximum file size, the vibration acceleration signal was digitized at a sampling frequency of 1 kHz and saved in a text file format during the 24-hour vibration data acquisition. The magnitude of the triaxial acceleration signals was calculated as the square root of the sum of the squares of the three-direction components (Vähä-Ypyä et al., 2015) and then was short-time Fourier transformed with 1-second Hamming windows to obtain the spectrogram.

3 Result

3.1 Acoustic characteristics of underwater operational noise with wind speed variation

A comparison between wind speed and rotor speed during the first measurement period is shown in Figure 2A. The wind speeds varied between 0.6 and 19.8 m/s over 9 days 5 hours. The wind turbine started operating at the cut-in wind speed (3 m/s) with a rotor speed of about 6.4 rpm. The rotor speed was maintained at ~6.4 rpm until the wind speed increased to about 4.8 m/s. After that, the rotor speed increased as the wind speed increased, but it was fixed at about 10.7 rpm from a wind speed of ~8 m/s, which is 2 m/s lower than the designed rated wind speed. Wind speeds between 3 and 8 m/s correlated highly with rotor speeds between 6.4 and 10.7 rpm, with an r-value of 0.88. The reason for the difference between the designed and measured rated wind speeds might be that the wind speed measured by the SCADA system was lower than the actual wind speed due to disturbance from the blades during turbine operation.

To investigate the correlation between underwater operational noise and wind speed and rotor speed, the intensity-averaged PSD estimated per 10 minutes is assumed to represent the PSD of the 10-minute averaged wind turbine rotor speed during acoustic measurements. Therefore, the 10-minute averaged rotor speed is referred to as simply the rotor speed. Figure 2B shows the spectrogram of underwater noise obtained using the PSDs estimated during the 9 days 5 hours of the first measurement window. Because the dominant tonal components of underwater noise caused by turbine operation occurred mostly at frequencies below 500 Hz, the spectrogram is shown up to 500 Hz. The wind speed and rotor speed at the same time as the spectrogram are shown in Figure 2A. A strong tonal component was observed at a frequency of ~99 Hz, along with its harmonics at 198, 297, and 396 Hz, when the wind speed was higher than the rated wind speed (approximately 8 m/s) and the rotor speed was constant at ~10.7 rpm. Interestingly, the tone at ~198 Hz had the strongest energy. In addition, several tonal components were observed at frequencies below 100 Hz. Those tonal components were observed even below the rated wind speed, varied with time, and showed a high correlation with wind and rotor speed variations. Tonal components caused by operational noise appeared to occur even below 60 Hz, but they were mostly masked by background noise with a semi-diurnal cycle coincident with the tidal variation measured by the depth recorder. The low-frequency noise below ~60 Hz was estimated to be flow noise caused by the tidal current in the region, which is beyond the scope of this paper because it has no correlation with the operational noise.

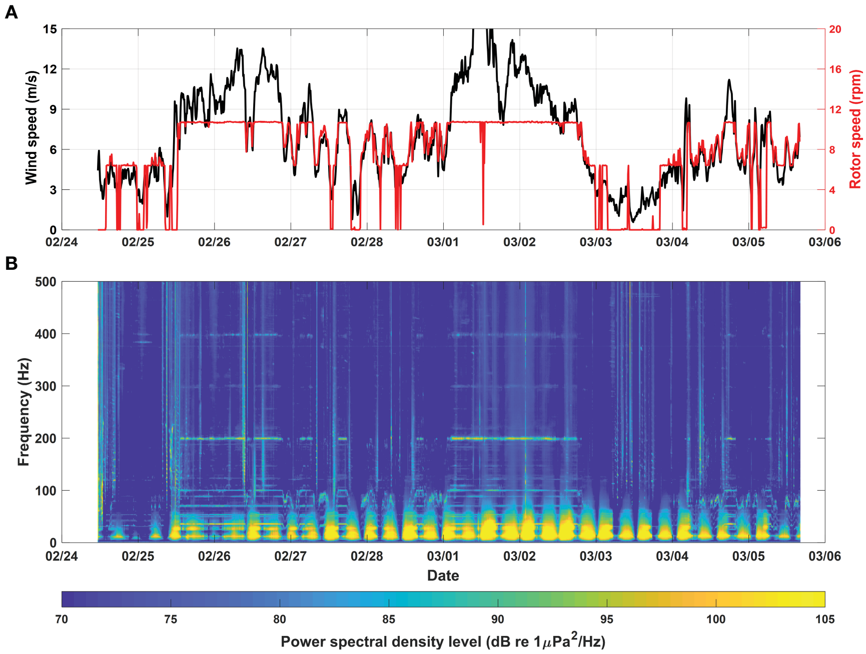

FIGURE 2
(A) Comparison of wind speed and rotor speed during the first measurement window. **(B)** Spectrogram of underwater noise measured approximately 70 m from wind turbine #16 over a period of approximately 10 days.

Figure 3 shows the average PSDs of each of the seven stages divided by 1-rpm intervals over the rotor speed range from 5.5 to 10.5 rpm. These are the averages of PSDs from at least 10 hours at each stage, with about 82 hours at the last stage. The first stage corresponds to rotor speeds below 5.5 rpm, and in most cases, was 0 rpm because the rotor was not running. The second stage contains the rotor speed of 6.4 rpm, which occurred at wind speed ranges from 3 to 4.8 m/s. The seventh stage corresponds to a rotor speed higher than 10.5 rpm. Cases with a rated rotor speed of 10.7 rpm that occurred when the measured wind speed was higher than ~8 m/s are included in the seventh stage. Noteworthy features were observed in the frequency range of ~65 to 100 Hz when the rotor was running. From the third stage, corresponding to a rotor speed between 6.5 and 7.5 rpm, the peak frequency in this frequency band tended to shift from ~70 to 99 Hz as rotor speed increased. Another feature is the strong tone generated at ~198 Hz when the rotor

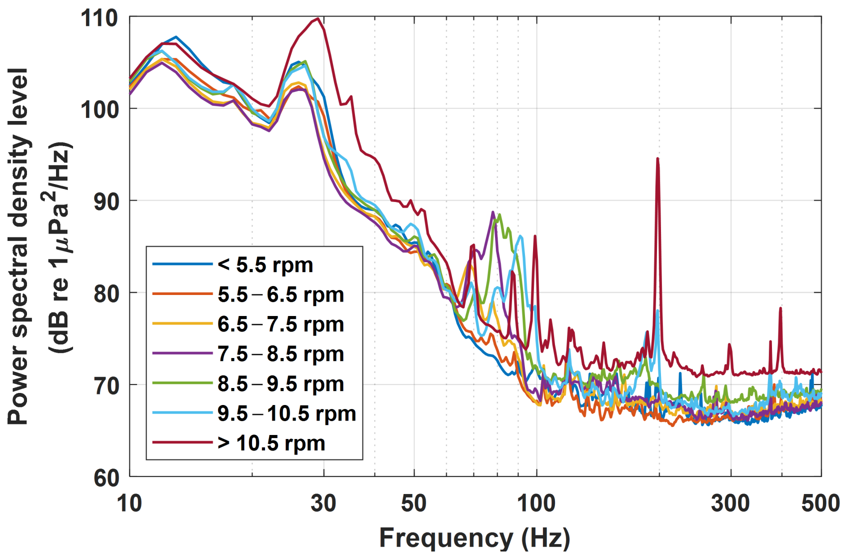

FIGURE 3
Average power spectral densities in seven stages divided at 1-rpm intervals across the measured rotor-speed range.

speed reached its rated speed, as shown in Figure 2. The PSD at ~198 Hz showed the highest level (~94.6 dB re 1 μPa^2/Hz) in the last stage including the rated rotor speed, but it decreased to ~78.0 dB re 1 μPa^2/Hz in the sixth stage, when the rotor speed was between 9.5 and 10.5 rpm. In the subsequent lower stages, the PSD converged to that of the surrounding frequency bands. The strong PSD level at ~198 Hz seems to be the second harmonic component of the tone observed at ~99 Hz, as discussed in Figure 2B. The third and fourth harmonic components were observed at frequencies of ~297 and ~396 Hz, respectively, at the last stage, but their PSD levels were much weaker than that at 198 Hz. These harmonic components are presumed to be the gear mesh frequency of the gearbox and its harmonics, and a detailed discussion will be given in section 4.

We next investigated the correlation between the band pressure level of operational turbine noise and rotor speed to determine the energy change in operational noise with rotor speed. As mentioned above, because the operational noise seems to be masked by strong tidal current noise at frequencies below 60 Hz, we obtained the band pressure level by summing the PSDs in the frequency band of 60 to 500 Hz. Figure 4 shows the band pressure levels as a function of rotor speed. Overall, the band pressure level tends to increase with rotor speed in the range from 6.4 to 10.7 rpm. However, the increase rate shows a large difference around 8 rpm. That is, the pressure level increases with a slope of ~3.1 dB/rpm below ~ 8 rpm but is nearly constant after that. As shown in Figure 3, the main energy of the operational turbine noise was dominated by peaks in the 70–100 Hz frequency range, with a strong tone occurring at ~198 Hz. In addition, the peak level in the 70–100 Hz frequency range increased with rotor speed, but from the fourth stage, which corresponds to the rotor speed range from 7.5 to 8.5 rpm, the peak level did not increase with rotor speed but tended to decrease slightly, shifting only the peak frequency upward. This effect seems to be the cause of the slope difference shown in Figure 4. After reaching the rated rotor speed, the peak frequency no longer increases at ~ 99 Hz. From that point, it and its harmonic components contribute to the energy increase in operational turbine noise.

3.2 Correlation between underwater operational noise and tower vibration

Because we did not measure tower vibration during the first measurement window, a second measurement of underwater operational noise was conducted along with tower vibration measurement for 24 hours. However, in the vibration acceleration signals during those 24 hours, data with a meaningful signal-to-noise level were collected only when the rotor speed was higher than about 8 rpm, which occurred only during the last 6 hours.

The tower vibration of the wind turbine is reported to be caused by various sources, such as the wind loads on the rotor blades and tower, the inertial forces of the rotating parts, the natural frequencies of various components, and the mechanical forces in the power transmission system including the gear meshing process (Escaler and Mebraki, 2018; Awada et al., 2021). Figure 5 shows spectrograms of the underwater operational noise and vibration acceleration signals from the tower for 6 hours, along with the wind and rotor speeds during the same time. The spectral levels of underwater operational noise and tower vibration were intensity-averaged every minute, whereas the wind and rotor speeds in Figure 5 are 10-minute averaged values. Since the flow noise was dominated at frequencies

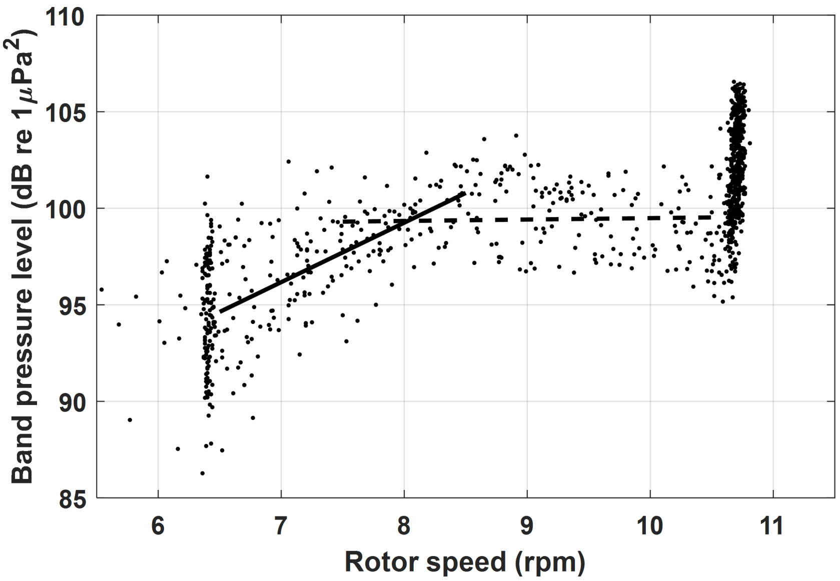

FIGURE 4
Band pressure levels of underwater operational noise measured during the first measurement window, shown as a function of rotor speed. The band pressure level was obtained by summing the PSDs in the frequency band from 60 to 500 Hz. Solid and dashed lines indicate slopes of ~3.1 and ~0.1 dB/rpm, respectively.

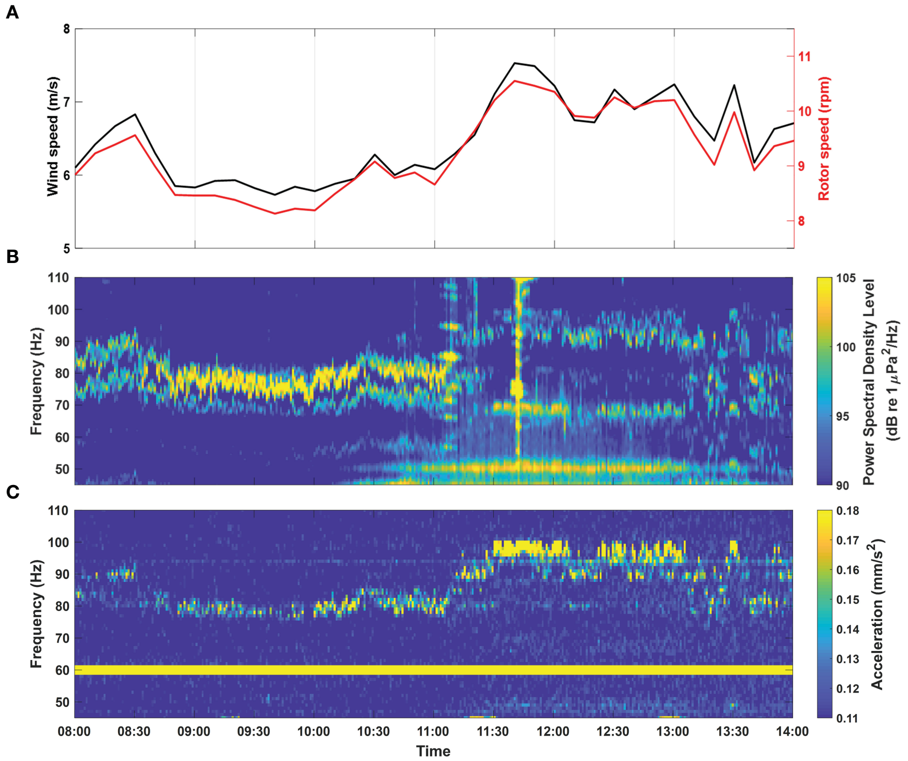

FIGURE 5
(A) Comparison of wind speed and rotor speed for 6 hours beginning at 08:00 local time on November 18, 2021. **(B, C)** Spectrograms of the underwater operational turbine noise and vibration acceleration signals from the wind turbine tower, respectively, measured during the same time.

below 60 Hz, the comparison was carried out at frequencies higher than 60 Hz. During the 6-hour measurement period, the wind speed and rotor speed tended to increase in the ranges of 5.7–7.5 m/s and 8.1–10.6 rpm, respectively. Unfortunately, the second measurement window did not contain any conditions above the rated wind speed. Therefore, it was not possible to measure the harmonic characteristics of underwater operational noise generated above the rated rotor speed. Interestingly, the frequencies of the dominant tower vibration acceleration signal and underwater operational noise were both in a range from ~72 to 100 Hz; overall, their frequency shifts correlated highly with each other and with wind speed and rotor speed, all with r-values higher than 0.95. These results imply that underwater noise during turbine operation was caused by tower vibration that was itself caused by rotor operation. The peak frequencies of both signals appear to be associated with the gear mesh frequency of the gearbox, which will be discussed in Section 4.

For the underwater operational noise shown in Figure 5B, the dominant energy occurred around 80 Hz, which corresponds to relatively low rotor speeds, below ~9 rpm, that occurred before about 11:10. Those results are consistent with the results from the first measurement window presented in Figure 3. On the other hand, in the vibration acceleration signals shown in Figure 5C, the highest energy occurred between ~95 and 100 Hz, after 11:30, when the rotor speed was ~10 rpm. The reason for the opposite trend in the magnitude of underwater operational noise and the tower acceleration signal could be the uncertainty of the receiving sensitivity associated with the frequency of the accelerometer.

4 Summary and discussion

The purpose of this study was to investigate the properties of underwater operational noise from offshore wind turbines according to wind speed variation as part of a preliminary investigation to evaluate the effects of underwater noise from offshore wind farms on marine ecosystems. All measurements were performed on a 3-MW jacket-type wind turbine in the Southwest Offshore Wind Farm off the southwest coast of Korea. During the measurement period, the wind turbine started operating with a rotor speed of ~6.4 rpm at a cut-in wind speed of 3 m/s, and the rotor speed was kept constant until the wind speed reached ~4.8 m/s. Then, the rotor speed increased linearly with wind speed, with a correlation coefficient r of 0.88, until it was fixed at ~10.7 rpm when the wind speed was ~8 m/s or higher. The wind speed measured by the SCADA system attached to the wind turbine might have been underestimated by ~20% due to disturbances caused by the blades during turbine operation.

Between rotor speeds of 6.4 and 10.7 rpm, which correspond to the cut-in rotor speed and the rated rotor speed, respectively, the frequencies of the dominant peaks below ~ 99 Hz shifted in the positive frequency direction with wind speed and rotor speed. In addition, the band pressure level for the frequency band from 60 to 500 Hz tended to increase with rotor speed. However, the increase rate was very small above a rotor speed of ~8 rpm because the peak level in the 70–100 Hz frequency range did not increase with rotor speed; only the peak frequency shifted upward. On the other hand, when the wind speed was higher than the rated wind speed, the rotor speed was held constant at ~10.7 rpm. In that case, multiple tones were observed in the PSD. A strong tonal component at ~ 99 Hz and its harmonics especially contributed to the increased energy of operational turbine noise. In the second window, we measured the underwater noise and tower vibration of the wind turbine simultaneously for wind conditions below the rated wind speed. The frequencies of the dominant tower vibration acceleration signal and underwater operational noise both varied within the range from ~72 to 100 Hz, and their frequency shifts were highly correlated with each other and with wind speed and rotor speed.

The acoustic properties of underwater operational noise correlated highly with wind speed, rotor speed, and tower vibration. However, it was difficult to investigate underwater noise at frequencies below 60 Hz because it was masked by flow noise from tidal currents. Figure 6A shows a spectrogram for the period from 18:00 on February 28 to 09:00 on March 1, obtained using 1-minute intensity-averaged PDSs. During that period, the wind speed varied from ~4.0 to 13.5 m/s. Consequently, the rotor speed changed from ~6.8 to 10.7 rpm; after 01:10 on March 1, the rotor was maintained at the rated speed of 10.7 rpm. Two periods with minimal flow noise and different wind speeds were selected for this investigation: 23:14 on February 28 and 04:44 on March 1, which are indicated by arrows T1 and T2, respectively, in Figure 6A. The rotor speed around T1 was less than the rated rotor speed, and that around T2 was the rated rotor speed. Interestingly, several tonal components can be observed at frequencies below 60 Hz during those two times.

Figure 6B shows the PSD for the underwater noise measured at T1, when the wind and rotor speeds were 6.3 m/s and 9.8 rpm, respectively. Two harmonic components were observed. One component has a first peak frequency of 89 Hz, and its first harmonic is observed at 178 Hz, marked with a blue 1X and 2X, respectively, in Figure 6B. The second and third harmonics could then be expected to exist at 267 and 356 Hz, respectively; relatively weak harmonic components were observed around 267 and 356 Hz, marked with 3X and 4X, respectively, in the spectrogram. These are followed by two relatively strong peaks at 370 and 375 Hz that represent an unknown noise that appears to be system noise. As mentioned in the Introduction, the gear mesh frequency is determined by multiplying the number of teeth on the gear by

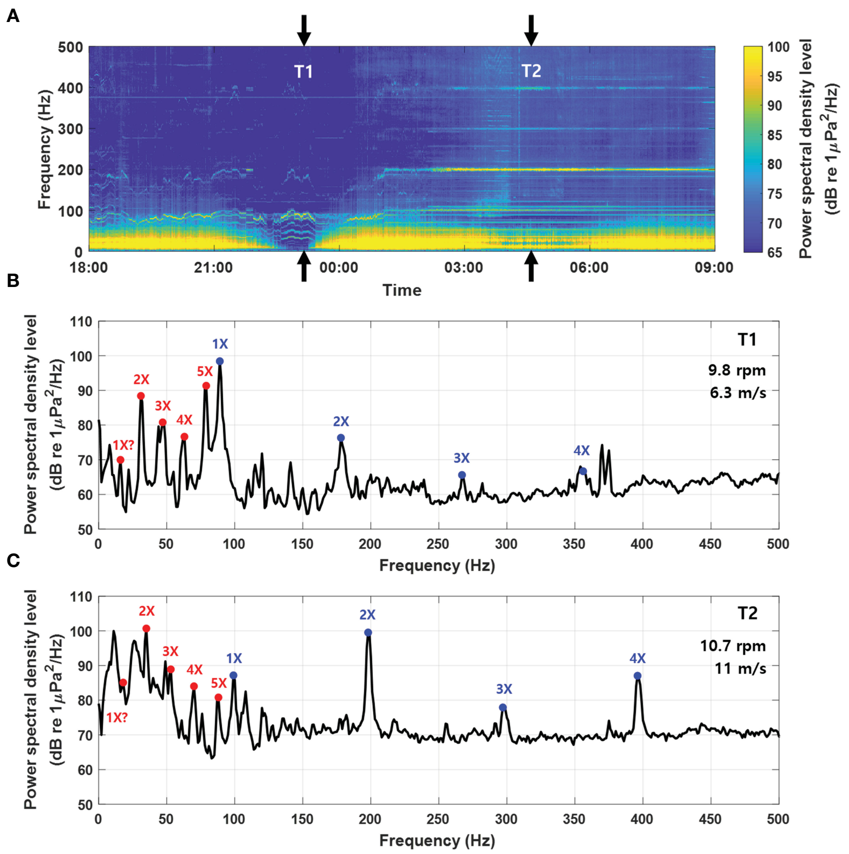

FIGURE 6
(A) Spectrogram for the 15 hours between 18:00 on February 28 and 09:00 on March 1, 2021. **(B)** PSD for underwater operational noise measured at T1, when the wind and rotor speeds were 6.3 m/s and 9.8 rpm, respectively. **(C)** PSD at T2, when the wind and rotor speeds were 11.0 m/s and 10.7 rpm, respectively. The red and blue dots indicate two gear mesh frequencies and their harmonics.

the shaft rotational speed. From this observation, the number of teeth on the corresponding gear is estimated to be approximately 545. The first peak of the second harmonic, marked with a red 2X in Figure 6B, was observed at about 32 Hz. However, the subsequent three peaks were observed at a frequency interval of about 16 Hz. Because harmonic components exist at multiples of the first peak frequency, a 16-Hz interval would indicate that the first peak exists at 16 Hz and not 32 Hz. In fact, a relatively small peak, marked with a red 1X in the spectrogram, does exist at ~16 Hz. The number of teeth on another gear can then be estimated to be about 98.

The spectrogram at the rated rotor speed of 10.7 rpm is shown in Figure 6C, which corresponds to T2. As reported above, the first peak of the harmonics at the rated rotor speed occurred at 99 Hz, which is marked with a blue 1X, and its three harmonics were observed at frequencies that are multiples of 99 Hz. In this case, the number of gear teeth was estimated to be about 555, which is a difference of 10 from the 545 estimated when the rotor speed was 9.8 rpm. At T2, the dominant peak at the lowest frequency was observed at 35 Hz, which is marked with a red 2X in Figure 6C. Among the peaks distributed between this peak and that at 99 Hz were three harmonic components with a frequency interval of ~18 Hz. The first peak frequency can then be estimated to be 18 Hz using the same method described above. A weak peak might be present at 18 Hz on the spectrogram, but it is difficult to accurately identify. The number of gear teeth would be estimated to be about 101 using 18 Hz as the gear mesh frequency and a rotor speed of 10.7 rpm. For the two cases shown here, the number of gear teeth estimated using the rotor speeds and gear mesh frequencies differed slightly. That difference might be caused by discrepancies between the actual instantaneous rotor speeds and our calculations because the rotor speeds used here were values averaged over 10 minutes. Unfortunately, the manufacturer did not provide the exact specification of the gearbox, including number of teeth.

The underwater operational noise of a wind turbine was measured over wide ranges of wind speeds and rotor speeds, and its acoustic properties have been presented in this paper. However, the results of this paper are limited to underwater noise generated by a 3-MW jacket-type wind turbine in a specific area off the southwest coast of Korea. Further studies are needed to characterize the properties of underwater operational noise generated by wind turbines of other types and sizes and to determine how it is spatially distributed in regions with different geoacoustic properties.

Data availability statement

The original contributions presented in the study are included in the article/supplementary material. Further inquiries can be directed to the corresponding author.

Author contributions

YY, D-GH, and JC contributed to conception and design of the study. YY performed data collection and analysis. YY and D-GH wrote the primary writing. JC contributed to the supervision and validation of the measurement. All authors contributed to manuscript revision, read, and approved the submitted version.

Funding

This work was partly supported by Korea Institute of Energy Technology Evaluation and Planning (KETEP) grant funded by the Korea government (MOTIE) (20203030020080, Environmental Impact Analysis on the Offshore Wind Farm and Database System Development) and National Research Foundation of Korea (NRF) grant funded by the Korea government (MSIT) (2020R1A2C2007772).

Conflict of interest

Author Dong-Gyun Han has founded Oceansounds Inc. since submitting this manuscript.

The remaining authors declare that the research was conducted in the absence of any commercial or financial relationships that could be construed as a potential conflict of interest.

Publisher's note

References

Amaral, J. L., Vigness-Raposa, K., Miller, J. H., Potty, G. R., Newhall, A., and Lin, Y.-T. (2020). The underwater sound from offshore wind farms. *Acoust. Today* 16, 13–21. doi: 10.1121/at.2020.16.2.13

Awada, A., Younes, R., and Ilinca, A. (2021). Review of vibration control methods for wind turbines. *Energies* 14 (11), 3058. doi: 10.3390/en14113058

Bergström, L., Sundqvist, F., and Bergström, U. (2013). Effects of an offshore wind farm on temporal and spatial patterns in the demersal fish community. *Mar. Ecol. Prog. Ser.* 485, 199–210. doi: 10.3354/meps10344

Bilgili, M., Yasar, A., and Simsek, E. (2011). Offshore wind power development in Europe and its comparison with onshore counterpart. *Renew. Sustain. Energy Rev.* 15, 905–915. doi: 10.1016/j.rser.2010.11.006

Bray, L., Reizopoulou, S., Voukouvalas, E., Soukissian, T., Alomar, C., Vázquez-Luis, M., et al. (2016). Expected effects of offshore wind farms on Mediterranean marine life. *J. Mar. Sci. Eng.* 4, 18. doi: 10.3390/jmse4010018

Cranmer, A., and Baker, E. (2020). The global climate value of offshore wind energy. *Environ. Res. Lett.* 15, 054003. doi: 10.1088/1748-9326/ab7667

Dahl, P. H., de Jong, C. A. F., and Popper, A. N. (2015). The underwater sound field from impact pile driving and its potential effects on marine life. *Acoust. Today* 11, 18–25.

Dannheim, J., Bergström, L., Birchenough, S. N. R., Brzana, R., Boon, A. R., Coolen, J. W. P., et al. (2020). Benthic effects of offshore renewables: identification of knowledge gaps and urgently needed research. *ICES J. Mar. Sci.* 77, 1092–1108. doi: 10.1093/icesjms/fsz018

Escaler, X., and Mebraki, T. (2018). Full-scale wind turbine vibration signature analysis. *Machines* 6, 63. doi: 10.3390/machines6040063

Galparsoro, I., Menchaca, I., Garmendia, J. M., Borja, Á., Maldonado, A. D., Iglesias, G., et al. (2022). Reviewing the ecological impacts of offshore wind farms. *NPJ Ocean Sustainability* 1, 1. doi: 10.1038/s44183-022-00003-5

Gill, A. B., Bartlett, M., and Thomsen, F. (2012). Potential interactions between diadromous fishes of U.K. conservation importance and electromagnetic fields and subsea noise from marine renewable energy developments. *J. Fish Biol.* 81 (2), 664–695. doi: 10.1111/j.1095-8649.2012.03374.x.

Hall, R., João, E., and Knapp, C. W. (2020). Environmental impacts of decommissioning: onshore versus offshore wind farms. *Environ. Impact Assess Rev.* 83, 106404. doi: 10.1016/j.eiar.2020.106404

Han, D. G., and Choi, J. W. (2022). Measurements and spatial distribution simulation of impact pile driving underwater noise generated during the construction of offshore wind power plant off the southwest coast of Korea. *Front. Mar. Sci.* 8, 1978. doi: 10.3389/fmars.2021.654991

Kastelein, R. A., Jennings, N., Kommeren, A., Helder-Hoek, L., and Schop, J. (2017). Acoustic dose-behavioral response relationship in sea bass (Dicentrarchus labrax) exposed to playbacks of pile driving sounds. *Mar. Environ. Res.* 130, 315–324. doi: 10.1016/j.marenvres.2017.08.010

Madsen, P. T., Wahlberg, M., Tougaard, J., Lucke, K., and Tyack, P. (2006). Wind turbine underwater noise and marine mammals: implications of current knowledge and data needs. *Mar. Ecol. Prog. Ser.* 309, 279–295. doi: 10.3354/meps309279

Marmo, B., Roberts, I., Buckingham, M. P., King, S., and Booth, C. (2013). Modelling of noise effects of operational offshore wind turbines including noise transmission through various foundation types. *Scot. Mar. Freshw. Sci.* 4, 100. doi: 10.7489/1521-1.

Mooney, T. A., Andersson, M. H., and Stanley, J. (2020). Acoustic impacts of offshore wind energy on fishery resources: an evolving source and varied effects across a wind farm's lifetime. *Oceanography* 33, 82–95. doi: 10.5670/oceanog.2020.408

Oh, K. Y., Kim, J. Y., Lee, J. K., Ryu, M. S., and Lee, J. S. (2012). An assessment of wind energy potential at the demonstration offshore wind farm in Korea. *Energy* 46, 555–563. doi: 10.1016/j.energy.2012.07.056

Pangerc, T., Theobald, P. D., Wang, L. S., Robinson, S. P., and Lepper, P. A. (2016). Measurement and characterisation of radiated underwater sound from a 3.6 MW monopile wind turbine. *J. Acoust. Soc Am.* 140, 2913–2922. doi: 10.1121/1.4964824

Popper, A. N., Hice-Dunton, L., Jenkins, E., Higgs, D. M., Krebs, J., Mooney, T. A., et al. (2022). Offshore wind energy development: research priorities for sound and vibration effects on fishes and aquatic invertebrates. *J. Acoust. Soc Am.* 151, 205–215. doi: 10.1121/10.0009237

Reinhall, P. G., and Dahl, P. H. (2011). Underwater mach wave radiation from impact pile driving: theory and observation. *J. Acoust. Soc Am.* 130, 1209–1216. doi: 10.1121/1.3614540

Stöber, U., and Thomsen, F. (2021). How could operational underwater sound from future offshore wind turbines impact marine life? *J. Acoust. Soc Am.* 149, 1791–1795. doi: 10.1121/10.0003760

Thomsen, F., Gill, A., Kosecka, M., Andersson, M., Andre, M., Degraer, S., et al. (2015). MaRVEN–environmental impacts of noise, vibrations and electromagnetic emissions from marine renewable energy. Final Study Report No. RTD-KI-NA-27-738-EN-N.

Thomsen, F., Ludemann, K., Kafemann, R., and Piper, W. (2006). Effects of offshore wind farm noise on marine mammals and fish. *Biola Hamburg: Germany behalf COWRIE Ltd* 62, 1–62.

Tougaard, J., Henriksen, O. D., and Miller, L. A. (2009). Underwater noise from three types of offshore wind turbines: estimation of impact zones for harbor porpoises and harbor seals. *J. Acoust. Soc Am.* 125, 3766–3773. doi: 10.1121/1.3117444

Tougaard, J., Hermannsen, L., and Madsen, P. T. (2020). How loud is the underwater noise from operating offshore wind turbines? *J. Acoust. Soc Am.* 148, 2885–2893. doi: 10.1121/10.0002453

Tsouvalas, A. (2020). Underwater noise emission due to offshore pile installation: a review. *Energies* 13, 3037. doi: 10.3390/en13123037

Vähä-Ypyä, H., Vasankari, T., Husu, P., Mänttäri, A., Vuorimaa, T., Suni, J., et al. (2015). Validation of cut-points for evaluating the intensity of physical activity with accelerometry-based mean amplitude deviation (MAD). *PloS One* 10 (8), e0134813. doi: 10.1371/journal.pone.0134813

Vaissière, A. C., Levrel, H., Pioch, S., and Carlier, A. (2014). Biodiversity offsets for offshore wind farm projects: the current situation in Europe. *Mar. Policy* 48, 172–183. doi: 10.1016/j.marpol.2014.03.023

Welch, P. D. (1967). The use of fast Fourier transform for the estimation of power spectra: a method based on time averaging over short, modified periodograms. *Audio Electroacous IEEE Trans.* 15, 70–73. doi: 10.1109/TAU.1967.1161901

Wilhelmsson, D., Malm, T., and Öhman, M. C. (2006). The influence of offshore windpower on demersal fish. *ICES J. Mar. Sci.* 63, 775–784. doi: 10.1016/j.icesjms.2006.02.001

Yang, C. M., Liu, Z. W., Lü, L. G., Yang, G. B., Huang, L. F., and Jiang, Y. (2018). Observation and comparison of tower vibration and underwater noise from offshore operational wind turbines in the East China Sea bridge of shanghai. *J. Acoust. Soc Am.* 144, EL522–EL527. doi: 10.1121/1.5082983

frontiers | Frontiers in Marine Science

TYPE Original Research
PUBLISHED 16 October 2023
DOI 10.3389/fmars.2023.1134776

Check for updates

OPEN ACCESS

EDITED BY
Per Reinhall,
University of Washington, United States

REVIEWED BY
Vanesa Magar,
Center for Scientific Research and Higher Education in Ensenada (CICESE), Mexico
Zhongchang Song,
Xiamen University, China

*CORRESPONDENCE
Yaxi Peng
y.peng@tudelft.nl

RECEIVED 30 December 2022
ACCEPTED 24 August 2023
PUBLISHED 16 October 2023

CITATION
Peng Y, Jarquin Laguna A and Tsouvalas A (2023) A multi-physics approach for modelling noise mitigation using an air-bubble curtain in impact pile driving. *Front. Mar. Sci.* 10:1134776.
doi: 10.3389/fmars.2023.1134776

A multi-physics approach for modelling noise mitigation using an air-bubble curtain in impact pile driving

Yaxi Peng[1*], Antonio Jarquin Laguna[2] and Apostolos Tsouvalas[1]

[1]Department of Structural Engineering, Delft University of Technology, Delft, Netherlands,
[2]Department of Maritime & Transport Technology, Delft University of Technology, Delft, Netherlands

Underwater noise from offshore pile driving has raised significant concerns over its ecological impact on marine life. To protect the marine environment and maintain the sustainable development of wind energy, strict governmental regulations are imposed. Assessment and mitigation of underwater noise are usually required to ensure that sound levels stay within the noise thresholds. The air-bubble curtain system is one of the most widely applied noise mitigation techniques. This paper presents a multi-physics approach for modeling an air-bubble curtain system in application to offshore pile driving. The complete model consists of four modules: (i) a compressible flow model to account for the transport of compressed air from the offshore vessel to the perforated hose located in the seabed; (ii) a hydrodynamic model for capturing the characteristics of bubble clouds in varying development phases through depth; (iii) an acoustic model for predicting the sound insertion loss of the air-bubble curtain; and (iv) a vibroacoustic model for the prediction of underwater noise from pile driving which is coupled to the acoustic model in (iii) through a boundary integral formulation. The waterborne and soilborne noise transmission paths are examined separately, allowing us to explore the amount of energy channeled through the seabed and through the bubble curtain in the water column. A parametric study is performed to examine the optimal configuration of the double bubble curtain system for various soil conditions and pile configurations. Model predictions are compared with measured data. The model allows for a large number of simulations to examine different configurations of a single bubble curtain and a double big bubble curtain.

KEYWORDS

underwater noise, offshore pile driving, soil conditions, vibroacoustics, noise mitigation, air-bubble curtains

1 Introduction

Offshore wind energy has been the main contributor to a sustainable and carbon-free energy supply. The monopiles are the main foundation of offshore wind turbines. The installation of the piles generates a significant amount of underwater noise, which causes serious concerns for the marine environment (Bailey et al., 2010; Hastie et al., 2019). To minimize the impact of noise emission on the marine ecosystem system and to protect the fish, invertebrates, crustaceans and marine mammals (Tidau and Briffa, 2016; Chahouri et al., 2022), strict regulations on the noise threshold have been imposed by the government in many countries (International Maritime Organization, 2014; Williams et al., 2014; National Oceanic and Atmospheric Administration, 2016; Merchant et al., 2022). To reduce noise levels at the source, vibratory installation of monopiles are utilized either by replacing or in combination with impact hammers. The change in the installation method can significantly alter the characteristics of the radiated wave field (Dahl et al., 2015; Tsouvalas and Metrikine, 2016b; Tsouvalas, 2020). Furthermore, the non-linear conditions at the pile-soil interface can have a substantial impact on the dynamic response of the pile and the wave field in the surrounding medium (Molenkamp et al., 2023; Tsetas et al., 2023).Various noise mitigation systems have been employed to block noise transmission in seawater, e.g., the air-bubble curtain system, the hydro-sound damper system, the noise mitigation screen and resonator-based noise mitigation systems (Lee et al., 2014; Verfuß, 2014; Nehls et al., 2016). The efficiency Hydro-Sound-Damper system (HSD) has been examined through measurements and offshore tests as shown in Elmer et al. (2012); Bruns et al. (2014), which indicates the significant influence of the soil conditions on the sound emsission and the effectiveness of the system. However, the HSD system is deployed in the pile vicinity and therefore any energy that is radiated into elastic waves in the soil cannot be blocked and can eventually leak back into the seawater column outside the HSD net. Moreover, the HSD net is based on linear principles of noise attenuation (resonances of the air-filled balloons and acoustic wave scattering) and as such the size of the elements attached to the net needs to be very large when it comes to dominant frequency ranges associated with large monopiles. Therefore, the efficiency of HSD nets still needs further investigation when it comes to noise radiation from large size monopiles (D>7-8m) that are installed nowadays. The innovative open-ended resonators were developed by AdBm Technologies and the University of Texas at Austin Lee et al. (2014). The acoustic behaviour of both the open-ended resonators and the encapsulated air bubbles was investigated through laboratory tests and open-water tests. Among these noise abatement technologies, the air-bubble curtain system is the most widely applied in the offshore industry. Before installing monopiles, perforated hoses are positioned at the seabed in a circle or an ellipse layout and air is injected from the air-compressor vessels through risers in connection with the hoses. The freely rising air bubbles are released from nozzles and create a layer of bubbly mixture. Significant noise reductions can be achieved by a large impedance mismatch between the seawater and the bubble-fluid mixture and the resonance of bubbles. Compared to the other sound abatement systems, the air-bubble curtain system is the only far-field noise mitigation technique deployed so far in full scale. The system can be positioned up to 200m away from the pile and can largely capture the energy channeled from the soil back into the water column. In contrast, the near-field noise mitigation systems, such as the hydro-sound damper system (Elmer et al., 2012; Bruns et al., 2014; Nehls et al., 2016) or noise mitigation screen can only mitigate the sound radiated directly from the pile surface into the seawater. The use of a double big bubble curtain system (DBBC) configuration is usually adopted for foundation piles with large dimensions, and can be used in combination with other mitigation techniques in the vicinity of the pile to achieve acceptable noise levels. The configuration of the bubble curtain is usually standard and is based on common engineering experiences.

Many noise prediction models for impact pile driving have been developed over the last decade (Reinhall and Dahl, 2011; Tsouvalas and Metrikine, 2013; Zampolli et al., 2013; Tsouvalas and Metrikine, 2014; Fricke and Rolfes, 2015; Lippert et al., 2016; Wilkes et al., 2016; Dahl and Dall'Osto, 2017; Lippert et al., 2018; Tsouvalas, 2020; Peng et al., 2021a). The sound levels are expected to exceed the limits of Sound Exposure and Peak pressure levels without the application of the noise abatement system. To examine the performance of an air-bubble curtain system, a semi-analytical model was developed in (Tsouvalas and Metrikine, 2016a). The dynamic interaction between the pile, water, soil, and air-bubble curtain is captured through a mode-matching technique. The acoustic properties of the bubble curtain are determined by an effective wavenumber theory (Commander and Prosperetti, 1989), assuming the bubbly layer is a homogeneous medium with mono-sized bubble distribution. The finite element (FE) model developed in (Lippert et al., 2017) uses a simplified approach by modeling the air bubble curtain with a fully absorbing layer. A model based on the hydrodynamic behavior of bubble breakup and coalescence is developed by Bohne et al. (Bohne et al., 2019). The various bubble generation and development phases are captured and the acoustic characteristics are determined with a depth- and frequency-dependent transfer function. The FE module, including the pile, water, soil and bubble layer described by the bubble dynamic model is used for the noise source generation and propagation. Subsequently, the bubble size distribution is optimized by the two fractions of bubbles, namely large and small bubbles in (Bohne et al., 2020). The results showed a reasonable agreement with the measurement data. A semi-analytical model (Peng et al., 2021b) is developed where the hydrodynamic module for describing the bubble formation process is coupled to the vibroacoustic model for noise prediction from pile driving through a boundary integral formulation. The results indicate that an accurate description of the acoustic characteristics of the bubbly layer is critical for modeling noise mitigation using the air-bubble curtain system. The performance of the air-bubble curtains can vary significantly in azimuth direction due to the inherent variations in the airflow circulation through the perforated pipes positioned on the seabed surface. As the air flow rate through the nozzle can have a significant impact on bubble generation and development, there is a need to determine the flow velocity of the air as generation and the development of the bubble curtain are sensitive to the initial conditions at the nozzle (Bohne et al., 2020).

In this paper, the authors developed a multi-physics model for modeling noise mitigation using the air-bubble curtain system. The complete model consists of four modules: (i) a compressible flow model to account for the transport of compressed air in the hose; (ii) a hydrodynamic model for capturing the characteristics of bubble clouds in varying development phases through depth and range; (iii) an acoustic model for predicting the sound insertion loss of the air-bubble curtain; and (iv) a vibroacoustic model for the prediction of underwater noise from pile driving which is coupled to the acoustic model in (iii) through a boundary integral formulation. The flow of the modeling activity is shown in Figure 1. The structure of the paper is as follows. In Section 2, the description of the compressible flow model is given together with the governing equations. The description of the hydrodynamic and acoustic models is given in Section 3. In Section 4, the vibroacoustic model for predicting the noise in the mitigated field are introduced. In Section 5, a sensitivity study is performed to examine the acoustic characteristics of the bubble curtain. In Section 6, the validation study based on an offshore installation campaign is presented. Finally, Section 7 gives an overview of the main conclusions of the paper.

2 Compressible flow model

In this Section, the pneumatic model is presented for modeling the transport of compressed air from the air-injection vessel to the perforated hose on the seabed. The governing equations are given and the field test is presented for examining the pressure variation along the hoses for various airflow rates.

2.1 Description of the model

An engineering model is being developed using compressible flow theory to predict the operational parameters of a given hose-nozzle configuration used for bubble curtain generation. The total amount of air that is being delivered by the series of compressors is used as the main input and given as a volumetric flow rate at free air delivery conditions (FAD[1]). The other input parameters consist of the density of seawater and air, water depth, and the geometrical characteristics of the feeding and perforated hose configuration. The results of the numerical model give the pressure distribution along the hose together with the average axial flow velocities and mass flow rates at each nozzle location. The total required upstream pressure considering the feeding hose can also be assessed.

The model considers a straight, horizontal hose with a constant diameter and uniform spacing of identical nozzles. The air is injected from from two sides of the hose. Hence, the model assumes symmetry and only half of the total length is required to characterize the flow and pressure distribution; this is represented through a zero flow boundary condition to make sure that all the air is depleted at 180° from the injected position. The hose is discretized into a fixed number of segments according to the total length L and the nozzle spacing S as shown in the schematic of Figure 2. As long as the number of segments is beyond 100, a regular polygonal approximation will closely resemble a circle and is visually indistinguishable for most practical purposes.

1 FAD conditions are defined at p = 101325Pa, T = 293.15K

2.2 Governing equations

For each segment i, isentropic compressible flow theory in combination with the state equation of the ideal gas law is used to obtain the mass flow rate $\dot{m}_{nz,i}$, across the nozzle with diameter d according to the following equations (Shapiro, 1953):

$$\dot{m}_{nz,i} = C_d \frac{\pi d^2}{4} \left(\frac{2\gamma}{\gamma - 1} P_i \rho_i \left[1 - \left(\frac{P_{hst}}{P_i} \right)^{\frac{\gamma-1}{\gamma}} \right] \left(\frac{P_{hst}}{P_i} \right)^{\frac{2}{\gamma}} \right)^{0.5} \quad (1)$$

$$\frac{P_i}{P_{hst}} = \left(1 + \frac{\gamma - 1}{2} M_i^2 \right)^{\frac{\gamma}{\gamma-1}} \quad (2)$$

$$M_i = \frac{U_i}{\sqrt{\gamma R T}} \quad (3)$$

Where the discharge coefficient $C_d = 0.55$ is used for each nozzle (Nehls and Bellmann, 2016), $\gamma = 1.402$ is the air adiabatic constant, $R = 287$J/kg/K is the specific air gas constant, $T = 291$K (18°C) is the air temperature, P_{hst} is the hydrostatic pressure outside the hose, P_i is the pressure inside the hose at each nozzle location, M_i and U_i are the Mach numbers and air velocities across the nozzles respectively. Conservation of mass is applied to the control volume of each segment to obtain the upstream mass flow rates $\dot{m}_i$ as a function of the flow rates through the nozzle and from the downstream segment.

$$\dot{m}_i = \dot{m}_{nz,i} + \dot{m}_{i+1} \quad (4)$$

Assuming that the velocity and fluid properties are constant across sections normal to the flow (i.e. no radial gradients), one-dimensional, isothermal compressible flow in pipes with a constant area is used to calculate the upstream pressure of each hose segment including friction. The pressure losses in each segment of length l include the friction factor f which is obtained by the Colebrook–White equation (Menon, 2015) according to the Reynolds number Re and hose roughness ϵ as described in the following equations:

$$(P_i^2 - P_{i+1}^2) = \frac{\dot{m}_i^2 RT}{(\frac{\pi D^2}{4})^2} \left(2 \ln \frac{P_i}{P_{i+1}} + f_i \frac{l_i}{D} \right) \quad (5)$$

$$\frac{1}{\sqrt{f_i}} = -2 \log \left(\frac{\epsilon}{3.7D} + \frac{2.51}{\mathrm{Re}_i \sqrt{f_i}} \right) \quad (6)$$

2.3 Field test

A series of medium-scale tests were performed in Sliedrecht, the Netherlands in July 2022. The main objective of the tests was to provide measurements of the pneumatic system used to generate the bubble curtain in order to gain insights into the pressure distribution along the length of the hoses for different volumetric flow rates of injected air. The tests comprise several configurations with different hose sizes, hose lengths, spacing between nozzles, and nozzle diameters. In this Section, the test results for one

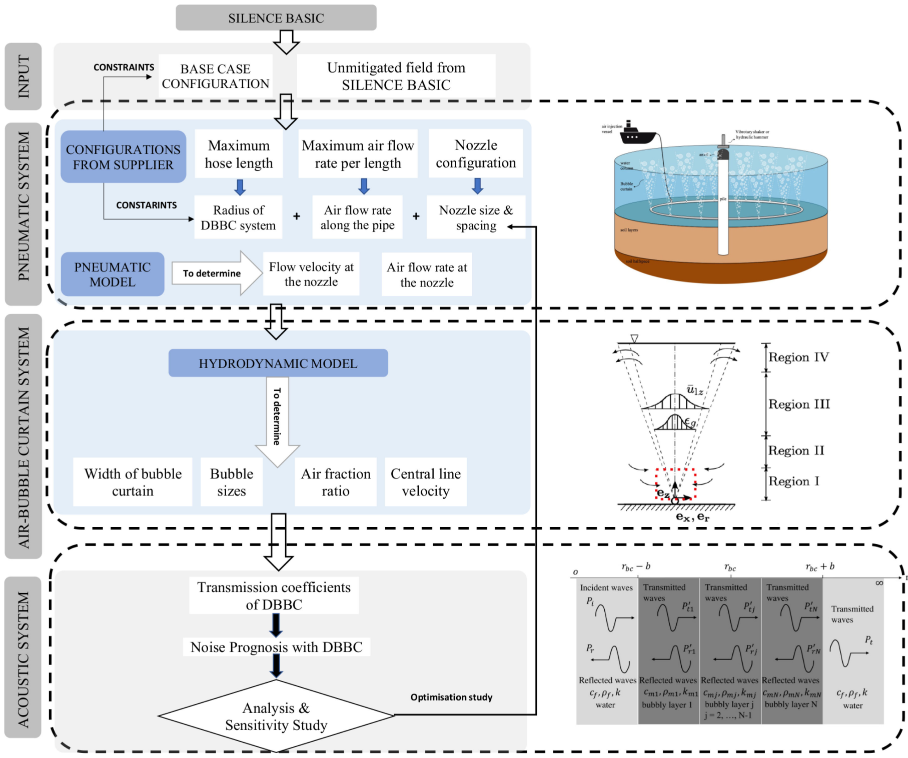

FIGURE 1
Activity flow of the complete model: 1) define the input of the model; 2) modelling of the pneumatic system; 3) modelling of the air-bubble curtain system; 4) modelling of the mitigated sound field with the use of DBBC.

configuration with varying air flow rates are presented to show the effect on the pressure distribution.

The measurements of the flow rate, pressure, and temperature sensors are continuously recorded during the entire measurement campaign. For each time trace of both flow and pressure measurements, several intervals under steady conditions were identified. The statistical values for each interval were calculated and reported for each pressure sensor located at certain distance from the feeding air as seen in Figure 3.

The test configuration for one of the field tests is presented in Table 1 with varying flow rates from 76.7m^3/hr to 200m^3/hr. This particular configuration has the closest similarity to the current practice setup from the scaled parameters. As shown in Figures 3A, B, for each flow rate, the pressure decreases nonlinearly with the distance between the pressure sensor and the air injection point. The pressure amplitude against the volume of air per unit time is also presented in Figure 3C for sensors at different horizontal distance from the air injection point. The numerical results are compard to the model as shown in Figures 3B–D, which indicates the results from the model and the field test agree reasonably well for pressure measurements below 3 bar. However, when it comes to higher pressures above 4 bar, the simulation shows lower pressure at the feeding point at all flow rates cases as the pressure is significantly underestimated. The discrepancy can be attributed to

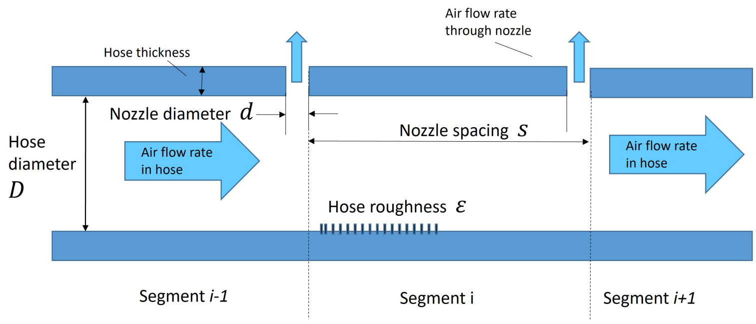

FIGURE 2
Schematic of the discretized model of the hose with nozzles for air transportation.

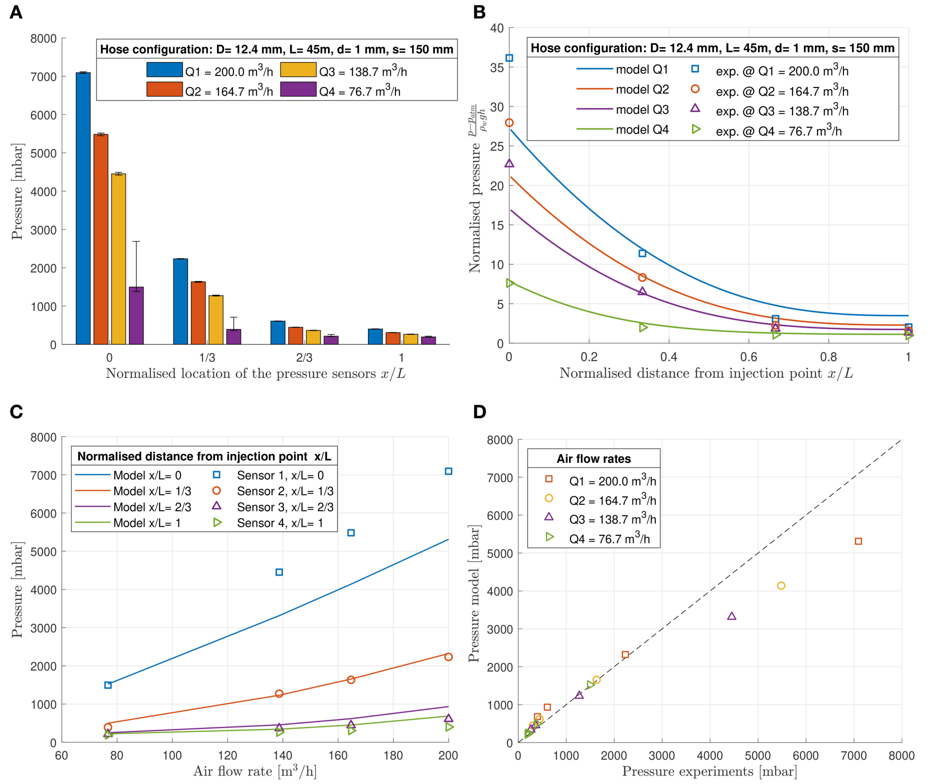

FIGURE 3
Comparison between simulation and experimental results for configuration tested at a water depth of 2.0m. L=45m, D=12.4mm, d=1.0mm, s=15cm. **(A)** Experimental results. **(B)** Pressure distribution along hose length. **(C)** Pressure vs airflow rate. **(D)** Comparison Model vs experiments.

the impact of the non-linear decrease of pressure closer to the air feeding point. The error bar on the top of each bar of the histogram in Figure 3 indicates the deviation from the mean value in the pressure during the recording at a constant flow rate. The nonlinear pressure drop indicates that the airflow circulation leads to the variation of the pressure and air flow through the nozzles in the azimuth, which has a significant impact on the performance of the air bubble curtain system along the circumference. By comparing the various airflow rates in the given hose-nozzle configuration, pressure at each location of the sensor increases nonlinearly with the airflow rate. The field test verifies the influence of the volumetric flow rate of the injected air on pressure distribution along the hose, which indicates that the performance of the air-bubble curtain varies along the circumference.

TABLE 1 Test configuration for the experiment.

Configuration	Value	Unit
Hose diameter	0.0124	m
Nozzle spacing	0.15	m
Nozzle diameter	0.001	m
Air Flow rate	76.7 to 200	m^3/hr
Hose length	45	m

3 Hydrodynamic and acoustic model for air-bubble curtain

The hydrodynamic model aims to capture the characteristics of bubble generation and development. The model describes a turbulent two-phase bubble flow, in which the bubble plume is developed from a nozzle and followed by the breakup and coalescence of bubbles. The modeling of the bubble formation is based on an existing model developed by (Bohne et al., 2019, 2020). Based on the airflow velocity through each nozzle derived from the pneumatic model, the input for the hydrodynamic model can be determined for a single bubble curtain configuration. The resulting set of equations reads,

$$\frac{d}{dz}\mathbf{m}(\mathbf{u},z) = \mathbf{q}(\mathbf{u},z) \tag{7}$$

In Eq. (7), $\mathbf{u}$ = [u_{lzm},b,ϵ_{gm1},ϵ_{gm2},v_1,v_2]. The results after solving the set of equations include the half-width of bubble curtain b, gas fraction ϵ_{gm1} and ϵ_{gm2}, flow velocity u_{lzm}, and mean bubble volume v_1 and v_2, which vary with the depth z. The expressions for the vector of the integral fluxes $m(\mathbf{u},z)$ and the integral source term $q(\mathbf{u},z)$ are presented in detail in (Bohne et al., 2020; Peng et al., 2021b) and are omitted here for the sake of simplicity.

The acoustic model includes the depth- and frequency-dependent transmission coefficients of each bubble curtain configuration. The model is based on a simplified one-dimensional acoustic wave propagation approach developed in (Commander and Prosperetti, 1989). Given the bubble characteristics obtained from the hydrodynamic model, the distribution of the local effective wavenumbers $k_m(\omega,z,r)$ is determined over the entire water depth as described in (Peng et al., 2021b). The transmission coefficients $\widetilde{H}(z,\omega)$ are then determined per z-coordinate and are constant within the vertical step size Δz of the integration. The transfer coefficient function is coupled to the noise prediction model through boundary integral equation. The local transmission loss (dB/m) is obtained as (Bohne et al., 2019; Peng et al., 2021b):

$$\mathbf{TL}(\omega) = 10\log\left(\sum_{i=1}^{M}\left|\widetilde{H}(z_i,\omega)\right|^2\frac{\Delta z}{T}\right) \tag{8}$$

in which T is the height of the bubble curtain, the Δz is the integration step in the water column and M are the total number of vertical steps.

4 Vibroacoustic model for noise prognosis

The noise prediction model for offshore pile driving is depicted in Figure 4. The noise prediction module comprises a pile modeled as a linear elastic thin shell and surrounding media modeled as horizontally stratified acousto-elastic half-space. The hammer and anvil are not modeled explicitly, but replaced by a forcing function F (t). The direct boundary element method (BEM) is deployed to couple the noise prediction model for non-mitigated field and the acoustic model for the air-bubble curtain as discussed in Section 3. The solution of the acousto-elastic wavefield employs Somigliana's identity in elastodynamics and Green's third identity in potential theory (Achenbach, 1973; Beskos, 1987; Jensen et al., 2011). The response functions from the noise prediction model are coupled to the sound propagation module through a boundary integral formulation on the cylindrical boundary surface $r = r_{bc}$. By utilizing Betti's reciprocal theorem in elastodynamics (Beskos, 1987) and Green's theorem for acoustic problem (Jensen et al., 2011), the complete solution for the acousto-elastic domain reads (Peng et al., 2021a):

$$\begin{aligned}
&\tilde{u}_{\alpha}^{\Xi}(\mathbf{r},\omega) = \tilde{u}_{\alpha}^{\Xi,f}(\mathbf{r},\omega) + \tilde{u}_{\alpha}^{\Xi,s}(\mathbf{r},\omega)\\
&= \sum_{\beta=r,z}\int_{S^s}\left(\widetilde{U}_{\alpha\beta}^{\Xi s}(\mathbf{r},\mathbf{r}_{bc},\omega)\cdot\tilde{t}_{\beta}^{\mathbf{n}}(\mathbf{r}_{bc},\omega) - \widetilde{T}_{\alpha\beta}^{\mathbf{n},\Xi s}(\mathbf{r},\mathbf{r}_{bc},\omega)\cdot\tilde{u}_{\beta}(\mathbf{r}_{bc},\omega)\right)dS^s(\mathbf{r}_{bc})\\
&+\int_{S^f}\widetilde{H}(z,\omega)\left(\widetilde{U}_{\alpha r}^{\Xi f}(\mathbf{r},\mathbf{r}_{bc},\omega)\cdot\tilde{p}(\mathbf{r}_s,\omega) - \widetilde{T}_{\alpha r}^{\mathbf{n},\Xi f}(\mathbf{r},\mathbf{r}_s,\omega)\cdot\tilde{u}_r(\mathbf{r}_{bc},\omega)\right)dS^f(\mathbf{r}_{bc}),\quad \mathbf{r}\in V
\end{aligned} \tag{9}$$

in which the fundamental solutions of Green's displacement tensors $\widetilde{U}_{\alpha\beta}^{\Xi\xi}(\mathbf{r},\mathbf{r}_s,\omega)$ are derived from the potential functions (Achenbach, 1973) given the receiver point at $\mathbf{r} = (r,z)$ (in medium Ξ) in α-direction due to a unit impulse at source, $\mathbf{r}_s = (r_{bc}, z_s)$ (in medium ξ) in β-direction $\mathbf{n}$ is the outward normal to the cylindrical boundary, $\widetilde{H}(z,\omega)$ is the transmission coefficient function of the air-bubble curtain with depthand frequency-dependence as discussed in Section 3.

5 Sensitivity analysis

In this Section, a parametric study is presented to examining the sensitivity of the acoustic characteristics of the air-bubble curtain system on the air volume injection rate, size of the bubble curtain, nozzle size of the hose, and DBBC configurations. As shown in Table 2, 13 scenarios are considered by varying the nozzle spacing and size, and flow velocity due to different air injection ratio and size of the bubble curtain. The base case nozzle configuration consists of a nozzle spacing of 0.3m, a nozzle diameter of 2mm, and a flow velocity of 100m/s, which is typically applied in offshore projects related to installation of foundation piles in offshore wind. To examine configurations for DBBC, three sets of analyses are performed for the varying radii of the outer BBC keeping the inner one at a fixed position, i.e., at 50m, 75m and 100m. For each configuration, three predictions are performed for the lower, upper and median values of the air flow rate.

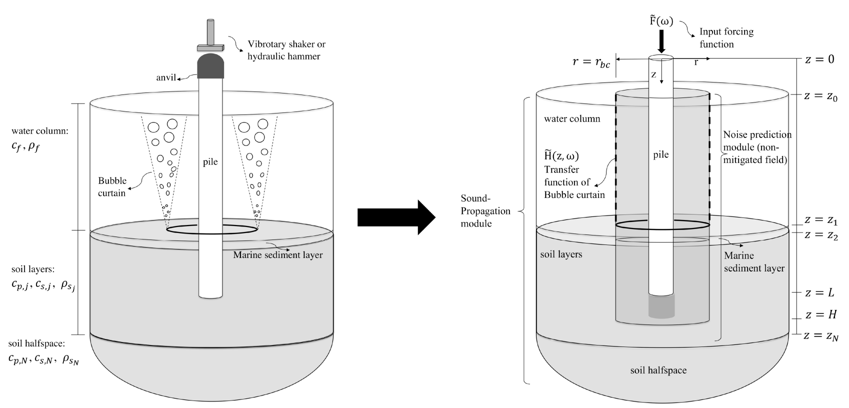

FIGURE 4
Geometry depiction of the complete system (left) and the coupled model (right) (Peng et al., 2021b).

TABLE 2 Varying input parameters of the bubble curtain system.

Case Nr.	Varying parameter	Value	Unit
1	Nozzle spacing	0.2	m
2	Nozzle spacing	0.3	m
3	Nozzle size	1	mm
4	Nozzle size	2	mm
5	Nozzle size	3	mm
6	Flow velocity	30	m/s
7	Flow velocity	50	m/s
8	Flow velocity	80	m/s
9	Flow velocity	100	m/s
10	Flow velocity	150	m/s
11	Flow velocity	200	m/s
12	Flow velocity	250	m/s
13	Flow velocity	300	m/s

5.1 Air volume injection rate

The air is injected into the perforated hose through two risers connecting to the air compressors and is distributed equally into the two semi-circles. Based on this deployment approach, the model adopts equal volumetric flow rates as input for two semi-circles of the hoses. As shown in Figure 5, the increase in the air volume injection rate can lead to an increase in the flow velocity at each nozzle along half of the hose length, while the other half has the same performance.

The air volume injection can significantly impact the bubble curtain formation process above the main hose. By examining Figure 5, we observe that for the bubble curtain with a radius of 75m, the variation in the flow velocity along the hose length, for a given volume injection rate, is relatively small. However, when the air volume injection is varied, differences up to ~20m/s (Δu) in the computed flow velocities at the nozzles are obtained. Subsequently, this can significantly change the initial turbulent kinetic energy at the nozzle and, thus, influence the air-bubble cloud formation process. The same naturally holds for bubble curtains of larger radii but those suffer additionally from a significant drop in the flow velocity at positions away from the air feeder lines as depicted in Figure 6.

5.2 Size of the bubble curtain

As shown in Figure 7, with the increase of the size of the BBC, the mean and lower bound of the flow velocity decrease, while the maximum of the velocity, which appears in the vicinity of the air injection inlet, remains within a small range. As the air is released from a nozzle, the pressure within the hose drops instantly, which leads to a decrease in the kinetic energy in the airflow. Considering the variation of the flow velocity due to both various air injection rates and the radius of the bubble curtain, the various flow velocities from 30m/s to 300m/s at the nozzle are considered in the analysis as shown in Table 2.

With the hydrodynamic model, the bubble formation process at the nozzle is predicted. To investigate the transmission of the bubble curtain over depth, the local distribution of the sound speed at 300Hz is depicted in Figure 8. The effective wave speed reduces up to 200m/s in the vicinity of the centerline. The darker zones indicate a large impedance mismatch between the seawater and air-seawater bubbly mixture, which widens as the flow velocity increases from left to right in Figure 8. Accordingly, this results in an increase in the transmission loss of the bubble curtain system as shown in Figure 9 from cases 6 to 13. Based on the deployed set of hoses, higher air injection rates can increase the acoustic performance of the bubble curtain. With an increase in the size of the bubble curtain, the efficiency of the bubble curtain can drop at positions away from the air-feeding lines due to the significant expected drop in the flow velocity.

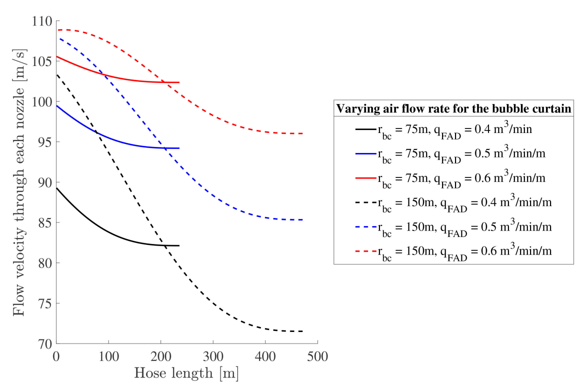

FIGURE 5
Computed flow velocities at the nozzles along the hose length for varying air volume injection rate for two different cases of bubble curtain radii, i.e. 75m and 150m.

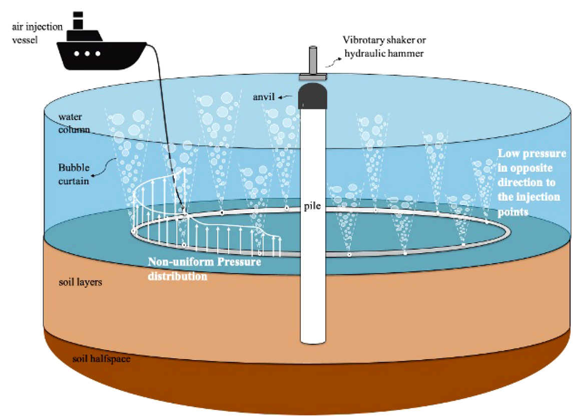

FIGURE 6
Schematic depiction of the non-uniform pressure distribution in the hose.

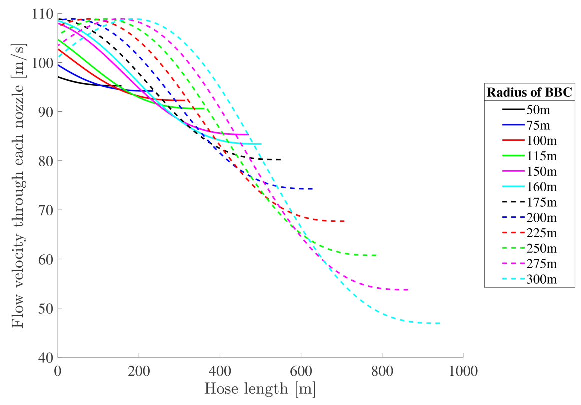

FIGURE 7
Computed flow velocities at the nozzles along the hose length for the varying radius of the bubble curtain.

5.3 Nozzle configuration

Typical nozzle sizes and spacing usually stay within a limited range in practice. In this analysis, a series of theoretical cases are considered. In cases 1 to 5, the nozzle configuration is investigated with the nozzle spacing being 0.2m and 0.3m and the nozzle size being 1mm to 3mm. Together with the variation in the flow velocities, the input for the varying parameters is shown in Table 2. To examine the impact of the aforementioned parameters on the acoustic insertion loss of the air-bubble curtain, the acoustic model is used to determine the transmission loss for each scenario. Figure 9A indicates that, within the typical nozzle configuration range, the acoustic insertion loss of the bubble curtain is more sensitive to nozzle size when flow velocity is constant, especially in the critical frequency range of ~60Hz to 200Hz.

5.4 Configuration of the DBBC

The sensitivity analysis is performed to examine the configuration of the DBBC, in which the scope of the operational constraints are considered. Three sets of the radius of the outer BBC are used, i.e., at 50m, 75m and 100m, while the inner one is at a fixed position. For each configuration, three predictions are performed for the median values of the air flow rates at the nozzle. The base case is set as the radius of the inner and outer BBC being 75m and 150m, respectively. The volumetric airflow rate in the hose is set as $0.5m^3/min/m$.

As can be seen in Figure 10, the noise reduction levels in both SEL and $L_{p,pk}$ increase with the radius of the inner bubble curtain shown by the blue, red and black lines. It is also clear that given a fixed position of the inner bubble curtain, there is an optimum distance in which the outer one should be placed. This may seem as counterintuitive in the first place as one would expect that a larger distance is always favorable. However, a longer pipe can result in larger pressure and air flow velocity drops away from the air-feeding lines which result in a suboptimal performance of the system on average.

The red and blue markers indicate the configuration of the base case with the volumetric air flow rate being 0.4 and $0.6m^3/min/m$, respectively. The bars and the marker indicate the predictions are performed for the same configuration and at the lower, higher and median values of the air flow rates at the nozzle. The comparison indicates that the increase in the mass flow rate by $0.1m^3/min/m$ in the hose can lead to up to ~1dB for both SEL and $L_{p,pk}$. However, the increase in the noise level cannot be obtained linearly from the volumetric airflow rate being $0.4m^3/min/m$ to $0.5m^3/min/m$ or 0.5 $m^3/min/m$ to $0.6m^3/min/m$. As discussed in Section 2.3, the pressure increases with the mass airflow rate, which leads to the nonlinear acoustic characteristics of the bubble curtain with increasing air flow rates. By comparing the noise levels for the lower, median and higher values of the air flow rates at the nozzle, a deviation of 1 dB can be expected as can be read from Figure 10. As observed from the field test, the pressure decreases nonlinearly with the distance between the sensor and the air feeding point, which leads to the variation in the airflow at the nozzle. The performance of the air-bubble curtain system relies strongly on both the volumetric airflow rates and the configuration of the DBBC.

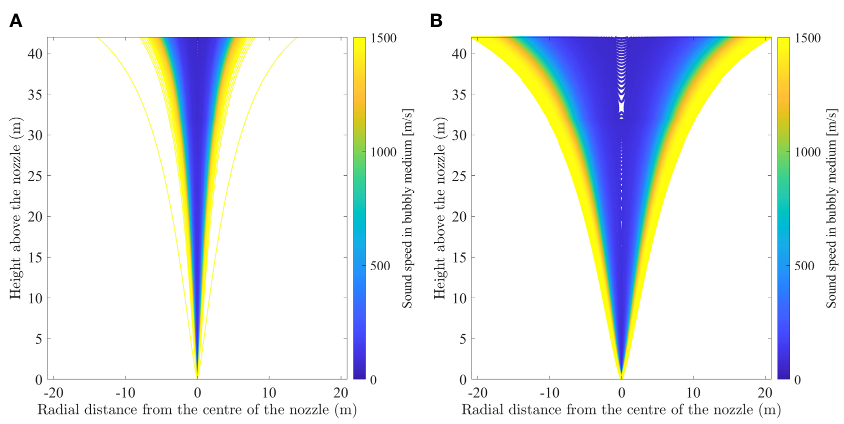

FIGURE 8
Comparison of the effective wave speed for various flow velocities of **(A)** 30m/s, **(B)** 300m/s for the frequency 300Hz.

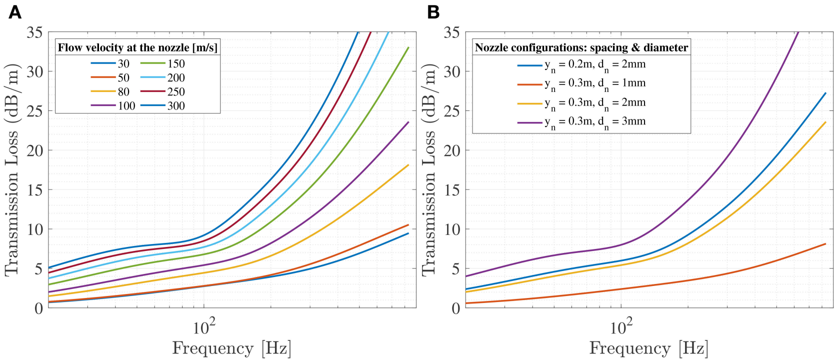

FIGURE 9
Transmission loss (TL) computed as a function of frequency for the cases examined in Table 2. **(A)** various nozzle configuration: spacing and diameter. **(B)** flow velocity at the nozzle.

5.5 Summary of the analysis

Due to the uneven distribution of the air flow velocity along the main hose, the acoustic insertion loss of the air-bubble curtain depends strongly on the air injection rate and the size of the bubble curtain. Within the critical frequency spectrum of interest in this project, the nozzle size and spacing seem to have less impact on the acoustic performance of the bubble curtain. However, the flow velocity through each nozzle can drop significantly away from the air-feeding points especially for longer pipes. This, in turn, can result in a strong azimuth-dependent acoustic field, i.e., the noise reduction achieved at different azimuthal positions may vary significantly due to the inhomogeneous air-bubble cloud formed.

6 Comparison with measured data

This section discusses a case based on an offshore wind farm foundation installation campaign in 2018 (Peng et al., 2021a, 2021b). The material properties and the geometry of the model are summarised in Table 3. The forcing function is defined as the smoothed exponential impulse as shown in Figure 11A, which results in approximately 2000kJ input energy into the pile. The seabed at this foundation consists of a thin marine sediment layer overlaying a stiff bottom soil half-space. The configuration of the DBBC system is presented in Table 4. The inner bubble curtain is positioned at 105m from the pile and the outer bubble curtain is positioned at 145m from the pile.

The variation in the flow velocity through the nozzles is shown in Figure 11B, which is due to the drop of the pressure during the transportation of the air. In Figure 12A, the evolution of the pressure field in time is shown for the point positioned 2m above the seabed at 750m radial distances from the pile.

The arrival of the pressure cones is at around 0.5s after the impact of the pile, which is in line with the expectations regarding the arrival time of the direct sound waves traveling with the speed of sound in the water at the distance of 750m from the pile. As can be seen, in the one-third octave band for both the unmitigated (the black line) and mitigated field (the grey line) in Figure 12B, the performance of the bubble curtain is more efficient at higher frequency bands approximately above 500Hz. The overall SEL and $L_{p,pk}$ for both unmitigated and mitigated fields are sumarised in Table 5. The zero-to-peak pressure level ($L_{p,pk}$) in dB re 1 μPa and the sound exposure level SEL in units of dB re 1 $\mu Pa^2 s$ are defined as:

$$\mathbf{L}_{p,pk} = 20\log\left(\frac{\max\ |p(t)|}{p_0}\right), \quad \mathbf{SEL} = 10\log\left(\int_{T_1}^{T_2}\frac{p^2(t)}{p_0^2}dt\right) \quad (10)$$

in which T_1 and T_2 are the starting and ending of the predicted time signature with the sound event in between and pulse duration $T_0 = T_2 - T_1$ being 1 second and $p_0 = 10^{-6}\mathbf{P}a$ is the reference underwater sound pressure.

The sound field without noise mitigation systems is predicted by the model developed in (Peng et al., 2021a). The prediction lies within the accuracy of the measurement equipment of the deviation within 1 or 2dB from the measured sound levels. The measured sound levels indicate a range of 14 to 17dB noise reduction at 750m achieved by the DBBC system for both SEL and $L_{p,pk}$. This reduction is calculated based on the difference between the modelled unmitigated sound field and the measured sound field collected while utilizing the DBBC system. The model used for the unmitigated sound field has been previously validated against the offshore measurement campaign conducted in 2018 (Peng et al., 2021a). At a further distance, the 1500m away from the pile, the noise reduction of 14 to 15dB can be achieved for SEL and 11 dB for $L_{p,pk}$. The modeling of the DBBC system showed an average noise reduction of 15dB for both SEL and $L_{p,pk}$ at 750m, and 14dB for SEL

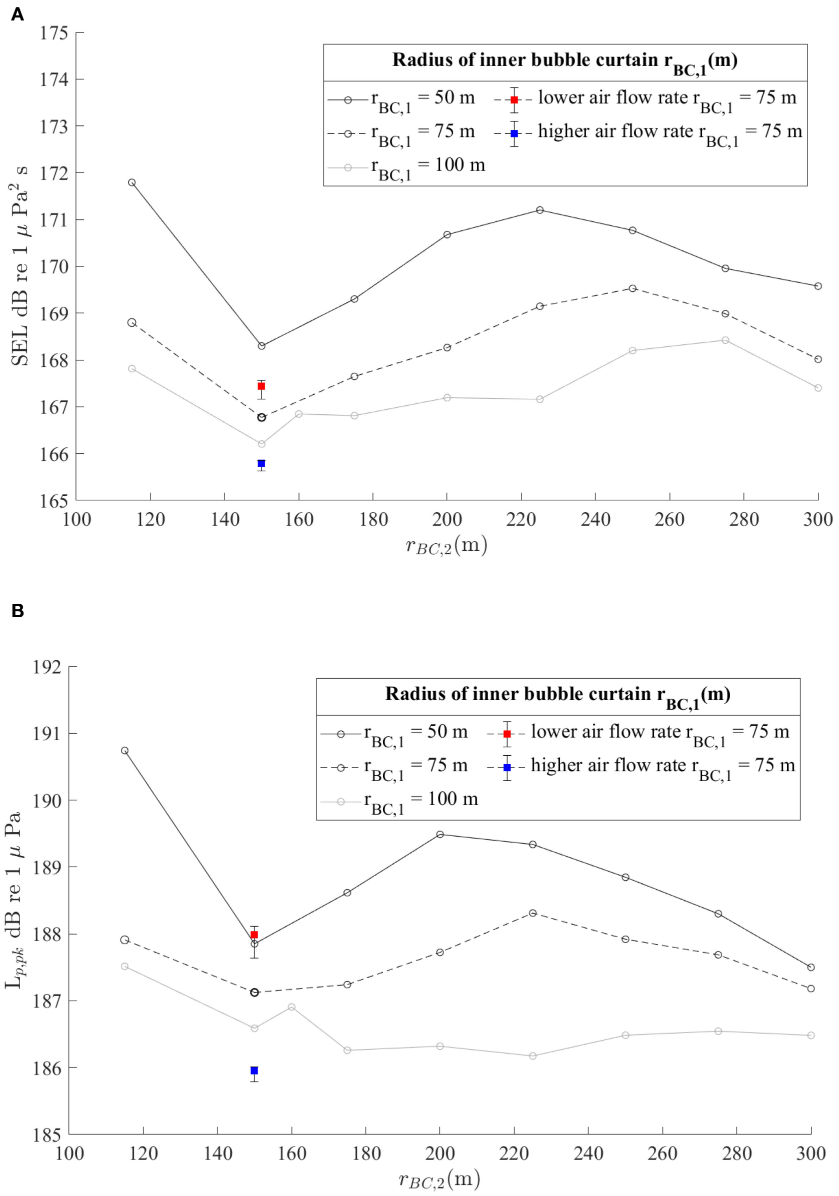

FIGURE 10
OWF foundation: comparison of the sound pressure levels for varying diameter of the outer bubble curtain with the radius of the inner bubble curtain being 50m (black solid line), 75m (black dashed line) and 100m (grey line). **(A)** SEL. **(B)** $L_{p,pk}$.

TABLE 3 Basic input parameters for the validation case.

Parameter	Pile	Parameter	Fluid	Marine sediment	Bottom soil
Length [m]	75	Depth [m]	40.1	1.5	∞
Density [kg/m^3]	7850	Density [kg/m^3]	1000	1621.5	1937.74
Outer diameter [m]	8	c_L [m/s]	1500	1603	1852
Wall thickness [mm]	90	c_T [m/s]	–	82	362
The penetration depth [m]	30.5	α_p $[dB/\lambda]$	–	0.91	0.88
Maximum Blow Energy [kJ]	2150	α_s $[dB/\lambda]$	–	1.86	2.77

- : it means the values are dimensionless.

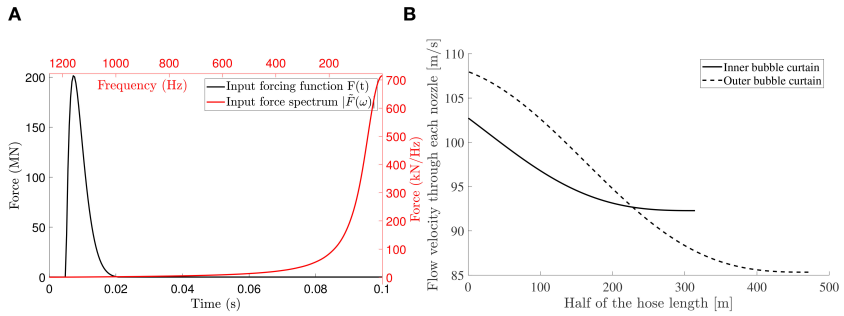

FIGURE 11
OWF foundation: **(A)** input forcing function in time and frequency domain; **(B)** flow velocity through each nozzle along the hose with the solid line indicating the air flow at the inner BBC and the dash line being the outer one.

and 15dB for $L_{p,pk}$ at 1500m. Due to variations in flow velocity through the nozzle at different azimuthal directions, a deviation of ±1dB in the noise reduction levels can be expected. The upper and lower bounds of the sound levels show that the range of prediction is within the measured data range, which indicates a great agreement between the noise prediction and the measured data at various horizontal distances from the pile.

TABLE 4 Basic input parameters of the air-bubble curtain system.

Parameter	Value
location of the inner bubble curtain r_{bc} [m]	105
location of the outer bubble curtain r_{bc} [m]	145
Nozzle diameter d_n [mm]	1.5
Nozzle spacing y_n [m]	0.30
Air flow rate q_{FAD} [m^3/min/m]	0.5
Spreading coefficient λ [-]	0.65

7 Conclusion

The paper presents a multi-physics approach for modeling the noise emission for offshore pile driving with the use of a DBBC system. The mathematical statement of the complete problem is given and the adopted method of solution is described for each module. The compressible flow model is developed to predict the operational parameters for bubble curtain generation from the hose and the nozzle. Nonlinear characteristics of the pressure distribution are observed both in the model results and in the field test. The pressure amplitude increases with volumetric airflow rates and decreases with the distance from the air injection point. The field test reveals the inherent variation in the airflow circulation, which leads to the varying performance of air-bubble curtain in azimuth direction. The hydrodynamic model aims to capture the fluid and bubble dynamic properties during the development of bubble curtains. The transmission coefficients derived from the acoustic module are coupled to the existing noise prediction model for the unmitigated field from pile driving. The sensitivity study has been performed to examine the critical parameters for the performance of the air-bubble curtain system. Both volumetric airflow rates and the configuration of the DBBC play significant roles in the efficiency of the air bubble

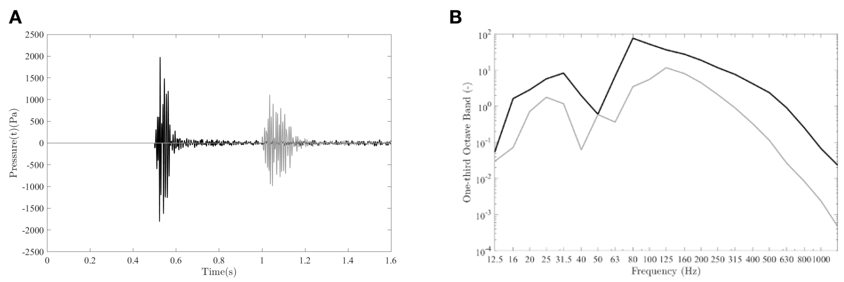

FIGURE 12
OWF foundation: **(A)** evolution of the pressure field for the mitigated field with the use of DBBC system at 750m (black line) and 1500m (grey line) from the pile; **(B)** one-third octave band of the pressure field at 750m for both unmitigated field (black line) and mitigated field (grey line).

TABLE 5 Noise mitigation assessment at the foundation.

Scenarios @750m	SEL	Lp,pk
Noise prediction for the unmitigated field	182	201
Noise prediction for the mitigated field with DBBC system	166 ± 1	185 ± 1
Measurement sound levels	165 168	184 187
Modelled noise reduction Δ_s	15 ± 1	15 ± 1
Measured noise reduction Δ_m	14 ~17	14 ~17
Scenarios @1500m	**SEL**	**Lp,pk**
Noise prediction for the unmitigated field	178	196
Noise prediction for the mitigated field with DBBC system	164 ± 1	181 ± 1
Measurement sound levels	163 164	185
Modelled noise reduction Δ_s	14 ± 1	15 ± 1
Measured noise reduction Δ_m	14 ~ 15	11

All values are given at a distance of 750m and 1500m from the pile. SEL are given in the unit of dB re 1μ Pa^2s and $L_{p,pk}$ in the unit of dB re 1μ Pa.

curtain system. Results are presented for an offshore pile installation campaign in the German North Sea. The comparison between the measured data and model predictions provides the validation of the model. The modeling approach couples four sub-modules and facilitate more accurate representation of the noise mitigation system. The multi-physics model allows for the examination of the optimal hose-nozzle and DBBC configurations under the operational constraints.

Data availability statement

The original contributions presented in the study are included in the article/supplementary material. Further inquiries can be directed to the corresponding author.

Author contributions

YP performed the data analysis, numerical modeling and produced the original draft of this manuscript. AJL conducted the original field test, data analysis, delivered the air transport model as well as the calibrated pressure and flow velocity data used by YP. AT contributed to the concept of the study, feedback on the results, and the discussion on the manuscript's content. YP, AJL and AT contributed to the review and revision of the original draft. All authors contributed to the article and approved the submitted version.

Funding

The author(s) declare that no financial support was received for the research, authorship, and/or publication of this article.

Acknowledgments

The authors wish to express their thanks to the BubbleJIP project for supporting this research, IHC IQIP for facilitating and supporting the experimental campaign on the bubble generation, and Van Oord for providing data from a recent offshore installation campaign.

Conflict of interest

The authors declare that the research was conducted in the absence of any commercial or financial relationships that could be construed as a potential conflict of interest.

Publisher's note

All claims expressed in this article are solely those of the authors and do not necessarily represent those of their affiliated organizations, or those of the publisher, the editors and the reviewers. Any product that may be evaluated in this article, or claim that may be made by its manufacturer, is not guaranteed or endorsed by the publisher.

References

Achenbach, J. D. (1973). "Wave propagation in elastic solids," in *North-Holland series in applied mathematics and mechanics, v. 16* (Amsterdam New York: North-Holland Pub. Co.; American Elsevier Pub. Co).

Bailey, H., Senior, B., Simmons, D., Rusin, J., Picken, G., and Thompson, P. M. (2010). Assessing underwater noise levels during pile-driving at an offshore windfarm and its potential effects on marine mammals. *Mar. Pollut. Bull.* 60, 888–897. doi: 10.1016/j.marpolbul.2010.01.003

Beskos, D. E. (1987). Boundary element methods in dynamic analysis. *Appl. Mechanics Rev.* 40, 1–23. doi: 10.1115/1.3149529

Bohne, T., Grießmann, T., and Rolfes, R. (2019). Modeling the noise mitigation of a bubble curtain. *J. Acoust. Soc. Am.* 146, 2212. doi: 10.1121/1.5126698

Bohne, T., Grießmann, T., and Rolfes, R. (2020). Development of an efficient buoyant jet integral model of a bubble plume coupled with a population dynamics model for bubble breakup and coalescence to predict the transmission loss of a bubble curtain. *Int. J. Multiphase Flow* 132, 103436. doi: 10.1016/j.ijmultiphaseflow.2020.103436

Bruns, B., Stein, P., Kuhn, C., Sychla, H., and Gattermann, J. (2014). Hydro sound measurements during the installation of large diameter offshore piles using combinations of independent noise mitigation systems. In Proceedings of the Inter-noise 2014 Conference, Melbourne, Australia.

Chahouri, A., Elouahmani, N., and Ouchene, H. (2022). Recent progress in marine noise pollution: A thorough review. *Chemosphere* 291, 132983. doi: 10.1016/j.chemosphere.2021.132983

Commander, K. W., and Prosperetti, A. (1989). Linear pressure waves in bubbly liquids: Comparison between theory and experiments. *J. Acoust. Soc. America* 85, 732–746. doi: 10.1121/1.397599

Dahl, P. H., and Dall'Osto, D. R. (2017). On the underwater sound field from impact pile driving: Arrival structure, precursor arrivals, and energy streamlines. *J. Acoust. Soc Am.* 142, 1141. doi: 10.1121/1.4999060

Dahl, P. H., Dall'Osto, D. R., and Farrell, D. M. (2015). The underwater sound field from vibratory pile driving. *J. Acoust. Soc. Am.* 137, 3544–3554. doi: 10.1121/1.4921288

Elmer, K.-H., Gattermann, J., Kuhn, C., and Bruns, B. (2012). Mitigation of underwater piling noise by air filled balloons and PE-foam elements as hydro sound dampers. *J. Acoust. Soc. Am.* 132, 2056–2056. doi: 10.1121/1.4755571

Fricke, M. B., and Rolfes, R. (2015). Towards a complete physically based forecast model for underwater noise related to impact pile driving. *J. Acoust. Soc. Am.* 137(3), 1564–1575. doi: 10.1121/1.4908241

Hastie, G., Merchant, N. D., Gotz, T., Russell, D. J. F., Thompson, P., and Janik, V. M. (2019). Effects of impulsive noise on marine mammals: investigating range-dependent risk. *Ecol. Appl.* 29(5), e01906. doi: 10.1002/eap.1906

International Maritime Organization (2014). Guidelines for the reduction of underwater noise from commercial shipping to address adverse impacts on marine life. *Tech. Rep*. Available at: https://cetsound.noaa.gov/Assets/cetsound/documents/MEPC.1-Circ%20883%20Noise%20Guidelines%20April%202014.pdf.

Jensen, F. B., Kuperman, W. A., Porter, M. B., and Schmidt, H. (2011). *Computational Ocean Acoustics* (New York: Springer).

Lee, K. M., McNeese, A. R., Wilson, P. S., and Wochner, M. S. (2014). Using arrays of air-filled resonators to attenuate low frequency underwater sound. *Proc. Meetings Acoustics* 22, 045004. doi: 10.1121/2.0000145

Lippert, T., Ainslie, M. A., and von Estorff, O. (2018). Pile driving acoustics made simple: Damped cylindrical spreading model. *J. Acoust. Soc Am.* 143, 310. doi: 10.1121/1.5011158

Lippert, S., Huisman, M., Ruhnau, M., Estorff, O., and van Zandwijk, K. (2017). "Prognosis of underwater pile driving noise for submerged skirt piles of jacket structures," in *Proceedings of the UACE 2017 4th Underwater Acoustics Conference and Exhibition*.

Lippert, S., Nijhof, M., Lippert, T., Wilkes, D., Gavrilov, A., Heitmann, K., et al. (2016). COMPILE—A generic benchmark case for predictions of marine pile-driving noise. *IEEE J. Oceanic Eng.* 41, 1061–1071. doi: 10.1109/JOE.2016.2524738

Menon, E. S. (2015). *Transmission Pipeline Calculations and Simulations Manual* (Waltham, MA: Gulf Professional).

Merchant, N. D., Putland, R. L., Andre, M., Baudin, E., Felli, M., Slabbekoorn, H., et al. (2022). A decade of underwater noise research in support of the european marine strategy framework directive. *Ocean* &. *Coast. Manage.* 228, 106299. doi: 10.1016/j.ocecoaman.2022.106299

Molenkamp, T., Tsouvalas, A., and Metrikine, A. V. (2023). The influence of contact relaxation on underwater noise emission and seabed vibrations due to offshore vibratory pile installation. *Front. Mar. Sci.* 10. doi: 10.3389/fmars.2023.1118286

National Oceanic and Atmospheric Administration (2016). Technical guidance for assessing the effects of anthropogenic sound on marine mammal hearing: underwater acoustic thresholds for onset of permanent and temporary threshold shifts. *Tech. Rep.* NOAA Technical Memorandum NMFS-OPR-55. Available at: https://www.fisheries.noaa.gov/resource/document/technical-guidance-assessing-effects-anthropogenic-sound-marine-mammal-hearing.

Nehls, G., and Bellmann, M. (2016). Weiterentwicklung und erprobung des "großenblasenschleiers" zur minderung der hydroschallemissionen bei offshore-rammarbeiten: Schlussbericht. *Tech. Rep.* Bio-Consult SH GmbH & Company KG; itap GmbH Oldenburg; Hydrotechnik Lubeck. doi: 10.2314/GBV:868671320

Nehls, G., Rose, A., Diederichs, A., Bellmann, M., and Pehlke, H. (2016). "Noise mitigation during pile driving efficiently reduces disturbance of marine mammals," in *Advances in Experimental Medicine and Biology 2214-8019* (New York, NY: Springer New York). doi: 10.1007/978-1-4939-2981-8_92

Peng, Y., Tsouvalas, A., Stampoultzoglou, T., and Metrikine, A. (2021a). A fast computational model for near- and far-field noise prediction due to offshore pile driving. *J. Acoust. Soc. Am.* 149, 1772–1790. doi: 10.1121/10.0003752

Peng, Y., Tsouvalas, A., Stampoultzoglou, T., and Metrikine, A. (2021b). Study of the sound escape with the use of an air bubble curtain in offshore pile driving. *J. Mar. Sci. Eng.* 9 (2), 232. doi: 10.3390/jmse9020232

Reinhall, P. G., and Dahl, P. H. (2011). Underwater mach wave radiation from impact pile driving: theory and observation. *J. Acoust. Soc Am.* 130, 1209–1216. doi: 10.1121/1.3614540

Shapiro, A. H. (1953). *The dynamics and thermodynamics of compressible fluid flow* (New York: Ronald Press).

Tidau, S., and Briffa, M. (2016). Review on behavioral impacts of aquatic noise on crustaceans. *Proc. Mtgs. Acoust.* 27, 010028. doi: 10.1121/2.0000302

Tsetas, A., Tsouvalas, A., and Metrikine, A. V. (2023). A non-linear three-dimensional pile–soil model for vibratory pile installation in layered media. *Int. J. Solids Structures* 269, 112202. doi: 10.1016/j.ijsolstr.2023.112202

Tsouvalas, A. (2020). Underwater noise emission due to offshore pile installation: A review. *Energies* 13(12), 3037. doi: 10.3390/en13123037

Tsouvalas, A., and Metrikine, A. V. (2013). A semi-analytical model for the prediction of underwater noise from offshore pile driving. *J. Sound Vib.* 332, 3232–3257. doi: 10.1016/j.jsv.2013.01.026

Tsouvalas, A., and Metrikine, A. V. (2014). A three-dimensional vibroacoustic model for the prediction of underwater noise from offshore pile driving. *J. Sound Vib.* 333, 2283–2311. doi: 10.1016/j.jsv.2013.11.045

Tsouvalas, A., and Metrikine, A. V. (2016a). Noise reduction by the application of an air-bubble curtain in offshore pile driving. *J. Sound Vibration* 371, 150–170. doi: 10.1016/j.jsv.2016.02.025

Tsouvalas, A., and Metrikine, A. V. (2016b). Structure-borne wave radiation by impact and vibratory piling in offshore installations: from sound prediction to auditory damage. *J. Mar. Sci. Eng.* 4, 44. doi: 10.3390/jmse4030044

Verfuß, T. (2014). *Noise mitigation systems and low-noise installation technologies* (Wiesbaden: Springer Fachmedien Wiesbaden : Springer Spektrum). doi: 10.1007/978-3-658-02462-8_16

Wilkes, D. R., Gourlay, T. P., and Gavrilov, A. N. (2016). Numerical modeling of radiated sound for impact pile driving in offshore environments. *IEEE J. Oceanic Eng.* 41, 1072–1078. doi: 10.1109/JOE.2015.2510860

Williams, R., Ashe, E., Blight, L., Jasny, M., and Nowlan, L. (2014). Marine mammals and ocean noise: Future directions and information needs with respect to science, policy and law in Canada. *Mar. Pollut. Bull.* 86, 29–38. doi: 10.1016/j.marpolbul.2014.05.056

Zampolli, M., Nijhof, M. J., de Jong, C. A., Ainslie, M. A., Jansen, E. H., and Quesson, B. A. (2013). Validation of finite element computations for the quantitative prediction of underwater noise from impact pile driving. *J. Acoust. Soc Am.* 133, 72–81. doi: 10.1121/1.4768886

Frontiers in Marine Science

Explores ocean-based solutions for emerging global challenges

The third most-cited marine and freshwater biology journal, advancing our understanding of marine systems and addressing global challenges including overfishing, pollution, and climate change.

Discover the latest Research Topics

See more →

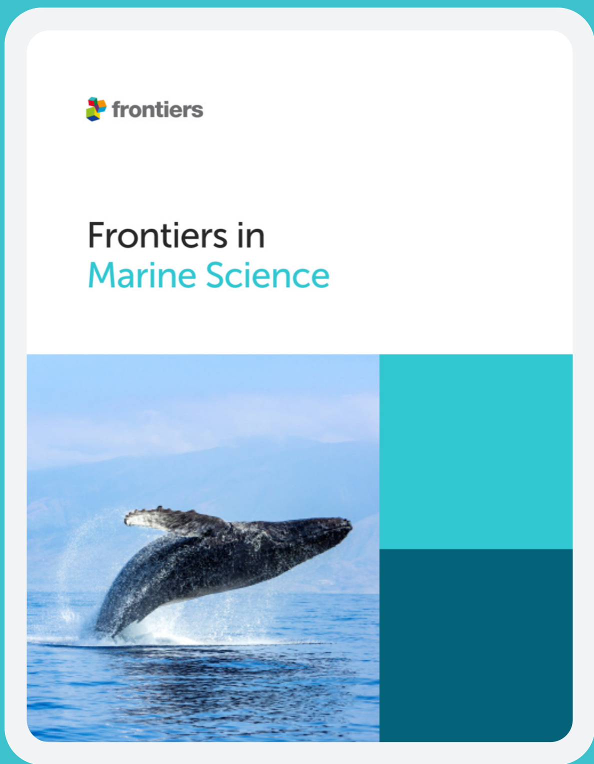

Frontiers

Avenue du Tribunal-Fédéral 34
1005 Lausanne, Switzerland
frontiersin.org

Contact us

+41 (0)21 510 17 00
frontiersin.org/about/contact